

MEASURING GEOMETRY AND TOPOLOGY
OF FLOQUET-BLOCH STATES
IN AND OUT OF EQUILIBRIUM
WITH ULTRACOLD FERMIONS

Dissertation
zur Erlangung des Doktorgrades
des Departments Physik
der Universität Hamburg

vorgelegt von
Dominik Vogel

Hamburg
2018

Gutachter der Dissertation:	Prof. Dr. Klaus Sengstock Prof. Dr. Andreas Hemmerich
Zusammensetzung der Prüfungskommission:	Prof. Dr. Klaus Sengstock Prof. Dr. Andreas Hemmerich Prof. Dr. Daniela Pfannkuche Prof. Dr. Markus Drescher Prof. Dr. Henning Moritz
Vorsitzender der Prüfungskommission:	Prof. Dr. Daniela Pfannkuche
Datum der Disputation:	07.06.2018
Vorsitzende des Fach-Promotionsausschusses PHYSIK:	Prof. Dr. Wolfgang Hansen
Leiter des Fachbereiches PHYSIK:	Prof. Dr. Prof. Dr. Michael Potthoff
Dekan der Fakultät MIN	Prof. Dr. Heinrich Graener

Abstract

The intriguing physics discovered with the famous quantum Hall effect was the first sign of what was later unraveled to be a whole, yet unknown class of phases of quantum matter. The study of these so-called *topological* quantum phases has become a deeply relevant topic for state of the art research bridging various disciplines of physics such as condensed matter physics, ultra cold atoms, trapped ions, and quantum computing.

As part of this work, two experiments on quantum many body systems in the vicinity of a topological phase transition were conducted. This thesis reports on their realization, results, and interpretation. In the first experiment the Berry curvature of a Floquet Bloch band is reconstructed with a high resolution in the Brillouin zone. The second experiment reports on the observation of dynamical vortices in nonequilibrium states after a quench into a topological system.

For both experiments ultracold atoms were employed as a platform to precisely engineer Hamiltonians with the desired geometrical and topological properties. For that we implemented a hexagonal optical lattice that provides a freely tunable offset between odd and even sites. Furthermore, the absolute lattice position can be dynamically controlled. This enables us to periodically drive the atomic ensemble and thereby create effective Floquet Hamiltonians, that have fundamentally different properties from the static system, including nontrivial topology, which requires the breaking of time reversal symmetry. The lowest two bands in the band structure of the considered systems form a family of s-bands, that is well separated from the rest of the spectrum. We study the non-interacting states in these bands at a filled lower band, and explore the phase diagram spanned by the Floquet driving frequency and modulation depth, with focus on the regime of near resonant driving, where the system undergoes a transition to a topological insulator.

In the first experiment we reconstructed the Berry curvature distribution within the first Brillouin zone of the described system via a complete state tomography measurement. The Berry curvature is a central geometric property of quantum systems subjected to adiabatic changes. The integral of the Berry curvature over the Brillouin zone yields the *Chern index*, which serves as a topological order parameter. The measurement of the Berry curvature is highly relevant because it opens the path towards a deeper understanding of the underlying geometric properties that lead to topological effects. Prior to this experiment the Berry curvature has not been measured for lattice periodic systems. The observables for the measurement are atomic density oscillations after time of flight expansion, caused by the dynamics following a quench into a system with flat bands. Similarly to a Rabi oscillation measurement, the observed oscillations fully characterize the respective quasimomentum eigenstate. In this thesis the experimental techniques and the acquired data that shows a

significant Berry curvature for a parameter regime close to the expected phase transition is presented.

The second part of this thesis reports on the observation of the creation, movement, and annihilation of dynamical vortex pairs in a highly excited state, during its evolution in a Floquet-Bloch system of the previously described type. The dynamics of the vortices constitute a link between the characteristics of nonequilibrium dynamics and the topological phase of the underlying system. From the trace of the vortices in quasimomentum space it is possible to determine the Chern number and thereby the topological phase of the system. In our system the mere emergence of the vortices signals the proximity in system parameter space to the phase transition. We further identify the number of vortices as a topological order parameter for a dynamical phase transition. While ordinary quantum phase transitions are defined for equilibrium systems and occur at a critical value of an adiabatic control parameter, like e.g. the magnitude of the applied magnetic field, a dynamical phase transition is defined for nonequilibrium states and appears under the evolution of the state at critical times. The measurements presented here extend the ones in the first part of the thesis. Here, instead of preparing an eigenstate of the system, a highly excited state is prepared by an initial quench from a topological trivial system into a nontrivial system. We reconstruct the state for a series of evolution times via a complete state tomography. In the acquired phase data the dynamics of the vortices can clearly be seen, and the parameter regime for their emergence coincides with our numerical simulation of the system.

In addition to these experiments, this thesis reports on a fiber phase lock, that has been developed as part of this work. The fiber phase lock is an optical and electronic setup that allows suppressing the phase noise, which a laser beam picks up upon passage through an optical fiber. For optical lattices this noise is transduced into the domain of the lattice position or the lattice structure. The presented solution employs a local end, heterodyne measurement of the picked up phase as an error signal for a digital feedback loop, that actuates on the phase via an acousto-optic modulator that is driven by a direct digital synthesis signal. The digital controller has been implemented on the platform of an embedded system with real time capabilities.

Zusammenfassung

Die faszinierende Physik die im Zusammenhang mit dem Quanten-Hall-Effekt entdeckt wurde, war ein erstes Zeichen für das was sich später als eine vollständige neue Kategorie von Quanten-Materie-Phasen herausstellte. Die Erforschung dieser sogenannten *topologischen* Quantenphasen hat sich zu einem höchst relevanten Themengebiet der aktuellen Forschung in verschiedenen Bereichen der Physik entwickelt, von Festkörperphysik über ultrakalte Atome, gefangene Ionen hin zu Quantencomputern.

Im Rahmen dieser Arbeit wurden zwei Experimente an Quanten-Vielteilchen-Systemen nahe topologischer Phasenübergänge durchgeführt. Diese Dissertation berichtet von der Umsetzung dieser Experimente, deren Ergebnissen und Interpretation. In dem ersten Experiment wird die Berry-Krümmung eines Floquet-Bloch-Bandes mit hoher Auflösung in der Brillouin-Zone rekonstruiert. Das zweite Experiment zeigt die Beobachtung dynamischer Vortices in Nichtgleichgewichtszuständen nach der Projektion in ein topologisches System.

Für beide Experimente dienten ultrakalte Atome als Plattform um kontrolliert Hamilton-Operatoren mit den gewünschten geometrischen und topologischen Eigenschaften zu konstruieren. Um dies zu erreichen errichteten wir ein hexagonales optisches Gitter mit einer frei einstellbaren Gittertiefendifferenz zwischen geraden und ungeraden Minima. Zusätzlich kann die absolute Gitterposition dynamisch kontrolliert werden. Damit ist es uns möglich das Atom-Ensemble periodisch zu treiben und so effektive Floquet-Hamilton-Operatoren zu schaffen, welche sich in ihren Eigenschaften fundamental von dem statischen System unterscheiden, u. a. durch ihre nicht-triviale Topologie, welche das Brechen der Zeitumkehrinvarianz erfordert. Die untersten zwei Bänder in der Bandstruktur des betrachteten Systems bilden eine Familie von s-Bändern die von dem Rest des Spektrums separiert ist. Wir untersuchen nichtwechselwirkende fermionische Zustände in diesen Bändern bei einem gefüllten unteren Band und erkunden das Phasendiagramm das durch die Floquet-Antriebsfrequenz und Modulationstiefe aufgespannt wird. Dabei liegt der Fokus im Bereich des nahresonanten getriebenen Systems in dem der Phasenübergang zur topologischen Isolatorphase stattfindet.

Im ersten Experiment rekonstruierten wir die Berry-Krümmungs-Verteilung innerhalb der ersten Brillouin-Zone des beschriebenen Systems mittels einer vollständigen Zustands-Tomographie-Messung. Die Berry-Krümmung ist eine zentrale geometrische Eigenschaft von Quantensystemen mit adiabatisch variierenden Parametern. Das Integral der Berry-Krümmung über die Brillouin Zone ist der *Chern Index*, welcher als topologischer Ordnungsparameter dient. Die Messung der Berry Krümmung ist höchst relevant, weil sie den Weg zu einem tieferen Verständnis der den topologischen Effekte zugrundeliegenden geometrischen Eigenschaften ebnet. Vor den hier vorgestellten Messungen wurde die

Berry-Krümmung noch nicht für gitterperiodische Systeme gemessen. Die Observablen der Messung sind die Oszillationen der atomaren Dichte nach time-of-flight Expansion, die durch die Projektion in flache Bänder hervorgerufen werden. Ähnlich zu einer Rabi-Oszillations-Messung, charakterisieren die beobachteten Oszillationen den zugehörigen Gitterimpuls-Eigenzustand vollständig. In dieser Arbeit werden die experimentelle Vorgehensweise und die erlangten Daten präsentiert, welche eine signifikante Berry-Krümmung in dem erwarteten Parameterregime nahe des Phasenübergangs zeigen.

Der zweite Teil dieser Arbeit berichtet von der Beobachtung der Erzeugung, Bewegung und Vernichtung von dynamischen Vortex-Paaren in einem hochangeregten Zustand während seiner Entwicklung in einem Floquet-Bloch-Systems des zuvor beschriebenen Typs. Die Dynamik der Vortices stellt eine Verbindung zwischen dem Feld der Nichtgleichgewichtsdynamik und der topologischen Phase des zugrundeliegenden Systems her. Von der Trajektorie der Vortices im Quasiimpulsraum ist es möglich die Chern-Zahl und damit die topologische Phase des Systems zu bestimmen. In dem von uns untersuchten System signalisiert das bloße Erscheinen der Vortices die Nähe im Systemparameterraum zu einem Phasenübergang. Desweiteren identifizieren wir die Anzahl der Vortices als einen topologischen Ordnungsparameter für einen *dynamischen Phasenübergang*. Während gewöhnliche Quantenphasenübergänge für Gleichgewichtssysteme definiert sind und beim adiabatischen Erreichen eines kritischen Wertes eines Kontrollparameters auftreten, wie zum Beispiel der Stärke des angelegten Magnetfeldes, ist der dynamische Phasenübergang für Nichtgleichgewichtszustände definiert und tritt bei der Entwicklung des Zustandes zu kritischen Zeiten auf. Die hier vorgestellten Messungen ähneln denen des erstens Teils dieser Arbeit, mit dem Unterschied, dass nicht Eigenzustände des zu untersuchenden Systems präpariert werden, sondern hoch angeregte Zustände, welche durch die Projektion von einem topologisch trivialen Systems in ein nicht triviales präpariert werden. Wir rekonstruieren den gesamten Zustand für eine Serie von Entwicklungszeiten mithilfe der vorgestellten vollständigen Zustandstomographie. In den aufgezeichneten Phasenprofilen ist die Dynamik der Vortices deutlich erkennbar, und das Parameterregime ihres Auftretens stimmt mit unseren numerischen Simulationen überein.

Zusätzlich zu diesen Experimenten berichtet diese Dissertationsschrift von einer sog. Faser-Phasen-Regelung, die im Rahmen dieser Arbeit entwickelt wurde. Die Faser-Phasen-Regelung ist ein optischer und elektronischer Aufbau, der es erlaubt das Phasenrauschen, das ein Laserstrahl bei dem Durchlaufen einer optischen Faser erleidet, zu unterdrücken. Die vorgestellte Lösung verwendet eine Laser-seitige AC-Messung der aufgesammelten Phase als ein Fehlersignal für eine digitale Feedback-Regelung, die per direkter digitaler Signalsynthese (DDS) einen akusto-optischen Modulator treibt. Der digitale Controller wurde auf der Basis eines embedded systems mit Echtzeitfähigkeit umgesetzt.

Contents

1	Introduction	1
1.1	Outline	5
2	Preparing and Probing Ultracold Trapped Fermions	9
2.1	Preparation of Ultracold Potassium	9
2.2	Laser Setup for a Hexagonal Lattice	12
2.3	Extended Experiment Control	17
2.4	Fringe Removal	18
3	Ultracold Atoms in Optical Lattice Potentials	25
3.1	The optical dipole potential	25
3.2	Lattice structures	26
3.2.1	Three beam lattices	28
3.2.2	In-plane lattices	31
3.2.3	Hexagonal lattices	32
3.3	Band Structure Description	34
3.3.1	Numerical Implementation	36
3.4	A Tight-Binding Model for Boron Nitride Lattices	41
3.4.1	Motivation	41
3.4.2	The Tight-Binding Description	42
3.4.3	Properties of Two-Band Hamiltonians	44
3.4.4	Boron Nitride Lattice	45
4	Geometry and Topology of Periodically Driven Boron Nitride Lattices	49
4.1	Geometric Phases in Non-relativistic Quantum Mechanics	49
4.2	Berry Calculus	50
4.2.1	Geometric Interpretation of the Berry Phase	53
4.2.2	Geometry of a Two-Dimensional Lattice Hamiltonian	55
4.3	Geometry of the Circularly Driven Boron Nitride Lattice	57
4.3.1	Periodically Driven Two-Band Tight-Binding Hamiltonian	61
4.3.2	Gauge Dependency and Adiabatic Launching	62
4.3.3	Full Evolution at the K-Point	63
5	State Tomography for an Optical Lattice	65
5.1	Time of Flight Imaging and the Sublattice Basis	66

5.2	State Tomography	68
6	Experimental Reconstruction of the Berry Curvature in a Floquet Bloch Band	71
6.1	Experimental Protocol	71
6.2	Data Analysis	74
6.3	Summary and Outlook	78
7	Nonequilibrium Dynamics in Topological Bands	79
7.1	Quench Dynamics in Bloch Bands	79
7.1.1	Kitaev-Chain with Next Nearest Neighbor Hopping	85
7.2	Dynamical Vortices and Topology in Shaken Boron Nitride Lattices	86
7.3	Connection to Dynamical Phase Transitions	90
7.4	Connection to the Pancharatnam Geometric Phase	96
8	Experimental Observation of Dynamical Vortices in a Topological Bloch Band	99
8.1	Experimental Scheme	99
8.2	Results	102
8.3	Interpretation and Outlook	108
9	Development of a Digital Fiber Phase Lock	111
9.1	Phase Discrimination and Phase Control	114
9.1.1	Model	116
9.1.2	Basic Phase Stabilization Scheme	116
9.1.3	Improved Phase Stabilization Scheme	118
9.1.4	Comparison	120
9.2	All digital phase-locked loop	124
9.2.1	Hardware implementation	126
9.2.2	Software implementation	129
9.3	Implementation and Performance	133
9.3.1	Cycle frequency	136
9.3.2	Step Response	136
9.3.3	Heterodyne Measurements	137
9.4	Outlook	141
	Appendix A Lattice Definitions	143
	Appendix B Band structure Code	145
	Appendix C Fiber Lock	147
	C.1 Electronics	147
	C.2 Fiber Lock Code	149
	Bibliography	151

1 Introduction

Topology and differential geometry are two closely related mathematical disciplines that form the foundation for the description of a wide range of advanced physical phenomena, in a similar manner as e.g. function analysis forms the foundation to Newton mechanics. Famous examples among those geometric or topological phenomena from the realm of classical physics are, among others, the rotation of the swinging plane of the Foucault pendulum [1] and the curved spacetime as the central concept of the special [2] and general [3] theory of relativity. Also for Quantum mechanics topology and geometry have become an important foundation, as for example for the description of the Aharonov-Bohm effect (*ABE*) [4] and the famous quantum Hall effect (*QHE*) [5, 6] which represents the embarquement of the field of condensed matter physics into a paradigm change by defining the new class of *topological* quantum phases of matter [7, 8]. But the journey into unraveling the mysteries of topological states of matter has not finished yet, and it forms a highly active field of current research (e.g. reviews [9–11]). This strong interest might be motivated by the high applicability of topological materials in technology development and other fields of research. The prime example for a field of applications is the development of quantum computers, which are a promising candidate for the next technological revolution. Probably the biggest hurdle [12] to be overcome in the quest for constructing a potent quantum computer is the problem of the fragility of the quantum states that encode the information on such a system, also known as QuBits. Here, the combination of a so-called topological insulator with a superconductor may allow the creation of topologically protected quantum states [13], that overcome the short-lived coherence of the QuBits.

Differential geometry as a field of mathematics can be depicted, in a simplified way, as the study of structures¹ attached to curved surfaces². A visual example is the angle sum of a triangle on a sphere: imagine drawing a line from the north pole down to the equator, then following it for a quarter rotation before closing the line again at the north pole. At each corner the sides enclose a right angle and therefore make up an angle sum of 270° , breaking the rule of the 180° angle sum for triangles on a flat surface. The reason for this mismatch is of course the *curvature* of the sphere. For more irregular shaped surfaces, the angle sum will generally be dependent on the position of the triangle on the surface.

While differential geometry is concerned with such local quantities of curved spaces, the field of topology studies global properties. Here the iconic example is the Gauss-Bonnet theorem, which states that the integral of the (gaussian) curvature over the full surface yields a total curvature of $2\pi(2 - g)$, where g is an integer number, a so-called topological

¹Structures in the sense of mathematical structures such as vector spaces, groups, etc.

²or more generally differentiable manifolds

index, that can be used to group surfaces into classes. This specific index counts the number of holes of the surface, i.e. zero for a sphere, one for a torus, two for a pretzel, and so on. This example illustrates two important properties of topological indices. Firstly, the number of holes can only be changed when the surface is “cut” and “glued” together again, which translates to the previously mentioned topological protection. Secondly, for determining g the full surface is involved, in the sense that any missing part might contain additional holes, and is therefore a *global* property.

For geometry and topology in the context of quantum physics, the spaces of interest are the high dimensional Hilbert spaces formed by the entirety of the possible quantum mechanical states of a system, and the “attached” spaces are the quantum mechanical phases of the wave functions³. In analogy to the previous example of the angle sum of the triangle, a non flat surface like the sphere here corresponds to geometrically nontrivial Hilbert spaces, and the angle sum deviation from 180° here corresponds to a *quantum geometric phase*. The quantum geometric phase leads to novel interference phenomena that are not present in geometrically trivial systems. For the case of a static system, i.e. a system that occupies a state that does not change with time⁴, the quantum geometric phase is called the Berry phase [14]. Because the wave function in this case can be derived from the system parameters, the Berry phase can be regarded as a phase “attached” to a parameter space. If the system is for example an electron, such a system parameter could be the position of the electron as it determines the present magnetic field (or rather the vector potential)[15]. Keeping the visualization via the angle sum of a triangle in mind, one can define a curvature in the parameter space derived from the Berry phase which is accordingly known as the Berry curvature⁵. The integral over the Berry curvature also defines a topological index called *Chern number*⁶ [7], which for the *QHE* corresponds [17] to the number of conduction quanta⁷, and for the *ABE* to the number of magnetic flux quanta.

The experiments presented in this thesis are concerned with the geometry and topology of systems with a spatial periodicity. In nature, such systems are typically realized in form of crystalline materials, such as most conducting metals and semiconductors, superconductors and the famous⁸ graphene, and are therefore classically studied in the context of condensed matter physics. While these systems have for a long time been primarily characterized by their excitation spectrum, i.e. the electronic band structure,

³or more mathematically, a $U(1)$ line bundle

⁴an eigenstate of the Hamiltonian, that gets varied adiabatically

⁵The analogy to the angle sum is not fully concise: The Berry phase is equal to the total curvature enclosed by the path in parameter space. For the angle sum this is only true on a sphere. For a better picture refer to Chap. 4

⁶The Chern index stems from a generalization of the Gauss-Bonnet theorem [8, 16].

⁷Given by the bulk-boundary correspondence principle [10] as the number of conducting chiral edge states.

⁸Nobel prize in physics was awarded for the experiments on graphene [18–20]

also the geometric properties have a significant impact on the material properties [21, 22]. Here we are using clouds of fermionic potassium, that have been cooled to quantum degeneracy, as a quantum simulation platform to study quantum geometric and topological phenomena. In analogy to condensed matter physics, the role of the crystal structure of the atomic cores is taken by an optical lattice potential created via the interference pattern of intersecting laser beams, and the role of the electrons by the ultracold atoms. Using ultracold atoms as a platform opens up new experimental pathways[23–27] as it has the advantage that many system parameters can be tuned that are otherwise fixed properties of the analyzed material or restricted due to technical limitations. One major shortcoming of the ultra cold atom platform is, however, the neutrality of the electric charge of atoms, and the entailed absence of the Lorentz force, which opposed to electrostatic forces, cannot simply be emulated by an optical dipole potential⁹. This shortcoming can be overcome by using geometrically non trivial, i.e. non-flat, systems, because the Berry curvature is a general quantity that in the case of an electron in a magnetic field can be identified with the magnetic field. This strategy is therefore also referred to as *engineering of artificial gauge fields* [15, 30–34].

The experimental research with ultracold atom systems has a long and successful history of the exploration of magnetic phenomena, ranging from the emulation of classical frustrated magnetism [32] to the realization of Ising models [35]. In the recent years, the past forty years of exploration of topological and geometrical effects in condensed matter physics found a fast forward revival on the new ultracold atom platform. One of the early experiments was, for example, the realization [36, 37] of the Hofstadter-Hamiltonian [38, 39], the very same system that was originally considered in the seminal paper by Thouless et al. that led to the paradigm shift in the definition of quantum phases. The energy spectrum of this system, which forms, as a function of the magnetic flux through its unit cell, the famous fractal structure called the Hofstadter-butterfly. In a condensed matter system only a very small region of this structure is accessible, because an average of one flux quantum per unit cell corresponds to magnetic fields of the order of tens of thousands of Tesla. In the cold atom realization, the geometric phases are tuned via the phase of laser assisted tunneling processes and the associated magnetic field can be freely tuned to arbitrary strengths [31]. Further important experiments in the exploration of topological quantum matter with ultra cold atoms were among others [40–42] the interferometric measurement [43] of the Zak-phase, which is the one-dimensional equivalent to the Chern index, the measurement [44] of chiral edge currents and the realization [45] of the famous Haldane model, which was originally [46] intended as a toy model, unthinkable to be ever realized in a condensed matter system, because it requires equally strong magnetic fields that alternate at a sublattice scale.

In this thesis I am going to present two main experiments. For both experiments

⁹It can, in limited extend, be emulated by a rotating frame of reference [28, 29]

hexagonal optical lattices [27, 41, 47] were explored. To be specific, the lattice is of the boron-nitride type, which is similar to the lattice structure of graphene, in the sense that its “sites”, i.e. the location of the atomic cores in a real material, coincide with the intersection points of a honeycomb structure. The difference from graphene is, that every second site is more strongly binding than the others. It can be shown [48] that the Berry curvature is an even function for inversion symmetric systems and an odd function for time reversal symmetric systems. This implies that it is zero for time and inversion symmetric systems, and its integral, the Chern number, is zero as soon as time reversal symmetry is given. In condensed matter systems this time reversal symmetry can be simply broken by applying a magnetic field. Also in ultra cold atom systems it can be broken to create nontrivial topological systems [45, 49]. A common realization is periodic driving [50–57] of lattice parameters, as for example the coupling of the laser assisted tunneling mentioned earlier. In the presented experiments we break time reversal symmetry by translating the absolute lattice position periodically over time, which is also known as *lattice shaking* [32, 33, 35, 58–61].

In the first experiment [62] we determined the Berry curvature with a high resolution and over the entire first Brillouin zone of this two dimensional lattice system via a complete state tomography [59]. In condensed matter system the effects of a changed Chern index are highly severe and easily observable. The underlying change of Berry curvature however, is not easily accessible and could therefore not be measured yet. In ultracold atom systems the Berry phase has been measured [63] interferometrically for isolated paths, but by providing a quasimomentum resolved measurement of the Berry curvature for the entire Brillouin zone, this experiment constitutes a novelty.

In the second experiment [64] we explore the relationship between nonequilibrium dynamics and the geometrical and topological properties of the system in which the dynamics take place. In the wave function of a state that has initially been prepared as a filling the lowest band of a deep undriven boron-nitride lattice with an essentially flat band structure, we observe the creation, movement, and annihilation of vortices during its evolution in the circularly driven system. The path of these vortices in quasimomentum space eventually forms a closed contour. This contour separates the two maxima of Berry curvature, the so-called Dirac points, only if the underlying Hamiltonian is topologically nontrivial [65–67]. Probing a topological Hamiltonian without preparing a topological state, as it is done here, is of special relevance because topological ground states are extremely difficult to create [68, 69].

We further explore the nonequilibrium dynamics in yet another context by identifying the pairs of dynamical vortices as an order parameter of a so-called dynamical phase transition [70–72] (*DPT*). For traditional phase transitions in physics, like the freezing of a liquid to a crystalline solid, the properties of a system at equilibrium change drastically upon reaching a critical value of its external parameters, like temperature, pressure or

magnetic field. In contrast to this DPTs describe nonequilibrium systems. Here, an initial state changes over time without the need for externally varied parameters. Such a nonequilibrium state is typically reached by preparing an equilibrium state, followed by a quench of a system parameter. During the evolution of the state, physical quantities associated to it may expose a nonanalytic behaviour at accordingly termed *critical times*. The nonanalytic behaviour in a traditional phase transition can be related [70, 73–76] to the occurrence of zeros, called Fisher zeros, in the partition function. The definition of dynamical phase transitions is motivated by [70] the mathematical analogy of the Loschmidt amplitude, i.e. the overlap of the evolved state with the initial state, with the (boundary) partition function [77] when replacing the spatial coordinate with imaginary time, which therefore also may entail critical behaviour in time [78]. In recent theoretical studies dynamical phase transitions could be related to the topological properties [68, 79–81] and phase transitions in general [82] of the underlying system. For one-dimensional systems the winding number of the Pancharatnam geometric phase [83] could be identified [84, 85] as a topological order parameter for the DPTs. In the present work we generalize this idea to higher dimensions and introduce the number of dynamical vortices as an experimentally well accessible order parameter.

Prior to our experiment, so-called Lee-Yang [86, 87] zeros, which, like the Fisher zeros, are a special case of zeros in the partition function, have for the first time been experimentally observed [88] in a molecule. The Lee-Yang zeros describe an equilibrium phase transition in terms of an imaginary magnetic field instead of relating it to the real time evolution of the Loschmidt amplitude. Shortly after the initial publication [89] of our findings, further experimental studies of DPTs in one-dimensional trapped ion systems [90, 91] and condensed matter systems [92] have been conducted.

Our experiment shows the accessibility of a dynamical order parameter as an experimental observable and opens the route towards a deeper exploration of the connection between nonequilibrium dynamics and topology in quasi continuous 2D systems. With the developed experimental techniques the topology of lattice Hamiltonians has been probed [65]. The study of topology of more complicated systems with interactions is a promising candidate for further exploration.

1.1 Outline

The thesis is structured in nine chapters. Chapt. 6 and 8 report on the main two experiments, that have been conducted as part of this work, namely the reconstruction of the Berry curvature and the observation of dynamical vortices. Chapt. 1-5 introduce the theoretical concepts and experimental setup relevant for both experiments and Chap. 7 introduces additional concepts relevant for the experiment on dynamical vortices. The final chapter analyses in depth a digital fiber phase lock as an experimental device, that

has been developed in the course of this work. The content of the individual chapters is as follows:

2. Preparing and Probing Ultracold Trapped Fermions

Chapter 2 deals with the experimental apparatus, that is used to conduct all the experiments presented in this thesis, with a special focus on the changes that have been implemented in the course of this work. These changes are: The setup of a laser system for the generation of a far detuned hexagonal optical lattice, the implementation of a Python¹⁰ scriptable experiment sequence control and the implementation of a post acquisition image processing algorithm, capable of removing interference patterns that arise when imaging the atoms with coherent light.

3. Ultracold Atoms in Optical Lattice Potentials

In this chapter the necessary theoretical background on optical lattices is established. Starting from general optical dipole potentials, optical lattice made from three beams are introduced. Secondly, the wide class of lattice structures and associated describing parameters is restricted further and further over in-plane lattices, to hexagonal lattices, to finally the balanced boron nitride lattice, that stands at the center of these experiments. Thirdly, the Bloch electron model for a quantum mechanical description of a single atom in an optical lattice and its numerical implementation are presented. And finally the tight-binding approximation, which is relevant for an analytic description of the conducted experiments, is introduced.

4. Geometry and Topology of Periodically Driven Boron Nitride Lattices

Chapter 4 introduces the concept of the geometric phase and the Berry curvature, two quantities that stand at the center of the experiment reported on in Chap. 6. Furthermore, Floquet theory for the description of periodically driven lattice is presented.

5. State Tomography for an Optical Lattice

In chapter 5 the central experimental technique for retrieving the information about the quantum state of the ensemble of ultracold atoms in the lattice is explained. This technique is central for the data in Chap. 6 and 8.

6. Experimental Reconstruction of the Berry Curvature in a Floquet Bloch Band

In this chapter the results of one of the two main experiments are presented. The experimental protocol for the data acquisition and the data analysis gets reported upon.

¹⁰Programming language

The data in this chapter has also been published in Ref. [62].

7. Nonequilibrium Dynamics in Topological Bands

Chapter 7 introduces the new concepts necessary to understand the data presented in Chap. 8 and analyses the relationship of dynamical vortices with topology, dynamical phase transition and the Pancharatnam geometric phase.

8. Experimental Observation of Dynamical Vortices in a Topological Bloch Band

Here I present the data of the second of the main two experiments in the thesis. The data in this chapter has also been published in Ref. [64].

9. Development of a Digital Fiber Phase Lock

Optical fibers transfer mechanical vibrations onto the phase of the light that they are guiding. In the present context of optical lattices these phase fluctuations lead to a stochastic shaking of the lattice, which in turn heats the confined ultracold atoms in an uncontrolled manner. The fiber phase lock subject to this chapter reduces the noise of such a fiber via an electronic negative feedback loop. In this chapter the optical, electronic and software setups are presented and characterized.

Publications

In connection with this work, the following articles have been published:

In Verbindung mit dieser Arbeit sind die folgenden Publikationen entstanden:

- **Experimental Reconstruction of the Berry curvature in a Floquet Bloch Band**
N. Fläschner, B. S. Rem, M. Tarnowski, D. Vogel, D. S. Lühmann, K. Sengstock, C. Weitenberg
Science 352, 1091–1094 (2016) DOI: 10.1126/science.aad4568
- **Observation of Topological Bloch-State Defects and their Merging Transition**
M. Tarnowski, M. Nuske, N. Fläschner, B. S. Rem, D. Vogel, L. Freystatzky, K. Sengstock, L. Mathey, C. Weitenberg
Phys. Rev. Lett. 118, 240403 (2017) DOI: 10.1103/PhysRevLett.118.240403
- **High Precision Spectroscopy of Ultracold Atoms in Optical Lattices**
N. Fläschner, M. Tarnowski, B. S. Rem, D. Vogel, K. Sengstock, C. Weitenberg
arXiv preprint arXiv:1801.05614 (2018)
- **Observation of Dynamical Vortices after Quenches in a System with Topology**
N. Fläschner, D. Vogel*, M. Tarnowski*, B. S. Rem, D. S. Lühmann, M. Heyl, J. C. Budich, L. Mathey, K. Sengstock, C. Weitenberg*
Nature Physics 14, 265 (2018) DOI: 10.1038/s41567-017-0013-8

*The marked authors contributed equally

2 Preparing and Probing Ultracold Trapped Fermions

The very foundation for the experiments presented in this thesis is an ensemble of confined, quantum degenerate fermions, that can be manipulated and probed, which is here given by a trapped cloud of ultracold fermionic ^{40}K atoms.

However, the phenomena studied here are fully independent of the specific choice of platform, as they do not principally rely on any of the atomic properties. Phenomena and techniques similar to those reported on here can also be found in realizations in the field of condensed matter physics, as for example the phenomena in illuminated graphene [93] and the technique of *angle resolved photoemission spectroscopy* (ARPES) [94, 95]. Over the last decades ultracold atoms have evolved [26] into a powerful and versatile *quantum simulation platform*, that offers a wide set of tools for engineering physical systems. In the present context this means specifically that in contrast to condensed matter samples, the lattice potentials can be systematically varied through simply accessible external parameters such as the polarization and the phase of the beams constituting the optical lattice potential.

In this chapter I will summarize how we produce and probe samples of ultracold ^{40}K , with a special focus on the relevant additions and improvements of the previously existing system, that have been implemented in the course of this thesis. I want to underline that these additions and improvement have been conducted as a communal effort in a team. My personal contributions are centered around the construction of the lattice laser setup (Sec. 2.2), the extension of the experiment control (Sec. 2.3) and the fringe removal via image post-processing (Sec. 2.4). Detailed information on the implementation of a gray molasses and the construction of the lattice telescopes can be found in the theses of my colleagues Nick Fläschner [96], Matthias Tarnowski [97] and Maria Langbecker [98].

2.1 Preparation of Ultracold Potassium

The apparatus described in this section is capable of producing samples of ultracold fermionic ^{40}K atoms in a continuous sequence of experimental cycles. For the two types of experiments presented in this thesis we require clouds of $2 \cdot 10^5$ atoms to create states that completely fill the lower band of the band structure of the typical lattice Hamiltonians. With the optimizations of the apparatus that we implemented [96], we can produce samples of this size, at a temperature between 10 to 20 percent of the *Fermi temperature* (T_F) typically within 14s. Because the apparatus is also capable of producing an ultracold

mixture of ^{40}K and bosonic ^{87}Rb it has been named *Bose-Fermi-mixture* apparatus or short BFM-apparatus.

The apparatus was conceptualized and built by Silke and Christian Ospelkaus [99, 100] starting in 2003. It is one of four apparatus [101–103] in the group led by Klaus Sengstock, which share a similar design, that has, over many years now, proven to be very reliable and successful. Among the main design parameters for those apparatus, in order to serve as a platform for a multitude of different experiments, are the optical access for the manipulation and probing of the atoms via laser light and the vacuum pressure of the residual background gas that disturbs the sample through collisions. For this reason the apparatus consist of two glass cells that on only one side are connected to a steel chamber that provides all stages of the vacuum pumping infrastructure.

The two cells are dedicated to different stages of the cooling process of the atoms. Both rubidium and potassium are earth alkali metals that are solid at room temperature. To create a gas, so-called dispensers are used. These are devices, located in the vacuum, that heat the metals electrically and thereby cause atoms to sublime into the gas phase. Those dispensers are located in the upper glass cell. We use commercial dispenser that supply an isotopic distribution that reflects the *natural abundance* (NA) for rubidium and for potassium is enriched with ^{40}K , to counter its extremely low NA of only 117 ppm [104].

From the generated background gas, atoms are captured and cooled using a specific constellation of two pairs of near resonant laser beams and a magnetic field gradient, which is know as a *magneto-optical trap* (MOT) [105]. Ordinarily a MOT consists of three perpendicular pairs of beams, but in this 2D-MOT the confinement in the vertical direction is omitted and the captured atoms are instead transferred via a *pushing beam* along that direction into the lower glass cell.

To create a ultra high vacuum with a background pressure below $1e - 11$ mbar in the lower glass cell, it is protected from the higher pressure of $1.5e - 10$ mbar due to the dispensers in the upper glass cell by a *differential pumping stage*, which is a thin an elongated tube that significantly decreases the diffusion rate. During the so-called *loading process* a stream of precooled atoms from the 2D-MOT, that passes through the differential pumping stage guided by the pushing beam, is captured in the lower glass cell by a 3D MOT.

Both MOTs, contrary to ordinary MOTs, consist of superimposed beams of different wavelengths, so that both rubidium and potassium can be trapped simultaneously. Even if exclusively fermions are required, as it is the case for all the experiments presented in this thesis, the simultaneous operation of the rubidium MOTs is required, because, as it will be explained later, the rubidium atoms are necessary for the efficient evaporative cooling of potassium.

The 3D MOT for potassium is a so-called *Dark-SPOT MOT* [99, 100, 106], which counteracts the loss mechanism of light assisted collisions, that becomes relevant when of trapping high densities of potassium in a MOT. In a dark-SPOT MOT the atoms at the center of the MOT are pumped into a dark state by imaging a dark spot into the cloud on

the repumper beams.

After a loading phase of typically three seconds, both MOTs and the pushing beam get turned off and optical molasses [105] are switched on for 10 ms to cool the atoms below the Doppler limit. For rubidium an ordinary *bright* molasses is employed and for potassium we implemented a *gray* molasses on the D1 line to reach lower molasses temperatures and thereby significantly shorten the time needed for the ensuing evaporative cooling phase. Details on the implementation and the improved performance of the gray molasses can be found in the theses of my colleagues [96, 97].

In order to cool the atoms into a quantum degenerate regime further evaporative cooling is required. For that, the atoms are first optically pumped into their corresponding hyperfine states of highest magnetic dipole moment which are

$$\begin{aligned} F = \frac{9}{2} \quad m_F = \frac{9}{2} & \quad \text{for } ^{40}\text{K} \\ F = 2 \quad m_F = 2 & \quad \text{for } ^{87}\text{Rb} \end{aligned} \tag{2.1}$$

and are then, on site, loaded into a magnetic trap which is a hybrid of a cloverleaf type and a 4Dee type¹. Subsequently, a radio frequency field is exponentially swept from 15 MHz down to 1 MHz within 10 seconds. As mentioned earlier, during the evaporation the presence of the rubidium is essential for cooling potassium. At low temperature, scattering is dominated by the s-wave mode, which is forbidden by the Pauli exclusion principle for pairs of fermions. With the resulting low scattering rate, the thermalization time is extremely increased, which would require excessively slow evaporation sweeps. Instead, the potassium atoms are cooled *sympathetically*, i.e. through collisions with the bosonic rubidium, that can be cooled evaporatively at much faster timescales, due to their bosonic nature.

To produce a pure fermionic sample, the rubidium atoms are fully evaporated from the trap by choosing the final evaporation frequency, such that the associated photon energy is smaller than the Zeeman splitting of the hyperfine structure of the trapped rubidium atoms, which leads to the transfer of even the coldest atoms into a non-confined state at some point of the ramp.

The sample of cold atoms is subsequently transferred into a crossed dipole trap [107]. Within 100 ms, two crossing beams are ramped up with waists² of

$$\begin{aligned} w_y^{(1)} = 70 \mu\text{m} & \quad w_z^{(1)} = 240 \mu\text{m} \\ w_y^{(2)} = 120 \mu\text{m} & \quad w_x^{(2)} = 120 \mu\text{m} \end{aligned} \tag{2.2}$$

where the elliptical beam (1) lies within the symmetry plane of the experiment, which will be defined later in Chap. 3, and the round beam (2) propagates perpendicularly to it.

¹For details the reader is referred to [99, 100]

²where the waist is defined as the distance where the intensity has dropped to $\exp(-2)$ of its maximum value. $I(w) = \exp(-2)\hat{I}$

The dipole potential is created at a wavelength of 825 nm, i.e. far red-detuned from all optical transitions in ^{40}K , to ensure a low scattering rate. When the dipole trap reaches its final depths, the magnetic trap is turned off slowly within 1 s to provide an adiabatic transfer into the new trapping geometry.

At this point there is a pure, spin polarized, atomic ensemble of $2 \cdot 10^5$ ^{40}K atoms at $0.1 - 0.2T_F$ trapped in the dipole field [96], which forms the starting point for the experimental sequences described in Chaps. 6 and 7. All experiments have in common that they will be conducted in a hexagonal optical lattice that is described in more detail in Sec. 3.2. The lattice potential is created through the dipole force of additional far red-detuned laser beams, that intersect at the position of the atomic cloud. To transfer the atoms into the lattice, the intensity of those beams is simply ramped up. The associated potential consists of two components: a pure lattice potential and an additional homogeneous background from the non-interfering components (see Sec. 3.2). Additionally the potential exposes an envelope due to the finite widths of the beam profiles [108], which we approximate as an additional harmonic confinement potential. For the two types of experiments presented here, we measured the overall harmonic confinement by the superposition of the lattice and the dipole trap to be given by the following trapping frequencies (*sup. mat.* of [62, 64])

$$\nu_x = 83(4) \text{ Hz} \quad \nu_y = 108(5) \text{ Hz} \quad \nu_z = 93(4) \text{ Hz} \quad (2.3)$$

The dipole trap is not switched off once the lattice has been fully loaded, in order to avoid further ramps that might induce oscillations.

The two presented experiments are concluded by switching of all potentials, leaving the cloud to unhindered expansion during a so-called *time of flight* (TOF) of 21 ms, limited by the geometrical constraints of the apparatus. This procedure effectively maps the momentum distribution into real space (see also Chap. 5). After the TOF the sample is imaged using standard absorption imaging (see Sec. 2.4), which enables the determination of the atomic density, spatially resolved within the lattice plane, and integrated perpendicular to it. As this measurement is of destructive nature, a typical experiment is conducted over many cycles of the described sequence, while the relevant control parameters are varied. The realization of the control over this sequencing is described in Sec. 2.3.

2.2 Laser Setup for a Hexagonal Lattice

A central upgrade of the BFM-apparatus implemented as a part of this work, was the construction of an optical setup for the creation of a hexagonal optical lattice potential at the site of the atomic cloud. Previous experiments had been conducted in a retro-reflected cubic lattice, which does not fulfill the requirements for the geometric and topological

effects that were of interest here³.

Hexagonal lattices and the properties of optical lattice potentials in general are discussed in detail in Chap. 3, here I will present the technical realization of the underlying optical setup. The hexagonal lattice is created by three non-retro-reflected beams that intersect a common point at an relative angle of 120° between each pair. In contrast to the retro-reflected lattices, the hexagonal lattice is sensitive to the phase noise induced by the optical fibers used to guide the light between the optical tables of the main experiment and the laser setup. To compensate for that detrimental noise we developed a *fiber lock* or *optical phase locked loop* in parallel to the presented main experiments. In Chap. 9 I present characterization data that convincingly qualifies the fiber lock as a powerful future upgrade of the experimental apparatus.

The laser setup is depicted in Fig. 2.1. It can be divided into two sections: on the left the beam generation on the laser table connected by four optical fibers to the right side for the beam shaping on the experiment table. For the beam generation we use a *Innolight/Coherent Mephisto MOPA 25 NE*, that produces a single mode field at 1064 nm with a power of 26.6 W. To protect it from counter propagating modes, as a first element, we guide the beam through an optical isolator/diode (Electro-Optics Technology, model 08-01037 for 1030-180 nm). This protection is especially relevant, because by the design of the fiber lock, a non-negligible fraction of light will be back reflected into a nearly identical spatial mode. In our first setup we placed the isolator directly in front of the laser head. However, the power density of the diverging beam caused significant thermal lensing effects within the isolator. By moving the isolator about 40 cm away from the Laser head, we could reduce the thermal lensing at full power, to what would correspond to a transfer matrix of a lens with a focal length of 267 mm^4 . With the two subsequent lenses ($f = -500\text{ nm}$ and $f = 400\text{ nm}$) the mode is shaped such that its focus coincides with the positions of the *acousto-optic modulators* (AOM) at a design waist of 1 mm. All other distances are chosen such that no further lenses are necessary to reach the maximum fiber coupling efficiency.

Thereafter the beam is split up into four arms by a series of pairs consisting of a *half wave plate* (HWP) and a *polarizing beam splitter cube* (pol-cube), that are arranged such that each arm is vertically polarized. The HWPs can be adjusted to obtain the desired distribution of power over the arms. The subsequent components are identical for each arm. First in line is a high power 110 MHz AOM (Crystal Tech. 3110-197), which fulfills three tasks: Controlling the phase to shake the lattice potential (see. Sec. 3.2.1 and Chap. 4), enabling future compensation of the phase noise the light will pick up in the fiber and stabilizing the light intensity via another feedback loop. The first diffraction order of the AOM is then led through a stage of a HWP, a pol-cube and another HWP. The first HWP rotates the polarization to the parallel plane, such that the beam passes

³It is however possible to creating a geometrically non trivial lattice by superimposing the cubic lattice with a linear lattice, as reported in Ref. [40]

⁴The beam profiles can be found in [98]

through the non-reflected port of the subsequent “polarization cleansing” pol-cube, that offers the higher extinction rate. The following HWP serves for the convenience to adjust the polarization axis to the principal axis of the *polarization maintaining* (PM)-fiber, fully decoupled from the spatial degrees of freedom. Finally the beam is coupled using a TOPTICA FiberDock™ into the fiber (nLight LIEKKI™ Passive-10/125-PM).

For a number of reasons we had to connectorize the bare fiber ourselves. At the time of construction, and to our best knowledge, there was no commercial manufacturer for readily connectorized fibers that fulfill all requirements for our setup. These are: operation at a desired input power of 5 W, one flat and one angle polished connector, and a high quality single mode gaussian beam profile. Usually fibers are connected with two angle polished ends to avoid interference through back reflections. Here we deliberately chose one flat end to create a back reflex at the end of the main experiment that can be used for the fiber lock (Chap. 9).

Earlier tests at the fiber optics prototype section of our research group had shown that the previously mentioned fiber model withstands this input power if correctly connectorized. We connectorized the fibers with standard (Thorlabs) connectors⁵ in a connectorizing process developed at the prototype section, which includes the etching of the cladding⁶. The etching protects the fiber against potentially damaging misaligned beams by creating a rough surface area on the part of the cladding, from where light can scatter into the ferrule. For the flat end no etching is needed as it is exclusively used as an outcoupling end. An additional advantage is that the fiber length could be fully adjusted to our needs. This is important because at high input powers the stimulated Brillouin scattering [109] depends strongly on the length of the fiber and can lead to significant losses.

The reflex from the silica air interface of the usual 4% propagates back through the fiber and passes a *beam splitter* (BS), where 1% gets picked up and directed to a photo detector, which provides the option of a local end intensity stabilization. Here we implemented a stabilization through a pick up on the remote end of the fiber. In the case of our nonretroreflected lattice the full laser power needs to be dumped after the light has passed the atomic cloud and thus an arbitrary fraction can be picked up. At these locations we implemented a polarimeter because a highly precise control of the polarization of the lattice beams is crucial for controlling the lattice geometry (see Chap. 3). Instead of adding another pick up for the intensity stabilization we use the signal for the p-polarization from the polarimeter. The implementation of the polarimeter is described in [96]. The photo detector signal serves as the input for a custom made feedback controller setup (see Ref. [101]), that actuates via the RF-power at the AOM of the corresponding arm.

All optical components for implementing a fiber lock are readily installed: the back

⁵Angle polished (FC/APC) connector with a ferrule of a $126 \pm 1 \mu\text{m}$ bore and a flat (FC/PC) connector with $140 \mu\text{m}$ bore

⁶ $(125 \pm 2 \mu\text{m})$ diameter

reflex on the laser table propagates unhindered back through the polarization cleaning stage to the AOM, where a fraction gets diffracted into the minus first order and finally gets blocked by the optical diode, and another fraction continues unaltered and is steered onto the fiber lock photo detector. To obtain an interference signal, this path is superimposed with a second beam, originating from the forward propagating beam that passes the AOM without being diffracted. Before it gets disposed in the beam dump a fraction of 4%, matching the reflectivity of the flat fiber end, is retroreflected at a coated glass slab. Upon its second transversal of the AOM, the undiffracted part gets eventually disposed in the optical diode and the diffracted part forms the desired reference for the interference signal. For the fiber lock setup on the laser table we initially implemented analog electronics following Ref. [101] but then realized that a fixed stable digital RF source yielded lower heating rates [97]. This motivated the development of the digital fiber lock that I present in Chap. 9.

At the main experiment table, where the ultracold fermions are produced in the glass cell, the flat fiber ends are mounted in telescopes to produce the optical lattice at the location of the atoms. Three of the four axis are arranged in the hexagonal lattice configuration (Chap. 3), i.e. at a regular angular spacing of 120° . To assure a maximally high stability of the lattice, two of the telescopes are mounted on a massive plate, which stands perpendicular to the table plane, where they can guide the beams directly to the atoms without passing further optical components, except for the *quarter-wave plate* (QWP) and HWP that serve the purpose of configuring the light to any desired polarization mode. The third telescope emits the beam into the plane parallel to the optical table from where it gets reflected over a single mirror in a right angle to the intersection point of the other two lattice beams. The foci of those beams all lie at their mutual point of intersection, where they meet their design e^{-2} -intensity radii of $160\ \mu\text{m}$ within a margin of about $4\ \mu\text{m}$ ⁷. Details on the telescopes, the polarimeter and the lattice calibration can be found in Refs. [96, 97].

⁷see [96] and [98] for the numbers of the individual axes.

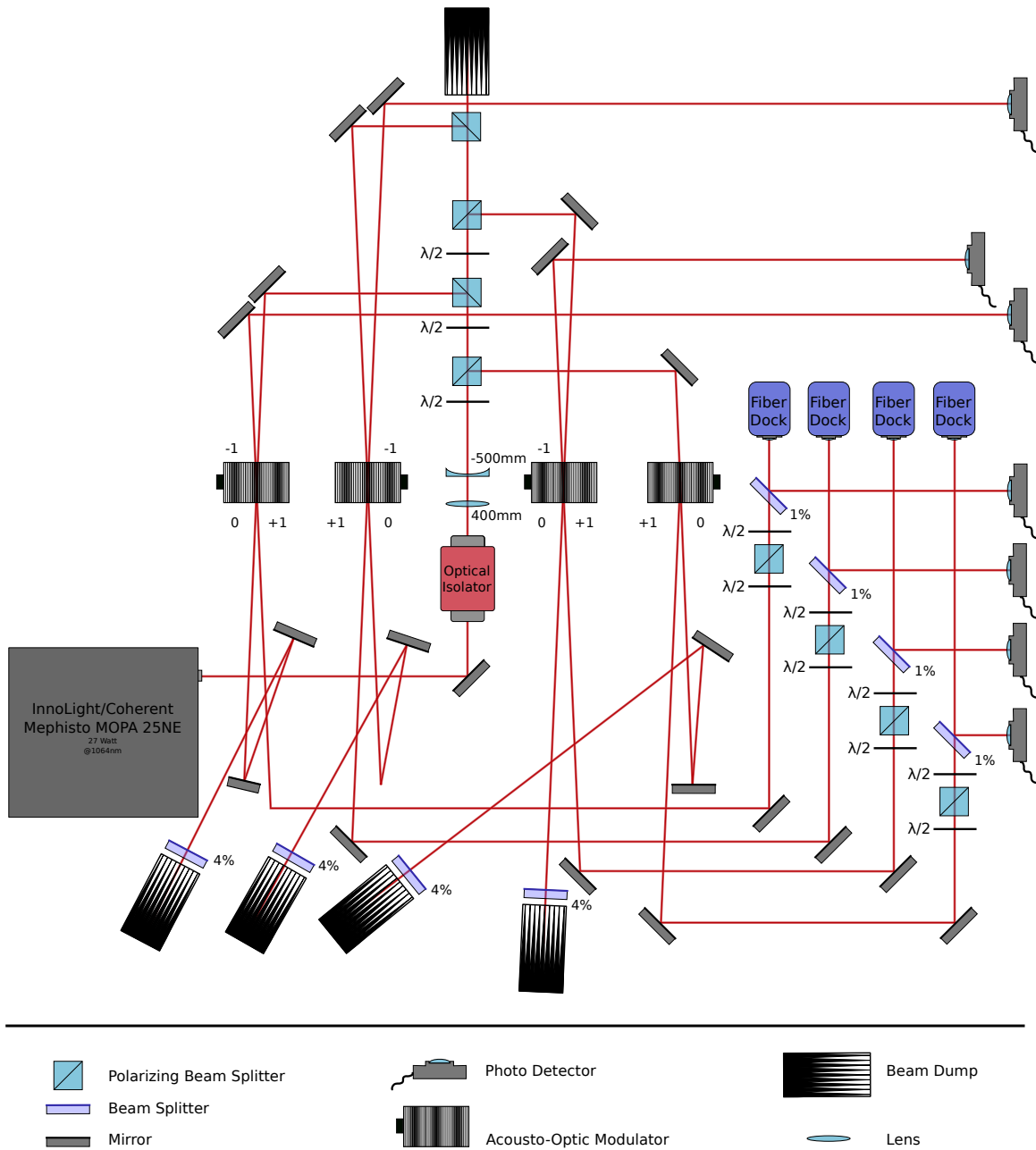


Figure 2.1: Schematic of the optical setup for the generation of the lattice laser modes.

2.3 Extended Experiment Control

The experimental cycle described in Sec. 2.1 is centrally controlled by a commercial *digital to analog conversion* (DAC) unit that offers control over digital and analog channels at a maximum resolution of 10 μs . Additionally to this, on every cycle further instruments, such as high current sources and wave form generators, are programmed remotely from a PC. To meet the strict timing requirements, these devices are triggered externally by the DAC unit. All devices get programmed by a custom LabVIEW program, which provides the possibility to sweep a single parameter of the experimental cycle, including its insertion into the VISA⁸-commands. The restriction to a sweep of a single parameter however, constitutes a significant limitation for the execution of experiments that surpass a certain magnitude of complexity of the controlled parameters. A partially manual control, i.e. the sequential user execution of single parameter sweeps, would not only open the possibility of errors, but it also reduces the yield of the apparatus.

To realize the experimental control of the experiments presented here, we extended the existing control system to be fully scriptable and thereby enable sequences with arbitrarily complex parameter dependencies. This *hybrid* approach unites the advantages of a purely programmed and an exclusively *graphical user interface* (GUI) driven system. It allows to fully operate the system from shot to shot with the existing LabVIEW GUI and in the scripted mode one only needs to describe the varied parameters. Technically this control was realized by implementing a Python⁹ library that facilitates the readout and generation of XML¹⁰-files that describe a single cycle and are compatible with the GUI. To the LabVIEW program we added a *scripting-mode* that simply plays back the list of generated files. A short example for such a script is shown in Fig. 2.2.

With this powerful extension to the experiment control extension we have realized long experimental protocols of a few thousand cycles that ran continuously over several days. This programmatic control of the experiment also lays the foundation for an adaptive experiment control, where the experimental parameters of the next cycle are determined dependent on the measured quantities of the previous cycles. This way it would be possible to sample a region of interest in the parameter space in dependence of the feature size or the gradient of the parameters.

⁸Virtual Instrument Software Architecture, a standardized protocol for programming remote devices

⁹Interpreted programming language, popular in the field of data science

¹⁰Extended Markup Language

```

1 import ExperimentControl as ep
2
3 infilename = r'C:\Protocols\exampleGenerated.xml'
4 outpath    = r'C:\Users\exampleInput.xml'
5 name       = 'Example'
6
7 VISAcmds1 = r"\
8 amp -99.0;
9 tri;
10 os1 110.  FREQ  FREQ 0.  0.0002 0.  6.  1.  0.004;
11 flush"
12 VISAcmds2 = ...
13 counter=1
14 for avg in range (0,10):
15     for k in range (1,20):
16         for i in range(1,26):
17             ep = ExperimentProtocol(infilename)
18             ep.setSlotDuration('LHC_mod', round(12500/(7500+500*k)*i))
19             ep.set('LatticeShakingPhase', 'WaveformGenerator1', VISAcmds1)
20             ep.set('LatticeShakingPhase', 'WaveformGenerator2', VISAcmds2)
21             ep.replaceVisaString('LatticeShakingPhase', '
22                 WaveformGenerator1', 'FREQ', str((120.0+1.0*k)/10000))
23             ep.replaceVisaString('LatticeShakingPhase', '
24                 WaveformGenerator2', 'FREQ', str((120.0+1.0*k)/10000))
25             ep.safeEnum(name, outpath, counter)
26             counter += 1

```

Figure 2.2: Example script for the extended experiment control. The above script controls a fictive experiment and describes the sequence for around 5000 cycles. Here two parameters k and i are varied to set the frequencies of waveform generators and also a slot duration in a bilinear form. This cycle is repeated 10 times for averaging.

2.4 Fringe Removal

In this section I will present the implementation and characterization of a model free defringing algorithm [110] for the BFM experiment, that is capable of reducing the image noise to close to the shot noise limit, with minimal computational effort. This algorithm has been used for all absorption image data presented in this thesis and improved the signal quality significantly. The idea of defringing atomic absorption images via post-processing and the implementation in Ref. [110] originates from the works of Jochen Kronjäger [111] and Micheal Erhard [112] in the Sengstock group.

The imaging of ultracold atomic ensembles works mostly analogous to the imaging of any other ordinary object, except for one aspect: the comparably narrow atomic spectral absorption line width. All light power outside the atomic spectrum is not absorbed and deteriorates the image quality by reducing the contrast. Therefore the spectral line width of the imaging light source is required to be at least as spectrally narrow as the absorption line width of the atoms.

It is customary to use a narrow laser light source whose frequency is electronically

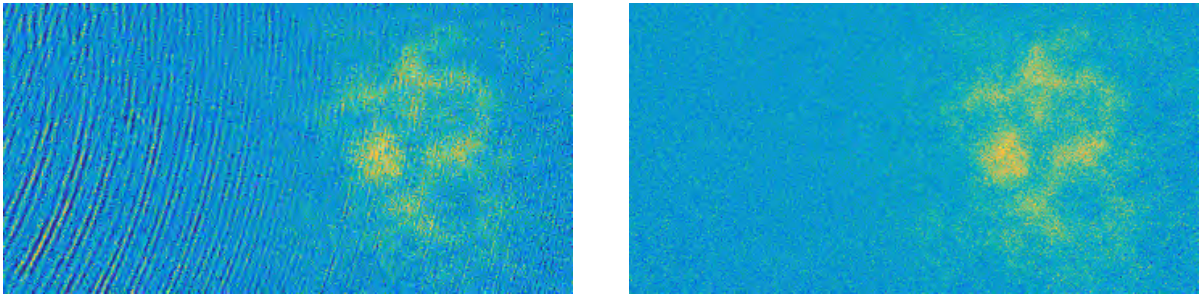


Figure 2.3: Single shot comparison. Left: a typical atomic density distribution, yielded by absorption imaging without defringing. Right: the same distribution, using the fringe removal algorithm.

locked to the atomic resonance. But using monochromatic light leads adverse interference effects, which manifest as fringes in the image. These interference fringes can have many different origins, such as dust and scratches on optical components, parallel surfaces, and ghost images from lenses.

The standard absorption imaging procedure [113] would be sufficient to remove the fringes, if they were of static nature. Here, the effects of inhomogeneous exposure canceled, by taking a reference image shortly after the first one, when the atoms have fallen out of the imaging region. The optical density (OD) of the atomic cloud is then determined by dividing the atom image by the reference image.

Unfortunately the fringes are of dynamic nature, i.e. they are different on the atom and reference images. The optical path length of the imaging beam is coupled to the environment on acoustic and thermal timescales. Vibrations are picked up by optical elements and temperature changes expand the optical path by changing the diffraction index of the surrounding air.

The fringes persist, though weakened, even when clean and sound optics are used in combination with suited anti-reflection coatings, an adequate optical path design and temperature stabilized laminar air flow. This persistence is not unexpected when considering that the modulation amplitude in two beam interference is determined as the geometric mean of the light intensities.

Several different approaches [111] were developed to suppress the fringes. We chose to use a fringe removal algorithm for the BFM experiment because it has proven effective and especially convenient for being of non invasive post-processing nature.

The Fringe Removal Algorithm

The key idea of the fringe removal algorithm is to replace the reference image, by an artificial reference image that is a weighted mean of the current and several previously taken reference images, while the weights are determined such that the OD is minimal in a region where no atoms can be expected (cf. Fig. 2.4).

That means even though, the fringes might have changed in the time between the atom

image and the reference image have been taken, we suppose that the fringe pattern in the atom image is still similar to previously taken reference images to some degree and can therefore be reconstructed by superimposing several of those. In the atom region it cannot be distinguished between real shadow of the atoms and an interference fringe. Therefore this region is excluded when finding the weights, but yet fringes will be successfully removed from that region due to the non-local structure of the fringes.

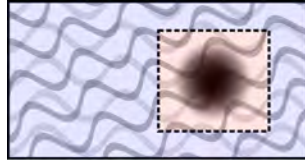


Figure 2.4: Schematic of defringing Regions. Shaded in blue, region without atoms. Shaded in red atom region.

This concept is very powerful and can be applied in a vast range of scenarios, because it is model free, in the sense that no assumptions are made about the column density distribution of the atoms, other than the existence of a sufficiently large atom free area. There are, however, two prerequisites that have to be met by the noise i.e. interference fringes.

Firstly, the noise has to be spatially correlated. Only information from outside of the atom region (AR) is used to construct the synthetic reference image. If there is no correlation, no information about the noise within the AR can be deduced. Therefore a lack of correlation can be the source of artifacts.

This prerequisite is perfectly met in the case of interference fringes due to their delocalized nature. Within the framework of Fourier optics it is evident that even a tiny disturbance like a grain of dust, will cause interference rings that extend over the full imaging region.

Secondly, the noise has to be correlated in time. If there was no correlation in time, the fringes of images taken in sequence would be completely distinct and therefore of no value for the fringe removal of one of them. Here *correlated in time* means that subsequent images resemble each other in average more than any two random images. This means, that if only certain shapes of fringes are observed the references can be considered temporally correlated, independently of the correlation of the occurrence of those shapes.

A judgment about the temporal correlation cannot be made based on model assumptions for an experimental system as complex as the one under consideration. On the one hand would slow thermal drifts most probably lead to a high correlation at the considered timescale of the 20-60 seconds experimental cycle. While on the other hand it would be plausible if vibrations of many coupled modes of many components would lead to a rather broad noisy background. Therefore, at this point the fulfillment of this requirement is postponed to the end of this section, where on the basis of experimental results it will be shown that temporal correlation is present.

The very first algorithm that has been implemented [112] for defringing, used the Gram Schmidt process to build an orthogonal set of basis reference images, onto which the image to be defringed is projected to obtain the weights for the new synthetic reference image. For the BFM experiment we chose to implement a more recent algorithm [110] that is computationally more efficient.

In order to get a formal understanding of the algorithm a few definitions have to be made. The pixel data provided by the camera can be naturally identified as elements of a vector space. An image can thus be written as a column vector \mathbf{x} of the following form

$$\mathbf{x} = \sum_i c_i \hat{\mathbf{e}}_i \quad (2.4)$$

where the coefficients c_i correspond to the light intensity shone onto a pixel with an index i and $\hat{\mathbf{e}}_i$ is the respective unit vector. The indexing of the pixels is fully arbitrary for the following considerations. However, we will consider image regions, that in this notation correspond to sub-vector-spaces. There are two regions of interest. The atom region, a region where a nonzero atomic density may be found, denoted by a subscript A, and the complimentary region, where any nonzero OD is caused by fringes, denoted by a subscript F.

The atomic density for absorption imaging is commonly [113] defined as

$$\mathbf{n} \propto \cdot \ln \left(\frac{\mathbf{x}_{\text{Absorption}} - \mathbf{x}_{\text{Dark}}}{\mathbf{x}_{\text{reference}} - \mathbf{x}_{\text{Dark}}} \right) = \mathbf{a} - \mathbf{r} \quad (2.5)$$

With those definitions the problem can be formulated as a standard minimization problem

$$\nabla_{\mathbf{w}} (\mathbf{a}_F - \mathbf{w}R_F)^2 = 0 \quad (2.6)$$

where R_F is a $p \times n$ matrix containing the n available previous reference images as rows and \mathbf{w} is a $1 \times n$ row vector containing the weights of the reference images. Note that all images are restricted to the region without atoms, where the OD is to be minimized.

Once the weights are determined the defringed image $\bar{\mathbf{a}}$ can be calculated using the unconstrained image \mathbf{a} and the unconstrained reference images R .

$$\bar{\mathbf{a}} = \mathbf{a} - \mathbf{w}R \quad (2.7)$$

In order to make the problem, formulated in eq. 2.6, numerically accessible it can be reformulated as

$$R_F R_F^T \mathbf{w} = R_F \mathbf{a}_F \quad (2.8)$$

Now a simple matrix inversion yields the desired weights \mathbf{w} . Bear in mind, that R cannot be canceled from the left, because there is no inverse operator for operators represented by a nonsquare matrix. But RR^T is symmetric by definition and thus invertible.

Implementation and Performance

For the BFM apparatus this algorithm has been implemented in MATLAB[®], to integrate seamlessly into the existing data analysis framework. We developed a graphical user interface, which allows to conveniently select the used regions, quickly browse through the resulting defringed images and view the used weights to produce the artificial reference image.

On a standard computer from 2010 the algorithm takes about one second to defringe 200 images using a base of 200 reference images. Compared to a typical experimental cycle time of around 30 seconds the computation time is of no issue. Thus the reduction of memory consumption is of higher priority than speed, when using large image sets.

Noise Reduction

For a quantitative statement about the quality of the defringed images and to compare the performance of this algorithm to the original one, a statistical noise analysis has been conducted.

In order to compare the pixel noise against the photon shot noise of the imaging beam, the difference images of the absorption and respective (synthetic) reference images have been considered instead of the OD, i.e. without prior taking of the logarithm. Further, the images have been converted to the domain of photon counts. The employed CCD camera (Andor iKon-M 934 BR-DD) is highly linear and the conversion therefore consists simply of a linear scaling factor that is determined by the quantum efficiency (0.93), the imaging wavelength and the chip gain value.

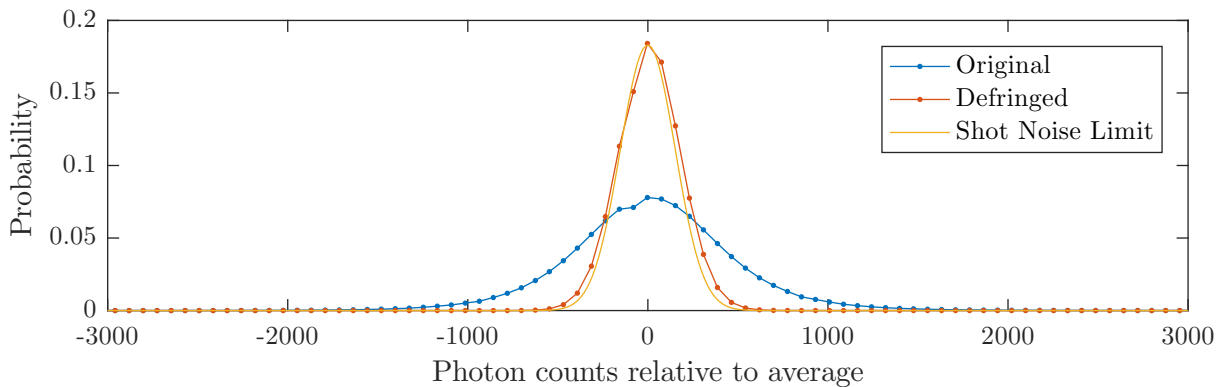


Figure 2.5: Comparison of photon background noise statistics for defringed and nondefringed images. The defringed image noise is very close to the shot noise limit of the given intensity corresponding to about 23000 photons. The histograms are obtained from the photon count difference between the atom and the reference image within a homogeneously illuminated region for 200 images.

To determine the intensity fluctuations, an atom-free region of constant illumination has been chosen. Fig. 2.5 shows a histogram of the set of all pixel values within that region

for 200 difference images.

The photon number distribution is fully characterized by the Poisson distribution, where the single parameter is the mean photon count. The plotted distribution corresponds to a mean photon count equal to the one obtained by the mean photon count in the atom images within the chosen region, which is about 23000 in the given case.

It becomes clear that the defringing procedure is capable of fully removing interference fringes and thus reduces the noise level almost to the shot noise limit. The remaining difference fits well be within the given scale of electron noise, that is specified by the manufacturer for the given parameters as an equivalent of ca. 13 photons. This electronic noise can not be removed by the algorithm as it does not fulfill the above mentioned requirements.

Temporal correlation of fringe patterns

In order to analyze the temporal correlation of the fringe pattern, a set of 8000 atom images has been defringed using the basis of all the corresponding reference images to construct a synthetic reference image for every atom image. The algorithm described here produces a matrix of 8000x8000 weights of which every row i contains the weights \mathbf{w}_i of the linearly combined reference images. To produce the temporal correlation, we shift the rows such that the previously diagonal entries, corresponding to the weights of the original reference image, that was taken in close succession of the absorption image, line up at one central column. Taking the average along the unshifted dimension, the mean weight for images that have been taken in an interval Δt can be obtained. The resulting data in Fig. 2.6 reveals that there is as expected a clear short term temporal correlation but only weak long term correlation of fringe patterns.

Outlook

The implemented algorithm has proven to be very robust, computationally inexpensive and highly effective. Considering that the noise floor limit is reached there is little space for improvement.

With respect to the implementation, an automatic noise analysis could be realized. A deviation from a Poisson statistic would thereby be capable to cause an alert in the case of an incorrect choice for the atom free region.

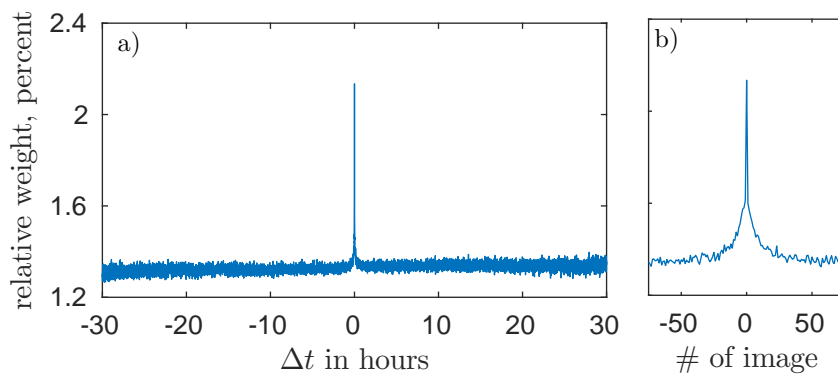


Figure 2.6: Averaged relative weight of reference image as a function of time. Around 8000 images have been defringed using all of the corresponding reference images. The obtained weights have been averaged for all atom and reference images that have been taken with the same time interval Δt . Panel a) shows that there is no long term temporal correlation, i.e. the fringe pattern does not repeat itself even after long times. Magnification. Panel b) shows that the previous and following 50 reference images contribute most significantly to the synthetic reference image.

3 Ultracold Atoms in Optical Lattice Potentials

All the experiments conducted in this thesis are based on the observation of the dynamics of an ensemble of ultracold fermions in the presence of three intersecting laser beams, whose interference pattern is called an optical lattice potential (OLP) due to its approximate discrete translational symmetry at their intersection point. The atoms interact with the interference pattern via the optical dipole force and experience a scalar potential proportional to the local light intensity. Optical lattices therefore enable the creation of "atomic crystals" that bear strong resemblance to those electronic many body systems that are studied in the context of solid state physics and materials sciences. In this analogy the atoms take the role of electrons, and the interference pattern takes the role of atomic cores. Many concepts that have been developed for and observed in electrons in solids can be mapped one to one to the realm of atoms, as for example, the emergence of a band structure in the excitation spectrum. But there are also substantial differences between the two systems. Most strikingly of which are probably the fact that optical lattices exist on one hundred times larger length scales with a harmonic cell potential as opposed to the superposition of singular Coulomb potentials created by the atom cores in an ordinary crystal, and the fact that the particles trapped in the optical lattice are atoms that are about 10^4 times heavier than the electrons and have a substructure but no total charge. Over several decades of research many of those differences have been overcome and others have been exploited, so that ultracold atoms in optical lattices have developed a very potent platform for quantum emulation of solid state systems and also for studying exotic many body systems that find no equivalent in the solid state world. The first optical lattices have attracted interest [114–116] even before the experimental creation of degenerate atomic ensembles [117]. One of the very first optical lattices that has been realized [118] was a lattice created by interfering three beams in a plane with an angle of 120° between each pair, which is called a hexagonal lattice, describing the form of the resulting unit cell. Hexagonal optical lattices have ever since continued revealing a plenitude of intriguing physics through generations of experiments [33, 40, 41, 45, 47, 63, 119–121], including the ones presented in this thesis.

3.1 The optical dipole potential

The effect of an OPL on the dynamics of an atomic ensemble can, under certain circumstances, be well approximated by adding an additional scalar potential, that is proportional

to the local light intensities, to the Hamiltonian of the system. This so-called optical dipole potential arises from the interaction energy between the oscillating electric field \mathbf{E} of the beams constituting the OPL and the electric dipole moments that it induces in the atoms. The dipole potential $V(\mathbf{r})$ can thus be written for an atom with polarizability α within linear response as [107]

$$V(\mathbf{r}) = -\frac{1}{2} \text{Re}\{\mathbf{E}\} \cdot \text{Re}\{\alpha\mathbf{E}\} \quad (3.1)$$

When neglecting both the inhomogeneity of the polarization of the electric field and the terms of twice the original field frequency, that are created in the mixing process described by Eq. 3.1 but are suppressed by the inertia of the atoms, the potential takes up the following more intuitive form that shows a proportionality of the potential to the local light intensity $I(\mathbf{r})$:

$$V(\mathbf{r}) = -\frac{1}{2\epsilon_0 c} \text{Re}\{\alpha\} I(\mathbf{r}) \quad (3.2)$$

Here ϵ_0 refers to the vacuum permittivity and c to the speed of light. The polarizability of the atom depends on the internal structure of the atom and is a function of the frequency ω of the driving field, but can be treated as a constant for all experiments presented in this thesis because all occurring field frequencies lie within a band width of $\sim 10\text{kHz}$ corresponding to a mere 0.1 ppb of ω , over which α does not vary significantly. The numeric value of α can be determined by modeling the atom as a two level system in a classical light field. By neglecting saturation effects, i.e. the excitation of the atom, and making a rotating-wave approximation the polarizability takes the form (derived from [107])

$$\alpha = -\frac{3\pi c^3 \epsilon_0}{2\omega_0^3} \frac{\Gamma}{\Delta} \left(1 - i \frac{\Gamma}{2\Delta} \right) \quad (3.3)$$

where ω_0 is the resonance frequency of the two level system, Γ the natural (electric dipole) linewidth of the system, and $\Delta = \omega - \omega_0$ the detuning. The necessary condition to neglect saturation effects is a detuning that is much larger than Γ while the rotating wave approximation requires a detuning small compared to the atomic resonance. For the system considered in this thesis of potassium atoms in an optical lattice of 1064 nm wave length, both of these conditions are perfectly fulfilled. The contribution of the imaginary part, which determines the scattering rate, is of the order of 10^{-4} for a linewidth of around 6 MHz for the D1 and D2 lines of potassium and will henceforth be neglected.

3.2 Lattice structures

The lattice potentials considered in this thesis are created by superimposing the foci of multiple beams incident from different directions. In a region around this common

intersection point the electric fields of the individual beams can be well approximated [108] as plane waves and can be put in the following form

$$\mathbf{E}_i(\mathbf{r}, t) = \text{Re}\left\{\bar{E}_i \mathbf{P}_i \exp(i(\mathbf{k}_i \cdot \mathbf{r}_i - \omega t))\right\} \quad (3.4)$$

where the sub index i enumerates the beams and \bar{E}_i is the amplitude of the electric field, \mathbf{k}_i is the wave vector, ω the frequency, and $\mathbf{P}_i \in \mathbb{C}(3)$ the complex polarization unit vector also known as *phasor*. For the rest of this thesis the commonly used complex field notation will be used, i.e. the Re symbol will be dropped and understood implicitly to improve the readability of the formulas. Here \mathbf{P}_i is defined in the full three dimensional space despite the fact that all components parallel to \mathbf{k}_i are unphysical. This facilitates the computation of the interference terms when beams of different \mathbf{k}_i are involved. To express \mathbf{P}_i more customarily as a polarization vector with the orthogonal and parallel components s and p one needs to chose a basis for the polarization space of each beam. For forming an orthonormal basis the polarization unit vectors $\hat{\mathbf{s}}_i$ and $\hat{\mathbf{p}}_i$ have to fulfill¹

$$\hat{\mathbf{s}}_i = \hat{\mathbf{k}}_i \times \hat{\mathbf{p}}_i \quad (3.5)$$

where $\hat{\mathbf{k}}_i$ is a unit vector in the direction of the wave vectors $\mathbf{k}_i = k_L \hat{\mathbf{k}}_i$ with k_L as the common wavenumber as given by the wavelength of the lattice beams. The last degree of freedom, that uniquely defines the polarization basis, can be chosen arbitrarily. Here a definition is presented where all $\hat{\mathbf{p}}_i$ are parallel to the xy-plane

$$\hat{\mathbf{p}}_i = \frac{\hat{\mathbf{z}} \times \hat{\mathbf{k}}_i}{\|\hat{\mathbf{z}} \times \hat{\mathbf{k}}_i\|} \quad (3.6)$$

This choice is particularly convenient for the description of the experiments in this thesis which are conducted in a lattice confined to this same plane. Using a spherical coordinate system the unit vectors can be written more explicitly as

$$\hat{\mathbf{k}}_i = \begin{pmatrix} -\cos \vartheta_i^{(k)} \sin \varphi_i^{(k)} \\ \cos \vartheta_i^{(k)} \cos \varphi_i^{(k)} \\ \sin \vartheta_i^{(k)} \end{pmatrix} \quad \hat{\mathbf{p}}_i = \begin{pmatrix} \cos \varphi_i^{(k)} \\ -\sin \varphi_i^{(k)} \\ 0 \end{pmatrix} \quad \hat{\mathbf{s}}_i = \begin{pmatrix} \sin \vartheta_i^{(k)} \sin \varphi_i^{(k)} \\ -\sin \vartheta_i^{(k)} \cos \varphi_i^{(k)} \\ \cos \vartheta_i^{(k)} \end{pmatrix} \quad (3.7)$$

Having made a choice for the polarization basis, the phasors \mathbf{P}_i can be written explicitly as

$$\mathbf{P}_i = \exp(i\varphi_i) (s_i \hat{\mathbf{s}}_i + p_i \hat{\mathbf{p}}_i) \quad (3.8)$$

with φ_i as an additional phase factor relevant for the description of the relative phase between the beams constituting the lattice. The relevance of this inconspicuous phase

¹up to sign.

factor will be elaborated upon in the next subsection, and Chap. 9 is solely concerned with its experimental control. The phasors can be alternatively parameterized in terms of the phase and mixing angles α_i and ϑ_i which describe the polarization as a vector on the Poincaré sphere

$$\mathbf{P}_i = e^{i\varphi_i} \begin{pmatrix} e^{i\alpha_i} \sin \vartheta_i \\ \cos \vartheta_i \end{pmatrix} \cdot \begin{pmatrix} \hat{\mathbf{s}}_i \\ \hat{\mathbf{p}}_i \end{pmatrix} \quad (3.9)$$

Having made all these definitions one can finally write the dipole potential associated with the interfering plane waves by inserting 3.9 into 3.4 as

$$V(\mathbf{r}) = -\frac{\alpha}{4} \left[\sum_i \bar{E}_i^2 + 2 \sum_i \sum_{j<i} \bar{E}_i \bar{E}_j \operatorname{Re}\{\mathbf{P}_i \cdot \mathbf{P}_j \exp(i(\mathbf{k}_j - \mathbf{k}_i) \cdot \mathbf{r})\} \right] \quad (3.10)$$

The first sum of this equation is merely a constant offset that has no influence on the dynamics of the atoms. The double sum in this equation is a sum over all the pairs of beams. Every pair contributes to the lattice potential with a homogeneous potential that is cosine modulated in the direction perpendicular to the bisection of the wave vectors of the involved beams. The complex amplitude of these fundamental 1D lattices is determined by the scalar product of the involved phasors, that will be abbreviated forth on as

$$P_{ij} = \bar{E}_i \bar{E}_j \mathbf{P}_i \cdot \mathbf{P}_j \quad P_0 = \sum_i |\bar{E}_i \mathbf{P}_i|^2 \quad (3.11)$$

Here shall be noted that there are two different conventions for defining the scalar product for complex valued vectors, in regard to which elements are complex conjugates. In this notation the complex conjugation of the first vector was chosen. Any optical lattice is thus fully characterized by these phasor products and the wave vectors of the involved beams.

3.2.1 Three beam lattices

Among the vast range of different optical potentials that can be described by Eq. 3.10, the class of potentials created by three non-colinear beams takes up a special role. Their interference creates a potential with a periodicity characterized by a two dimensional lattice $\operatorname{Span}_{\mathbb{Z}}\{\mathbf{a}_1, \mathbf{a}_2\}$, whose lattice vectors \mathbf{a}_1 and \mathbf{a}_2 are exclusively determined by the involved wave vectors [122]. A fourth beam, that does not lie in the lattice plane, yields a three-dimensional lattice with the same properties. A fourth beam within the plane or any number of additional beams would create a dependence on the phases of the involved beams. In the three beam case a change of the relative phase results simply in a translation of the whole lattice. The ability to control the position of the lattice potential while leaving its structure untouched is a crucial ingredient for engineering effective Floquet lattice potentials, that result from translating lattice potentials on periodic trajectories and will be discussed in Sec. 4.3. This relationship can be best understood by analyzing

the periodicity of the lattice potential within in terms of a Fourier expansion. A three beam potential is, following Eq. 3.10, determined by the sum of the three pairs of beams and can thus be written as

$$V(\mathbf{r}) = -\frac{\alpha}{4} \left[\frac{1}{2}P_0 + P_{12}e^{i\mathbf{b}_1 \cdot \mathbf{r}} + P_{23}e^{i\mathbf{b}_2 \cdot \mathbf{r}} + P_{13}e^{i(\mathbf{b}_1+\mathbf{b}_2) \cdot \mathbf{r}} + \text{c.c.} \right] \quad (3.12)$$

The vectors \mathbf{b}_i that define the periodic axes are called *Bravais* vectors. Due to their relation to the coordinate vector \mathbf{r} via a scalar product they are defined in a dual space which is commonly referred to as the reciprocal space. In the case of a three beam lattice they are determined by the wave vectors

$$\begin{aligned} \mathbf{b}_1 &= \mathbf{k}_1 - \mathbf{k}_2 \\ \mathbf{b}_2 &= \mathbf{k}_2 - \mathbf{k}_3 \\ \Rightarrow \mathbf{b}_2 + \mathbf{b}_1 &= \mathbf{k}_1 - \mathbf{k}_3 \end{aligned} \quad (3.13)$$

Eq. (3.12) shows also that the phasor products are the Fourier coefficients of the potential. To make this point clearer consider the reformulation in the square lattice form:

$$\tilde{V}(\mathbf{t}) = \sum_{m,n} V_{mn} e^{i(mt_1+nt_2)} \quad V(\mathbf{r}) = \tilde{V}(\mathbf{B} \mathbf{r}) \quad \mathbf{B} = (\mathbf{b}_1 \mathbf{b}_2)^T \quad (3.14)$$

with the matrix elements

$$V_{mn} = -\frac{\alpha}{4} \left(\begin{array}{c|ccc} m \backslash n & -1 & 0 & 1 \\ \hline -1 & P_{13}^* & P_{12}^* & 0 \\ 0 & P_{23}^* & P_0 & P_{23} \\ 1 & 0 & P_{12} & P_{13} \end{array} \right) \quad (3.15)$$

The fact, that the normal vector of the third pair is a linear combination of the two others is essential here. If there was another vector \mathbf{b}_3 that lay in the plane spanned by \mathbf{b}_1 and \mathbf{b}_2 , as it would be the case for a 2D lattice composed of more than three beams, the potential could not be written in this simple form where the Bravais vectors are given by the wave vector differences and the Fourier components by the products of phasors. Instead one would need to find two shorter Bravais vectors, with which there exist pairs of integers to linear combine every difference $\mathbf{k}_i - \mathbf{k}_j$ of wave vectors. The wave vectors can be chosen such that the Bravais vectors become arbitrarily short and thereby create a lattice that can have an arbitrarily long period as exemplarily shown in Fig. 3.1. These lattices are therefore referred to as *quasi periodic* crystals or short *quasicrystals*.

To understand the relationship between the phasors and the translation consider the subspace spanned by the two Bravais vectors. In this subspace the Bravais vectors have a two dimensional representation and the coordinate transformation matrix \mathbf{B} becomes invertible. With the definitions from eq. (3.14) a translation of the potential $\tilde{V}(\mathbf{t} + \Delta\mathbf{t})$

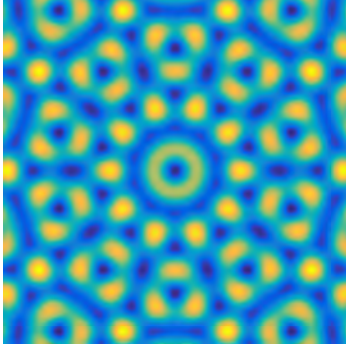


Figure 3.1: Quasicrystal. This optical potential is created by the interference of five s polarized beams with equal angles between the wave vectors of neighboring pairs. The image is produced using the band structure simulator.

corresponds to $V(\mathbf{r} + \mathbf{B}^{-1} \Delta \mathbf{t})$ and as \tilde{V} has a periodicity of 2π in both t_1 and t_2 , the real space lattice vectors can be identified as

$$\mathbf{a}_1 = \mathbf{B}^{-1} \begin{pmatrix} 2\pi \\ 0 \end{pmatrix} \quad \mathbf{a}_2 = \mathbf{B}^{-1} \begin{pmatrix} 0 \\ 2\pi \end{pmatrix} \quad (3.16)$$

Translations of the lattice other than 2π will create additional phase factors for the Fourier coefficients. The resulting coefficients, however, correspond to the lattice obtained from a phase shift of the phasors. Put the other way round: a change in phases of the phasors creates an identical lattice potential that is shifted in space. Inserting the phase shifts $\Delta\varphi_1$, $\Delta\varphi_2$ and $\Delta\varphi_3$ into the definitions of the corresponding phasors will yield coefficients V_{mn} with additional phase factors that can be absorbed into t_1 and t_2 , which creates a translation in real space of

$$\Delta \mathbf{r} = \mathbf{B}^{-1} \begin{pmatrix} \Delta\varphi_1 - \Delta\varphi_2 \\ -\Delta\varphi_3 + \Delta\varphi_2 \end{pmatrix} \quad (3.17)$$

The Bravais vectors span a lattice themselves, which is commonly referred to as the reciprocal lattice or the dual lattice. Through the relationship of the dual space the lattice G and the reciprocal lattice Γ can be defined via

$$\begin{aligned} \begin{pmatrix} m \\ n \end{pmatrix} \cdot \mathbf{B} \mathbf{r} &= \mathbf{B}^T \begin{pmatrix} m \\ n \end{pmatrix} \cdot \mathbf{r} \\ G &= \left\{ \mathbf{a}_{mn} \mid m, n \in \mathbb{Z}, \mathbf{a}_{mn} = 2\pi \mathbf{B}^{-1} \begin{pmatrix} m \\ n \end{pmatrix} \right\} \\ \Gamma &= \left\{ \mathbf{b}_{mn} \mid m, n \in \mathbb{Z}, \mathbf{b}_{mn} = \mathbf{B}^T \begin{pmatrix} m \\ n \end{pmatrix} \right\} \end{aligned} \quad (3.18)$$

3.2.2 In-plane lattices

In the special case of a lattice where all three beams lie in a plane, the orthogonal polarization modes of the beams decouple, and the total lattice potential can be split into the sum of an s and p contribution, which have an identical lattice structure², but their depths and position can be controlled independently by changing the phase and population of their corresponding polarization mode. This can be seen when considering how the scalar product of the pairs of phasor vectors simplifies. With the definitions for the direction of wave vectors in eq. (3.7) such an in-plane lattice is given for $\vartheta_k^{(1,2,3)} = 0$. The polarization basis as chosen in Eqs. 3.6 takes a particularly simple form for in-plane lattices. Here the s polarization basis vectors $\hat{\mathbf{s}}_{(1,2,3)}$ are all identical $\hat{\mathbf{s}}_{(1,2,3)} = \hat{\mathbf{z}}$ and thereby orthogonal to all other p polarization unit vectors. The scalar products of the phasors therefore lose their mixed terms

$$\mathbf{P}_j \cdot \mathbf{P}_i = s_i s_j^* \hat{\mathbf{s}}_i \cdot \hat{\mathbf{s}}_j + \cancel{s_i p_j^* \hat{\mathbf{s}}_i \cdot \hat{\mathbf{p}}_j} + \cancel{p_i s_j^* \hat{\mathbf{p}}_i \cdot \hat{\mathbf{s}}_j} + p_i p_j^* \hat{\mathbf{p}}_i \cdot \hat{\mathbf{p}}_j \quad (3.19)$$

and reduce to

$$\mathbf{P}_j \cdot \mathbf{P}_i = s_i s_j^* + p_i p_j^* \cos(\varphi_i^{(k)} - \varphi_j^{(k)}) \quad (3.20)$$

In the Poincaré sphere basis for the polarizations this is

$$\mathbf{P}_j \cdot \mathbf{P}_i = \exp(i(\varphi_i - \varphi_j)) \left[\exp(i(\alpha_i - \alpha_j)) \sin(\vartheta_i) \sin(\vartheta_j) + \cos(\varphi_i^{(k)} - \varphi_j^{(k)}) \cos(\vartheta_i) \cos(\vartheta_j) \right] \quad (3.21)$$

The lattice potential can now be split up into a part V_s with only the $s_i s_j^*$ terms and one part V_p with only the $p_i p_j^*$ terms, where the relative phase angles α_i take up a role that is identical to the role taken by the absolute phase angles φ_i and will therefore cause the same translation but only for V_s

$$V(\mathbf{r}) = V_s(\mathbf{r}) + V_p(\mathbf{r}) \quad \longrightarrow \quad V_s(\mathbf{r} + \Delta\mathbf{r}_s + \Delta\mathbf{r}) + V_p(\mathbf{r} + \Delta\mathbf{r}) \quad (3.22)$$

$$\Delta\mathbf{r}_s = \mathbf{B}^{-1} \begin{pmatrix} \Delta\alpha_1 - \Delta\alpha_2 \\ -\Delta\alpha_3 + \Delta\alpha_2 \end{pmatrix} \quad (3.23)$$

This means, that experimental control over the polarization and relative phase not only allows to position a lattice potential accurately in space, but also allows to precisely vary its shape by moving the two components relative to each other.

²The sign of the two lattices may be inverted changing the role of minima and maxima and leading to potentially different number and relative position of lattice sites within the unit cell. This is e.g. the case for hexagonal lattices which will be discussed later

3.2.3 Hexagonal lattices

The hexagonal lattice is a special case of the three-beam in-plane lattice, which is of special interest in the context of this thesis because it is the lattice type that has been used to conduct the presented experiments. The hexagonal lattice derives its name from the fact that its Wigner-Seitz-Cell has the shape of a hexagon. It is attained by symmetrically arranging the three beams in the plane, such that all three pairs of beams enclose an angle of 120°

$$\forall_{i,j \in [1,2,3]} \quad \left| \varphi_i^{(k)} - \varphi_j^{(k)} \right| = \frac{4\pi}{3} \quad \Longrightarrow \quad \hat{\mathbf{p}}_i \cdot \hat{\mathbf{p}}_j = -\frac{1}{2} \quad (3.24)$$

The resulting numerical values describing the geometry of the hexagonal lattice are summarized in appendix A. All restrictions that have been made so far only concerned the choice of the wave vectors and thereby the geometry of the lattice. Despite those restrictions, the class of hexagonal lattice potentials still spans a parameter space of six free phasor parameters, when excluding changes under rotation, translation and an overall potential scaling factor. As a final restriction the subspace of balanced hexagonal lattice potentials will be considered in the following.

Balanced hexagonal lattices

With the term balanced optical lattice potential it shall be referred to a lattice with a symmetric choice mixing angles $\vartheta_i = \vartheta$ and field amplitudes $\bar{E}_i = \bar{E}$. Owed to this choice the lattice acquires a rotational symmetry of order three and has only three free parameters. Its Fourier components take the simple form

$$\mathbf{P}_j \cdot \mathbf{P}_i = \exp(i(\varphi_i - \varphi_j)) \left[\sin^2(\vartheta) \exp(i(\alpha_i - \alpha_j)) - \frac{1}{2} \cos^2(\vartheta) \right] \quad (3.25)$$

The three parameters determine the relative position of the two polarization sublattice potentials (α_i) and the relative strength (ϑ). The polarization sublattice potentials themselves do not have any free parameters and are inverse of each other (factor $-1/2$). Potentials of this form are commonly referred to as honeycomb and triangular lattice potentials. Which sign refers to which potential depends on the sign of the polarizability. In the case of potassium atoms in a red detuned lattice as in the experiments of this work, the former is the triangular and the latter the honeycomb potential. Both lattice geometries have already been realized in the context of ultracold atoms ([40, 47]).

Boron nitride lattice

The boron nitride type lattice is a special type of hexagonal lattice. It is similar to the honeycomb lattice in that way, that is has two local minima per unit cell, but reduces the order of the rotational symmetry from six to three by reducing the depths of one of the two minima. Such a lattice can be created by choosing the polarization angles for the

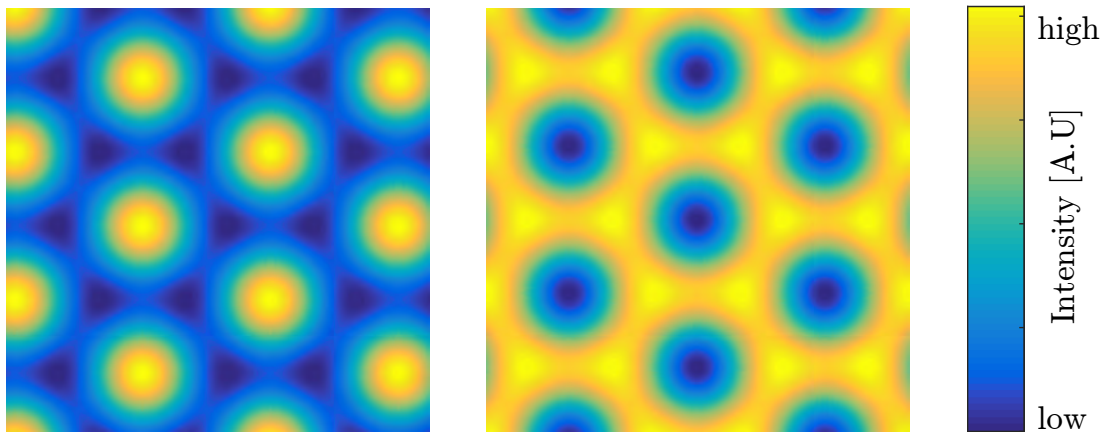


Figure 3.2: Interference pattern of triangular and honey comb lattices. For ^{40}K the atoms are trapped in the intensity maxima, thus the left panel depicts the triangular lattice and the right one the honeycomb lattice.

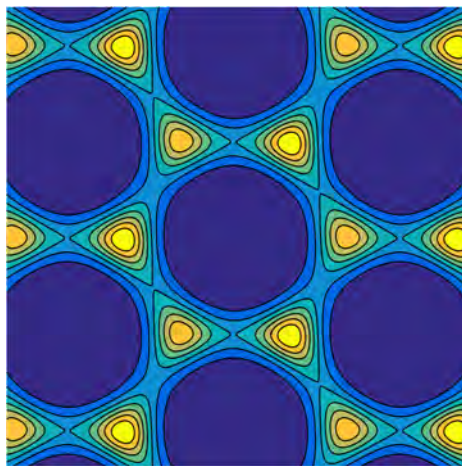


Figure 3.3: The boron nitride lattice. The interference pattern for a balanced hexagonal lattice with polarizations determined by the mixing angles all of 9° and phase angles of 0° , 60° and 120° . The scale is exponential, and contours have been added to make the relatively small offset between the A and B sites visible

hexagonal lattice such that the triangular lattice component is translated to a position, where its maximum coincides with one of the minima of the honeycomb component. This is for example the case for the polarization phase angles $\alpha_{1,2,3} = \frac{2\pi}{3} \begin{pmatrix} 0 & 1 & 2 \end{pmatrix}$. The mixing angle ϑ , as the remaining degree of freedom controls the offset of the two types of sites of this so-called A-B-lattice. In the context of this thesis, the boron nitride lattice has been chosen, because it breaks inversion symmetry, which has important consequences for the geometric properties of its band structure.

The s- and p-contributions (as of Eq. 3.22) to the overall potential of the boron nitride

lattice are obtained by inserting the phase angles into Eq. 3.25 and further into Eq. 3.12

$$\begin{aligned}
 V_s(\mathbf{r}) &= -2V_L \sin^2 \vartheta \left[\cos(\mathbf{b}_1 \cdot \mathbf{r} + \varphi_{12} - 2\pi/3) + \right. \\
 &\quad \cos(\mathbf{b}_2 \cdot \mathbf{r} + \varphi_{23} - 2\pi/3) + \\
 &\quad \left. \cos((\mathbf{b}_2 + \mathbf{b}_1) \cdot \mathbf{r} + \varphi_{31} - 4\pi/3) \right] \\
 V_p(\mathbf{r}) &= V_L \cos^2 \vartheta \left[\cos(\mathbf{b}_1 \cdot \mathbf{r} + \varphi_{12}) + \right. \\
 &\quad \cos(\mathbf{b}_2 \cdot \mathbf{r} + \varphi_{23}) + \\
 &\quad \left. \cos((\mathbf{b}_2 + \mathbf{b}_1) \cdot \mathbf{r} + \varphi_{31}) \right]
 \end{aligned} \tag{3.26}$$

where the overall lattice depth has been gathered into

$$V_L = \frac{\alpha}{4} I \tag{3.27}$$

with I being the light intensity of one of the three equal beams.

3.3 Band Structure Description

In quantum mechanics the dynamics, stationary states and excitation spectra of any physical system can be derived from its Hamiltonian operator. The Hamiltonian of a quantum many-body system, such as an ensemble of atoms in an optical lattice, takes into account quantum statistics and interactions between atoms. An essential building block for the construction of a many-body Hamiltonian are the eigenstates and energies of the single particle Hamiltonian, which describes a single interactionless particle. In the present case of ultracold fermions, which exhibit negligible interactions and can, to most respects, be well approximated by a zero temperature description, the spectrum of the single particle Hamiltonian is identical to the one of a many-body Hamiltonian and thereby also the eigenstates can be trivially extended. Therefore the subject of discussion of the following section will be the single particle Hamiltonian of an atom in an optical lattice and the solutions to its eigenvalue equation, i.e. the stationary Schrödinger equation.

The Hamiltonian operator arises by canonical quantization from the Hamiltonian function. With the Fourier representation of the lattice potential as given in Eq. 3.14 and Eq. 3.15 the Hamiltonian thus reads as

$$H_0 = \frac{\mathbf{p}^2}{2m_A} + \sum_{m,n} V_{mn} \exp(i\mathbf{b}_{mn} \cdot \mathbf{r}) \tag{3.28}$$

where \mathbf{p} and \mathbf{r} are the momentum and position operators and m_A the mass of the particle, here the atomic mass of ^{40}Na . Without any restrictions on the Fourier coefficients, this Hamiltonian represents a particle in an arbitrary two dimensional periodic potential. For convenience the Hamiltonian will from now on be expressed unitless. Its natural energy

scale is given by the recoil energy $E_{\text{Rec}} = \hbar^2 k_L^2 / 2m_A$, which describes the kinetic energy an atom gains/loses upon the absorption/emission of a lattice photon. Rescaling the Hamiltonian by $H = (E_{\text{Rec}})^{-1} H_0$ allows to write it in the compact form

$$H = \mathbf{k}^2 - \sum_{m,n} v_{mn} \exp(i\mathbf{b}_{mn} \cdot \mathbf{r}) \quad (3.29)$$

where also the potential has been expressed in terms of atomic recoil units $V_{mn} = E_{\text{Rec}} v_{mn}$, and the unitless wavenumber operator $\mathbf{k} = \mathbf{p} / \hbar k_L$ has been introduced.

Eq. 3.29 has the same functional form of the Hamiltonian used in solid state physics to describe an electron in an atomic crystal structure. In the solid state case, the Fourier series is infinite because the lattice potential results from the superposition of the coulomb potentials of the atomic cores, which are of singular nature. As shown in Sec. 3.2.1, for an optical lattice with two dimensions, created by three beams, there are only nonzero Fourier coefficients for $|m|, |n| \leq 1$. Despite the simplicity and compactness of the eigenvalue equation for a Hamiltonian with this highly harmonic potential, there is no general analytic solution and it has to be treated similarly to the solid state case. This implies that the following calculations are not restricted to three beam lattices. For a higher number of beams the Bravais vectors have to be determined (see Sec. 3.2.1), and in general there will also be non zero Fourier coefficients for higher orders of m and n .

The spatial periodicity of the Hamiltonian can be expressed in the form of a discrete translation symmetry, which manifests in the fact that the Hamiltonian commutes with the lattice translation operator T_{mn} . They can thereby be diagonalized simultaneously

$$H |\psi_{\mathbf{q}n}\rangle = E_n(\mathbf{q}) |\psi_{\mathbf{q}n}\rangle \quad (3.30a)$$

$$T_{mn} |\psi_{\mathbf{q}n}\rangle = \exp(i\mathbf{q} \cdot \mathbf{a}_{mn}) |\psi_{\mathbf{q}n}\rangle \quad (3.30b)$$

which give rise to an additional quantum number q which is, in analogy to the momentum quantum number for continuous translation symmetry, called quasimomentum. The quasimomentum is defined within the Wigner-Seitz cell of the reciprocal space, which is also known as the (first) Brillouin Zone. Eq. 3.30 also introduces the band index n which owes its name to the fact that the spectrum $E_n(\mathbf{q})$ forms bands, that are generally continuous in \mathbf{q} and discrete in n .

The states of the eigenbasis $|\psi_{\mathbf{q}n}\rangle$ are the so-called Bloch states. Opposed to the Hamiltonian, they are eigenstates to the translation operator and therefore not invariant under lattice translation (for eigenvalues other than unity). They can however be decomposed into a lattice periodic wavefunction $|u_{\mathbf{q}n}\rangle$ and the momentum translation operator, as stated by the so-called Bloch theorem

$$|\psi_{\mathbf{q}n}\rangle = T_k(\mathbf{q}) |u_{\mathbf{q}n}\rangle \quad (3.31)$$

The momentum translation operator conducts a boost into a moving frame and is defined by the translation of the momentum eigenstates $|k\rangle$ as follows

$$T_k(\mathbf{k}) |k'\rangle = |\mathbf{k} + \mathbf{k}'\rangle \quad (3.32)$$

and it can be expressed in terms of the position operator

$$T_{\mathbf{k}}(\mathbf{k}) = \exp(-i\mathbf{k} \cdot \hat{\mathbf{r}}) \quad (3.33)$$

In this sense, the Bloch theorem is equivalent to stating that the non zero Fourier components of the Bloch functions coincide with the reciprocal lattice that has been shifted by their quasimomentum.

It is convenient to use eq. (3.33) to reformulate the potential operator as a function of the momentum translation operator

$$H = \mathbf{k}^2 - \sum_{m,n} v_{mn} T_{\mathbf{k}}(-k_{\mathbf{L}} \mathbf{b}_{mn}) \quad (3.34)$$

In this form, not only the description of the lattice in the Bragg picture becomes evident, but also the separability of the Hamiltonian into quasimomentum eigenspaces. This means, that when the momentum operator is separated into the quasimomentum contribution and the reciprocal lattice contribution, i.e.

$$\mathbf{k} = \mathbf{q} + \mathbf{b}_{mn} \quad (3.35)$$

then the matrix elements in the momentum basis split up into a product of a \mathbf{q} -dependent term and a lattice index dependent term

$$\begin{aligned} \langle \mathbf{k}' | H | \mathbf{k} \rangle &= \mathbf{k}^2 \delta(\mathbf{k} - \mathbf{k}') - \sum_{m,n} v_{mn} \delta(\mathbf{k} - \mathbf{k}' - \mathbf{b}_{mn}) \\ \langle \mathbf{q}' + \mathbf{b}_{s't'} | H | \mathbf{q} + \mathbf{b}_{st} \rangle &= \delta(\mathbf{q} - \mathbf{q}') \underbrace{\left[(\mathbf{q} + \mathbf{b}_{st})^2 \delta_{ss'} \delta_{tt'} + \sum_{mn} v_{mn} \delta_{(s-s')m} \delta_{(t-t')n} \right]}_{\langle \mathbf{b}_{s't'} | H_{\oplus}(\mathbf{q}) | \mathbf{b}_{st} \rangle} \end{aligned} \quad (3.36)$$

which, for a finite dimensional case, could be visualized as a block diagonal form. For the infinite dimensional case this decomposition can be expressed by the direct integral, a continuous extension of the direct sum

$$H = \int_{\text{BZ}}^{\oplus} H_{\oplus}(\mathbf{q}) d\mathbf{q} \quad [H_{\oplus}(\mathbf{q}), H_{\oplus}(\mathbf{q}')] = \delta(\mathbf{q} - \mathbf{q}') \quad (3.37)$$

Here \mathbf{q} ceases to be an operator and becomes an index, because for this separation a partial choice of basis has been made. This separation of spaces forms the foundation to geometry and thereby topology in periodic systems.

3.3.1 Numerical Implementation

As a part of this thesis a software has been developed that allows a fast and intuitive exploration of band structures and lattice potentials within the vast parameter space of optical lattices generated by three beams. The core algorithm is based upon and tested

against a previous version that has been created by Dr. Christoph Becker [101], which was restricted to triangular and honeycomb lattices. The new algorithm extends the functionality to any type of optical lattice. A GUI has been created and to allow a fluent usage of it, the performance has been improved tenfold for the single threaded case, plus a strongly machine dependent improvement by parallelization. Fig. 3.4 shows the user interface, and the caption summarizes its features.

The Hamiltonian in Eq.3.37 acts on an infinite dimensional Hilbert space. In order to compute a numerical solution, the problem has to be reduced to a finite dimensionality. The chosen Fourier basis is especially suited for this reduction, because higher Fourier frequencies are associated with higher bands. For the study of the lowest two bands, which are of principal interest for the remainder of this thesis, it is sufficient to use a truncated space that only includes Fourier components up to an order of $c = 5$, i.e. the indices from Eq. 3.35 (later in Eq. 3.36 called s and t) are restricted to $|n|, |m| \leq c$. The validity of this approach becomes plausible by calculating the convergence of the band structure with increasing Fourier order. Fig. 3.5 shows the error of the truncated band structure relative to a reference calculation based on the order $c = 10$.

Even with this reduction of dimensionality eq. (3.36) does not resemble a standard eigenvalue problem in matrix form. This is because the Fourier basis for the two dimensional wave functions is indexed by two indices corresponding to the two dimensions of the reciprocal space. Linear algebra is however completely agnostic to the order of the base elements and the two indices can therefore be replaced by a single one. In computer algebra systems this conversion is common practice and is known as *subindexing* or *index raveling*. The mapping between the indices is arbitrary and here we chose the simplest possible, corresponding to enumerating the matrix elements column by column or more formally expressed by indexing functions

$$\begin{aligned} m &= u \bmod d - c \\ n &= u \operatorname{trunc} d - c \\ \iff u &= (n + c)d + (m + c) + 1 \end{aligned} \tag{3.38}$$

where u is the new flattened index ranging from 1 to $D = d^2$, $d = 2c + 1$ is the number of Fourier components in one dimension, and mod and trunc describe the modulus and truncated division (i.e. division with subsequent truncation after the decimal point) operations. While eq. (3.38) describes a two dimensional subindexing, the extension to arbitrary dimensions is trivial. For a short code snippet illustrating the matrix representation of the potential, the reader is referred to App. B.

With this subindexing the Hamiltonian can be cast in matrix form and standard algorithms can be used to determine the eigenvalues and vectors. In this concrete case for the Hamiltonian as a hermitian matrix, the used algorithm is the built-in Cholsky decomposition. With respect to the few nonzero elements of the matrix an algorithm for sparse matrices could yield further speedup. In the non sparse case care has to be taken to avoid unnecessary copies of the data. With the chosen truncation of Fourier

components the matrix has a size of 121×121 which amounts to about one gigabyte when rasterizing the Brillouin zone in a 100×100 . Even though one gigabyte of data can be handled easily by modern computers, multiple copies of the data set, or data leaks, quickly fill the RAM and cause swapping, which slows down the calculation by several orders of magnitude. While the current implementation only allows a near real-time exploration of the parameter space for an extremely low resolution of the reciprocal space, the problem is ideally suited for an implementation on a GPGPU³-system, because of the high degree of parallelizability. It is also conceivable to implement a progressive algorithm that starts out by solving the problem for a highly truncated space and iteratively includes more Fourier components.

³general-purpose computing on graphics processing unit

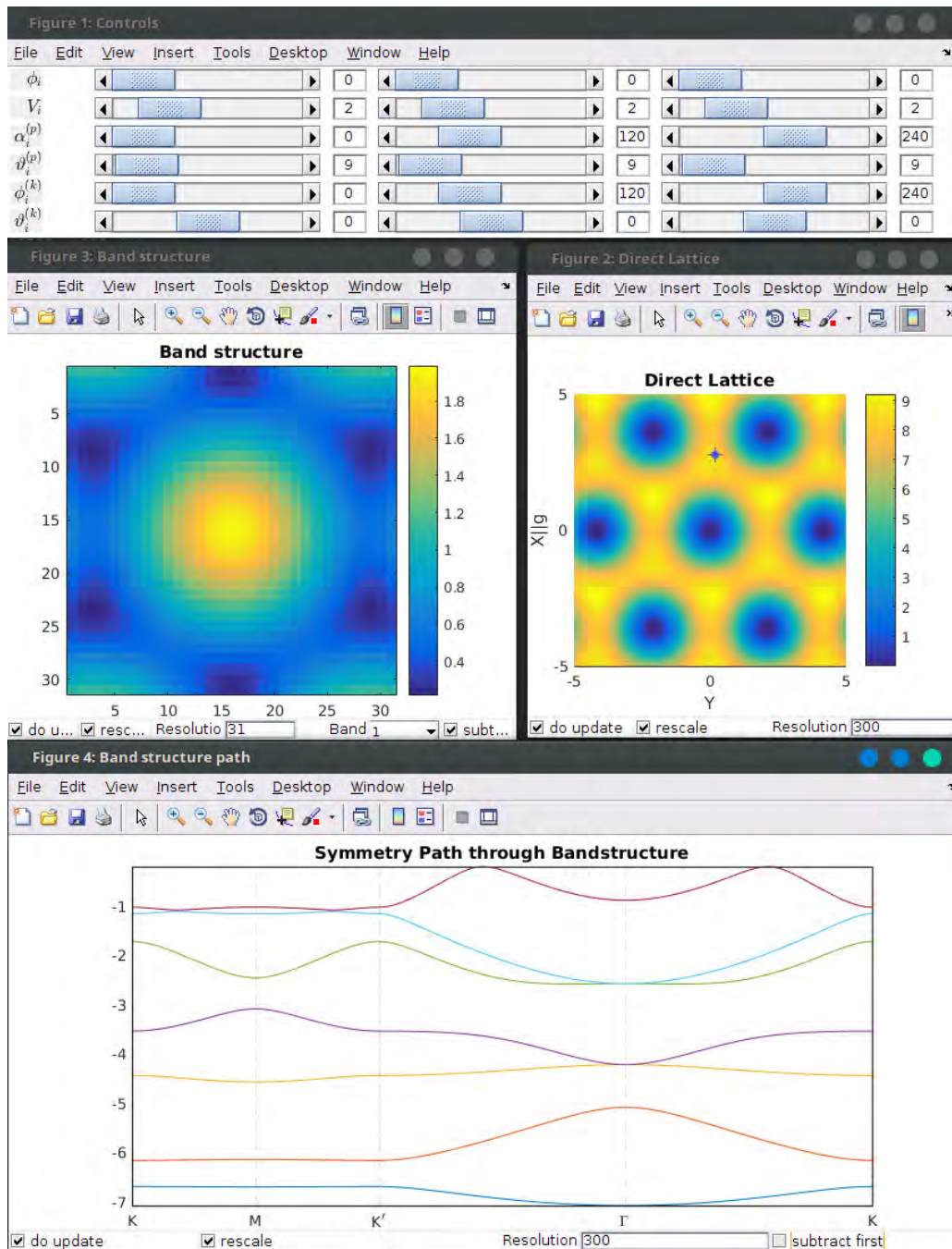


Figure 3.4: Screenshot of the band structure simulation program, developed as part of this thesis. The upper window allows to set all parameters of the three lattice beams. The values can be entered directly or a slider can be used. Upon changes the update of the remaining windows is triggered immediately. In the second row the band structure and the direct lattice (intensity) are shown. The resolution can be changed, and in case of the band structure, the band desired for display as well as the subtraction of the first band can be chosen (all options in bottom status bar of the window). The lower window shows the band structure along the high symmetry path. Here only the points along the path are calculated to enable a responsive update of the plot.

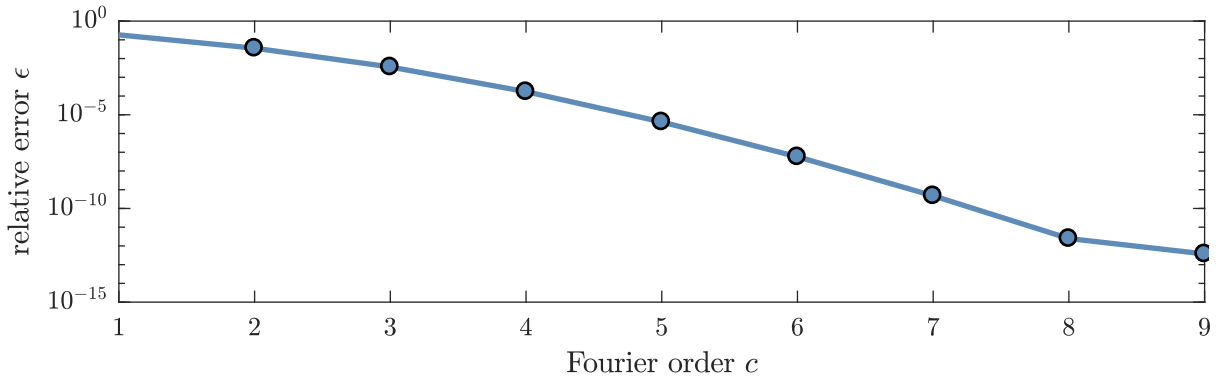


Figure 3.5: This plot shows the dependency of the relative error $\epsilon(c) = \sum_{k_x, k_y \in \text{BZ}} 1/E_{\text{Ref}} N (E(c) - E_{\text{Ref}})$ as a function of the truncation order c . Here $E(c)$ represents the integrated energy difference between the lowest two bands of a boron nitride lattice ($\theta = 9^\circ, V = 15.5 E_{\text{Rec}}$) arising from a calculation of the order c while E_{Ref} was determined including orders up to $c = \pm 10$. The sum is carried out over the smallest square including the hexagonal Brillouin zone on a regular grid of $N = 225$ points. The observed breakdown of convergence for orders > 8 is most likely due to the limit imposed by numerical precision.

3.4 A Tight-Binding Model for Boron Nitride Lattices

3.4.1 Motivation

The experiments conducted at this thesis are all concerned with the geometric effects of the lowest two bands, the so-called s-bands, of a Boron nitride lattice. Even though geometric properties can be assigned to certain bands, they are generally dependent on the complete Hamiltonian (see Chap. 4, e.g. the definition of the Berry curvature in Eq. 4.14). In the case of the boron nitride lattice in the chosen parameter regime (see Chap. 6), there is however a strong separation of energy scales between the family of the lowest two Bloch bands and the rest of the spectrum. Therefore the Hamiltonian projected onto this two-band sub-Hilbert space constitutes a good approximation of the actual system.

This approximation is motivated by the intuitive picture of the geometric and topological effects it can be used to develop, by allowing to express the Hamiltonian and the states as a bundle of two level systems over the first Brillouin zone.

Furthermore, the reduced Hilbert space enables a fast and yet precise computation of the properties of the driven system. The full Hamiltonian is represented, as described in Eq. 3.36 in the case of ± 5 Fourier components, by a matrix of 121x121 entries. With a reduction to the projected space it can be represented by a simple 2x2 matrix, which yields an estimated speed up of the order of 10^4 for calculating the effective Hamiltonian representing the driven system, as discussed in Sec. 4.3.

The s-bands of a boron nitride lattice form a so-called family [123] of Bloch bands, or are alternatively referred to as different branches of a single *complex* Bloch band.

The existence of a complex band is closely related to the concept of Wannier functions [124] and the fact that the boron nitride lattices have two stable local minima of similar depth within one unit cell.

For the subspace of each band or family of bands, the associated Wannier functions [124] form an alternative complete basis. They are the Fourier transform of the Bloch functions and are thereby contrary to them in the sense that they have (for an adequate choice of Bloch gauge) a probability density that is localized at the lattice sites and are invariant under lattice translations.

In condensed matter physics the Wannier functions are reminiscent of the atomic orbitals, because the potential of the atomic core dominates the shape of those localized states. This means, that in the limit of increasing lattice spacing, or potential depth, the Wannier functions converge towards the stationary atomic wave functions. Following this analogy the bands are attributed names of the corresponding s, p, d, ... orbitals.

For our description of the boron nitride lattice, the Wannier functions are relevant in two distinct ways. Firstly, they enable the construction of a basis for the reduced Hamiltonian, that can be identified with the two sublattices, formed by the A and respectively B sites. And secondly, they are necessary for the creation of a tight-binding model, with which the Hamiltonian can be well approximated by a simple analytic expression with only few

parameters.

In regard to both aspects, the explicit calculation of the Wannier function is not strictly necessary and has not been conducted here. The reason for this is, that, while for Bravais lattices with a one atomic basis, i.e. with only one local minimum per unit cell, the determination of the Wannier functions follows a relatively simple recipe [124], for a lattice with multiple minima, there is no unique way of constructing the two sets of Wannier functions from the two branches Bloch functions, that cannot be associated to any sublattice. Different choices however lead to different parameters of the associated tight-binding model [125–131].

In the case of the tight-binding model the Wannier functions are needed to determine the values of the parameters of the model, as it will be discussed below. One obvious quantifier for the choice of Wannier functions is therefore how well the resulting Hamiltonian resembles the band structure as compared to the original model without the tight-binding approximation. Here we decided to directly determine a set of tight binding parameters suitable for our lattice with respect to the same quantifier via a standard least square fit of the band structures [132].

A two-band tight-binding model for the boron nitride lattice has already been studied in 1984 by Semenoff [133] in the context of topology. The model was extended and then used by Haldane in his famous paper to unravel the analog to a quantum Hall effect in form of a nontrivial topology of honeycomb lattice with a staggered magnetic field.

The model that is used here for the non-driven lattice is identical to the one used by Haldane when the magnetic flux is set to zero ($\phi = 0$ in [46]).

The central definitions and derivations will be summarized in this section because they are of central importance for the understanding of the presented experiments.

3.4.2 The Tight-Binding Description

The tight-binding model was born in the context of condensed matter physics, and in the past it has led to quite some breakthrough insights into the electronic properties of solids by its capacity to produce an approximative lattice Hamiltonian with a highly reduced complexity, that nevertheless capture many of the essential properties of the system. The name *tight-binding* stems from the fact that in this model electrons are regarded as well localized around, i.e. tightly bound to, an atomic core. The approximation consists in neglecting tunneling processes to distant sites. It is carried out in the Wannier basis, where the diagonal elements of the Hamiltonian correspond to the on-site energy for the associated Wannier function and the off-diagonal elements correspond to the tunneling amplitudes between the two associated sites. They decay exponentially with the increasing distance of the sites, and therefore only tunneling up to a certain relative distance between sites is considered in this model.

It is customary [46, 133] to describe the tight-binding boron nitride Hamiltonian in second quantization, even though it is a single particle operator, to make the resemblance

to quantum field theories explicit.

The Hamiltonian for an isolated sub-band (with possibly multiple branches) can then be expressed by a sum over the complete Wannier basis, represented in second quantization by the creation and annihilation operators w_i^\dagger and w_i , that create/annihilate a particle in a Wannier eigenfunction centered at the lattice sites with index i .

$$H = \sum_{i,j,k,l \in \mathbb{N}} t^{(kl)} w_i^\dagger \left(A \binom{m}{n} \right) w \left(A \binom{m+k}{n+l} \right) \quad (3.39)$$

where the $t^{(kl)}$ are the matrix tunnel elements, or in the case of equal indices t_{ijij} the on-site energy.

For a lattice with multiple local minima per unit cell and multiple Bloch band branches, the sum can be rearranged to reflect the fact that the lattice can be composed of multiple sublattices that have distinct Wannier functions. For a lattice composed of the two sublattices A and B the Hamiltonian becomes

$$H = \sum_{\substack{i,j,k,l \in \mathbb{N} \\ \alpha,\beta \in \{A,B\}}} t_{\alpha\beta}^{(kl)} w_\alpha^\dagger \left(A \binom{m}{n} + \delta_\alpha \right) w_\beta \left(A \binom{m+k}{n+l} + \delta_\beta \right) \quad (3.40)$$

To take advantage of the translation symmetry of the system the plane wave basis has to be chosen. In analogy to the Fourier pair relation of the Wannier function and the Bloch wave for simple bands, in the case of complex bands the Fourier pair of a Wannier function is called a *quasi Bloch wave* [123]. The operators associated with the Wannier states can thus be expressed in terms of the quasi Bloch wave operators $u_\alpha(\mathbf{k})$ as follows

$$w_\alpha(\mathbf{r}) = \frac{1}{B_{\text{BZ}}} \int_{\mathbf{k} \in \text{BZ}} d\mathbf{k} \exp(i\mathbf{k} \cdot \mathbf{r}) u_\alpha(\mathbf{k}) \quad (3.41)$$

With this definition and the identity

$$\sum_{m,n \in \mathbb{N}} \exp(i(\mathbf{k} - \mathbf{k}') \cdot A \binom{m}{n}) = B_{\text{BZ}} \delta(\mathbf{k} - \mathbf{k}') \quad (3.42)$$

The Hamiltonian can be expressed in the plane wave basis

$$H = \frac{1}{B_{\text{BZ}}} \int_{\mathbf{k} \in \text{BZ}} d\mathbf{k} \sum_{\substack{k,l \in \mathbb{N} \\ \alpha,\beta \in \{A,B\}}} t_{\alpha\beta}^{(kl)} \exp\{-i\mathbf{k} \cdot (A \binom{k}{l} + \delta_\alpha - \delta_\beta)\} u_\alpha^\dagger(\mathbf{k}) u_\beta(\mathbf{k}) \quad (3.43)$$

This expression of the Hamiltonian in terms of quasi Bloch waves is of special relevance, because the integral over the Brillouin zone can be, in analogy to Eq. 3.37, interpreted as a direct sum integral, so that the Hamiltonian breaks down into a parameterized set of

Hermitian operators of rank 2. To emphasize this the sum over α and β can be written in matrix form

$$\mathbf{H} = \frac{1}{B_{\text{BZ}}} \int_{\mathbf{k} \in \text{BZ}} d\mathbf{k} \begin{pmatrix} u_A^\dagger(\mathbf{k}) & u_B^\dagger(\mathbf{k}) \end{pmatrix} \mathbf{H}(\mathbf{k}) \begin{pmatrix} u_A(\mathbf{k}) \\ u_B(\mathbf{k}) \end{pmatrix} \quad (3.44)$$

with

$$\mathbf{H}(\mathbf{k}) = \sum_{k,l \in \mathbb{N}} \exp\{-i\mathbf{k} \cdot \mathbf{A} \binom{k}{l}\} \begin{pmatrix} t_{AA}^{(kl)} & t_{AB}^{(kl)} \exp(-i\mathbf{k} \cdot \delta) \\ t_{BA}^{(kl)} \exp(i\mathbf{k} \cdot \delta) & t_{BB}^{(kl)} \end{pmatrix} \quad (3.45)$$

where without loss of generality $\delta_A = 0, \delta_B = \delta$ was chosen.

3.4.3 Properties of Two-Band Hamiltonians

For most considerations of two level systems it is extremely helpful to use the Bloch sphere representation. Because the description of the Hamiltonians in the shape of Eq. 3.45 is central to the topic of this thesis and there are many possible different conventions, I will briefly summarize the definitions that have been used.

Any traceless Hermitian operator of rank two can be decomposed into a linear combination of Pauli matrices. One can thus write

$$\mathbf{H} = h_0 \mathbb{I} + \mathbf{h} \cdot \boldsymbol{\sigma} \quad (3.46)$$

where $h_0 = 1/2 \text{tr} \mathbf{H}$, \mathbb{I} the identity operator, \mathbf{h} a vector containing the coefficients representing \mathbf{H} in this picture, and $\boldsymbol{\sigma}$ a vector containing the Pauli matrices as entries. For any \mathbf{H} the Bloch sphere representation and corresponding matrix representation are then given by

$$\mathbf{h} = \begin{pmatrix} h_{12} + h_{21} \\ i(h_{12} - h_{21}) \\ h_{11} - h_{22} \end{pmatrix} \quad \mathbf{H} = \begin{pmatrix} h_0 + h_3 & h_1 - ih_2 \\ h_1 + ih_2 & h_0 - h_3 \end{pmatrix} \quad (3.47)$$

or most conveniently in spherical coordinates

$$\mathbf{h} = R \begin{pmatrix} \sin \theta \cos \varphi \\ \sin \theta \sin \varphi \\ \cos \theta \end{pmatrix} = R \hat{\mathbf{h}} \quad (3.48)$$

$$\mathbf{H} = h_0 \mathbb{I} + R \begin{pmatrix} \cos \theta & \sin \theta \exp(-i\varphi) \\ \sin \theta \exp(i\varphi) & -\cos \theta \end{pmatrix} = h_0 \mathbb{I} + R \hat{\mathbf{H}}$$

and inversely

$$R = \|\mathbf{h}\| = \sqrt{-\det(\mathbf{H} - h_0)} \quad \theta = \arccos(\hat{h}_3) \quad \phi = \arctan(\hat{h}_2, \hat{h}_1) \quad (3.49)$$

The characteristic polynomial in two dimensions can be solved generically and lead to the eigenvalues and vectors

$$\begin{aligned} \epsilon_{\pm} = h_0 \pm R \quad |+\rangle &= \cos \theta/2 |A\rangle + \sin \theta/2 \exp(i\varphi) |B\rangle \\ |-\rangle &= -\sin \theta/2 \exp(i\varphi) |A\rangle + \cos \theta/2 |B\rangle \end{aligned} \quad (3.50)$$

Here the convention has been chosen that for $\theta = 0$ the eigenstate belonging to the higher eigenenergy corresponds to the A-sublattice. The spectral projectors are

$$|+\rangle\langle+| = \frac{1}{2} (1 + \hat{\mathbf{H}}) \quad |-\rangle\langle-| = \frac{1}{2} (1 - \hat{\mathbf{H}}) \quad (3.51)$$

and the propagator can be written in terms of the natural timescale $\tau = Rt/\hbar$ as

$$U(\tau) = \exp\left(-i\frac{h_0\tau}{R}\right) \exp(-i\tau\hat{\mathbf{H}}) = \exp\left(-i\frac{h_0\tau}{R}\right) (\cos \tau - i\hat{\mathbf{H}} \sin \tau) \quad (3.52)$$

In the same spirit any two level state $|\psi\rangle$ can be defined (up to a phase) through a pair of polar and mixing angles θ^S and φ^S or a vector $\boldsymbol{\psi}$ on the Bloch sphere. Identifying a state with the eigenvector belonging to the positive eigenenergy this leads to

$$|\psi\rangle = c_A |A\rangle + c_B |B\rangle = \cos \frac{\theta^S}{2} |A\rangle + \sin \frac{\theta^S}{2} \exp(i\varphi^S) |B\rangle \quad (3.53)$$

$$\boldsymbol{\psi} = \begin{pmatrix} \sin \theta^S \cos \varphi^S \\ \sin \theta^S \sin \varphi^S \\ \cos \theta^S \end{pmatrix} \quad (3.54)$$

$$\theta^S = \arccos(\boldsymbol{\psi}_3) \quad \phi^S = \arctan(\boldsymbol{\psi}_2, \boldsymbol{\psi}_1) \quad (3.55)$$

3.4.4 Boron Nitride Lattice

For the tight-binding description of the boron nitride lattice all that is left to do is chose the order of the Fourier expansion of the tunnel matrix elements and consider the symmetries of the lattice. Because the association of the $t_{\alpha\beta}^{(kl)}$ depends on the choice of lattice vectors, one usually uses the term (next)-nearest neighbor tunneling. Fig. 3.6 shows how the neighborhood of a boron nitride lattice can be defined. To reflect its coordination number of three, we defined three lattice vectors δ_l for the translation from one sublattice site to its three next neighbor, which are members of the other sublattice, and the three lattice vectors \mathbf{a}_l from one site to its next nearest neighbors, which lie within the same sublattice. While Semenoff [133] chose a model including only nearest neighbor tunneling, Haldane

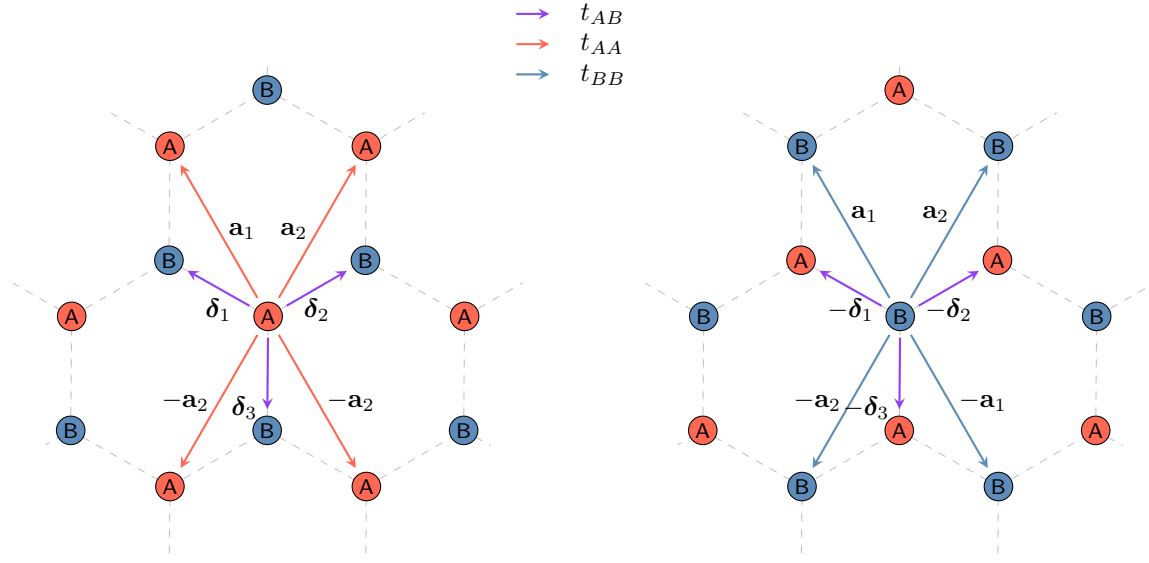


Figure 3.6: Tunneling parameters for a boron nitride lattice. The two sub-figures show the real space lattice for the tunneling from A sites (left) and for tunneling from B-sites (right). A negative sign of the lattice vectors is equivalent to a negative sign in the tunneling amplitude.

also included next nearest neighbors [46]. Here we made the same choice as Haldane, but with real tunneling matrix elements, which reflects the presence of time-reversal symmetry. In this case the $t_{\alpha\beta}^{(kl)}$ are identical regardless of the direction of tunneling. Furthermore we suppose ideal rotational symmetry of order three, which results in a model with only three free parameters, when neglecting the average energy σ that bears no significant contribution. The superscripts are no longer necessary and due to the symmetry of the potential tunneling in the directions \mathbf{a}_l are pairwise equal. With the shorthands the Hamiltonian takes the simple form

$$H(\mathbf{q}) = \begin{pmatrix} \frac{\Delta}{2} + 2t_{AA} g(\mathbf{q}) & t_{AB} f(\mathbf{q}) \\ t_{AB} f^*(\mathbf{q}) & -\frac{\Delta}{2} + 2t_{BB} g(\mathbf{q}) \end{pmatrix} \quad (3.56)$$

where Δ is the difference in on-site energies of the two sublattices. The diagonal terms $g(\mathbf{q})$ and the coupling element $f(\mathbf{q})$ are given by

$$\begin{aligned} f(\mathbf{q}) &= \sum_l \exp(-i\mathbf{q} \cdot \delta_l) \\ g(\mathbf{q}) &= \sum_l \cos(\mathbf{q} \cdot \mathbf{a}_l) \end{aligned} \quad (3.57)$$

There are isolated quasimomenta for which the two sublattices are fully decoupled even though the overall coupling strength t_{AB} is non-vanishing. These points, identified by $f(D_i) = 0$, are called *Dirac points*. They owe their name to the analogy of their local

dispersion relation to the Dirac equation. In case of the honeycomb lattice, where there is no offset between the sublattices ($\Delta = 0$), the two bands become degenerate, and the dispersion in their vicinity becomes linear. For half filling their intersection coincides with the Fermi energy, and low energy excitations of the system can be considered as quasi particles described by the Dirac equation, following the same relativistic dynamics as e.g. photons. The concept can be extended to the Boron nitride lattice. Here, the energy offset between the sublattices lifts the degeneracy and causes the Dirac points to open. Those Dirac points are also referred to as *massive* because the low energy excitations mimic the dispersion of a massive relativistic particle. This extension makes clear that the Dirac points are of geometric nature, in the sense that they can appear for any shape of band structure and only depend on the coupling of the two bands. Therefore their description in the Bloch sphere picture, which is purely concerned with the coupling terms, is adequate for an intuitive visualization. Here the Dirac points are represented by the poles of the sphere, which means that a Dirac point can come in two flavours. The two poles correspond to the two different situations where the subband under consideration coincides with either the A or the B sublattice at the quasimomentum of the Dirac point. This sign of Dirac points also serve as a sufficient measure for the Chern number of the system: the Chern number is equal to (half) the difference in the number of Dirac points [134] with positive and negative signs.

4 Geometry and Topology of Periodically Driven Boron Nitride Lattices

The effects of non-euclidean geometry are abundant in physics. Prominent examples are the special and general theory of relativity, whose effects can be entirely described in terms of the geometry of a curved space-time. Another popular example of geometric effects in classical mechanics is the Foucault pendulum, whose plane of oscillation precesses dependent on the latitude of its geolocation. In non-relativistic quantum mechanics however, geometric effects have not been discovered until 1983, when Micheal Berry reported [14] on the existence of a phase factor for eigenstates of systems under an adiabatic change of parameters, that can be considered geometric, in the sense that it does not depend on time but on the trajectory of the varied parameters through the configuration space. Barry Simon established [8] the connection between this so-called Berry phase, which will be discussed in detail in the next section, and the general mathematical field of geometry. Therefore the Berry Phase lays the foundation, in the same way as in the previously mentioned examples, for defining a curvature, a parallel transport law and topological order. While the late discovery of this geometrical phase could be misunderstood as a very rare and unimportant detail, quite the opposite is the case. The concepts of geometry and topology relate the Berry phase to the quantum Hall effect [5, 7, 135], one of the most intriguing effects of condensed matter physics.

4.1 Geometric Phases in Non-relativistic Quantum Mechanics

The concept of geometry in quantum mechanics is build upon the idea that the total phase δ_{total} , that is accumulated by a state $|\psi(t)\rangle$ during its evolution in a system described by a time-dependent Hamiltonian $H(t)$, can be split into two parts: a dynamical phase δ_{dyn} and a geometric phase γ which is thereby defined as

$$\gamma = \delta_{\text{total}} - \delta_{\text{dyn}} \tag{4.1}$$

This separation is made due to the distinct origin of the two phases. The dynamical phase evolves with time at a rate determined by the instantaneous energy of the state.

$$\delta_{\text{dyn}} = -\frac{1}{\hbar} \int_0^T \langle \psi(t) | \mathbf{H}(t) | \psi(t) \rangle dt \quad (4.2)$$

The geometrical phase, in contrast, does not have any time dependency and derives its name from the fact that it is determined by the shape of the trajectory in the projective¹ Hilbert space the state under consideration traces out. In contrast to the dynamical phase it cannot be defined in a simple form without any further restrictions. It is therefore generally simply defined as in Eq. 4.1.

However simple this definition of a geometric phase may seem at the first glance, yet the concepts it involves are quite intricate. This fact is reflected in the history of its discovery. Even though the concept of an additional phase factor was described in detail by Pancharatnam in 1956 [83] in the context of the evolution of polarization states of a light beam under the passage through a sequence of polarization changing optical components, the mere existence of a geometrical phase in general quantum system has not been realized until the rediscovery by Berry as late as 1984 [14].

Before the connection to the Pancharatnam phase was made, the Berry phase has been solely specified for the restricted case of an energy eigenstate under an adiabatic and cyclic evolution. Later, the restriction of the adiabaticity has been removed by Anandan and Aharnov [136] and finally also the restriction to cyclic Hamiltonians has been lifted by Samuel and Bhandari [137], who realized the equivalence to the scenario studied by Pancharatnam. All the experiments conducted in the context of this work, fulfill the condition of adiabaticity and do not require to consider non-cyclic trajectories. Their geometry are therefore well described by the Berry phase and quantities derived thereof.

4.2 Berry Calculus

In the non-adiabatic case a geometric phase is an attribute of a specific trajectory of a state in the projective Hilbert space. It is not an attribute of an Hamiltonian, however each trajectory can be associated with a class of different time-dependent Hamiltonians that realize this trajectory for a given initial state. The restriction to an adiabatic change of the Hamiltonian simplifies this description greatly because it permits to attribute the phase to trajectories in the finite dimensional parameter space, which all belong to the same time-independent parametric Hamiltonian. Berry [14] deduces the geometric phase, simply by contemplating carefully the evolution, as determined by the time-dependent Schrödinger equation, for a state in a form in accordance with the adiabatic theorem [138].

¹All states of the Hilbert space that differ only by a phase are projected onto the same element in the projective Hilbert space. Otherwise a trajectory would uniquely correspond to one Hamiltonian and would thereby also have a time dependency. For details see [136]

It is probably fair to summarize the essence of the adiabatic theorem by stating, that an eigenstate of a time-dependent Hamiltonian remains an eigenstate to the new Hamiltonian under time evolution, if the Hamiltonian varies sufficiently slow, i.e. adiabatically with time². Formally this means, that for a Hamiltonian $H(\mathbf{q})$ parameterized by the vector \mathbf{q} , which endows the projective Hilbert space with a natural basis through the stationary Schrödinger equation

$$H(\mathbf{q}) |n(\mathbf{q})\rangle = E_n(\mathbf{q}) |n(\mathbf{q})\rangle \quad (4.3)$$

the adiabatic evolution of a non-degenerate initial eigenstate $|n(\mathbf{q}(0))\rangle$, following a trajectory in parameter space described by $\mathbf{q}(t)$, can be written as

$$|\psi(t)\rangle = \exp(i\delta_n(\mathbf{q}, t)) |n(\mathbf{q}(t))\rangle \quad (4.4)$$

Here the phase factor δ_{total} has been assumed in the most general form, i.e. with an explicit dependence on both the parameter \mathbf{q} and the time t . Without making any further assumptions, these dependencies have to be considered as necessary. At this point one can already see that a separation as in Eq. 4.1 of δ_{total} into a \mathbf{q} -dependent geometric part and a t -dependent part is desirable. In the following the index n will be dropped for convenience, bearing in mind that all deductions are equally valid for every other set of non-degenerate eigenstates. In the case of degenerate eigenvectors there appears a similar geometric phase described by so-called Wilson lines [139], which have also recently been observed in a ultracold lattice system [120]. The concept of Berry curvature, which is relevant here, is however restricted to the non-degenerate case.

To find the dependency of the phase factor on the adiabatic parameter and on time, Berry simply inserts Eq. 4.4 into the time-dependent Schrödinger equation

$$\left(i\hbar \frac{\partial}{\partial t} - E(\mathbf{q}(t)) \right) \exp(i\delta(\mathbf{q}(t), t)) |n(\mathbf{q}(t))\rangle = 0 \quad (4.5)$$

By carrying out the chain rule and multiplying from the left with the bra $\langle n(\mathbf{q}(t))|$ with a subsequent rearranging of the summands this yields the derivative of the phase

$$\dot{\delta}(\mathbf{q}(t), t) = i \langle n(\mathbf{q}(t)) | \frac{\partial}{\partial t} |n(\mathbf{q}(t))\rangle + \frac{1}{\hbar} E(\mathbf{q}(t)) \quad (4.6)$$

Integration over time and employing the fundamental theorem of calculus renders the aspired separation into the sum of a geometrical and a dynamical part

$$\delta(\mathbf{q}(T), T) = i \underbrace{\int_{\mathbf{q}(0)}^{\mathbf{q}(T)} d\mathbf{q} \langle n(\mathbf{q}) | \nabla_{\mathbf{q}} |n(\mathbf{q})\rangle}_{\gamma} + \underbrace{\frac{1}{\hbar} \int_0^T dt E(\mathbf{q}(t))}_{\delta_{\text{dyn}}} \quad (4.7)$$

²Messiah formulates the adiabatic theorem a lot more detail, specifying what adiabatic means and describing the dynamical phase evolution with time

The notation used for the partial derivatives with respect to the parameter $\nabla_{\mathbf{q}}$, may be misleading and it shall therefore be explicitly stated here that the object $\nabla_{\mathbf{q}}|n(\mathbf{q})\rangle$ is element of the composite space $\mathbb{Q} \times \mathcal{H}^3$ of the parameter space \mathbb{Q} and the Hilbert space \mathcal{H} . It collapses to a scalar phase through the induced scalar product with $d\mathbf{q} \langle n(\mathbf{q})|$ as an element of its dual space.

To understand Eq. 4.7 it is imperative to remember that the eigenstates for each parameter value are only defined up to a phase by the eigenvalue equation Eq. 4.3. One is free to chose a different, yet fully equivalent, set of eigenstates defined by

$$|\widetilde{n(\mathbf{q})}\rangle = \exp(i\chi(\mathbf{q})) |n(\mathbf{q})\rangle \quad (4.8)$$

As will become clear later, the function $\chi(\mathbf{q})$ is a gauge field, but for now it shall only be noted that it fulfills the role of a gauge in that way, that it influences the description of the system without causing any observable physical change.

The gauge choice is thereby reflected in the phase of the evolved state

$$|\psi(t)\rangle = \exp(i(\delta(\mathbf{q}, t) - \chi(\mathbf{q}))) |\widetilde{n(\mathbf{q}(t))}\rangle \quad (4.9)$$

which means that a definition of δ is only meaningful in combination with a specific choice of $|n(\mathbf{q})\rangle$.

At this point it is not clear that the geometric phase given by Eq. 4.7 carries any physical meaning. It is always possible to find a gauge choice such that the geometric phase vanishes along a given (open) path. Furthermore, the observable state of a system is not defined by a vector in the Hilbert space but rather by a ray, i.e. an overall or global phase factor does not change the state. A relative phase, however, would lead to observable changes to the system through interference. Whether the phase in the given case is of global or relative nature cannot be straightforwardly determined but requires to recognize how its description can be sensibly embedded into the mathematical framework of line bundles [8, 137]. This difficulty can be illustrated by the naïve attempt to determine the relative phase and the observed interference between a state that has adiabatically evolved under a Hamiltonian following some trajectory to a point \mathbf{q} and a state that has evolved under a constant Hamiltonian at \mathbf{q}_0 . The evolved states $|n(\mathbf{q})\rangle$ and $|n(\mathbf{q}_0)\rangle$ are generally not parallel to each other, so that the relative phase remains undefined without further assumptions. To circumvent this problem Berry imposes the restriction to systems, where the trajectories through parameter space are closed and the start- and end-state are parallel to each other so that the relative phase is trivially given. In such a cyclical system with a period T the phase for a closed path \mathcal{P} is then obtained from Eq. 4.7

$$\gamma[\mathcal{P}] = i \oint_{\mathcal{P}} d\mathbf{q} \langle n(\mathbf{q}) | \nabla_{\mathbf{q}} | n(\mathbf{q}) \rangle \quad (4.10)$$

This phase $\gamma[\mathcal{P}]$ becomes physically manifest, for example, if the returned state is interfered with one that has not undergone the adiabatic evolution.

³To be precise, this space is not a product space but also a fiber bundle

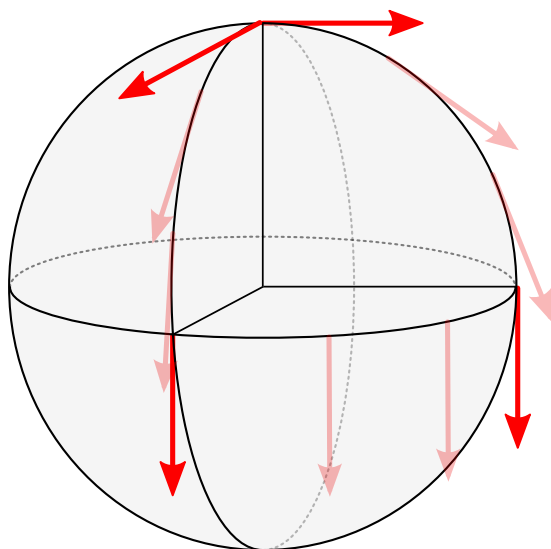


Figure 4.1: Illustration of the Hannay angles. A vector in the tangent bundle of sphere is parallelly transported from the north pole to and along the equator, and back to the north pole. After the transport there is a mismatch with respect to the initial vector. This illustrates the holonomy of the Berry phase at the simple geometric example of the sphere.

4.2.1 Geometric Interpretation of the Berry Phase

In a geometric interpretation the Berry phase is described by a Hermitian line bundle. The base space of this bundle is a adiabatic parameter manifold Q in which \mathbf{q} is defined. In the case considered in this thesis, this manifold is the torus of quasimomenta defined by the Brillouin zone. The fiber is given by a cyclic one dimensional complex vector space and describes the phase factor for any given parameter in the base space. The difference between a bundle and a simple map between the two involved spaces can be illustrated at the example of the Hannay angles [140] as shown in Fig. 4.1. Here the base space is a sphere and the fiber bundle is the tangent fiber bundle. A vector in the fiber bundle can in close analogy to the Berry phase be described by an angle. Then its transport along the sphere is equivalent to the change of the adiabatic parameter. Following the closed trajectory in Fig. 4.1 the vector acquires an additional angle upon the completion of one loop, which in this analogy corresponds to a nonzero Berry phase. In general terms the emergence of such a mismatch is called a *holonomy*. The reason for the holonomy is the curvature of the surface.

In this example the transport of the vector along the sphere is quite intuitive and is determined by the geometry the sphere. The mathematical term for transporting a vector from the vector bundle along the base space is called *parallel transport*. The parallel transport can be defined by a *connection*, which describes how adjacent fibers are connected in the sense of describing how a vector is transferred between them. In the case of the sphere this connection is so intuitive because the embedding of the sphere in space, i.e. a coordinate description of the sphere in three dimensions is given. In the case of the Berry Phase this is different. For the aforementioned example of a two dimensional band structure the base space has a topology of a torus, but the actual geometry of a possible spatial embedding does not necessarily correspond to an ideal torus. Here it becomes

obvious that the geometry is a local property, while the topology is a global property. The connection describing the parallel transport of the Berry phase is determined by the Schrödinger equation [137]. The so-called Berry connection is defined as the integrand in Eq. 4.7 and Eq. 4.10

$$\mathbf{A}(\mathbf{q}) = i \langle n(\mathbf{q}) | \nabla_{\mathbf{q}} | n(\mathbf{q}) \rangle \quad (4.11)$$

and defines the parallel transport of any phase in parameter space to the corresponding phase at a different point in parameter space via the integral along the connecting trajectory. Please note, that unlike the example of the parallel transport of the Hannay angles on the sphere, the Berry connection is not gauge invariant.

Based on this observation we can define the gauge invariant *Berry Curvature*. The line integral in Eq. 4.10 can be converted through Stokes' theorem into a surface integral

$$\gamma[\mathcal{P}] = \oint_{\mathcal{P}} \mathbf{A}(\mathbf{q}) \cdot d\mathbf{q} = - \int_{V(\mathcal{P})} \text{Im} (\nabla \times \mathbf{A}(\mathbf{q})) dV \quad (4.12)$$

where the integrand of the surface integral is called Berry curvature

$$\Omega(\mathbf{q}) = \text{Im} \nabla \times \mathbf{A}(\mathbf{q}) \quad (4.13)$$

As in the example of the Hannay angles, the enclosed Berry curvature is a measure for the holonomy resulting for a closed trajectory in parameter space. Accordingly it is a physical, gauge invariant quantity. It gives rise to a number of effects especially in the field of condensed matter physics e.g. the polarizability of the electronic wave function [21] and the anomalous Hall conductivity [141].

Numerical Determination of the Berry Curvature

The formula in Eq. 4.13 defines the Berry curvature in terms of derivatives of the gauge dependent eigenstates. This form has two disadvantages: firstly, the eigenvectors are generally not single-valued in \mathbf{Q} and secondly, a their numeric computation yields them in a random gauge, such that neighboring eigenvectors are not smoothly connected, which renders the derivative undefined. To circumvent this difficulty one can apply their completeness relation [14] and arrive at an expression where the derivatives are applied to the Hamiltonian, which is gauge invariant

$$\Omega(\mathbf{q}) = \text{Im} \sum_{m \neq n} \frac{\langle n | [\nabla H] | m \rangle \times \langle m | [\nabla H] | n \rangle}{(E_n(\mathbf{q}) - E_m(\mathbf{q}))^2} \quad (4.14)$$

It is important to notice here, that the Berry curvature fully characterizes the geometric properties of the line bundle associated with the Berry phase of the system. Furthermore it can be seen from Eq. 4.14, that the Berry curvature is a propriety of the system that is complementary to its spectrum, because the Berry curvature can be varied through transformations of the Hamiltonian that keep the spectrum unchanged. On the other hand, a singular curvature can for a smooth dependence on the adiabatic parameter, only be achieved through degeneracies of the spectrum.

Topological Indices

In generalization of the Gauss-Bonnet theorem, one can define an integer index called *Chern number*, which allows to define equivalent classes for Hamiltonians of equal topology. The Chern number is invariant under transformations that result in a smooth transformation of the Berry curvature, i.e. transformations of the Hamiltonian that can be performed without inducing level crossings in the spectrum.

The typical example for visualizing such a topological invariant is the example of a two dimensional (orientable) surface embedded in three dimensional space, as in the example of the Hannay angles. Here the integral over the Gaussian curvature of the full surface always renders an integer number. This integer number is preserved for any smooth deformations of the surface. A transformation that changes the topological index can be visualized as punching a hole into the surface and sticking it back together in a different way, as for example when forming a torus from a sphere.

The Chern number as a topological invariant appears in many physical phenomena, as for example as the quantized enclosed flux-quanta in the Aharonov-Bohm effect [4] or the quantized conductivity in the quantum Hall effect. Formally it can be simply defined as [48] the integral of the Berry curvature over the complete parameter space Q

$$C = -\frac{1}{2\pi} \int_Q d\mathbf{q} \cdot \boldsymbol{\Omega}(\mathbf{q}) \quad (4.15)$$

In the next section a more pictorial definition will be given that applies to two-band lattice Hamiltonians only.

4.2.2 Geometry of a Two-Dimensional Lattice Hamiltonian

The concept of geometry described by the Berry phase has no further restrictions and applies to all systems that can be described by a Hamiltonian that is adiabatically parameterized as, for example, spins in magnetic fields, light in fibers, and most relevant here, condensed matter systems. The adiabatic parameter in the geometric description of condensed matter systems is the quasimomentum and the Berry phase can, for example, manifest itself in the interference of a quasimomentum eigenstate that has transversed a closed loop in the reciprocal space (for an experimental realization see [63]) To establish an analogy to the typical example of a spin in a magnetic field, the quasimomentum eigenstate can be considered as a pseudo spin, where the energy eigenstates correspond to the spin projections. The choice of the quasimomentum as the adiabatic parameter brings also along some peculiarities that cannot be translated into this analogy. One of them concerns the symmetries of the system [48]. Opposed to the ordinary position coordinate, the quasimomentum changes its sign under time-reversal \mathcal{T} . In systems where the adiabatic parameter is invariant under \mathcal{T} the Berry curvature is rendered flat [8] while for a condensed matter system time-reversal only leads to a Berry curvature which changes

sign under parameter space inversion and thus yields a zero Chern number[21]

$$\mathcal{T}\Omega(\mathbf{x}) = -\Omega(\mathbf{x}) \quad \mathcal{T}\Omega(\mathbf{q}) = -\Omega(-\mathbf{q}) \quad (4.16)$$

If the condensed matter system itself (i.e. the Hamiltonian), however, is symmetric under inversion $\mathcal{I} : \mathbf{x} \rightarrow -\mathbf{x}$ also the Berry curvature will be inversion symmetric [21]

$$\mathcal{I}\Omega(\mathbf{q}) = \Omega(-\mathbf{q}) \quad (4.17)$$

which implies, that for a nonzero Berry Curvature in a condensed matter system, either the time-reversal symmetry or the inversion symmetry have to be broken.

Another difference is the fact that the parameter manifold, i.e. the quasimomentum space, itself has a nontrivial toroidal topology. For a formal description, the lattice Hamiltonian, which is split up into a direct integral of operators restricted to quasimomentum eigenspaces in Eq. 3.37, serves as a starting point. On the first sight it fulfills the assumptions made in the previous section as a parameterized Hamiltonian with the Bloch states as its eigenstates, so that Eq. 4.3 seemingly can be identified with

$$H_{\oplus}(\mathbf{q}) |\psi_{\mathbf{q}n}\rangle = E_n(\mathbf{q}) |\psi_{\mathbf{q}n}\rangle \quad (4.18)$$

The analogy however is breaks down when realizing, that here the eigenstates for different quasimomenta are all orthogonal to each other by construction and likewise that $H_{\oplus}(\mathbf{q})$ is not simply parameterized in the sense of Eq. 4.3, as it acts on disjunct subspaces for different \mathbf{q} . The proper analogy is drawn by states that are defined in the same Hilbert space⁴ [21, 142]. This problem is solved by simply translating the eigenfunctions in reciprocal space by \mathbf{q} back onto the reciprocal lattice. Those translated functions coincide with the cell periodic lattice states $|u_{\mathbf{q}n}\rangle$. The Hamiltonian transforms accordingly

$$H(\mathbf{q}) = T_{\mathbf{k}}(\mathbf{k}) H_{\oplus}(\mathbf{q}) T_{\mathbf{k}}^{\dagger}(\mathbf{k}) \quad (4.19)$$

With this transformation⁵ the cell periodic states $|u_{\mathbf{q}n}\rangle$ can be identified with the eigenstates $|n\rangle$ of the previous chapter.

In the case of a two dimensional problem as, for example, the boron nitride lattice, the Hamiltonian has only dependencies on the two adiabatic coordinates. Without loss of generality this can be expressed by $\partial_{\mathbf{q}_3} H = 0$. For the Berry curvature, which generally is a vector quantity, this implies that it becomes unidirectionally orthogonal to the parameter plane and can be considered a scalar. Eq. 4.14, which describes the non-vanishing component, collapses to only one addend and can be further simplified by

⁴Strictly speaking, also the $|\psi_{\mathbf{q}n}\rangle$ can be defined in the same Hilbert space (spanned by all momentum states), but the space spanned by the Bloch states over all band indices but for one quasimomentum are disjunct from those spanned at a different quasimomentum.

⁵The projection into the space of lattice periodic functions is implicitly understood.

defining a relative coupling strength $F(\mathbf{q})$, normalized to the band gap $R(\mathbf{q})$ and becomes

$$\Omega = \Omega_3(\mathbf{q}) = \text{Im} \partial_{\mathbf{q}_1} F(\mathbf{q}) \partial_{\mathbf{q}_2} F^*(\mathbf{q}) \quad \text{with} \quad F(\mathbf{q}) = \frac{\langle -\mathbf{q} | \mathbf{H}(\mathbf{q}) | +\mathbf{q} \rangle}{R(\mathbf{q})} \quad (4.20)$$

In the representation of the Hamiltonian as a vector on the Bloch sphere, introduced in Sec. 3.4.3, this evaluates to

$$\Omega(\mathbf{q}) = \partial_{\mathbf{q}_1} \mathbf{h}_1 \partial_{\mathbf{q}_2} \mathbf{h}_2 - \partial_{\mathbf{q}_1} \mathbf{h}_2 \partial_{\mathbf{q}_2} \mathbf{h}_1 \quad \Omega(\mathbf{q}) = -1/2 \sin \theta \left(\partial_{\mathbf{q}_1} \theta \partial_{\mathbf{q}_2} \phi - \partial_{\mathbf{q}_2} \theta \partial_{\mathbf{q}_1} \phi \right) \quad (4.21)$$

Also the Chern number can be expressed in a fairly simple form [143] for the two-level system

$$\mathcal{C} = \frac{1}{4\pi} \int_{\text{BZ}} d\mathbf{q} \mathbf{h} \cdot \left(\partial_{\mathbf{q}_1} \mathbf{h} \times \partial_{\mathbf{q}_2} \mathbf{h} \right) \quad (4.22)$$

This form of is of special importance to develop a pictorial understanding of the Chern invariant. The integral of Eq. 4.22 is a triple product and takes the value of the volume spanned by the three vectors it is constituted of. The first vector, \mathbf{h} is per definition normalized to unity and is orthogonal to the other two, so that it contributes only with a sign to the overall value. The integrand therefore corresponds to the oriented area subtended by $\partial_{\mathbf{q}_1} \mathbf{h}$ and $\partial_{\mathbf{q}_2} \mathbf{h}$. The complete Hamiltonian $\mathbf{h}(\mathbf{q})$ can be visualized as a map from the Brillouin torus onto the Bloch sphere. In this image the Chern number becomes equal to the overall directed area of the image of this map on the sphere. There are two simple scenarios that come to mind, when trying to imagine how to wrap a torus onto a sphere: the torus can lie outside on some part of the sphere like a flat inner bicycle tube, or the sphere can be inside the torus and the parts of the torus that are not directly in contact with the sphere lie in a double layer on the surface that has already been covered once. In the first case all parts of the torus exist in a double layer, so that for every part of the integral in Eq. 4.22 has a counter part with an opposite orientation and the total integral evaluates to a Chern invariant of zero. In the second case the complete sphere is surrounded by a single layer of uniform orientation and some parts find an additional double layer with two opposed orientations on top, which evaluates to a total Chern number of one. To change from one situation to the other one would need to cut the torus open. In this picture it becomes clear that the integral is invariant under smooth transformations of $\mathbf{h}(\mathbf{q})$ and the Chern number is indeed an integer topological invariant of the system. Higher Chern numbers follow the same logic, but cannot be perfectly described in this picture of an elastic torus on a sphere because here the torus is required to intersect itself.

4.3 Geometry of the Circularly Driven Boron Nitride Lattice

As argued earlier, it is necessary to both break time reversal symmetry and inversion symmetry, to realize systems with nontrivial topology. Inversion symmetry can be simply

broken by choosing an adequate lattice potential, as here for example, the boron nitride lattice. Even though breaking time reversal symmetry is generally more difficult to achieve, there exist many different paths of realization. These are mostly discussed in the context of artificial gauge fields [15, 144]. For a summary of the different schemes the reader is referred to reference [15, 144]. In the context of the experiments presented in this thesis we decided to break time reversal symmetry by circularly driving the lattice. This means that the lattice position in real space is controlled such that every site describes a circular trajectory. For the experimental realization of the positional control of the lattice please refer to Sec. 3.2.2.

Temporally periodic systems can be described within Floquet theory (see. Sec. 4.3) by a static effective Hamiltonian that describes the dynamics of the system for stroboscopic times. This effective Hamiltonian has a band structure that may significantly differ from the initial Hamiltonian. In this sense, Periodic driving is a means of *band structure engineering*⁶ that is a well established experimental tool for degenerate matter in optical lattices⁷, and has also been implemented for the merit of lifting TRS [33]. Periodic driving refers very generally to any kind of periodically varied Hamiltonian. Here we will only consider what is commonly known as *lattice shaking*, i.e. a periodically changed lattice position.

While for one-dimensional periodic driving there are paths that do not break TRS, in two dimensions every periodic path, that is not quasi-one-dimensional, spans a number of orientable areas, whose orientation changes sign when the time axis is reversed. For circular shaking this simply means that the chirality of the circle changes from right to left and vice versa upon time reversal. Among all possible trajectories, the circle is of special interest in the present context of a hexagonal lattice, as it closely resembles the effect of illuminating graphene with circularly polarized light [93, 146].

The resulting driven Hamiltonian can be determined [147] by transferring the position operator and the wave function into the dynamic frame with the unitary transformation $U(t)$ given by the translation operator $T_r(\mathbf{s}(t))$ for the trajectory $\mathbf{s}(t)$. The resulting time-dependent Schrödinger equation can be brought into the form of an effective Schrödinger equation with a modified Hamiltonian describing the system in the moving frame

$$\begin{aligned} i\hbar\partial_t U(t) |\psi(t)\rangle_{\text{MF}} &= [U(t) H U(t)^\dagger] U(t) |\psi(t)\rangle_{\text{MF}} \\ i\hbar\partial_t |\psi(t)\rangle_{\text{MF}} &= \underbrace{\left(U(t)^\dagger H U(t) - i\hbar U(t)^\dagger \partial_t U(t) \right)}_{H_{\text{MF}}} |\psi(t)\rangle_{\text{MF}} \end{aligned} \quad (4.23)$$

Evaluating the derivative for the translation operator and the application of the quadratic complement yields an Hamiltonian, which is formally equivalent to the minimal substitution

⁶please note, that in the present context should more precisely be *band geometry engineering*, because the geometry is a property of the system that is related to the band structure, but cannot be deduced from it.

⁷For a review see e.g. [57, 145]

Hamiltonian of a particle with unit charge in a magnetic field.

$$\begin{aligned} H_{\text{MF}}(t) &= \mathbf{p}^2/2m + V_{\text{Lattice}} - \mathbf{p} \cdot \partial_t \mathbf{s}(t) \\ &= \frac{(\mathbf{p} - \mathbf{A})^2}{2m} + V_{\text{Lattice}} + \text{const.} \quad \mathbf{A} = m\partial_t \mathbf{s}(t) \end{aligned} \quad (4.24)$$

For a circularly driven lattice this means that the problem is equivalent to the one of a charge in a lattice in the presence of a constant uniform rotating magnetic field, whose frequency is identical to the driving frequency and whose amplitude is derived from the radius of the trajectory, acting as the coupling strength.

Systems with a time-dependent Hamiltonian are generally hard to solve. As the term *driving* suggests, energy will be exchanged with the environment and it therefore ceases to be a preserved quantity. A periodically driven system, however, does not fully remove the time translation symmetry, but it rather reduces it to a discrete time translation symmetry, i.e. Hamiltonians that are one period T in time apart are identical

$$H(t) = H(t + T) \quad (4.25)$$

Mathematically this problem is therefore closely related to the problem of periodic lattice Hamiltonian and it is treated within the *Floquet-Bloch theory* that generalizes the Bloch theory to the time domain. The analogy between the two cases might not be apparent on first sight because time is customarily treated as a parameter in quantum mechanics, as opposed to the space and momentum coordinates that are expressed through operators. The Floquet-Bloch theory however, does not consider any physical system but it is a theory for describing solutions to differential equations. Applying separation of variables to the Schrödinger equation yields two ordinary differential equations with the same type of symmetry in the boundary conditions. The full analogy between time and space coordinate can also formally be reestablished, as it was done by Sambe et. al. [148], by introducing an extended Hilbert space that includes the time dependency of the states.

For a detailed discussion of Floquet theory in the context of driven systems the reader is referred to Refs. [57, 149]. Here only the most important aspects shall be summarized in analogy to the lattice case and with respect to the special case of a two level tight-binding model of the boron nitride lattice.

The most important result of the Floquet description for the engineering of band structures via periodic driving is the fact, that similar to the quasimomentum, here, quasi energies that lie in Brillouin zones, are conserved. This allows, under certain restriction, to treat the shaken system as if it were a static system with a modified band structure. One should bear in mind, that the solutions to the *time-dependent Schrödinger equation* (TDSE) generally have a nontrivial time-dependency and do not expose the same periodicity in time as the Hamiltonian. Within the Floquet formalism, special solutions to the TDSE, so-called *Floquet modes*, can be identified, which expose, up to a phase, the same periodicity

as the Hamiltonian and form a complete basis for the solution space. In the Sambe space, one can define an eigenvalue equation, much alike the stationary Schrödinger equation [148]

$$\mathcal{H} |\Phi_\alpha\rangle = \epsilon_\alpha |\Phi_\alpha\rangle \quad (4.26)$$

where $\mathcal{H} = H - i\hbar\partial_t$ defines the Floquet Hamiltonian, the eigenvectors $|\Phi_\alpha\rangle$ are the Floquet modes and the eigenvalues ϵ_α are the quasi energies. The Floquet states, i.e. the solutions to the TDSE are then given by

$$|\Psi_\alpha\rangle = \exp(-i\epsilon_\alpha t/\hbar) |\Phi_\alpha\rangle \quad (4.27)$$

There are many different approaches [30] to numerically solve Eq. (4.26). In analogy to the band structure calculations, presented in Sec. 3.3, a finite subspace of the Sambe space can be used, that only includes time-periodic functions up to a certain Fourier order. Within this subspace simple diagonalization yields the approximations for the Floquet modes and the quasi energies. Here, an alternative method [132], will be used, that is computationally superior in the given context. The central idea of this method is to numerically calculate the evolution operator over one cycle and make use of the fact, that its eigenvectors are the Floquet modes.

The evolution operator in a perturbative form, for the evolution from a time t_0 to $t_0 + t$ is described by the Feynman-Dyson series [149]

$$U_{t_0}(t) = \mathcal{T} \exp\left(-i/\hbar \int_{t_0}^{t_0+t} H(\tau) d\tau\right) \quad (4.28)$$

where \mathcal{T} is the time-ordering operator. The composition property of the evolution operator allows to write it as the product integral of infinitesimal partial evolution operators

$$U_{t_0}(t) = \lim_{\Delta t \rightarrow 0} \prod_{n=0}^{N=t/\Delta t} U_{t_n}(\Delta t) \quad t_n = t_0 + n\Delta t \quad (4.29)$$

For sufficiently small time intervals Δt , the Hamiltonian can be considered constant and the product integral can be substituted by a simple matrix product.

$$U_{t_0}(t) = \prod_{n=0}^N U_n \quad U_n = \exp[-i/\hbar H(t_n) \Delta t] \quad (4.30)$$

For a numeric simulation of the complete dynamics of the system for longer time scales at a lower temporal resolution, the periodicity of the evolution operator can be exploited, such that only one matrix multiplication per time step is necessary. For a driving with a

period T and a time discretization such that one period is divided in C steps the evolution operator is

$$\prod_{n=0}^N U_n = U_C^m \prod_{n=0}^V U_n \quad \text{with} \quad N = mC + V \quad V \leq C \quad (4.31)$$

Here it is important to realize that the evolution operator is not time-periodic, even though its constituents U_n are

$$U_{t_0}(t + T) = U_C U_{t_0}(t) \quad (4.32)$$

For U_{t_0} to be time-periodic the evolution operator for one period U_C would need be unity. Following the same line of reasoning it can be seen that the eigenstates of U_C , are the time periodic Floquet modes.

For the experiments in this thesis, we are going to consider stroboscopic measurements only, where the state will only be measured at times $t_m = mT + t_0$. The state of the system at these times is simply given by

$$|\psi(t_m)\rangle = U_C^m |\psi(t_0)\rangle \quad (4.33)$$

This evolution is identical to one under an effective time independent Hamiltonian $H_{\text{effective}}$, because U_C as a unitary operator can be written as an exponential of a hermitian operator

$$U_C = \exp(-i/\hbar H_{\text{effective}} T) \quad (4.34)$$

This method is especially useful for the simulation of the dynamics induced by tight-binding Hamiltonian restricted to the lower two bands of the boron nitride lattice, because here the evolution operator is given by a two-by-two matrix.

4.3.1 Periodically Driven Two-Band Tight-Binding Hamiltonian

In the special case of a two level system, the effect of driving can be visualized on the Bloch sphere which allows to develop a concise and intuitive picture of the relationship of the states and operators used in the formal theory. Furthermore, the fact that the Hilbert space is two-dimensional allows for an analytic description of the matrix exponential from Eq. (4.34) as described earlier in Eq. (3.52).

In terms of the \mathbf{q} -dependent tight-binding Hamiltonian defined in Eq. (3.56), the effect of the driving in Eq. (4.24), is described through a shift in the quasimomentum

$$\mathbf{q}(t) = \mathbf{q}_{\text{static}} - m/\hbar \partial_t \mathbf{s}(t) \quad \mathbf{q}_n = \mathbf{q}(t_n) \quad \text{with} \quad \mathbf{q}_{n+C} = \mathbf{q}_n \quad (4.35)$$

Fig. 4.2 shows how the dynamics in every quasimomentum eigenspace are governed by the Hamiltonian of other eigenspaces whose offset is described by the shaking trajectory.

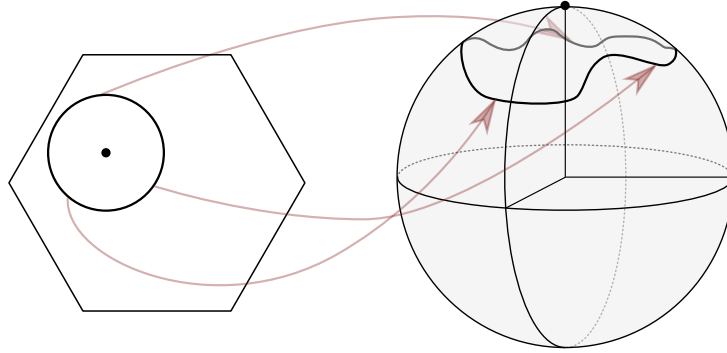


Figure 4.2: Mapping of the shaking trajectory onto the Bloch sphere. The left part of the image shows a path in the first Brillouin of a hexagonal lattice. The considered circular driving path in real space translates (Eq. (4.35)) into a circular displacement of the quasimomentum eigenspaces of the Hamiltonian. The dot marks a single quasimomentum, for which the instantaneous Hamiltonians are illustrate on the Bloch sphere in the right part of the image.

Neglecting the common energy offset, the discretized evolution operators for the n^{th} step are then obtained by inserting Eq. (4.35) and Eq. (3.56) into Eq. (4.34)

$$U_n = \cos(R(\mathbf{q}_n)\Delta t/\hbar) + i\hat{H}(\mathbf{q}_n) \sin(R(\mathbf{q}_n)\Delta t/\hbar) \quad (4.36)$$

Using Eq. (4.36) and (4.34), the effective Hamiltonian for the shaken system is straightforwardly determined. For the numeric implementation the most time intensive step is the determination of the matrix logarithm, which is generally implemented with an iterative approximation method⁸. In the two 2D case, however the eigenvectors of any matrix can be determined analytically and therefore the matrix logarithm can be replaced by a regular logarithm of the eigenvalues. The complex logarithm is furthermore a multi-valued function. This corresponds to picture of quasi energies and the multiple copies of bands that are generated. Without loss of generality forth on the first branch, i.e. the first Brillouin zone will be used.

4.3.2 Gauge Dependency and Adiabatic Launching

So far the dependency of the effective Hamiltonian on the initial time t_0 has not been taken into account. In the case of circular shaking this corresponds to the initial phase of the shaking. To make this dependency become more apparent consider the discrete cycle evolution operator for a different choice of initial time

$$U_{t_0}(t) = \underbrace{U_1 U_2 U_3 \cdots U_{c-2} U_{c-1} U_c}_{U_C} \overbrace{U_1 U_2 U_3 \cdots U_{c-2} U_{c-1} U_C}_{\tilde{U}_C} U_1 U_2 U_3 \cdots \quad (4.37)$$

⁸see e.g. [<https://doi.org/10.1137/110852553>] as used in MATLAB[®]

Here \tilde{U}_C is the cycle evolution operator for $t_0 \rightarrow t_0 + 2\Delta t$ and it is connected to U_C through the unitary transformation characterized by the so-called *kick*-operator K [30]

$$\tilde{U}_C = U_K U_C U_K^\dagger \quad U_K = \exp(-i/\hbar K) \quad \text{here} \quad U_K = U_1 U_2 \quad (4.38)$$

The effective Hamiltonian is accordingly transformed

$$\tilde{H}_C = U_K H U_K^\dagger \quad (4.39)$$

The change of t_0 obviously does not change the driven system and can be regarded as a gauge transformation [147]. At the first sight, this might be contradictory to the fact, that different choices of t_0 lead to different evolved states. This difference stems from the initial state, which is not gauge invariant from within the moving frame. For the experimental reconstruction of the Berry curvature that will be described in Chap. 6, it is desirable to minimize this dependency. For this we employ a *adiabatic launching* scheme, as it is suggested in [30]. In the scheme the modulation depth, i.e. the radius of the shaking trajectory, is controlled to increase adiabatically from zero to its final value. This entails that an initial state, that is in eigenstate of the static Hamiltonian, will adiabatically follow to become an eigenstate of the driven system.

4.3.3 Full Evolution at the K-Point

In this section the complete dynamics of a state at the K-point of the boron nitride lattice will be exemplarily discussed. Fig. 4.3 shows the θ - and φ -component of the full Brillouin zone. For a low shaking amplitude, the path described by the Hamiltonian in

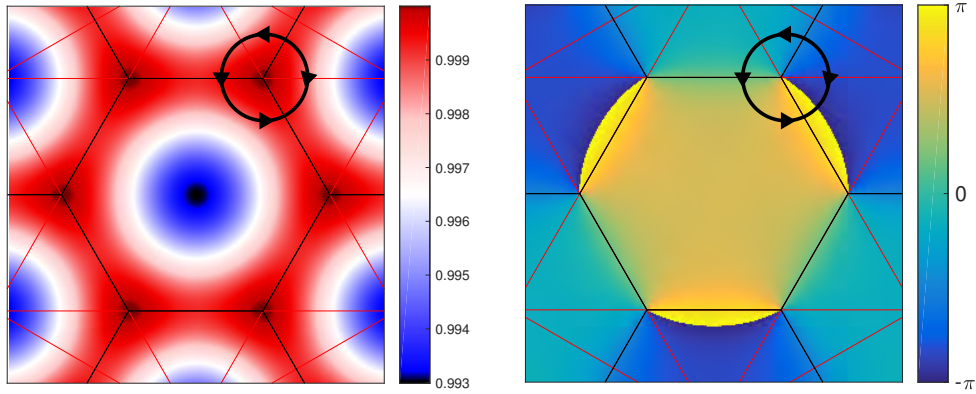


Figure 4.3: Cyclic shaking at the K-Point. On the left $\phi(\mathbf{q}_k)$ and on the right $\theta(\mathbf{q}_k)$ of the static boron nitride Hamiltonian are shown. The path indicates the different values ϕ and θ assume at the k-point (center of circle) when circularly shaking with a relatively low amplitude.

the pseudo-spin representation on the Bloch sphere, for an adiabatically launched state at the K-point, exposes a particularly simple form. The mixing angles stays approximately

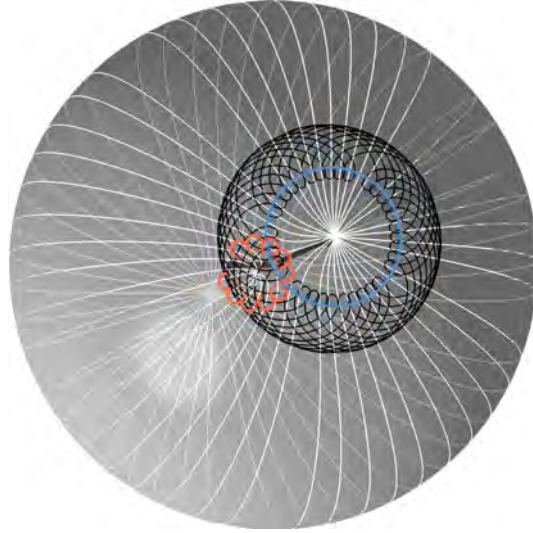


Figure 4.4: Micromotion and stroboscopic dynamics in a quasimomentum eigenspace. See main text for a closer description of the different trajectories.

constant and the phase angle has a nearly linear slope. Fig. 4.4 shows dynamics for an arbitrary initial state for this periodic Hamiltonian.

The blue line in fig. 4.4 indicates the trajectory of the instantaneous Hamiltonian for the driven system. One shaking period corresponds to one circuit of the circle.

The black line shows the evolution over 12 periods of some initial state (left arrow) under this Hamiltonian. It can be clearly seen, that the state is not periodic. For this choice of initial state close to the initial Hamiltonian and a sub-resonant driving frequency, the origin of the term *micromotion* becomes evident. Micromotion here refers to the fast spiralling deviations of the state around the slow circular motion of the Hamiltonian.

The white line is traced out by one of the eigenstates of the evolution operator for an arbitrary, but with respect to the state dynamics equivalent, gauge t_0 . As there is no rule for the enumeration of the eigenstates for the evolution operators for different times, they have been chosen such that the scalar product is minimized for adjacent time steps and thereby trace out a continuous line. The simulation shows that $U_{t_0}(t)$ is not periodic, but upon completion of one cycles at times mT returns to the same point (or to its inverse, which corresponds to the other of the arbitrarily chosen eigenvectors).

The red circles mark the points of the state trajectory at times mT . It can be seen that they are, as expected, arranged in a circle around the crossing point of the evolution operator and thereby trace out the stroboscopic evolution under the effective Hamiltonian, with its eigenvectors at the crossing points.

One should bear in mind that the depiction of the states on the Bloch sphere only shows their shadow in the projective Hilbert space (i.e. without considering relative phases between states of different times).

5 State Tomography for an Optical Lattice

The results of both of the two main experiments presented in this thesis, are obtained by performing a complete tomography of the states associated with s-band family of the periodically driven boron nitride lattice. The term *complete state tomography* refers to measuring the coefficients of the Bloch states in the sublattices basis, for all quasimomenta in the Brillouin zone. Even though neither the relative phases between different quasimomentum states nor the associated eigenenergies, i.e. the band structure are directly accessible through this method, it can be used, as explained in detail in Chap. 6 and Chap. 8 respectively, to extract the complete information of the geometry of lattice Hamiltonian, and as well to study its nonequilibrium dynamics. In the first experiment in this thesis, the tomography is employed to determine the eigenstates of the effective Floquet-Bloch system, so that its geometry can be inferred from the identical geometry of the state. In the second experiment, series of tomography measurements are conducted to observe the dynamical evolution of a nonequilibrium state under the influence of the Bloch-Floquet Hamiltonian.

For the realization of the state tomography for the considered two-band Bloch state we follow a scheme that was proposed by P. Hauke et. al. [150]. This publication proposes the state tomography as a means of determining the Berry curvature and derived quantities in one- and two-dimensional optical lattice potentials. In the present work we follow this proposal and find a experimentally accessible realization by engineering and control an effective Floquet-Bloch Hamiltonian through shaking of an optical lattices potential. A similar tomography proposal, but for atoms with internal (spin-)degrees of freedom, has been published in Ref. [143, 151].

The central idea of these tomography schemes is to infer the state under investigation from the momentum resolved density oscillations in a time of flight image after a quench of the lattice Hamiltonian. The concept is similar to a tomography measurement of Rabi-oscillation, with the main difference that the density oscillations does not represent the population of the state in the new pseudospin basis as in the Rabi case, instead it is proportional to a quadrature component of the new basis. In the Bloch sphere picture this means, that the observable is not a projection to the z-axis, but one to the x-axis.

An important prerequisite for the quench is, that the periodicity of the lattice remains unchanged, so that the quasimomentum is preserved and its eigenspaces can be considered individually. Even though the method can be extended to more complicated scenarios,

we will follow Refs. [143, 150] and restrict it to the case of two-band tight-binding Hamiltonians. Within this restriction there are only a limited number of parameters over which a quasimomentum preserving quench could take place. Another important prerequisite in this scheme is, that the post-quench Hamiltonian has flat bands. One readily controlled parameter of the lattice that can be quenched such that a flat band Hamiltonian is reached is the lattice depth. A quench of the lattice depth however, can become incompatible with the two-band approximation of a realistic Hamiltonian with two isolated bands, in the sense that a for a significant change in lattice depth the previously well separated higher bands will become resonant in the deep lattice. An alternative that circumvents this problem consists in quenching the energy offset between the A and B sublattices.

For our setup we considered tuning the sublattice offset through the control over the lattice beam polarization in form of optical components such as AOMs, EOMs, or mechanically controlled wave plates. The difficulty for the implementation of an additional AOM or EOM on the laser table is that the polarization mode cannot be transported cleanly to the main experiment table, because polarization maintaining fibers only maintain the polarization on their main axes but not their relative phase¹. However, an implementation on the side of the main apparatus would deteriorate the lattice stability and homogeneity by introducing additional optical components in the otherwise direct beam path. The option of a motorized wave plate is difficult, if not impossible, to implement with rotation velocities suited for the timescales relevant for these quench experiments². Here we employ yet another method, which is specific to the case of a periodically driven system, namely a quench of the modulation depth. The effective Hamiltonian of the Floquet-Bloch system in which we conduct the experiments, is created by near-resonant shaking of a flat band Hamiltonian. By abruptly switching off the shaking, we effectively project onto a flat band Hamiltonian as required for the tomography scheme.

5.1 Time of Flight Imaging and the Sublattice Basis

For the time of flight measurement all trapping potentials are abruptly switched off and the atomic clouds expand freely. Under the assumptions of negligible interaction of the spin-polarized fermions, and an expansion time long enough that the initial distribution is small compared to the final cloud size, the expanded atomic density reflects the momentum distribution of the state prior to the expansion [25, 153]

$$n(\mathbf{k}) = |\langle \mathbf{k} | \psi \rangle|^2 \quad \rightarrow \quad n_x(\mathbf{x}) = n \left(\frac{m}{\hbar t_{\text{TOF}}} \mathbf{x} \right) \quad (5.1)$$

¹A viable but more involved solution would be to use two PM-fibers for each lattice beam with an adequate fiber phase lock.

²this option has been studied by the team, in form of a supervised Bachelor thesis [152].

This expression can be evaluated in the Wannier sublattice basis that has been introduced in the context of the tight-binding description (see Sec. 3.4)

$$n(\mathbf{k}) = \left| \langle \mathbf{k} | \int_{\text{BZ}} d\mathbf{q} \left(c_A^{\mathbf{q}} | \mathbf{q} A \rangle + c_B^{\mathbf{q}} | \mathbf{q} B \rangle \right) \right|^2 \quad \text{with} \quad \langle \mathbf{k} | \mathbf{q} \sigma \rangle = w_\sigma(\mathbf{k}) \delta(\mathbf{q}_\mathbf{k} - \mathbf{q}) \quad (5.2)$$

$$= |c_A^{\mathbf{q}_\mathbf{k}} w_A(\mathbf{k}) + c_B^{\mathbf{q}_\mathbf{k}} w_B(\mathbf{k})|^2$$

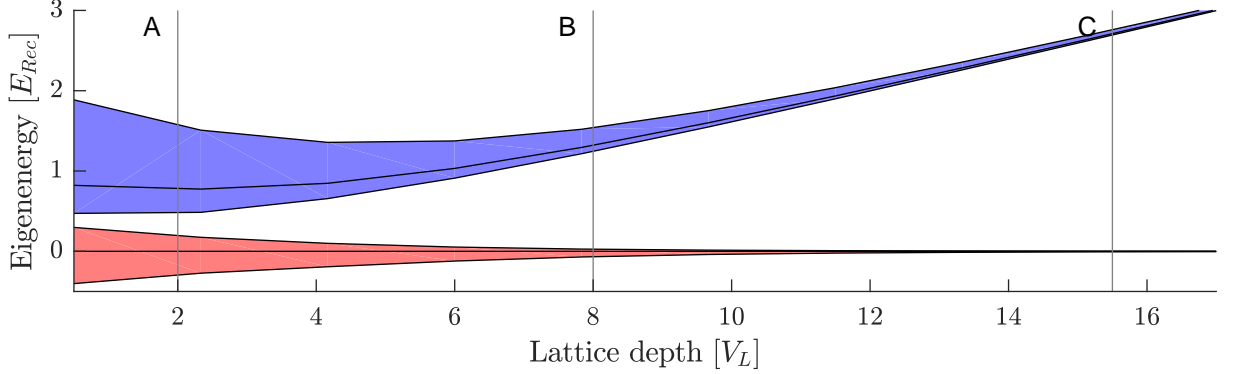


Figure 5.1: Band width as a function of lattice depth. The figure shows how the width of the lower two bands decreases drastically with increasing lattice depth V_L . The black lines show the average band energy. The energy scale is relative to the average energy of the lowest band.

Here $w_\sigma(\mathbf{k})$ are the generalized Wannier functions in momentum representation of the sublattices $\sigma \in A, B$ and $\mathbf{q}_\mathbf{k}$ is the quasimomentum related to the momentum \mathbf{k} via a reciprocal lattice vector. Eq. 5.2 shows that the information about the Wannier functions and the initial state are intertwined and further knowledge about the Wannier functions is required for the tomography. To circumvent this difficulty we use a lattice potential that is deep enough to produce a Hamiltonian with flat bands (see Fig. 5.1) as the reference system. For the limiting case of such a flat band Hamiltonian, the Wannier functions are fully located at the lattice sites around which it can be approximated as a local harmonic potential. Furthermore for a boron nitride type lattice they become identical. As a consequence the expression for the atomic density simplifies to

$$n(\mathbf{k}) = |w(\mathbf{k})|^2 \left(|c_A^{\mathbf{q}_\mathbf{k}}|^2 + |c_B^{\mathbf{q}_\mathbf{k}}|^2 + 2 \operatorname{Re}\{c_A^{\mathbf{q}_\mathbf{k}} c_A^{*\mathbf{q}_\mathbf{k}}\} \right) \quad (5.3)$$

The first two summands are simply equal to one, because the total occupation of a quasimomentum state stays constant, and the third summand embodies the relevant interference observable that characterizes the initial state. To make this relationship clearer, consider Eq. 5.3 in the Bloch sphere picture. Here the interference term is equal to the expectation value of the x -component of the pseudo spin. In spherical coordinates the projection on the x -axis takes the form

$$n(\mathbf{k}) = |w(\mathbf{k})|^2 (1 - \sin(\theta(\mathbf{q}_\mathbf{k})) \cos(\phi(\mathbf{q}_\mathbf{k}))) \quad (5.4)$$

A time series of this projection observable is sufficient to reconstruct the initial state if the Hamiltonian of the dynamics is known.

5.2 State Tomography

For the same limit of a flat band boron nitride Hamiltonian, that has been exploited for the TOF description, the lattice Hamiltonian becomes trivial, because the presence of flat bands (see Fig. 5.1) implies that the eigenstates of the upper and lower band approximate the eigenstates of the A and B sublattices (see Fig. 5.2).

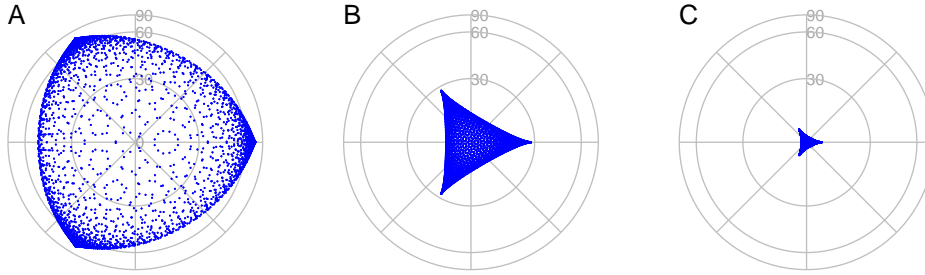


Figure 5.2: Reference Hamiltonian for increasing lattice depth. This figure shows the Hamiltonian of boron nitride lattices represented through their eigenvectors. Every dot marks a Bloch state in the AB-sublattice basis for a selected grid of quasimomenta from a top perspective onto the Bloch sphere. The subfigures A, B and C correspond to lattice depths $V_L = \{2, 8, 15.5\} E_{\text{Rec}}$ and coincide with the vertical markers in Fig. 5.1

Within this approximation the evolution of every initial quasimomentum state is simply given by a rotation about the z -axis of the Bloch sphere and the TOF flight observable, i.e. the projection onto the x -axis, becomes an oscillation (see Fig. 5.3) whose amplitude corresponds to the mixing angle, whose phase corresponds to the phase angle and whose frequency is given by the band gap of the reference Hamiltonian. Formally the local atomic density of an ensemble that has evolved over a time t in the post-quench reference system can thus be described by

$$\begin{aligned} n(\mathbf{k}, t) &= |w(\mathbf{k})|^2 \langle \psi_0 | U_{t_0}^\dagger(t) \sigma_x U_{t_0}(t) | \psi_0 \rangle \\ n(\mathbf{k}, t) &= |w(\mathbf{k})|^2 \left[1 - \sin(\theta_0(\mathbf{q}_\mathbf{k})) \cos(\Delta_{\mathbf{q}} t / \hbar + \phi_0(\mathbf{q}_\mathbf{k})) \right] \end{aligned} \quad (5.5)$$

This means, that given a series of TOF absorption images, the initial pre-quench state can be reconstructed by fitting fitting a curve to a time series for each pixel in the first Brillouin zone. Please note, that the tomography will only yield $\sin(\theta_0(\mathbf{q}_k))$ and not $\theta_0(\mathbf{q}_k)$ itself. In other words, the method does not allow to determine whether the measured states are located on the north or south hemisphere. This information however, can be supplemented by employing ordinary band mapping [154]. In the established picture the band mapping process can be described by a projection onto the z -component and thereby allows the distinction of the hemisphere. The band mapping process is however expected to induce significant errors due to the fact that during the mapping process additional dynamics occur. As a supplementary measurement, however, band mapping still might be of value, as the data obtained through the state tomography is a smooth function of the

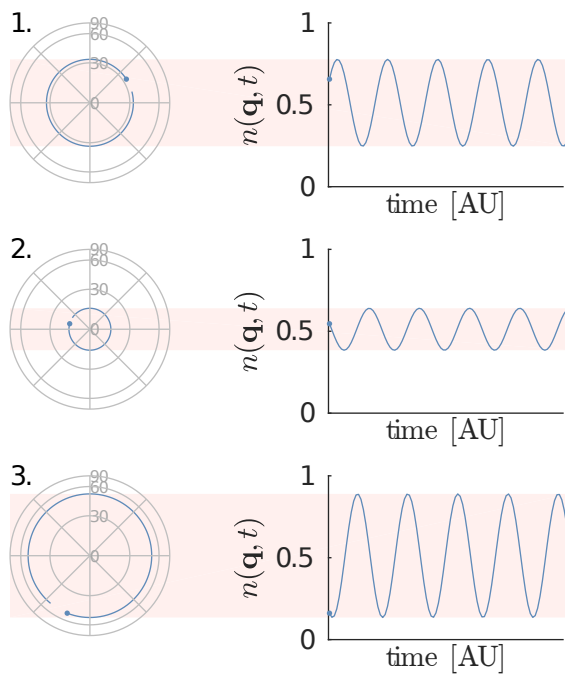


Figure 5.3: Oscillation of the atomic density after TOF. This figure exemplarily shows the oscillations observed for three different initial states. The left column shows a Bloch sphere as in Fig. 5.2 and the trivial evolution in the approximated reference Hamiltonian. The right column shows the atomic density oscillations as the projection onto the x -axis. The amplitudes and phases enable the reconstruction of the initial state marked as a solid dot in the left column.

quasimomentum and the band mapping thus is only needed to identify the hemisphere of complete regions in the Brillouin zone that are separated by an equator crossing. For the experiments presented in this thesis the projected data provided by the TOF state tomography is fully sufficient.

6 Experimental Reconstruction of the Berry Curvature in a Floquet Bloch Band

In this chapter, all the concepts introduced in the previous chapters will be joined to describe the experimental realization of a complete state tomography of a resonantly circularly shaken boron nitride lattice as well as the extraction of the momentum resolved Berry curvature of the system. The experiment has been realized as part of this thesis in a team effort together with my colleagues Nick Fläschner, Benno Rem and Matthias Tarnowski, under the supervision of Christof Weitenberg and Klaus Sengstock. My principal contributions are centered around the implementation of the hexagonal lattice setup, the simulations and the data analysis. This experiment was published article in Ref. [62], upon which most of the figures in this section are based.

This section is structured in two main parts. In the first part I will describe how the presented experimental methods have been used to prepare a state in a system with a strong localization of Berry curvature and how this state has been measured. In the second part the measured states will be analyzed and discussed in the previously established framework of the Berry curvature and Chern invariant.

6.1 Experimental Protocol

Fig. 6.1 gives an overview of the experimental sequence that has been systematically repeated and parametrically modified to generate a data set for 50 different evolution times, each of which having been repeated 10 times for averaging.

Preparation

As a first step a cloud of degenerate spin-polarized ^{40}K atoms is produced through the cascade of optical cooling techniques which have been summarized in Chap. 2. Because all atoms occupy the same spin state their interaction through s-wave scattering is suppressed by *Pauli blocking* and because the higher order scattering processes are extremely weak, the dynamics of the system can be well approximated by a single-particle Hamiltonian.

Subsequently the atoms are loaded into the optical boron nitride lattice at a phase mixing angle of $\theta_p = \pi/20$, as it has been described in detail in Chap. 3. For the loading

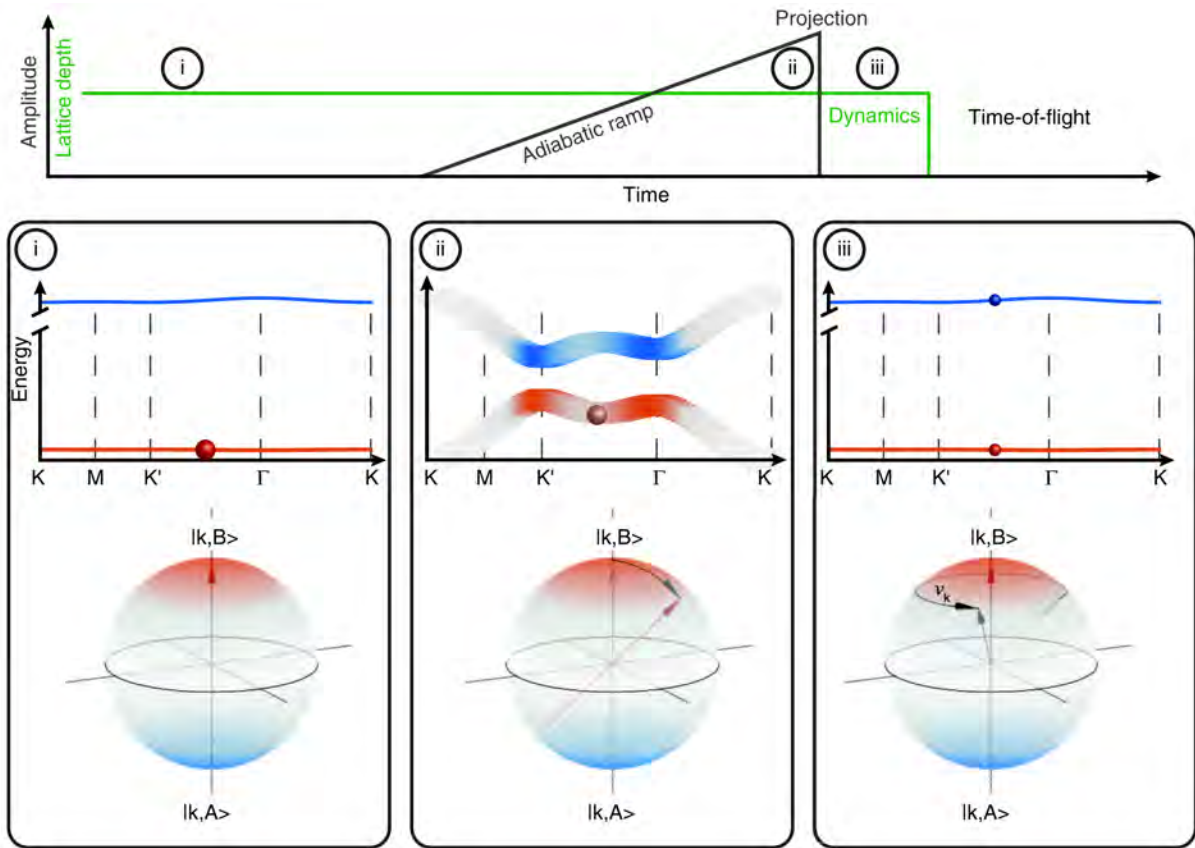


Figure 6.1: Experimental scheme. The upper half sketches how the two main experiment control parameters, lattice depth and coupling strength of the driving, evolve throughout the phases of the experimental cycle. The lower half shows the effective band structure for those phases and the Bloch sphere representation of a selected state (marked as a dot) . Adapted from our publication [64].

process the intensity of the three lattice beams is linearly increased and allows for an adiabatic transfer of the cloud into a deep lattice. Due to the low scattering rate of the Fermions this loading process can be conducted within a short ramping time of 10 ms. The light employed for the lattice has a wave length of 1064 nm, which is far-detuned for any atomic transitions in ^{40}K and thereby ensures a low heating rate through photon scattering. The number of atoms has been chosen such that after the loading the ensemble occupies all the quasimomentum states of the lowest band. For the chosen lattice parameters filling the lowest band is achieved by a particle number of about 50.000 atoms.

For a hexagonal lattice, there is no standard convention to define the lattice depth. Here we use the parameter V_L as defined in Eq. 3.27. In these terms the lattice depth at the end of the adiabatic ramp is given by $V_L = 15.15(15)E_{\text{Rec}}$. To determine this value up to the given precision it is insufficient to measure the light intensities of the lattice beams, because of a variety of uncertainty factors, such as the reflection on the glass cell, slight

imperfections in the mode shape, small deviations from the polarization angles, to name just a few. Therefore the lattice depth has been determined by measuring the resulting band structure with the atoms and subsequently fitting the lattice model to the band structure (for details see *sup. mat.* of Ref. [89]).

The chosen value of V_L corresponds to a deep lattice in the sense of Chap. 5, such that the contribution of the kinetic energy of the atoms is so small that the band structure is almost flat (cf. Fig. 6.1-(i)). Quantitatively this means that the band width of the lowest two bands is 335 Hz and 48 Hz respectively, which is, compared to the energy scale given by the band gap of 11.68 kHz, a relative width of 3.9% and 0.4% respectively. The flatness of the bands is of special importance for the validity of the approximations for the state tomography scheme described in Chap. 5.

From the experimentally determined lattice depth, the tight-binding representation of the lattice can be calculated. The fit of the band structures results in the following parameters

$$\Delta = 11.65(11) \text{ kHz} \quad t_{AB} = 250 \text{ Hz} \quad t_{BB} = 0 \text{ Hz} \quad t_{AA} = 32 \text{ Hz} \quad (6.1)$$

The error in the sublattice offset Δ is of systematic nature and is owed to the fact that the lattice depth varies over the extent of the atomic cloud due to the Gaussian shape of the lattice beams and the additional dipole trap.

Adiabatic launching into the driven system

As explained earlier, an adiabatic launching is necessary to transfer the atoms into the ground state of the shaken system. In our setup the relative real-space position of the lattice is controlled by AOMs. The relationship between the lattice position and the driving frequency is described in detail in context of the optical lattice in Sec. 3.2.2 (Eq. 3.23), and in the context of the fiber lock in Sec. 9.1.1 (Eq. 9.2). For the launching procedure the two relevant parameters are the driving frequency and the coupling strength or driving amplitude. It can thereby be represented by a trajectory through a two dimensional parameter space. Due to adiabaticity, there may not be any discontinuities of this parameter ramp. For the driving frequency this entails that the range of frequencies that is swept through may not contain any lossy resonances, as for example two photon resonances. For our system we found that the best results are achieved with two consecutive linear ramps. First we ramp the shaking amplitude within 5 ms from the resting system to a system shaken with an amplitude of 223 nm, while holding a constant frequency of 9 kHz. Subsequently, we increase the driving frequency within 2 ms to a close resonant value of 11 kHz. After the ramp the system populates the quasimomentum eigenstates of the Floquet system whose eigenenergies form the lower band, which is marked as step ii) in Fig. 6.1.

Quenchedynamics

In the next step the lattice shaking is instantaneously turned off. As discussed in detail in Sec. 4.3, the quasimomentum continues to be preserved and the dynamics of every quasimomentum eigenstate are now driven by the Hamiltonian of the static system. In the approximation of flat bands this static Hamiltonian is diagonal in the sublattice basis, i.e. the A and B sub-lattice states are its eigenstates. The dynamics of the Floquet eigenstates can now be evaluated by considering its components in the sublattice basis. These components can be described by a population and a phase for each sublattice. Being eigenstates of the Hamiltonian the two sublattice states evolve fully independently, as one would expect from a flat band Hamiltonian where the tunneling to other sites is suppressed strongly enough that the dynamics are completely decoupled. The evolution of each sublattice is trivially given by a dynamic phase factor oscillating with the respective eigenenergy. The interference between the two sublattices thereby oscillates with a frequency according to the energy difference between the two bands, an amplitude according to the population imbalance and a phase according to the initial phase of the respective components. The equivalent dynamics in the Bloch sphere picture are shown in Fig. 6.1 (inset iii).

State tomography

The state tomography follows the method detailed in Chap. 5. After a variable time t_Q all potentials are abruptly switched off and the cloud expands for 21 ms in free fall. During the expanse the A and B sublattice sites interfere and the quasimomentum gets mapped to real-space. In the flat band approximation the column atomic density of a the cloud after the expansion therefore behaves according to Eq. 5.5:

$$n(\mathbf{q}, t_Q) = |w(\mathbf{k})|^2 \left[1 - \sin(\theta_0(\mathbf{q}_k)) \cos(\Delta_{\mathbf{q}} t_Q / \hbar + \phi_0(\mathbf{q}_k)) \right] \quad (6.2)$$

which enables the extraction of the angles $\vartheta_{\mathbf{q}}$ and $\phi_{\mathbf{q}}$ of the Floquet state by a fit.

6.2 Data Analysis

The TOF absorption images were defringed (see Sec. 2.4) and the resulting atomic densities were averaged over the 10 repetitions for each time step. Those processed atomic density distributions are depicted in the upper part of Fig. 6.2 for five selected time steps. Subsequently every pixel trace was fitted with a sinusoidal function with an exponential damping factor to model the effects of decoherence and heating

$$f(t_Q) = A \left[1 - B \exp(-t_Q C) \cos(t_Q D + E) \right] \quad (6.3)$$

The lower part of Fig. 6.2 shows those fits for three different pixels. The resulting parameters were mapped to the quasimomentum space using Eq. 5.1 with a pixel size of $13 \mu\text{m}$ and

a magnification factor of 2.15, which yields a resolution of 57(2) pixel along the Bravais vector \mathbf{b}_2 (see appendix A).

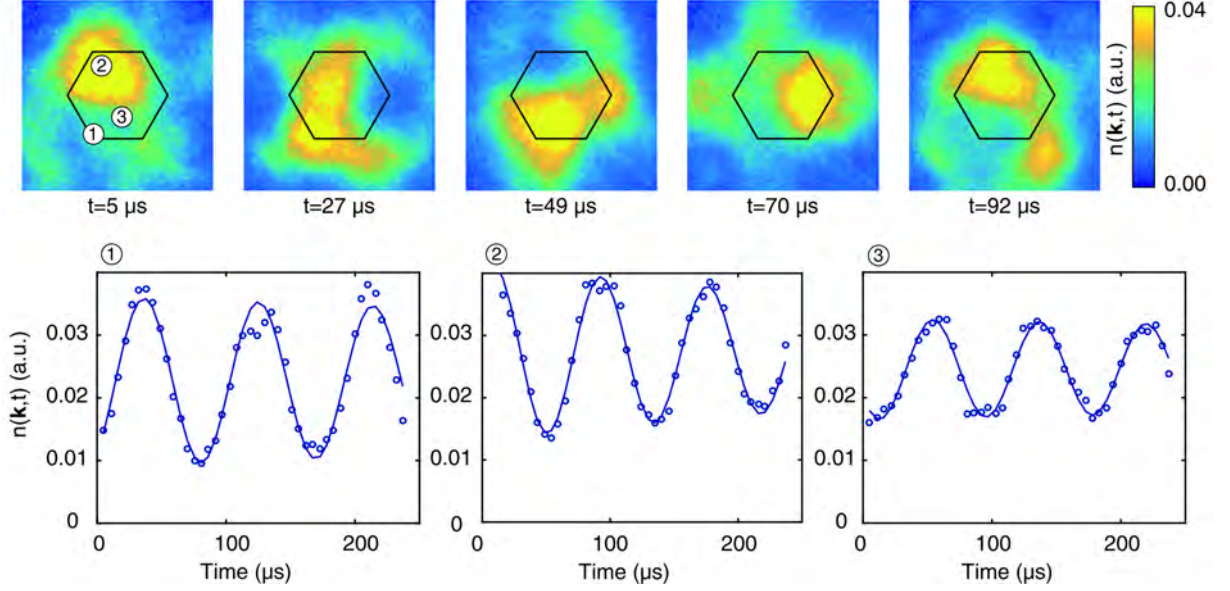


Figure 6.2: TOF images and fit to pixel series. The upper row consists averaged TOF absorption images for five different post quench evolution times t_Q . The lower row shows the fit to a time series for individual pixels located at three different quasimomenta. Adapted from our publication [64].

To finally reconstruct the Berry curvature according to Eq. 4.21, the extracted angles $\vartheta_{\mathbf{q}}$ and $\phi_{\mathbf{q}}$ need to be differentiated with respect to the quasimomenta. Here a Savitzky-Golay filter of third order with a window size of 15 pixels was applied. The principal results of this experiment are shown in Fig. 6.3. Here the measured amplitude, phase and Berry curvature of the Floquet-Bloch band are compared against their theoretical values, obtained from a tight-binding simulation (see Sec. 4.3) with the frequency $\Delta_{\mathbf{q}}$ extracted from the fit as the input parameter.

The Berry curvature along the high symmetry path $M - K' - \Gamma - K - M$ has been additionally plotted for both shaking directions in Fig. 6.4. The Chern number, i.e. the integral of the Berry Curvature over the first Brillouin zone, can be simply calculated as the sum of the pixel values within the BZ normalized by the number of pixels contained in the BZ. For the two chiralities of the driving we obtain experimental values for the Chern numbers of

$$C^+ = 0.005(6) \quad C^- = -0.016(8) \quad (6.4)$$

while for the present topologically trivial system a zero value for both cases is expected.

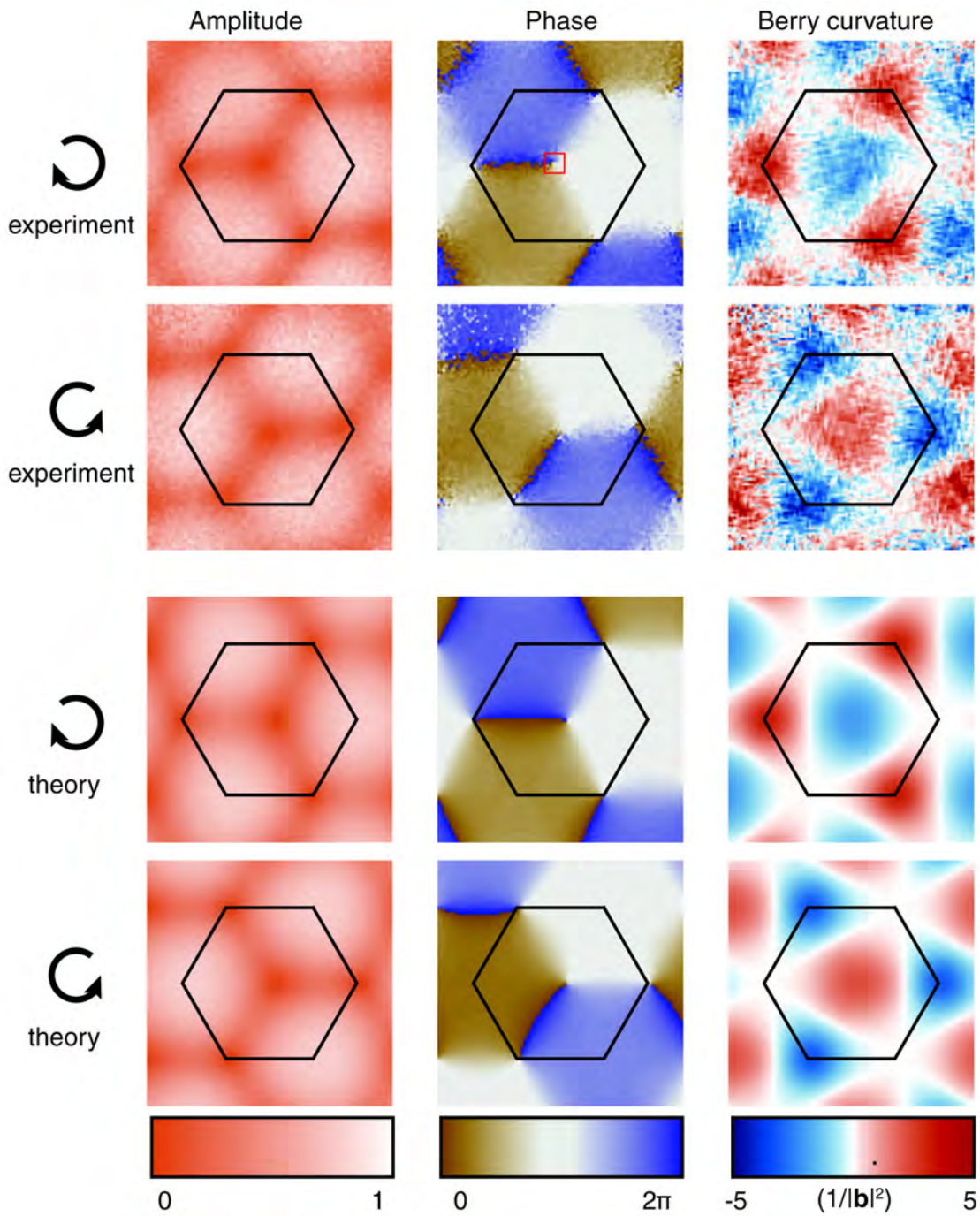


Figure 6.3: Measured and simulated amplitude, phase and Berry curvature of a Floquet Bloch band. Adapted from our publication [64].

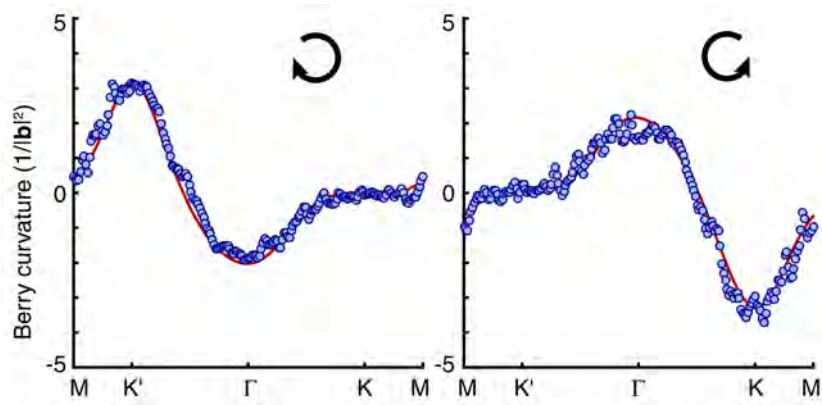


Figure 6.4: Berry curvature along the high symmetry path. The filled circles show the Berry curvature on the path, linearly interpolated from the nearest pixels. The red solid line represents the theoretical Berry curvature. The left and right graph are distinguished by the chirality of the driving. Adapted from our publication [64].

6.3 Summary and Outlook

In this chapter I presented a new measurement scheme that allows the reconstruction of the Berry curvature in a driven lattice system, based on a complete state tomography [150]. This scheme was applied to a boron-nitride type lattice that was shaken circularly near the resonance of the transition of the initially flat bands. The acquired data shows very clear sinusoidal density oscillations for over three periods. The fits to the oscillations reveal a representation of the wave function in quasimomentum space in terms of its phase angle and the sine of its polar angle. Both quantities are highly resolved and show clear features. Both the amplitude and phase data show a rotational symmetry, which is reduced as compared to the undriven system from sixth order to third order. The azimuthal phase angle distribution shows the location of the Dirac points in form of two vortices in the BZ of opposed chirality. The Dirac points are located at the Γ - and K-points, while in the undriven system they were located at the K and K' points. The amplitude data shows clear minima that coincide, as expected, with the locations of the Dirac points. The Berry curvature distribution, that has been computed from those two quantities, shows a high amplitude with maxima of opposite signs at the two Dirac points, as it is expected from theory. We also performed the state tomography for an identical system but an inverse shaking direction. Inverting the shaking direction corresponds to an inversion in quasimomentum space ($\mathbf{q} \rightarrow -\mathbf{q}$) and is reflected in the measured phase and amplitude. For the Berry curvature this additionally yields the expected inversion of its sign. Furthermore we compared the results with our simulation (see Chap. 4) of the system and find excellent agreement both in scale and structure.

The presented experiment demonstrates that the Berry-curvature is a experimentally accessible quantity for lattice periodic system. This paves the way towards the exploration of further, more complicated quantum geometric phenomena in e.g. interacting systems or for topologically nontrivial states. It might also spark the motivation for the measurement of Berry phases in condensed matter experiments. Chaps. 7 and 8 report on another experiment, where we extended the experimental technique of a complete state tomography to study the relationship between the dynamics of a nonequilibrium state and the underlying topology of the system.

7 Nonequilibrium Dynamics in Topological Bands

In this chapter I am going to present the nonequilibrium dynamics of a general two-band model, with the application to the class of effective Floquet-Bloch Hamiltonians in mind, that are considered throughout this thesis. The goal of this chapter is to develop a formal description and an intuitive understanding of the experiment presented in the next chapter. The focus will be on the vortex pairs in the nonequilibrium wave function, that emerge during its evolution under a Hamiltonian near a topological phase transition, subsequently move through the quasimomentum space and finally annihilate in pairs. These *dynamical vortices* will be identified as an order parameter for a *dynamical phase transition* [70] and will be studied in this context. The calculations presented in this chapter were conducted by me and the conceptual development of the ideas leading to the experiment arose in close collaboration with the members of the research team as named previously in Chap. 6.

7.1 Quench Dynamics in Bloch Bands

In the two-band model introduced in Sec. 3.4.3, the dynamics of a state can be described straightforwardly by an analytic time evolution operator (Eq. 3.52), as it has been done in Chap. 5 to describe the full-state tomography. In that case however, the time evolution was reduced to an additional trivial phase factor, i.e. an uniform rotation about the z-axis on the Bloch sphere, because the associated flat band Hamiltonian has no geometric structure, in the sense that its eigenvectors point to the poles of the Bloch sphere for all quasimomenta. In contrast to this, in the following chapter, general Hamiltonians will be considered, including those with a significant geometric structure and nontrivial topology. In this case, the time evolved state has a complicated dependency on both the initial state and the Hamiltonian of the system. To reduce this complexity we limit our description to the dynamics induced into a geometrically trivial initial eigenstate. As will be discussed in detail in Chap. 8, this situation can be realized experimentally with the same class of shaken boron nitride lattice systems as described in the previous chapter (Chap. 6), when the eigenstate of the reference Hamiltonian is not adiabatically transferred but quenched into the Floquet-Bloch-Hamiltonian.

In the sublattice basis the evolution of a B-sublattice eigenstate $\begin{pmatrix} 0 \\ 1 \end{pmatrix}$ for an arbitrary Hamiltonian, defined through the angles $\varphi_{\mathbf{q}}^H$ and $\vartheta_{\mathbf{q}}^H$ in the BZ, is represented by the

following time-dependent state vector (Eq. 3.48 in Eq. 3.52 applied to $\begin{pmatrix} 0 \\ 1 \end{pmatrix}$):

$$|\psi_{\mathbf{q}}(t)\rangle = \begin{pmatrix} g_{\mathbf{q}}^{\text{A}} \\ g_{\mathbf{q}}^{\text{B}} \end{pmatrix} = \exp\left(-i\frac{h_{0,\mathbf{q}}t}{\hbar}\right) \begin{pmatrix} \cos(\tau_{\mathbf{q}}) - i \cos(\vartheta_{\mathbf{q}}^{\text{H}}) \sin(\tau_{\mathbf{q}}) \\ -i \sin(\vartheta_{\mathbf{q}}^{\text{H}}) \exp(i\varphi_{\mathbf{q}}^{\text{H}}) \sin(\tau_{\mathbf{q}}) \end{pmatrix} \quad (7.1)$$

Here $g_{\mathbf{q}}^{\text{A/B}}$ are introduced as a shorthand notation for the sublattice coefficients, and the superscript H marks the angles of the Hamiltonian to avoid confusion with the angles describing the evolved state which shall be marked with a superscript S. The angles describing the evolved state can be calculated with the definitions in Eq. 3.55 and standard trigonometric identities

$$\begin{aligned} \varphi_{\mathbf{q}}^{\text{S}} &= \text{atan}[\cot(\tau_{\mathbf{q}}), \cos(\vartheta_{\mathbf{q}}^{\text{H}})] - \varphi_{\mathbf{q}}^{\text{H}} \\ \vartheta_{\mathbf{q}}^{\text{S}} &= 2 \text{acos}[\sin(\vartheta_{\mathbf{q}}^{\text{H}}) \sin(\tau_{\mathbf{q}})] \end{aligned} \quad (7.2)$$

In these equations we make use of the *four-quadrant inverse tangent* function (see e.g. [155]). By using two arguments it simplifies the extraction of an angle in the form of $\alpha = \text{atan}[\sin \alpha, \cos \alpha]$ for $\alpha \in [-\pi, \pi]$.

Fig. 7.1 depicts an exemplary evolution of an initial sublattice eigenstate as a series of time steps for an associated Hamiltonian, that can be produced by circularly driving a boron nitride lattice. The evolution shows a number of interesting features. First of all, the evolved state reflects the 3rd order rotational symmetry¹ of the Hamiltonian. This is a natural consequence of the choice of the singular initial state. Furthermore, the phase profile of the state resembles the phase profile of the Hamiltonian up to a constant offset. Taking the limit $t \rightarrow 0$ in Eq. 7.2 confirms this observation formally

$$\lim_{t \rightarrow 0} \varphi_{\mathbf{q}}^{\text{S}}(t) = \pi/2 - \varphi_{\mathbf{q}}^{\text{H}} \quad (7.3)$$

Intuitively this can be understood, by imagining the trace of the evolution of an arbitrary quasimomentum mode on the Bloch sphere as a *small circle* around the corresponding eigenstate, intersecting with the initial state at the pole. For short times the evolution follows the tangent and the state thus acquires the offset of $\pi/2$. The chosen Hamiltonian breaks the Brillouin zone up into three symmetrical areas in which its phase takes almost homogeneously the values $0, -2/3\pi$ and $2/3\pi$. Each of those areas corresponds to one of the three wings formed by the evolved state in the BZ, which can be clearly seen in the first image of the third row of Fig. 7.1. This symmetric trinary phase distribution leads inevitably to the appearance of a static phase vortex at every point where the three areas are joined. Within the BZ there are two static vortices (one at the Γ -point and three times a third of a vortex at the K-points), which are of opposite handedness. We will refer to those vortices as *static vortices* as they are preserved under the evolution of the state.

The main focus of this chapter is however directed to the creation of pairs of vortices and anti-vortices that propagate with the evolution of the state and will thus be referred to

¹This symmetry is slightly broken by the initial *kick* (see Sec. 4.3.2)

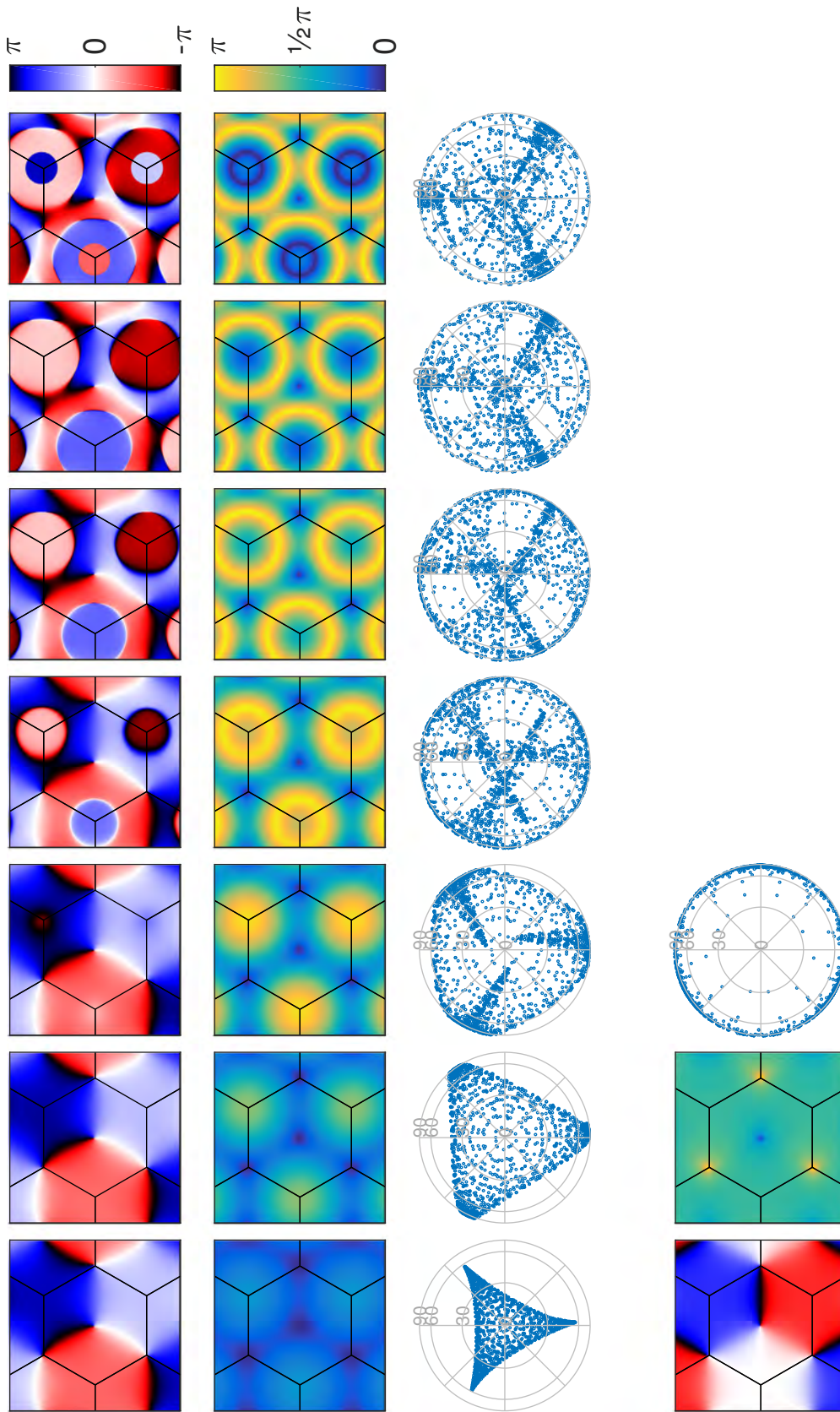


Figure 7.1: Exemplary state evolution in an effective, near-resonantly circularly shaken, boron nitride lattice with initially flat bands. The first row shows the evolution of the phase angle of the wavefunction in the Brillouin zone. The second row shows the evolution of the state representation on the Bloch sphere. The third row shows the projection of the state representation on the Bloch sphere. The evolution is shown for consecutive time steps, with the state moving from a flat band to a dispersive band and back to a flat band.

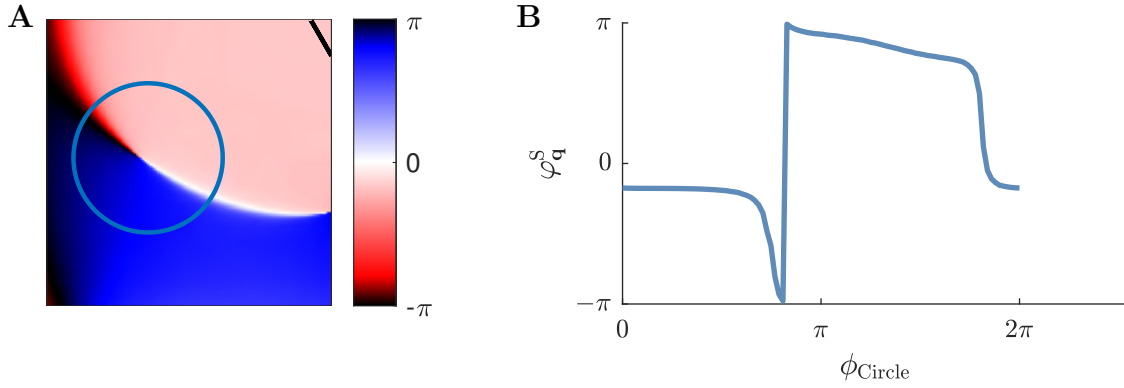


Figure 7.2: Phase profile around a vortex. Subfigure **A** shows the enlarged phase profile in the vicinity of a vortex as e.g. in the seventh time step of Fig. 7.1. Subfig. **B** visualizes the phase along the circular path marked in Subfig. **A**. The phase has not been unwrapped - along the path an overall phase of 2π is collected.

as *dynamical vortices*. Under careful observation of Fig. 7.1 one can identify the appearance of such a dynamic vortex pair at time step number six of the depicted example system. For a clearer view of the vortex, Fig. 7.2 shows a magnified version and the phase along a circular shaped path around the vortex. Owing to the topological nature of the vortex any arbitrary closed path that includes a single vortex will collect an overall phase of $\pm 2\pi$ depending on the handedness of the vortex.

Another noticeable feature in the phase profile is the appearance of sharp phase jumps. In the example plotted in Fig. 7.1 they appear in the form of circles around the k points in the last shown time step. Before discussing the dynamics of vortices in more detail, I will present an approach that we developed for a more intuitive understanding of the complicated dynamics and to handle the transcendental nature of Eq. 7.2 more easily by reducing it to its here relevant topological properties. In Sec. 7.4 the relation to the *Pancharatnam* phase will be illustrated, whose winding number was introduced as a *dynamical topological order parameter* in Ref. [84] and is closely related to the topological nature of the vortices described here.

In this approach we unfold the dynamics of the sphere onto two flat maps for the two angles, which are shown in Fig. 7.3 and visualize the state at a given point in time as the projection of the closed BZ surface onto their preimage. These maps are described by Eq. 7.2, where the phase $\varphi_{\mathbf{q}}^H$ has been set to zero, because it can be trivially restored through a simple unitary transformation and does not have any influence on the dynamics. At an initial time $\lim t \rightarrow 0$ the projection of the surface onto the map would correspond to an infinitely thin vertical line approximating the $t = 0$ -axis, within which the point distribution is equal, as argued earlier, to the one of the Hamiltonian of the system. An example of such a surface in the case of a one-dimensional Hamiltonian will be presented

later in Sec. 7.1.1 and Fig. 7.5. The evolution of the state in this picture is described by a purely horizontal movement of every point of the surface within the maps, at a speed which is given by the band structure of the system. Bear in mind, that here $R_{\mathbf{q}}$ refers to the relative band gap at a given quasimomentum and the coordinate in τ -space is thus given by the linear relation

$$\tau_{\mathbf{q}}(t) = \frac{R_{\mathbf{q}}t}{\hbar} \quad (7.4)$$

and that the maps $\varphi_{\mathbf{q}}^{\text{S}}$ and $\vartheta_{\mathbf{q}}^{\text{S}}$ are π -periodic.

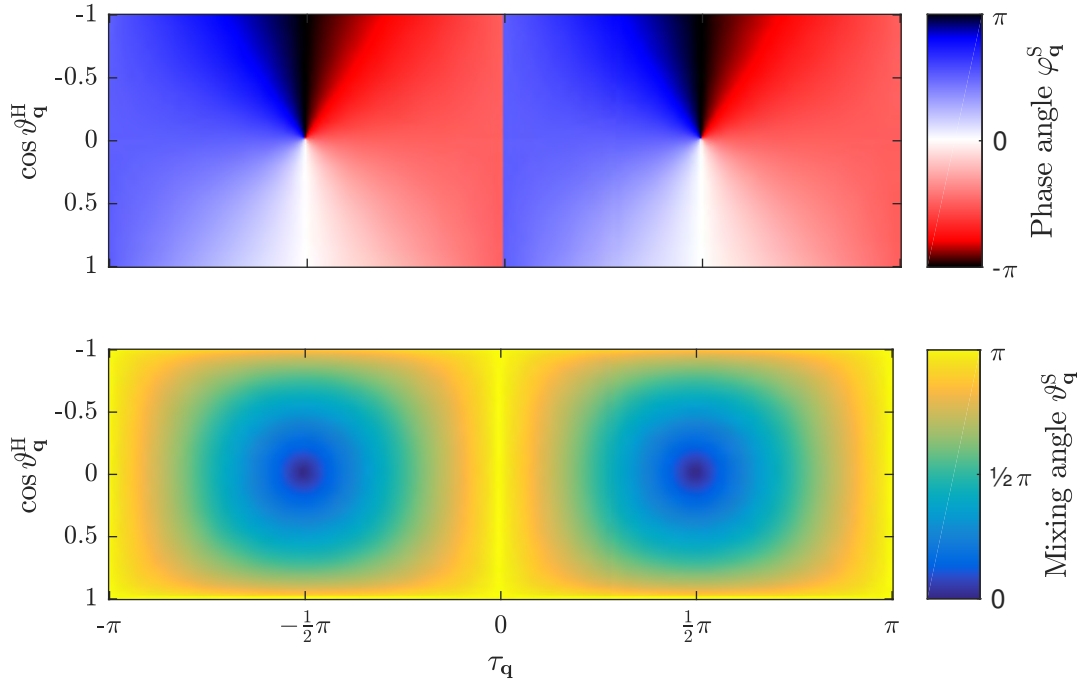


Figure 7.3: Relative phase angle $\varphi_{\mathbf{q}}^{\text{S}}$ (top) and mixing angle $\vartheta_{\mathbf{q}}^{\text{S}}$ (bottom) of the evolved state as a function of the effective time and the polar angle of eigenstate of the Hamiltonian governing the dynamics. In this basis the dynamical vortices become apparent. The dynamics are fully captured by the shown dependencies, so that any evolved state of a two-band Hamiltonian could be depicted as a surface on the shown maps.

Regarding the concrete representation of those mappings in Fig. 7.3, one can identify the same features, that have been discussed earlier in this section (Fig. 7.1) for a specific choice of an exemplary Hamiltonian, as being generic features i.e. independent of any concrete form of the Hamiltonian. The phase map $\varphi_{\mathbf{q}}^{\text{S}}$ exposes a vortex (within every π -period), that can be associated with the vortex-anti-vortex pairs that are created at critical times. Because of the toroidal topology of the Brillouin zone, the surface representing a Hamiltonian that produces dynamical vortices will always cover the vortex on this map in such a way that pairs of points with normals of opposite orientation will be mapped

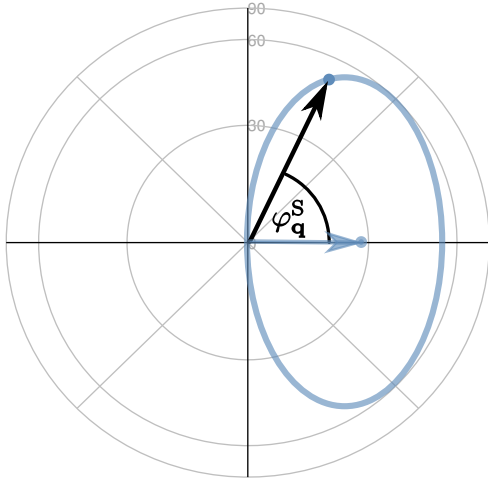


Figure 7.4: View of the trajectory of an initial state at the pole of the Bloch sphere under evolution of an arbitrary Hamiltonian, whose eigenstate is here indicated by a blue dot. Upon completing one period, the phase angle of the state makes a π -jump.

to the vortex, which results in dynamical vortices of opposite chirality. The phase map also shows the π -phase jump at times $t = n\pi$. Because the jump is independent of $\cos \vartheta_{\mathbf{q}}^H$ it will always appear in the form of a closed line in the BZ. From the second map $\vartheta_{\mathbf{q}}^S$ of Fig. 7.1 we can infer that the vortices can be associated exclusively with the singularities at the pole of the Bloch sphere opposite to the chosen initial state, where $\cos \vartheta_{\mathbf{q}}^S = \pm 1$. The pole of the initial state is reached at the lines of the π -phase jumps and at the upper and lower edges of the map. Formally the condition for the appearance of a dynamical vortex at a point \mathbf{q} is thus defined by

$$\vartheta_{\mathbf{q}}^H = \frac{\pi}{2} \quad (7.5a)$$

$$t_{\text{crit}} = \frac{\hbar}{R_{\mathbf{q}}}(n + 1/2)\pi \quad (7.5b)$$

These equations constitute a first sign to the intimate connection of dynamical vortices to the topological nature of the static Hamiltonian: only if the Hamiltonian spans parts of the two Bloch hemispheres dynamical vortices will appear.

The condition for the appearance of dynamical vortices in Eq. 7.5 can also be easily understood in the Bloch sphere picture: A state on one pole of the sphere can only reach the opposite pole through a rotation along an axis that lies in the equator plane. This is equivalent to the evolution through a Hamiltonian that fulfills the condition in Eq. 7.5a. On this trajectory the poles are reached for every half rotation. With a period of the Hamiltonian of $T = 2R_{\mathbf{q}}/\hbar$ this coincides with Eq. 7.5b.

The nature of the π -phase jumps is illustrated in Fig. 7.4. Here it becomes very clear that for any trajectory including the initial state will approach an angle of $\pi/2$ and upon traversal of the pole will jump to $-\pi/2$.

The projective view of an arbitrary trajectory in Fig. 7.4 furthermore shows that there

exists an isomorphism between the quasimomentum modes in projective Hilbert space restricted to one hemisphere and the complex numbers. This isomorphism can especially be used to describe the vortices as ordinary singularities known from complex analysis.

7.1.1 Kitaev-Chain with Next Nearest Neighbor Hopping

To illustrate how this approach can be applied to understand dynamical vortices and dynamical phase transitions in real physical systems and to show how it naturally embeds the phase windings studied in one-dimensional systems [84] and two-dimensional systems [79] in the same framework, the Kitaev chain with next nearest neighbor hopping will be considered as an example. Note that the phase considered in the given Ref. [84] is not the polar phase of the state but the Pancharatnam Phase, concerning their winding number, however they are identical (see Sec. 7.4).

In analogy to Ref. [84] the Hamiltonian of the quenched system can be defined using the previously introduced notation as

$$h_{\mathbf{q}} = \begin{pmatrix} 0 & \\ & \sin(\mathbf{q}) \\ 1 + \cos(2\mathbf{q}) + \lambda \cos(\mathbf{q}) & \end{pmatrix} \quad (7.6)$$

At a parameter value $\lambda = 2$, the system undergoes a topological phase transition, which in this system, means that the Hamiltonian will form a closed circle in the $x = 0$ -plane around the Bloch sphere and that $\cos \vartheta_{\mathbf{q}}^H$ will span the region from -1 to 1 . Fig. 7.5 shows the evolved state of the system, represented by a line in the domain of the phase map $\vartheta_{\mathbf{q}}^S$, for a topologically trivial realization of the system ($\lambda = 1$) in blue and for a nontrivial one ($\lambda = 3$) in red. The states are depicted at three different evolution times, from left to right: $0, \pi, 5$. The features of the map are depicted schematically, marked in gray: the periodic vortices as $+$, the π -phase jump as a dashed line and the pole coinciding with the initial state as a line at the bottom all of which describes a single state in the image of the mapping. In this figure it can be clearly seen how the time evolution in these coordinates corresponds to a simple stretch of the $\tau_{\mathbf{q}}$ axis. At the critical time $t_{\text{crit}} = \pi$ (left side of Fig. 7.5) both states transverse the singularity and thereby acquire a phase winding. For the topologically trivial system (blue) the phase winding is fully obvious as the line forms a loop around the vortex. At a later time the loop will pass the vortex, which will unwind the phase again. At still later times the loop will grow wide enough to include multiple vortices. The state, evolving in the topologically nontrivial system (red), also effectively wraps the singularity. This means that the appearance of a dynamical vortex pair, or here in the one-dimensional case the equivalent appearance of a phase winding, does not necessarily signal an underlying topological Hamiltonian, instead, in this case, the monotonic increase of the winding number with time is a clear indicator of nontrivial topology in the considered system.

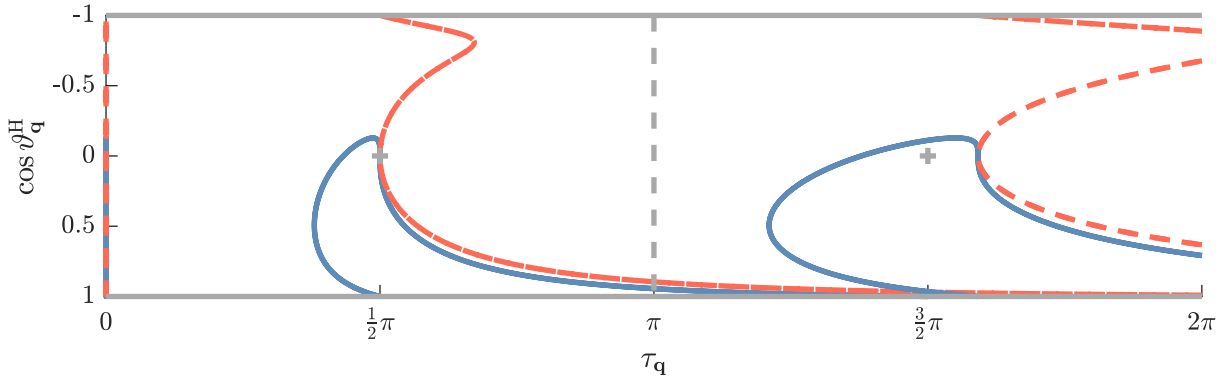


Figure 7.5: State evolution in the Kitaev chain model - phase windings and accidental phase windings. This figure depicts the evolution of a state after a quench in a Kitaev chain model in terms of the topological features of the polar and azimuthal angles. The axes are the same as for the maps shown in Fig. 7.3 but the features of the maps have been reduced to the principal topological characteristics: + marks the vortices and the gray dashed and solid lines the north and south pole respectively. The evolved states in a topologically trivial (blue solid line) and a nontrivial system (red dashed line) are depicted for three different evolution times (left to right). The time evolution corresponds to a simple stretch of the x-axis.

7.2 Dynamical Vortices and Topology in Shaken Boron Nitride Lattices

For the shaken boron nitride lattice that we study in this work, there is also a relationship between the appearance of dynamical vortices and the topology of the underlying system. When considering the conditions in Eqs. 7.5 individually they can be depicted as two sets of lines through the BZ as depicted in Fig. 7.6. Here the white line represents the first condition and marks all quasimomentum modes which are associated with a Hamiltonian that lies on the equator of the Bloch sphere. This line represents a static property of the Hamiltonian and is thus equal for all time steps. The (solid) yellow line represents the second condition and marks all quasimomentum modes that have evolved half a period of their oscillatory dynamics at the respective time step.

The intersections of those two lines thus mark locations of a dynamical vortex. Fig. 7.6 now shows clearly how a vortex-anti-vortex-pair gets created (just before time step 2), moves in opposite directions along the white *equator line* (steps 3-5) before the vortices annihilate with other pairs (last time step). The observation of one full cycle, therefore allows to trace the full equator line.

The topology of the system can be characterized by the properties of the Dirac points [134]. The Hamiltonian at the Dirac points is by definition represented by a vector that points to one of the poles of the Bloch sphere. In the present case of two Dirac points, the system is topologically nontrivial if both Dirac points have different

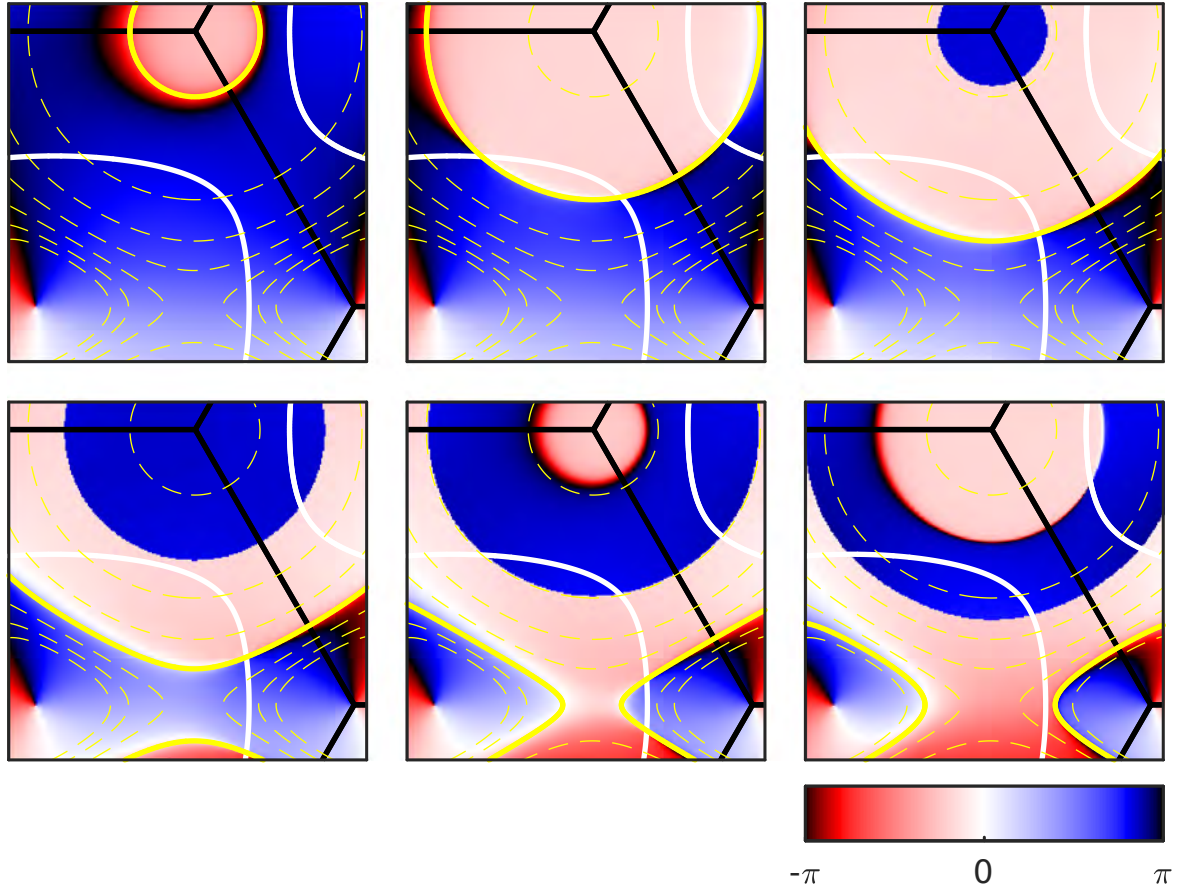


Figure 7.6: Conditions for dynamical phase vortices. This series of six images shows the phase profile of a sublattice eigenstate upon evolution in a topologically nontrivial shaken boron nitride lattice. The static white line and the dynamical yellow line visualize the conditions for the occurrence of a dynamical phase vortex (Eqs. 7.5).

signs, i.e. are associated with opposed poles. While the location of the Dirac points in the BZ can be easily determined from the static vortices in the phase profile, their signs are experimentally less accessible. But an equator line that encloses a static vortex, i.e. the location of a Dirac Point, yields that any path connecting the two Dirac points will cross the equator an odd number of times, meaning that they are located on opposite poles. In this sense it is possible to relate the Chern number of the Hamiltonian to the winding number² of the equator line, which can be directed by defining its orientation dependent on the handedness of the dynamical vortices. This way, tracing out the path of dynamical vortices in respect to the static ones allows to determine the topology of the system without making any further assumption of its structure and without populating its

²Not to be confused with the winding number relating to the quantum mechanical phase, as used here for defining the vortices. Instead winding number refers to the mathematical concept of how a curve winds around a point and describes the winding of the polar angle of the trajectory with respect to that point.

ground state, which is difficult to reach because it is topologically protected [69]. Note, that for a nonequilibrium system it is necessary to distinguish between the Chern number of a state and the Chern number of the Hamiltonian. The common definition of the Chern number is based on the definition of the Berry connection in terms of the eigenstates of the system (see Eq. 4.11). Formally it is possible to apply this definition to any other, possibly nonequilibrium, state and thereby deduce a Berry curvature and Chern number for this state. In the case of quench dynamics without dissipation, the unitary time evolution preserves [69] the zero-valued Chern number of the initial state, even when Chern number of the Hamiltonian changes.

Following our initial publication [89], Wang et. al. [67], generalized this concept. They consider not only the trajectories that are traced out by the static and dynamical vortices, i.e. those belonging to the north and south pole of the Bloch sphere, but those that map to any constant point on the Bloch sphere. They prove that for any two points of the Bloch Sphere, the associated paths have a linking number³, that reflects the Chern number of the Hamiltonian. In the special case presented here the trajectory of the static vortices reduces to a point and the linking number becomes the winding number. In this spirit Yu [66] studied the phase vortices of the Haldane model.

With our simulations, for an ideal circularly driven boron nitride lattice and an initial state originating from an infinitely deep sublattice (i.e. fully localized at a pole), we could not find a parameter regime with a equator line that does not enclose a Dirac Point. Our data, however, shows closed vortex traces that do not enclose the Dirac points and will be discussed in Chap. 8). In general, the appearance of dynamical vortices is a necessary condition for a topologically nontrivial systems and thus can potentially be exploited as an experimentally accessible signature of a topological phase transition.

In Fig. 7.7 the fundamental branch of the phase diagram for a circularly shaken boron nitride lattice ($V_L = 15.363$, $\vartheta = 9^\circ$) is shown. It exposes only three phases which can be characterized through the Chern numbers 0, +1 and -1. The nontrivial phases are only present in a narrow band, here of a relative width of about 1% of the shaking frequency.

Number of Vortex Pairs

For longer evolution times more and more vortices will be created. To understand how the number of vortex pairs evolves with time, consider the band structure of the system along the equator line as marked in Fig. 7.8.

Fig. 7.9 visualizes the condition in Eq. 7.5b by splitting it up as

$$\frac{\hbar}{R_{\mathbf{q}}} = \frac{t_{\text{crit}}}{(n + 1/2)\pi} \quad (7.7)$$

where the left hand side is simply the inverse of the band structure (ondulating line in the figure) and the right hand side a set of \mathbf{q} -independent lines. Dynamical vortices exist at the

³The linking number defines how many times a path winds around another.

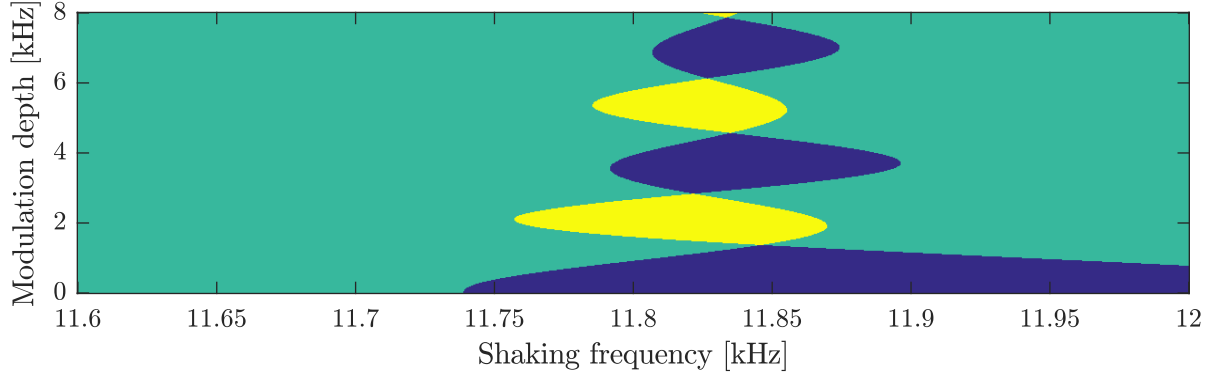


Figure 7.7: Numerical simulation of the phase diagram of the circularly shaken boron nitride lattice. This phase diagram shows three different phases corresponding to Chern numbers equal to 0 (green), -1 (blue) and 1 (yellow). The Chern number has been determined as the difference in orientation of the Hamiltonian at the Dirac points. The lattice is defined as previously by a polarization mixing angle of 9° and a lattice depth of $V_L = 15.363$

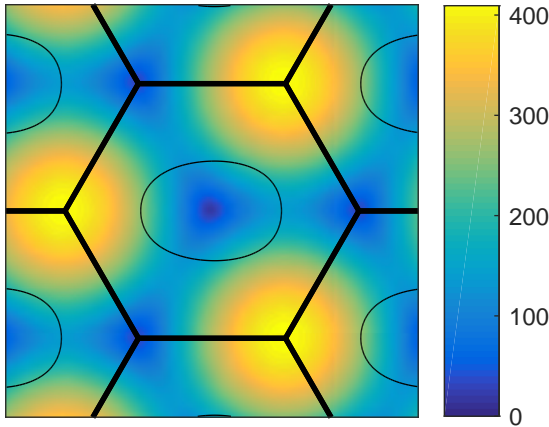


Figure 7.8: Relative band structure with marked equator line. The black *equator line* in this plot marks the quasimomentum states in the BZ which evolve under an Hamiltonian whose eigenstates lie on the equator of the Bloch sphere, i.e. $\vartheta_{\mathbf{q}}^H = \pi/2$. The color mapping indicates the difference in energy between the considered two bands. A cut along this line is shown in Fig. 7.9. The maxima of energy on the equator line indicate the points where vortex pairs are created and the minima where they annihilate.

intersection of those two sets of lines. In this picture time evolution is represented by scaling the vertical axis for the set of horizontal lines corresponding to the linear time dependency of the right hand side of Eq. 7.7. In the plot also the previously mentioned breaking of the three fold symmetry due to the choice of Floquet gauge becomes clearly visible. The left and right box indicate the minima and maxima where vortices get created and annihilated in the two asymmetric regions. It becomes clear that the number of simultaneously visible vortices is approximating a linear increase, even though not a monotonic one. To make this relationship still clearer the vortex number as a function of time is explicitly shown in Fig. 7.10.

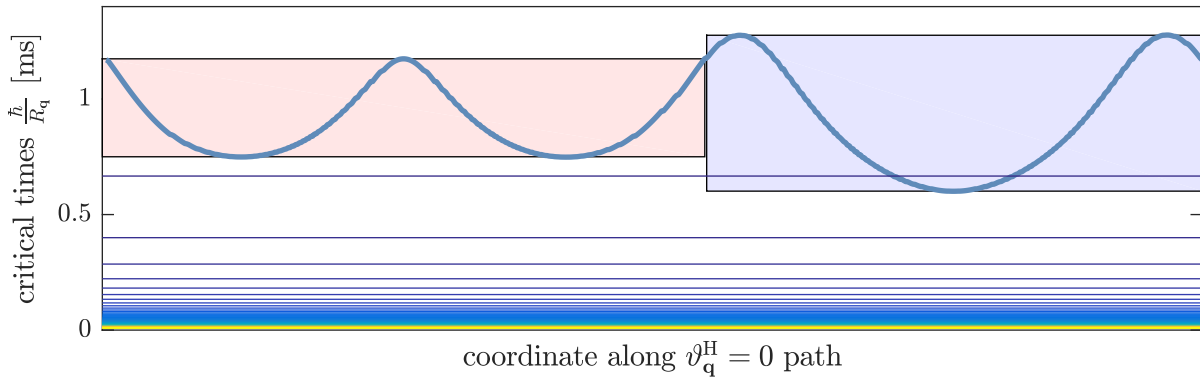


Figure 7.9: Inverse band structure (blue, undulating line) along equator line cut and critical times (horizontal lines). In this picture dynamical vortices exist at the intersections of the two sets of curves and time evolution corresponds to scaling the vertical axis for the set of lines associated with the critical times.

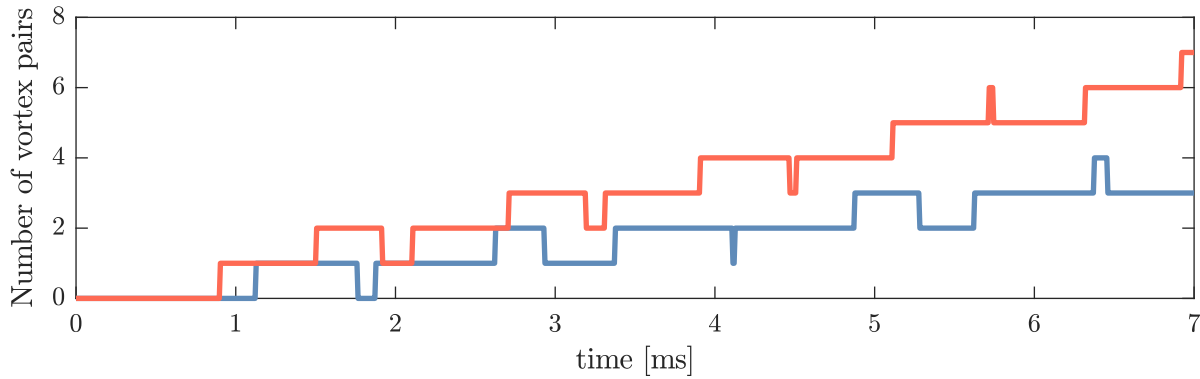


Figure 7.10: Number of dynamical vortex pairs as a function of time. The two lines correspond to the number of vortices in the two regions arising from the symmetry breaking by the Floquet gauge.

7.3 Connection to Dynamical Phase Transitions

The phenomenon of dynamical vortices in the evolution of pseudo spin states, as it has been presented in this chapter, is closely connected to the recent concept of *dynamical quantum phase transitions* (DQPT) as introduced in Ref. [70]. Please note, that there exist multiple concepts associated with the term *dynamical phase transition* as e.g. the transition from localized to non-localized states in disordered systems [156–158]. In the context of this thesis, by DQPT it will be exclusively be referred to those defined in Ref. [70]. While quantum phase transitions have been studied extensively [159, 160] for systems at equilibrium, the framework for the description of nonequilibrium systems is still under active research (for an overview see e.g. [161]). Quantum phases are canonically defined through a local order parameter or a global topological invariant associated with the state or Hamiltonian. In equilibrium systems a phase transition can occur for the change of an external parameter such as the magnetic field. For a nonequilibrium system, in

contrast, a differentiated classification needs to be established, because the quantum state constantly evolves. The definition of a DQPT in [70] allows to carry over a broad tool set from equilibrium phase transition into the nonequilibrium domain by establishing a formal analogy between the static partition function Z of a quantum many body system and the dynamical property \mathcal{G} , the so-called *Loschmidt amplitude*. The Loschmidt amplitude, sometimes also referred to as *return amplitude*, is defined as the overlap of an evolved state with the initial state [70]. For a time-independent system this is expressed through the expectation value of the evolution operator for the initial state

$$\mathcal{G}(t) = \langle \Psi_0 | \exp(-i/\hbar H t) | \Psi_0 \rangle \quad (7.8)$$

For a field theory with imposed equal boundary conditions expressed through the state $|\Psi_0\rangle$ at a distance z between the boundaries, a so-called *boundary partition function* [70, 77] can be defined

$$Z(z) = \langle \Psi_0 | \exp(-z H) | \Psi_0 \rangle \quad (7.9)$$

which is identical to the Loschmidt amplitude for complex distances

$$z = it/\hbar \quad (7.10)$$

Even though the partition function at complex values bears no direct physical meaning, the extension into the complex parameter plane allows important insights into its behavior restricted to the real axis. From complex analysis it is known⁴ that any entire function, such as $Z(z)$ for a finite number of particles [70], can be fully expressed through a product of its zeros. This fact has been used by M. E. Fisher [162] to analyze the canonical partition function to describe phase transition as a function of temperature and analogously by Lee and Yang [86, 87] for phase transitions driven by a magnetic field. Therefore these zeros are also referred to *Fisher zeros* or *Lee-Yang zeros*.

A phase transition is typically signaled by a sudden change of some of the system's thermodynamic properties, as for example a jump from zero to finite magnetization. As all thermodynamic properties can be expressed in terms of the according thermodynamic potential, such a non-analytic behaviour is rooted in a nonanalyticity of the potential itself and is ultimately connected to the partition function. In the case of the free energy as the potential this relationship is given by [70]

$$f(z) = - \lim_{N \rightarrow \infty} 1/N \ln[Z(z)] \quad (7.11)$$

The logarithm in Eq. 7.11 will create a singularity in the complex plane causing nonanalytic behaviour for every Fisher zero in the partition function. Taking the thermodynamic limit, the Fisher zeros usually condense in the complex plane to lines [70], in the case of

⁴as the Weierstrass factorization theorem

one-dimensional system, or planes [79], in the case of two-dimensional systems. The intersections of those, with the real axis, marks the critical parameters at which phase transitions occur, as any singularity on the real axis induces a noncontinuous behaviour of the thermodynamic potential.

In the case of the DQPT, Fisher zeros appear in the domain of time, where the evolved many-body state becomes orthogonal to the initial state. In this analogy the role of the free energy is taken by the rate function [82]

$$g(t) = - \lim_{N \rightarrow \infty} 1/N \ln[\mathcal{L}(t)] \quad (7.12)$$

where $\mathcal{L}(t) = |\mathcal{G}(t)|$ is the *Loschmidt Echo*. Following the same argument, the rate function will show a non-analytic behaviour at critical times. Here however, the critical times are not identified by the intersection of the Fisher Zeros with the real axis, but with the imaginary axis, because within the analogy the parameters z and t are related through the proportionality factor of i (see Eq. 7.10).

In a system of noninteracting fermions, as it is considered in this thesis, a Fisher zero is encountered if any one of the single particle modes $|\psi_{\mathbf{q}}\rangle$ becomes orthogonal to its initial state. Here the full many-body state is given as a direct product at any given point of time

$$|\Psi(t)\rangle = \prod_{\mathbf{q}} \exp(-i/\hbar H(\mathbf{q})t) |\psi_{\mathbf{q}}(0)\rangle \quad (7.13)$$

and the Loschmidt amplitude equally decomposes into a product of partial Loschmidt amplitudes $g_{\mathbf{q}}$ as contributions of the individual modes \mathbf{q}

$$\mathcal{G}(t) = \prod_{\mathbf{q}} g_{\mathbf{q}}(t) \quad \text{with} \quad g_{\mathbf{q}}(t) = \langle \psi_{\mathbf{q}}(0) | \exp(-i/\hbar H(\mathbf{q})t) | \psi_{\mathbf{q}}(0) \rangle \quad (7.14)$$

so that the total Loschmidt amplitude becomes zero if a single term of the product is zero.

In the context of a two-band lattice Hamiltonian we identify the Fisher zeros with the previously described dynamical vortices: If for a specific quasimomentum mode \mathbf{q} the sublattice eigenstates, which are represented by the poles of the Bloch sphere, are given by $\{|A \mathbf{q}\rangle, |B \mathbf{q}\rangle\}$ and the initial state is, without loss of generality, chosen to be $|\psi_{\mathbf{q}}(0)\rangle = |A \mathbf{q}\rangle$, then the partial Loschmidt amplitude of the associated mode becomes zero if, and only if, the evolved state coincides with $|B \mathbf{q}\rangle$

$$g_{\mathbf{q}}^A(t) = \langle A \mathbf{q} | \psi_{\mathbf{q}}(t) \rangle \quad (7.15a)$$

$$g_{\mathbf{q}}^A(t_{\text{crit}}) = 0 \quad \iff \quad \psi_{\mathbf{q}}(t_{\text{crit}}) = |B \mathbf{q}\rangle \quad (7.15b)$$

which is identical to the conditions for a dynamical vortex as in Eq. 7.5a and 7.5b.

The description that has been established in the previous section for the dynamical vortices can be transferred to the field of complex phasors of the partial Loschmidt amplitudes, because it is almost identical to the phase distribution $\varphi_{\mathbf{q}}^S(t)$ of the quasimomentum eigenstates. Their relation is given by the following expression

$$\varphi_{\mathbf{q}}^S(t) = \arg(g_{\mathbf{q}}^A(t)) - \arg(\langle \mathbf{B} \mathbf{q} | \psi_{\mathbf{q}}(t) \rangle) \quad (7.16)$$

The second term in Eq. 7.16 contains merely the static phase of the Hamiltonian, that has also been neglected earlier, and the discussed π -phase jump at the initial pole, rooting from the sign of $\sin(\tau_{\mathbf{q}})$. Fig. 7.11 shows the phase profile of the partial Loschmidt amplitude, similar to the one in Fig. 7.3, and underlines the similarity between the two quantities. In

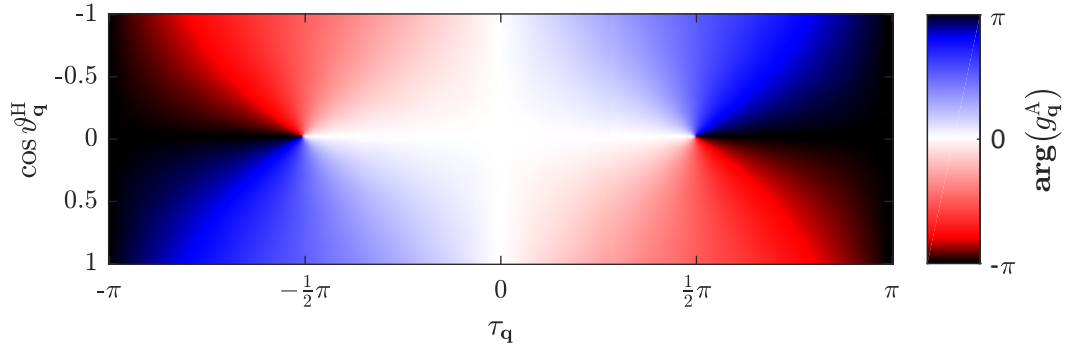


Figure 7.11: Phase of the partial Loschmidt amplitude for a quasimomentum mode \mathbf{q} . Similar to the phase of the wavefunction in fig. 7.3, there is a vortex in every π -period, but here the overall periodicity is changed from π to 2π .

summary, the observation of a dynamical vortex a necessary and sufficient condition for a dynamical quantum phase transition.

The location of the Fisher zeros $z_n(\mathbf{q})$ in the complex plane for a two-band model can be expressed [79] in a closed form by inverting the condition given in Eq. 7.15b for the real and imaginary part individually

$$z_n(\mathbf{q}) = \frac{i\pi\hbar}{R_{\mathbf{q}}} \left(n + \frac{1}{2} \right) - \frac{\hbar}{R_{\mathbf{q}}} \operatorname{arth} [\mathbf{h}_{\mathbf{I}} \cdot \mathbf{h}_{\mathbf{Q}}] \quad (7.17)$$

Here arth refers to the inverse hyperbolic tangent, which accounts for the complex argument of the inverse tangent ($\operatorname{arth} z = 1/i \operatorname{atan}(iz)$), and $\mathbf{h}_{\mathbf{I}}$ and $\mathbf{h}_{\mathbf{Q}}$ are the vector representations of the initial pre-quench and post-quench Hamiltonians, respectively. Including an arbitrary initial state $\mathbf{h}_{\mathbf{I}}$ makes this expression more general than the previously discussed situation with an initial state that occupies the same single particle state for all modes. The two situations can be brought into agreement by identifying

$$\mathbf{h}_{\mathbf{I}} \cdot \mathbf{h}_{\mathbf{Q}} = \cos \vartheta_{\mathbf{q}}^H \quad (7.18)$$

and interpreting $\vartheta_{\mathbf{q}}^H$ as the relative angle between the two Hamiltonians. This notion is by some authors [71, 84] also referred to as the *relative Bloch sphere*. The integer n in Eq. 7.17 indexes the period of the DQPT. In terms of the vortex map in Fig. 7.11, the left vortex corresponds to $n = -1$, the right to $n = 0$ and so forth.

In analogy to the study of Fischer zeros in the Haldane model in Ref. [79], here Fig. 7.12 shows the domain of Fisher zeros for a circularly shaken boron nitride lattice, as it has been realized in the experiments presented in this thesis. In contrast to the Haldane case, for the studied system there is no analytic model available and instead of plotting the density of Fisher zeros, the position of Fisher zeros is plotted for single particle modes in the Brillouin zone, that lie on a finite, rectangular grid of 800 by 800 states. Here only the zeroth order ($n = 0$ in Eq. 7.17) domain of the zeros is shown. Higher order domains have a related shape that results from a simple stretch along the imaginary axis.

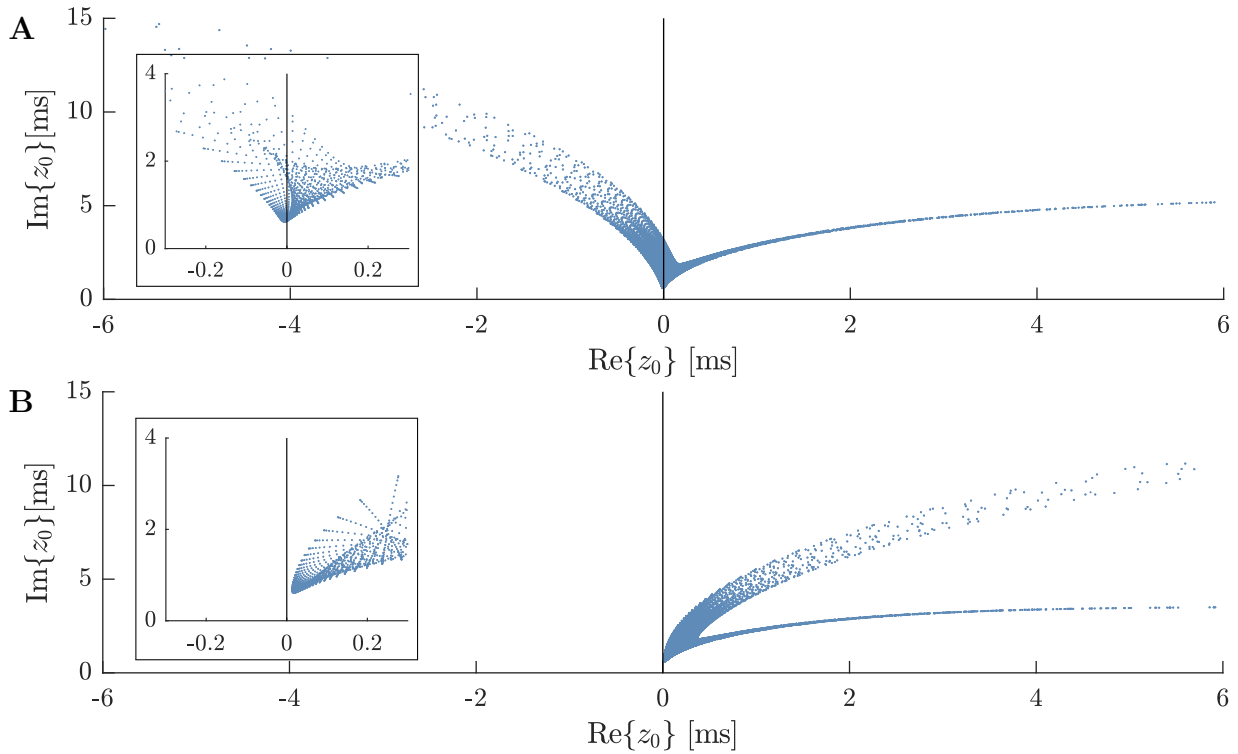


Figure 7.12: Fisher Zeros in the complex plane for a circularly shaken boron nitride lattice. Subfigure **A** shows the zeros due to a topologically nontrivial Hamiltonian at a shaking frequency of 11.85 kHz that exposes a DQPT and subfigure **B** shows the trivial case at 11.9 kHz. The insets show a magnification of the region of interest around the imaginary axis and clarify that only in subfigure **A** the FZs cross the imaginary axis.

The system chosen for the simulation corresponds to the one presented in the previous chapter, of a lattice stemming from beams with equal polarization mixing angles of $\theta_p = 9^\circ$, a depth of $V_L = 15.363 E_{\text{Rec}}$ that is circularly shaken with modulation depth of 2 kHz at

frequencies of 11.85 kHz (subfigure A) and 11.9 kHz (subfigure B). Despite the the small difference of 50 Hz, i.e. under half a percent of the shaking frequency, the Fisher zeros distributions of the two subfigures are completely distinct. The reason for this behaviour roots in the intimate connection between DQPTs and the topology of the underlying system, as it has been discussed in Sec. 7.2. In the inset of subfigure B, it can be seen that the Fisher zeros approach the imaginary axis without touching it, while in subfigure A the domain of the Fisher zeros fills a dense area that is intersected by the imaginary axis which marks the critical times for the creation and annihilation of the dynamical vortices at its edges.

At those edges, as mentioned earlier, the rate function is expected to acquire a discontinuity. While for a one-dimensional system, the existence of a kink in the rate function, due to the intersection of a line of Fisher zeros with the imaginary axis at a single point is trivially clear, the analog case for a two dimensional domain, where, in the thermodynamic limit, there are infinitely many densely packed FZs within a region of the imaginary axis, is more complicated. For this case *Vajna et al.* [79], deduce a jump Δg^s of the second derivative of the rate function

$$\Delta g^s = -2\pi D \cos^2(\phi) \quad (7.19)$$

that is dependent on the jump of the normalized density of zeros D and the angle of intersection ϕ . From the shape of the Fisher area in Fig. 7.12-A it can be concluded that the kinks are expected to be less pronounced compared to the ones present in the Haldane model where, the Fisher area intersects almost vertically with the imaginary axis [79]. The density distribution in 7.12-A also indicates a stronger first kink. Furthermore Eq. 7.19 allows to deduce that the signs of a pair of kinks are always opposing each other.

Based on the numerical simulation of the system studied here, we calculated the derivative the singular part of the rate function g^s as defined in Ref. [70]. The attribute *singular* refers to the Weierstrass factorization that establishes the relationship between the zeros and the rate function, by allowing to express the partition function in terms of the zeros z_j and a entire function $h(z)$

$$Z(z) = \exp(h(z)) \prod_j \left(1 - \frac{z}{z_j}\right) \quad (7.20)$$

The singular part of the rate function is obtained by setting $h(z) = 0$, and since it contains all singularities, it is sufficient to be considered here.

Fig. 7.13 visualizes $\frac{dg^s}{dt}$ for a system with identical parameters as the one shown in Fig. 7.12-A.

In agreement with the previous qualitative considerations, the simulation exposes the expected kinks with the expected signs and strengths at the critical times. At close examination of Fig. 7.13 one may discover that the plotted function actually exposes

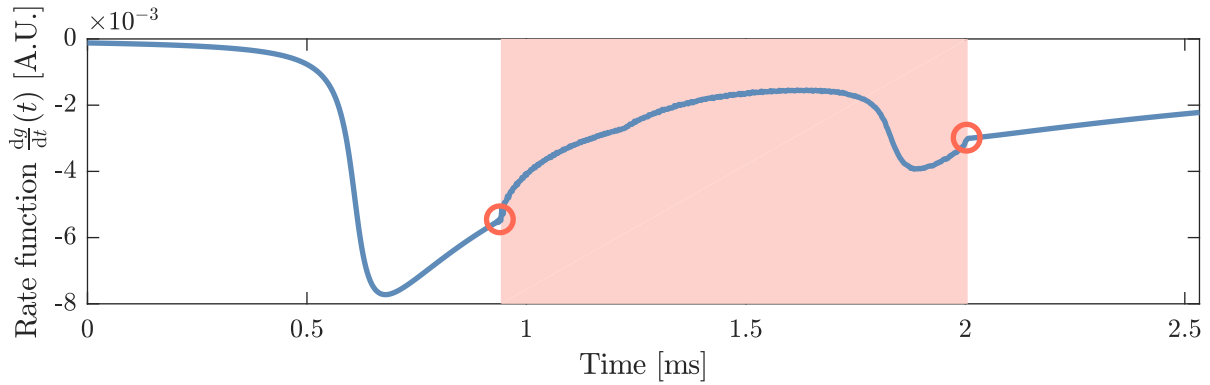


Figure 7.13: First derivative of the singular part of the rate function. The red circles mark the expected kinks stemming from the second order nonanalyticity at the critical times, where the density of FZs on the imaginary axis jumps to a finite value. The kinks frame the range of time during which a DQPT is present in the system, here marked with a red background. Adapted from our publication [89].

many densely packed small kinks during the range of time where DQPTs are present (red background), while outside of that region it is perfectly smooth. Those kinks are numerical artifacts that stem from the finite grid spacing in quasimomentum space of the eigenstates, that have been considered in the simulation. For Fig. 7.13 we chose a grid of 1200 by 1200 modes, so that the kinks at the edges can be clearly distinguished from the artifacts. The reduction of the grid spacing also corresponds to taking the thermodynamic limit, so that for a real system in parallel to the simulated case the impact of the phase transition is expected to become physical for finite systems of a corresponding size.

Comparing the location of the critical times in Fig. 7.13 with the ones in 7.12-**A** a slight mismatch can be discovered. The reason for this mismatch is the slightly broken discrete rotational symmetry of the system, due to the initial phase of the shaking. In that system the vortices in the three regions do not appear at the same time. In Fig. 7.13 one of those regions has been isolated, while in Fig. 7.12-**A** the FZs for the full BZ are shown. If one were to include the full BZ further kinks would show up in Fig. 7.13.

7.4 Connection to the Pancharatnam Geometric Phase

The dynamics of a two-band Hamiltonian, as presented in this chapter, can also be put into context [84] of the so-called Pancharatnam geometric phase, which has been introduced in Sec. 4.1. As a generalization of the Berry phase, the Pancharatnam phase allows to establish a phase relation between the evolved state $|\psi_{\mathbf{q}}(t)\rangle$ and the initial state $|\psi_{\mathbf{q}}(0)\rangle$ that purely depends on the path that the state has taken through the (projective) Hilbert space under time evolution. As a reminder it shall be mentioned that for the state $|\psi_{\mathbf{q}}(t)\rangle$ a Berry phase cannot be defined, because firstly, it is most likely a nonequilibrium state of the system

and secondly, its trajectory is generally not closed. While the Berry phase characterizes the Hamiltonian (through its eigenstate) the Pancharatnam phase is a property of the evolved state. For present case of quench induced dynamics, however, these two quantities are tightly connected, because the Hamiltonian does not vary with time and is (up to sign) uniquely defined by the trajectory of a state. By inserting Eq. 4.2 into Eq. 4.1 for the two-level system under discussion, one obtains an analytic expression of the Pancharatnam phase γ_P :

$$\gamma_P(\mathbf{q}, \tau_{\mathbf{q}}) = \arg(g^A(\mathbf{q})) - \underbrace{\tau_{\mathbf{q}} \cos \vartheta_{\mathbf{q}}^H}_{\delta_{\text{dyn}}} \quad (7.21)$$

Because of the trivial, monotonic contribution of the dynamical phase, the Pancharatnam phase exposes the same singularities as discussed in detail throughout this chapter for the partial Loschmidt amplitudes and the polar phase of the evolved state itself. To illustrate this consider the modified map shown in Fig. 7.14 corresponding to the ones from Fig. 7.3 and Fig. 7.11.

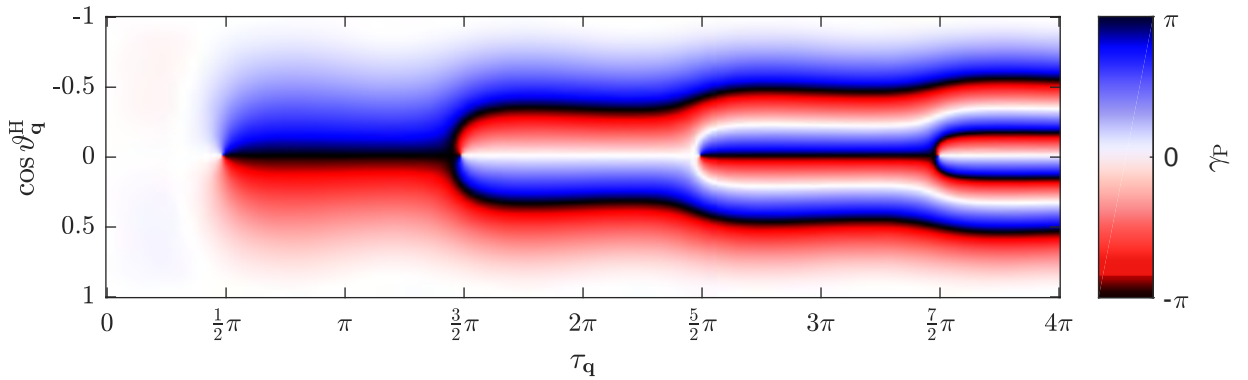


Figure 7.14: The Pancharatnam phase for a quasimomentum mode \mathbf{q} . Similar to the phase of the wave function in Fig. 7.3 and the phase of the partial Loschmidt amplitudes in Fig. 7.11, there is a vortex in every π -period. Despite the more quickly oscillating phase, all vortices have the same overall phase winding (n of one handedness on the left and $n + 1$ of the opposite handedness on the right).

In this figure the vortices become visible as the typical branching points. The condition for the vortices and their phase winding stays clearly unchanged.

8 Experimental Observation of Dynamical Vortices in a Topological Bloch Band

This chapter reports on the experimental observation of the creation, evolution and annihilation of dynamical vortices in a Haldane like model, that is realized by near resonant circular shaking of a boron nitride lattice. We interpret the number of dynamical vortices as an order parameter and compare the system with the theoretically expected phase diagram. The measurements presented here, contribute to the understanding to the young field of dynamical phase transitions (DPTs) [70]. Shortly after the preprint publication of the results [89], other groups reported [90–92] on the observation of DPTs. The results presented in this chapter have also been published as an article [64] and the figures are adapted from this publication. The experiment has been realized as part of this thesis in a team effort together with my colleagues Nick Fläschner, Benno Rem, and Matthias Tarnowski under the supervision of Christof Weitenberg and Klaus Sengstock. My principal contributions are centered around the interpretation, the simulation and the data analysis.

8.1 Experimental Scheme

The experimental scheme, we followed to observe dynamical vortices, is based on the complete state tomography presented in Chap. 5. The system and the preparation thereof are very similar to the those of the experiment presented in Chap. 6. In detail this means that we start by preparing a sample of $1 \cdot 10^5$ ultracold, spin polarized ($F = 9/2, m_F = 9/2$) ^{40}K (Sec. 2.1) atoms and load it into a boron nitride lattice with a polarization mixing angle of $\vartheta = 9^\circ$ (Sec. 3.2.3), by adiabatically ramping up the lattice beams (Sec. 2.2) to a final lattice depth between $V_L = 14.07 E_{\text{Rec}}$ and $V_L = 14.90 E_{\text{Rec}}$. This regime has been chosen such that topologically trivial and also potentially nontrivial Floquet Hamiltonians are produced in the shaken system, for a fixed shaking frequency. It is furthermore important to note, that for the given particle number, the atomic ensemble fills the lowest band of the band structure throughout this region of lattice depths. For the following it is convenient to specify the final lattice depth in terms of the parameters of the tight-binding approximation (Sec. 3.4.4) of the lowest two bands of the associated band structure. Here, the lattice depth range corresponds to a sublattice offset energy (divided by the Plank constant h) Δ/h between 10750 Hz and 11460 Hz, a inter-sublattice tunnel amplitude t_{AB}/h between

256 Hz and 280 Hz, an A-sublattice tunnel amplitude t_{AA}/h between 33 Hz and 38 Hz, and a negligible small B-sublattice tunnel amplitude. Again, the sublattice energy offset is the dominating parameter and we assume the flat band approximation (Sec. 5.2). At the relevant lattice depths the tight-binding parameters can be considered proportional to the lattice depth (see Fig. 8.1). Experimentally the lattice depth is extracted from the tomography data, as will be explained at the end of this section.

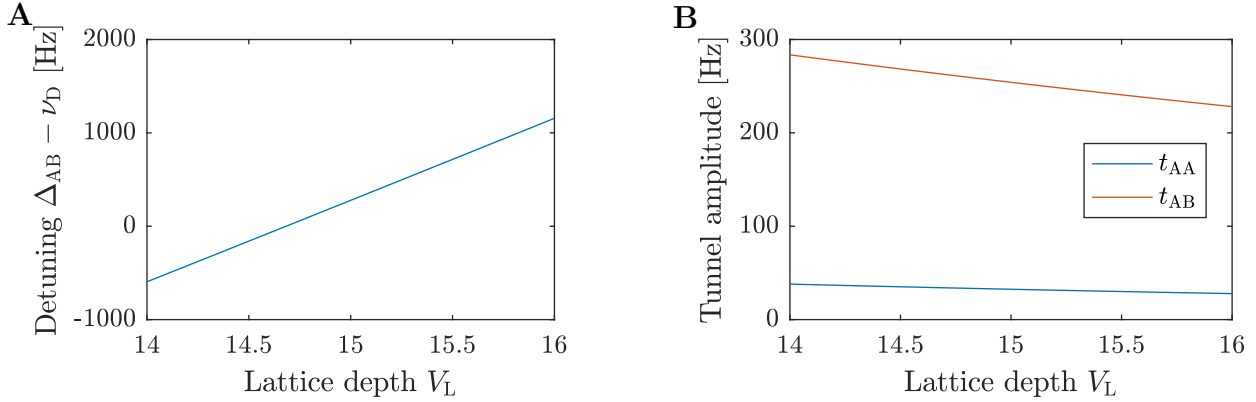


Figure 8.1: Tight-binding lattice parameters as a function of the lattice depth. Subfig. A shows the sublattice energy offset as a detuning, i.e. relative to a the shaking frequency, which is here chosen to be 1.65 kHz. Subfig. B shows the corresponding tunnel amplitudes t_{AB} and t_{AA} . t_{BB} is not shown as it is vanishingly small.

The experimental scheme is depicted in Fig. 8.2. The upper half shows the change of the shaking amplitude and the lattice depth and in the lower half the associated evolution of an arbitrary single particle in the quasimomentum basis of the unshaken lattice is displayed on the Bloch sphere. The sequence can be divided into four phases. First the aforementioned state-preparation phase (i), second the state-evolution phase in the shaken system (ii), followed by the spectroscopy evolution phase (iii) and finally the time of flight phase.

After the state preparation phase, instead of adiabatically launching the prepared state into a shaken system, as it was performed (Chap. 6) for measuring the Berry curvature, it is quenched into the Floquet system by abruptly starting the shaking of the lattice. Due to this quench, the state ceases to be an eigenstate of the system, and a nontrivial evolution under the influence of the Floquet-Hamiltonian begins. This evolution time is denoted here as t . As before, the quasimomentum remains a good quantum number and the evolution can be described individually for every quasimomentum mode. In the flat band limit, all modes start out in the lower sublattice eigenstate, which is represented here by the south pole of the Bloch sphere. The evolution under the influence of an arbitrary Hamiltonian (black arrow) of a quasimomentum mode is indicated as red small circle in Subfig.(ii). The subsequent state tomography is conducted as before, with the only difference, that

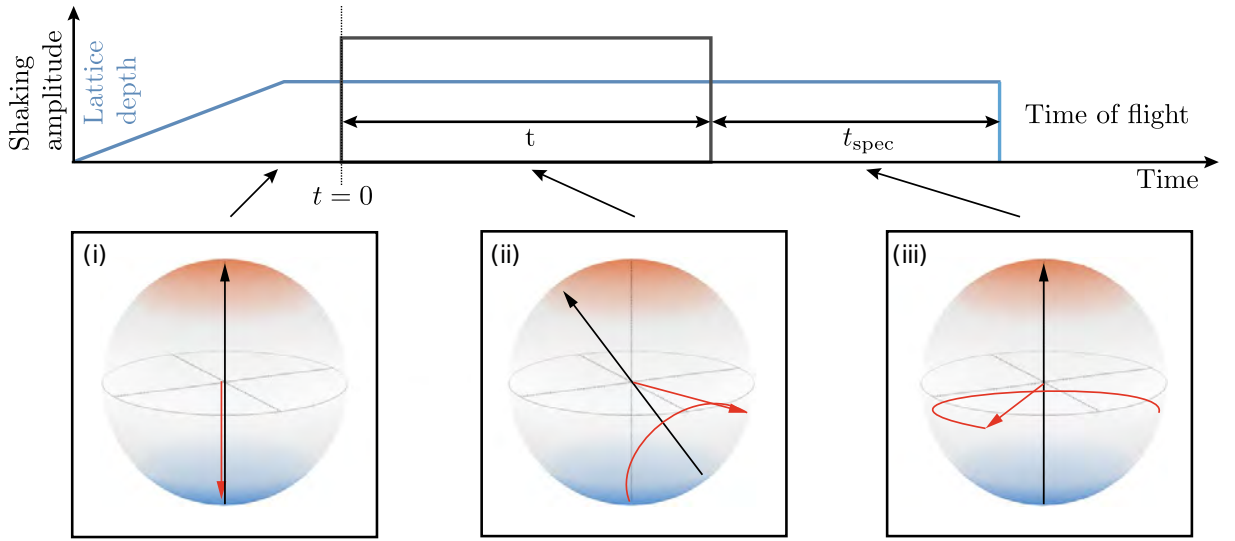


Figure 8.2: Experimental sequence. The upper row shows schematically how the shaking amplitude and the lattice depth are varied over time. The lower row indicates the Hamiltonian (black arrow) and the nonequilibrium state (red arrow) for a single quasimomentum on the Bloch sphere. Adapted from our publication [64].

the state being reconstructed is not an eigenstate of the shaken system. This difference is, however, insignificant for the tomography procedure. After an evolution time t in the shaken system, another quench takes place, this time into the static flat band Hamiltonian, which leads to an evolution that can be described by a rotation around the horizontal axis on the Bloch sphere (iii). After a time t_{spec} in the static system, all potentials are turned off for letting the cloud expand freely and being imaged after a the TOF phase. An exemplary TOF image for a chosen pair of times (t, t_{spec}) is shown in Fig. 8.3 (right), together with the tomography time series (left) at a specific pixel for two selected times t .

For each tomography a series of 32 images with a temporal resolution of $5.5 \mu\text{s}$ were taken. Each image was convoluted with a $5 \text{ px} \times 5 \text{ px}$ Gaussian kernel with a spread of 5 px. Here no Savitzky-Golay was applied. The scaling is $58(2) \text{ px}$. To extract the phases characterizing the state the same fit-routine was applied as described in Sec. 6.2.

While for determining the Berry curvature a single static, effective Hamiltonian was the object of the tomography, here the focus lies on the nonequilibrium dynamics of the state, which means that for every time step of its evolution, a complete tomography sequence had to be conducted. We measured the state for 10 sequential time steps at stroboscopic times for the chosen shaking frequency.

To obtain the lattice depth for the following measurements, it is insufficient to purely measure the light powers of the lattice beams and deduce the intensity, because for the required relative precision over the measured parameter range (compare Fig. 8.1) this method is prone to many sources of significant errors like partial reflections on the glass

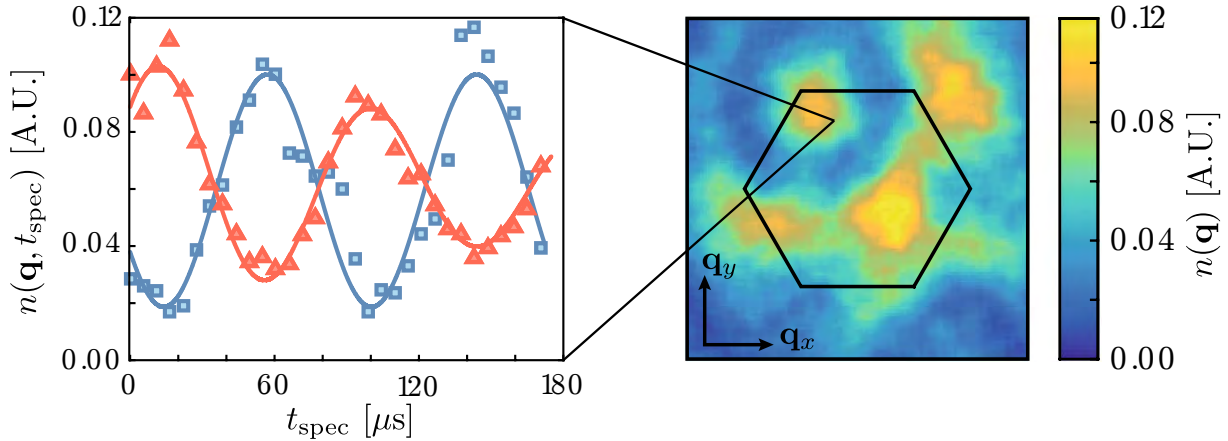


Figure 8.3: Atomic density evolutions during the complete state tomography for different quench times. The left plot shows the atomic density oscillations for two different quench times $t = 0.267$ ms (blue/rectangles) and $t = 0.801$ ms (red/triangles) with their respective fitted model (solid line) of a damped sine (see Chap. 5). The x-axis is given by the time t_{spec} of free expansion of the cloud and the y-axis by the atomic density in an absorption image given by the quasimomentum bin defined by the pixel marked in the picture on the right (for filtering see text below). The right pane shows a typical absorption image for a pair (t, t_{spec}) . Adapted from our publication [64].

cell, the propagation of the error in the determined beam waist, imperfections in the mode profile, and a possible slight misalignment of the beam intersection centers. Instead we perform a band spectroscopy via amplitude modulation for each of the three pairs of beams to calibrate the relative intensities of the beams to be equal. For the absolute value of the lattice depth, we average the momentum resolved oscillation frequencies extracted from the previously acquired state tomography data and compare those values to our model. For a more detailed description the reader is referred to the *sup. mat.* of Ref. [89].

8.2 Results

Bloch Sphere Representation

As a result we reconstruct the dynamics of the quasimomentum resolved state. For three chosen time steps, the state is depicted in Fig. 8.4 as a point cloud on the Bloch sphere. Here every point corresponds to a quasimomentum mode. In this form of visualization it can be seen how the three *wings* of the momentum mode, belonging to the initial three uniform phase regions of the BZ, start reaching around the Bloch sphere until they finally meet the south pole, where as discussed in the previous chapter a vortex pair is created by each wing. The point clouds shown here have been scaled to reach the maximum amplitude (i.e. equator). The reason for the necessity of this scaling is that the oscillations show a dephasing, probably due to the gaussian envelope of the lattice potential, which reduces the apparent amplitude. The dynamical vortices, however, are more insensitive to this

mechanism, as they are an exclusive feature of the phase of the oscillation.

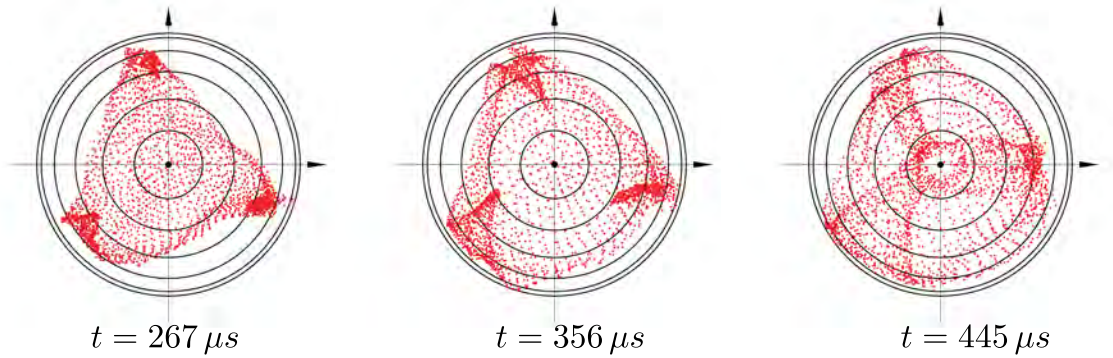


Figure 8.4: Top view on the Bloch sphere representation of a nonequilibrium state for different evolution times t . Every red dot represents a quasimomentum component of the state. The amplitudes have been scaled to compensate for dephasing by 14%, 21%, and 28%. Adapted from our publication [64].

Phase Profiles

The vortices are not visible in the Bloch sphere representation. Therefore we consider the phase evolution as shown in Fig. 8.5. For ten stroboscopic steps at times $t = (n + 2) \times 89 \mu\text{s}$ ¹. The images (I) and (II) are, as expected, reminiscent of the phase profile data shown

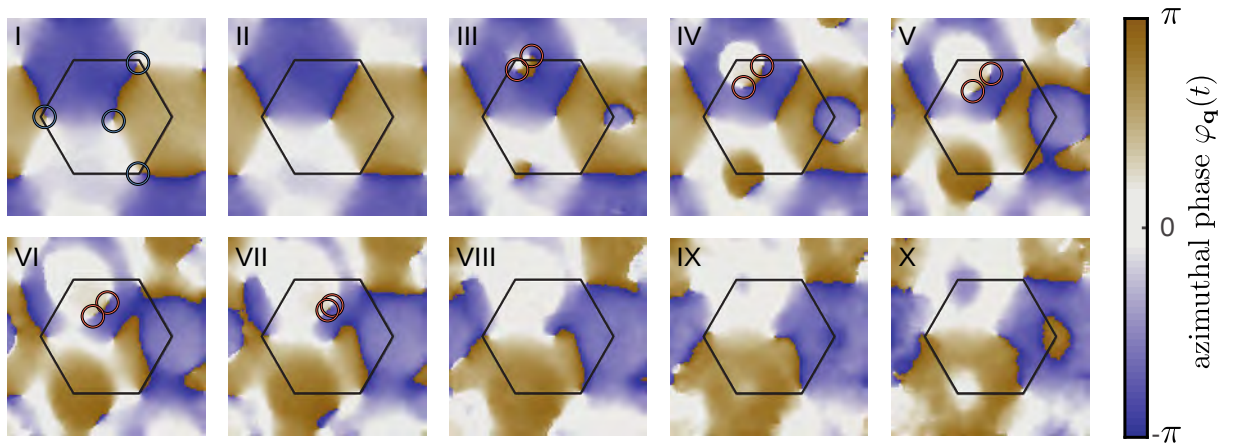


Figure 8.5: Phase profile $\varphi_{\mathbf{q}}^{\text{S}}(t)$ for stroboscopic evolution times $t = (n + 2) \times 89 \mu\text{s}$, where n is the index of the image. The hexagon indicates the BZ and the circles in the first image mark the static vortices. The circles in the later images mark the dynamical vortices. Adapted from our publication [89].

in Chap. 6 that have been used for determining the Berry curvature. At the third step, however, ring-structures appear around the K-points of the BZ. The ring-structures are

¹The first two steps have been omitted as they resemble (I), i.e. with no dynamical structure.

coined by their sharp edges of strong gradients, bridging two regions with values about π apart, as it is expected for states in the vicinity of the south pole. For most parameter regimes these features do not expose any vortices, since the state passes in close proximity of the south pole without actually transversing it. For the chosen data set the south pole is clearly reached for one of the branches. Here a pair of phase vortices appears on the line separating the two regions of nearly constant phase. Fig. 8.6 shows an enlargement of the fourth time step. Here it is clearly visible that there is one point on the phase front (three o'clock) where, when drawing a circle around it, the phase varies from 0 (white) over $-1/2\pi$ (light purple) and $1/2\pi$ (golden) back to zero and thereby constitutes a right handed vortex. Further along the vortex front (at six o'clock) the situation is reversed and a left handed vortex is encountered. As the phase front grows in the next steps in

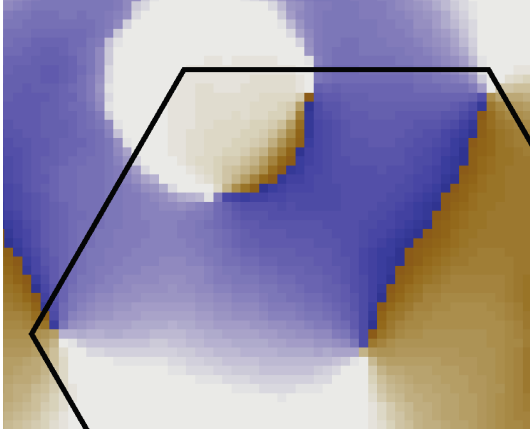


Figure 8.6: Zoom into the phase profile at $t = 365 \mu\text{s}$, also shown in Fig. 8.5-IV of Fig. 8.5. The two dynamical vortices with opposed chiralities are clearly visible. The color scale is equal to Fig. 8.5.

Fig. 8.5, the vortices move further along it until they finally meet in time step (VII) and are annihilated in step (VIII). In the last time step the appearance of another phase front is visible. This is in full agreement with the simulations presented in the previous chapter, according to which this next phase front corresponds to the completion of a full oscillation cycle of the corresponding quasimomentum mode where the Bloch vector representing the state revisits the south pole. In the experimental data the expected π -phase-jump is not fully pronounced, which is most likely due to the not fully fulfilled approximation of flat bands, i.e. the remaining spread of the initial state and tomography Hamiltonian around the poles, but also in part due to diminishing signal amplitude for longer evolution times, as will be discussed in the following.

Amplitude Profiles

The state tomography also reveals the distribution of the polar angle $\vartheta_{\mathbf{q}}^{\text{S}}$ in form of its sine: $\sin \vartheta_{\mathbf{q}}^{\text{S}}$. This data is shown in Fig. 8.7 for the same data set and in correspondence to Fig. 8.5.

Here, as expected, the vortices appear as zeros. Both, static vortices, corresponding to the north pole ($\vartheta_{\mathbf{q}}^{\text{S}} = \pi$), and dynamical vortices, corresponding to the south pole ($\vartheta_{\mathbf{q}}^{\text{S}} = 0$),

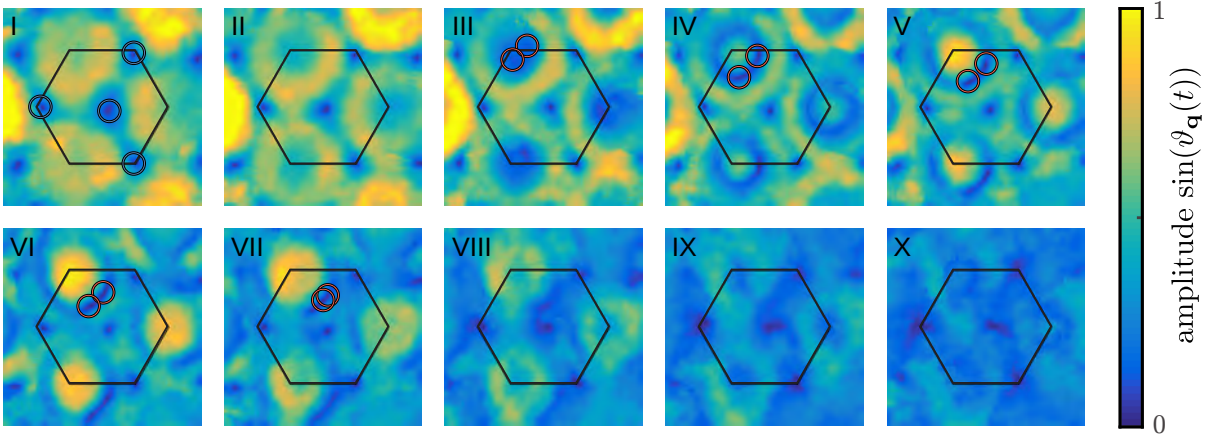


Figure 8.7: Amplitude profile $\sin \vartheta_{\mathbf{q}}^{\text{S}}(t)$ for the matching data set and times as of Fig. 8.5. The circles again mark the static and dynamical vortices. Adapted from our publication [64].

are associated with a zero amplitude ($\sin \vartheta_{\mathbf{q}}^{\text{S}} = 0$). In Fig. 8.7 the vortices are marked, as before, with circles. While the vortices are clearly visible for most time steps as local minima, it is generally more difficult to uniquely identify the vortices, because the signal is less pronounced and further minima seem to exist, that are not associated with vortices. In time step III for example, the minima of the dynamic vortices can barely be identified. In time step IV to VII those minima are clearly visible, but their position along the groove associated with the phase front is not very well defined. In the following steps VIII to X local minima can still be found, even in the absence of vortices. Fig. 8.7 also shows how the maximum amplitudes decay further and further with every time step, even though they are expected to stay constant at a value of one. This decay is potentially caused by a dephasing due to heating the sample while periodically shaking it or due to fact that, opposed to the assumed model, in the experiment the factual lattice depth varies spatially with the gaussian profile of the lattice beams.

Vorticity

To extract the vortex positions in an automated way, free of human bias, we determine a quantity we denote by *vorticity*. We define the vorticity as the curl of the gradient of the phase profile. From electrodynamics it is well known that the curl of the gradient of a scalar field, such as the phase profile, is an identity with zero. Here, however, this identity does not apply, because the phase is only defined modulo 2π . Formally we define the vorticity of a phase field as

$$v(\mathbf{q}, t) = \frac{1}{\pi} \nabla \times [\text{mod}(\nabla \cdot \varphi_{\mathbf{q}}^{\text{S}} + \pi, 2\pi) - \pi] \quad (8.1)$$

Here the modulo operator is understood as acting element-wise on its two-vector argument, and both instances of π are also added and subtracted element-wise.

The vorticity of a right handed vortex will therefore yield a charge of plus one and for a left handed vortex a charge of minus one. Everywhere else the vorticity yields zero. We numerically calculate the vorticity for the data on $\varphi_{\mathbf{q}}^S(t)$ by approximating the gradient in Eq. 8.1 through the finite symmetric difference between neighboring pixels, i.e. the average of the left and right/top and bottom differences. This effectively corresponds to a convolution with a discrete kernel and every vortex yields thereby a finite vorticity in a region of four pixels containing the vortex. The vorticity proves itself as a reliable local quantity for identifying phase vortices. Fig. 8.8 shows the total vorticity, i.e. the sum

$$v_{\text{tot}} = \sum_i v(\mathbf{q}, t_i) \tag{8.2}$$

over the time steps of the data set shown previously in Fig. 8.5 and 8.7. Here one can

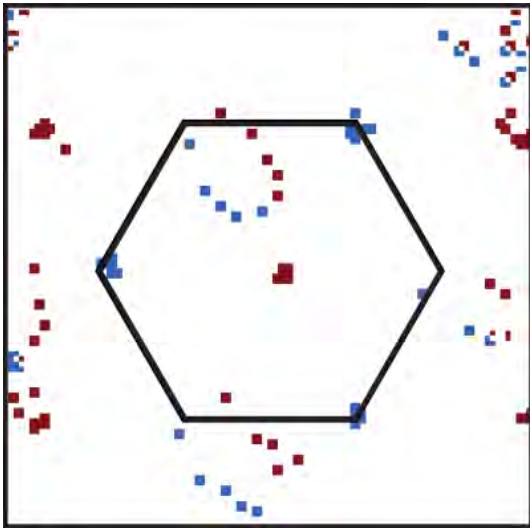


Figure 8.8: Vorticity extracted from the phase profiles and summed over all time steps in Fig. 8.5. The color scale is truncated to the vorticity of a single vortex. In the center (Γ - point) and in three of the corners (K-points) the static vortices appear as clusters, due to a slight noise on imaging method, leading to small offsets in quasimomentum space. In this particular data set the three-fold symmetry is disturbed such that only one vortex pair is created within the BZ. Please note, that below the first BZ another copy of the vortex pair is visible. Adapted from our publication [64].

clearly see the two static vortices with opposed handedness at the K and Γ points. It is also visible that the system seems to be slightly perturbed, which leads to small deviations of their positions for different time steps. The dynamical vortices trace out a curve, that, when linearly interpolated, forms a closed trajectory². This trajectory shows how a vortex-anti-vortex-pair is created, moves through the BZ and finally annihilates.

Vortices as an Order Parameter

One of the main results of the previous chapter, was the introduction of the dynamical vortex pair count as a discrete order parameter for a dynamical phase transition. The number of vortices for the presented data set is visualized in Fig. 8.9. It indeed behaves as

²The total vorticity is chosen as a quantity of convenience. The vorticities of the individual time steps confirm that the trajectory is indeed traced out in the right order, with one vortex pair per time step that also corresponds to the intuitive interpretation of the phase profile images.

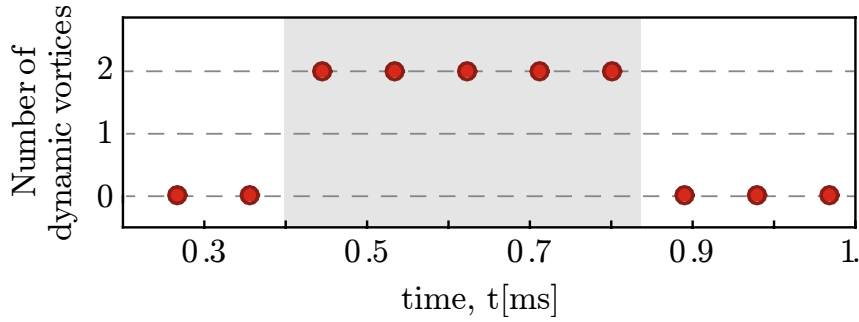


Figure 8.9: Number of vortices as a function of the time step. The vortices can be interpreted as an order parameter for a DPT. The gray square marks the occurrence of the DPT. Adapted from our publication [163].

expected by jumping from 0 to 2 and thereby marking a region of critical times where a dynamical phase transition is occurring. For longer times the appearance of multiple simultaneous vortex pairs is expected.

Connection to Topology

In order to relate the observed dynamical vortices to the topology of the quenched Hamiltonian, we recorded a series of measurements at different lattice depths. Fig. 8.10-A, shows the occurrence of dynamical vortices as a function of the evolution time in the quenched system and the detuning between the fixed driving frequency and the frequency associated to the energy offset between the A and B sublattice states, which is effectively varied through the different lattice depths. In contrast to the previously presented data, this data set has not been taken at a modulation depth of 2 kHz but 1.65 kHz. Fig. 8.10-B shows a simulated phase diagram of the Chern index as a function of the shaking modulation depth and the detuning. The bar at 1.65 kHz represents the data set from Fig. 8.10-A, where the gray shaded area again marks the detunings for which dynamical vortices are created during the time of observation. From the phase diagram it is clearly visible, that the region of dynamical vortices does not exactly coincide with the topological phase transition. Dynamical vortices were however exclusively observed in the close vicinity of the topologically nontrivial regions.

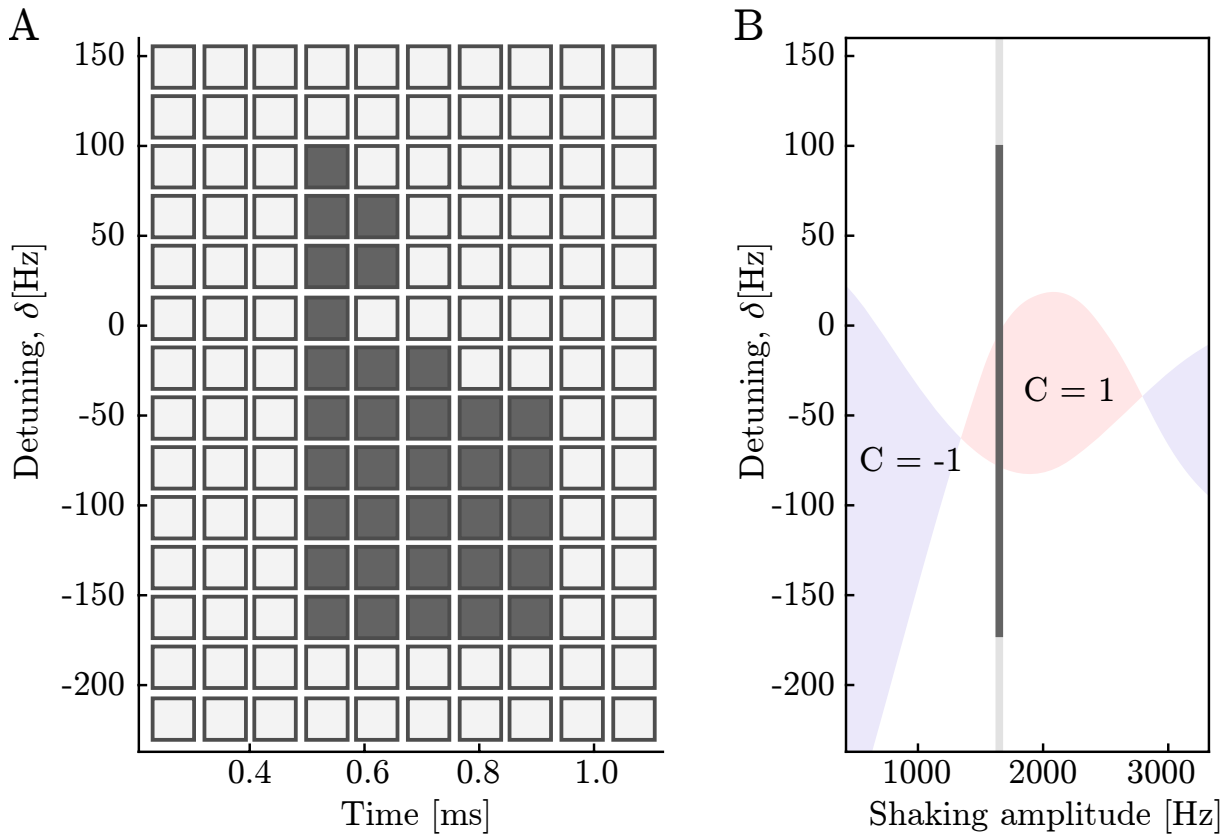


Figure 8.10: Critical regions and topology. Subfigure A marks the presence (gray squares) of dynamical vortices at different times steps for measurement series at 14 different lattice depths. Subfigure B shows a simulated phase diagram of the considered system in terms of the shaking amplitude and detuning. There are topologically trivial regions (white) and regions with Chern index -1 (blue) and 1 (red). The light gray bar marks the region at 1.65 kHz which has been probed and is shown in Subfig. A. The dark gray region marks the range of detuning for which we observed dynamical vortices. Adapted from our publication [64].

8.3 Interpretation and Outlook

The data shown in this chapter shows clearly the creation, movement and annihilation of dynamical vortices. In its character, it is in full agreement with the simulations presented earlier in Chap. 7 and thereby poses an observation of a dynamical phase transition, which we experimentally characterized by the number of vortex pairs as a discrete order parameter that changes with time. The shape of the trajectory traced out by the vortices, however, does not correspond to the trace expected from numerical simulations, and we were not able to observe a trace that encloses one of the Dirac points in order to characterize the system as topologically nontrivial. Nevertheless, the parameter regime in which dynamical vortices have generally been observed, covers and only slightly extends the expected domain of the topological phase. The appearance of dynamical vortices for

quenches between Hamiltonians of equal Chern indices, so-called *accidental* vortices, is indeed expected for general systems [79]. Inspired by our publication, the relationship between topology and the appearance of dynamical vortices has been studied in detail in Refs. [66, 67], and it has been shown that without regarding the trajectory of the vortices, the mere appearance is only a sufficient indicator for a topological phase transition, if the initial state corresponds to an eigenstate of a Hamiltonian with flat bands, as it was also assumed in our simulations. In the real experimental system this condition cannot be perfectly met (see also Sec. 5.2), which explains the observation of the accidental vortices.

A plausible explanation for the mismatch of the observed and simulated trajectories can be found when considering the difficulty we experienced when trying to tune the parameters into a regime with dynamical vortices. Our simulations have shown, that in proximity to the topological phase transition, the shape of the vortex trajectory is highly sensitive to most system parameters. On traversal of the topological phase, through varying the lattice depth V_L by less than 1%, the trajectory emerges from one Dirac point, travels through the full BZ and finally vanishes enclosing the other Dirac point.

While in the simulation a perfectly homogeneous lattice potential was used, the real lattice potential has a Gaussian envelope in real space, which means that the observed atomic densities, that form the basis for the extracted phase profiles, should rather be modeled by a superposition of a continuous spectrum of lattice depths. In a follow-up experiment [65] at the same setup, this shortcoming has been overcome by reducing the lattice depth and thereby creating a larger topological regime, where the observed traces clearly form a closed loop around one of the Dirac points.

The experiment (Chap. 8) and conceptual work presented here (Chap. 7) pave the way towards a deeper understanding of the interplay of topological systems with nonequilibrium dynamics. In particular the description of nonequilibrium dynamics from the relatively recent perspective of dynamical phase transitions has the potential to deepen our understanding by further developing the analogy to equilibrium phase transitions. Since our initial publication [89], further groups reported [90–92] on the observation of dynamical phase transition. While the system presented in this work is comprised of noninteracting fermions it lays out the basis for further research to gain understanding of the connection between the nonequilibrium dynamics of two dimensional, interacting many body systems and their topology.

9 Development of a Digital Fiber Phase Lock

This chapter reports on the conception, implementation and performance of a new experimental fiber lock setup, that effectively suppresses optical phase noise induced by the spurious mechanical coupling of a fiber to its environment. Among countless application fields, this setup is specifically relevant in the context of this work, because here fiber phase noise affects the beams forming the optical lattice potential and thereby causes detrimental heating of the atomic quantum states under analysis.

In the presented setup, fiber noise is compensated for by an *optical phase-locked loop* (OPLL). A negative feedback control system imparts a compensating phase shift to the beam on the local end via an acousto-optic modulator, while an error signal, representing the double transit phase shift, is obtained via a local end heterodyne measurement of a reflex from the flat remote fiber end. The setup sets itself apart from conventional OPLL setups by employing a fully digital feedback loop that with a *direct digital synthesis* (DDS) *radio frequency* (RF) source. DDS signals feature intrinsically low phase noise and the possibility to control the phase rather than frequencies eliminates the need for relocking. Compared to previous setups, this setup enables the use of *polarization maintaining* (PM) fibers, the error signal offers a more favorable dependence on light power improving the performance for ramps and the number of required optical components is reduced.

The adaptability, comfort and automation potential of digital control loops been fully exploited by a software design that features scripting and programmatic real-time in loop control of all parameters via a flexible network interface. The feedback loop operates at a loop repetition rate of 772 kHz with a total signal loop delay of 1355 ns. It reaches a suppression of up to 30 dB of the phase noise power spectrum of a 20 m fiber.

Over the course of the past decades, optical fibers have become a key technology for many technical applications as well as for most modern research apparatus that involve optical radiation. In general optical fibers can transport a signal coherently over long distances at low loss rates. In ultracold atom experiments for example, optical fibers are commonly used, among many other applications, to decouple functional groups of components of a setup as e.g. here the lattice laser table from the main experiment. Despite the tremendous advantages over free air propagation, optical fibers can not be considered as an ideal transmitter, that outputs a signal identical to the coupled input signal at the remote location. Apart from obvious nonlinear dispersion effects, there are further changes to the signal spectrum: optical fibers couple mechanical noise and thermal drifts in their environment to the optical phase of the guided light, leading to extraneous

phase modulation of the transmitted signal spectrum. This effect roots in the fact that the refractive indices of the fiber waveguide will generally expose a small, but non-vanishing, dependence on temperature and mechanical stress. Over the full length of a fiber these add up to a significant and time varying optical path length difference.

Unavoidably most optics laboratories are however highly mechanically polluted by an orchestra of e.g. vibrating fans in power supplies and compressors in air dehumidifiers. Even normal speech can cause phase shifts of several radians [164, 165].

For vast range of modern experiments the associated phase shift can be disruptive. In metrology for example, where optical frequency standards have long outperformed the classical microwave standards, an unperturbed transmission of optical clock signals is essential, for instance to detect a possible drift of fundamental constants by comparing two distant optical clocks based on different atomic isotopes [166].

Another example are ultracold atoms trapped in optical lattices. Here changes of the relative phases between the lattice beams can cause a translation of the lattice potential (see Sec. 3.2), or even to change its fundamental structure [167]. Thus stochastic phase shifts become detrimental by causing undefined lattice structures, heating or, in case of pinning lattices [168, 169] for single site resolved fluorescence imaging, washed out exposures.

Given this tremendous impact of fiber induced phase noise, it is not surprising that a variety of solutions have been developed [101, 164, 166, 167, 170–173]. These can be categorized into passive and active solutions.

Passive solutions reduce the optical phase noise by shielding the fiber mechanically and thermally from its environment. Significant shielding however can often be unsatisfactory or impossible due to the additionally required volume and material around the fiber. A fiber to connect two optical clocks might for example be several hundred kilometer long, inaccessible dark fiber of the telecommunication network [166].

Active solutions, however, have proven to be very effective and less invasive. Active in this case refers to the use of an electronic feedback controller to compensate for the fiber induced phase noise, instead of avoiding it.

Already in 1994 Ma et. al. [164] implemented the first active fiber noise cancellation. They interferometrically detected the phase shift induced by the fiber and imprinted its negative onto the incoming beam. Such a system that synchronizes the phase of two optical signals, in this case the phases of the unperturbed and the fiber output beam, is called an *optical phase locked loop* (OPLL).

The fiber noise cancellation concept by Ma et. al. has been refined and was implemented [101] for the first phase stabilization of optical lattice potentials in 2008. This implementation bears special relevance for this work, because it was realized for an apparatus, which is very similar to the BFM apparatus and is run by the same research group. In the following it will be referred to as the Spinor apparatus.

The lattice phase stabilization developed at the Spinor apparatus was also implemented

for other experiments [170] and an extended version became the central technology for experiments with variable lattice geometries [167]. Recently a closely related scheme led to the construction of a *polarization synthesizer* [174], that permits the implementation of an atom sorting algorithm by precisely moving individual atoms with respect to each other in two overlapping, swiftly controlled 1D lattices with highly suppressed phase noise.

In the context of the BFM apparatus, fiber induced phase noise played an important role for the construction of the hexagonal optical lattice, that stands at the heart of all experiments presented in this thesis. Because all three lattice beams experience suffer the phase noise induced by $\tilde{8}$ m long fibers, we decided to implement a fiber noise cancellation setup. We chose the *Spinor* implementation as a references because it was the only stabilization for optical lattices we were aware of, when we started the construction in 2012.

To implement the *Spinor* setup for the BFM apparatus, it had to be modified. The most crucial improvement was the lifting of the restriction to non-polarization maintaining fibers. In contrast to the *Spinor* apparatus, the BFM apparatus is designed to conduct experiments with ultracold atoms in non-state-selective lattices, i.e. a lattice where all spin components of the gas experience the same optical dipole potential. Therefore a far-detuned lattice at 1064 nm is employed, which in turn requires higher optical powers (see Sec. 3.1). And the, to our knowledge, only commercially available type of single mode fiber¹ that prove capable of guiding the desired 5 W of 1064 light in a Gaussian shaped mode, was a PM fiber.

The implemented fiber noise cancellation successfully proved to suppress [98] the phase noise, as compared to the open loop operation. For the open loop operation however, we noticed a relatively broad output spectrum of the voltage controlled oscillator, that has been used in combination with an acousto-optic modulator to imprint the negative feedback on the optical phase. Further analysis of the fiber noise cancellation revealed [97], that replacing the controlled VCO with a static low noise digital frequency source reduced the heating rate in a 1d lattice from $120^{\text{mHz}}/E_{\text{rec}}$ to $55^{\text{mHz}}/E_{\text{rec}}$. For this reason we decided to continue using a static digital RF source and to develop a fiber lock based on a DDS RF-source that is capable to suppress the fiber induced noise further by additionally providing feedback on the phase of the signal.

As a beneficial side effect, the digital controller we developed for the fiber lock setup has proven to be a new valuable asset in our lab infrastructure. Due to its low cost of components and the flexible software architecture we implemented, it can readily be used in a variety of other scenarios, e.g. as a remote² controlled AOM driver, as a simple network analyzer or as a intensity stabilization.

An overview of the fiber lock and how it will be implemented into the main experiment is

¹nLight LIEKKI Passive-10/125-PM

²VISA over ethernet and USB are supported.

given in Fig. 9.1. On the left side it shows a schematic of the optical setup that corresponds to the main lattice laser setup briefly described in Sec. 2.2. From a feedback perspective this part constitutes as well an optical phase discriminator as a phase actuator and thereby couples the electronic part of the feedback loop, depicted on the right hand side, to the optical domain.

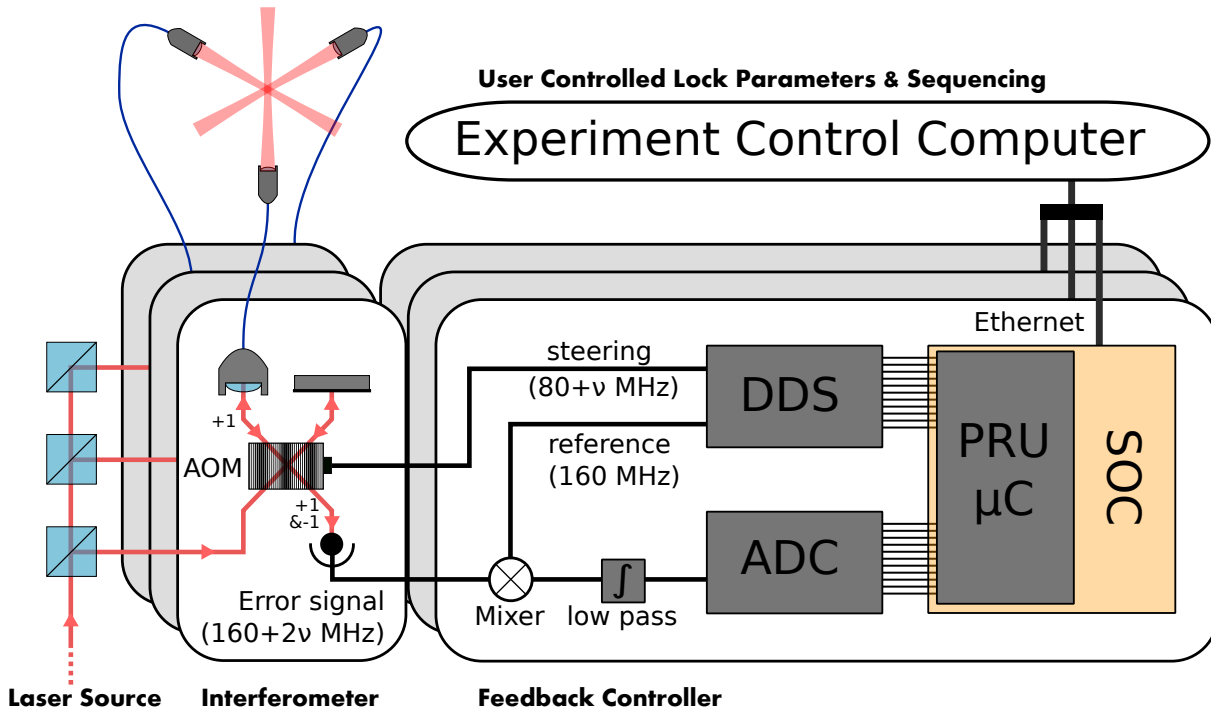


Figure 9.1: Schematic of the fiber lock. Shown is one of the three identical copies responsible for stabilizing one fiber each. The schematic divides the setup into two parts: the interferometer in the optical domain and the feedback controller in the RF domain. The numbers next to the AOM refer to the diffraction orders.

In this chapter I will first present the optical part of the setup in Sec. 9.1, comparing it to the setup of the Spinor apparatus. I will then go on to describe in Sec. 9.2 the hardware and software that we developed for the digital feedback controller and finally in Sec. 9.3, I will report on the quantitative performance and the setup that we used to determine it.

All fiber lock related development has been principally carried out by me in the supportive environment of the research group, except for the heating rate measurements mentioned above which have been realized by my colleague Matthias Tarnowski.

9.1 Phase Discrimination and Phase Control

Both, controlling the phase of a light field before it enters an optical fiber and determining the phase of the field where it emerges, sound like easily solved experimental problems.

An AOM, for example, reliably transfers a phase signal of the electronic domain to the light field, while by heterodyne detection, i.e. beating two beams on a photo diode, the signal can be transferred back into the electronic domain. But both, the imprinted, as well as the measured phase, only reflect a relative phase, which is in this case the phase difference between the diffracted and undiffracted beams and the difference between the two interfered beams.

In general a local oscillator signal is needed as a ‘clock’ to determine the time frame relative to which a phase is measured. Because optical frequencies are very high this clock is required to be extremely precise. When e.g. using light at 1064 nm, as in the case of the lattice beams of the BFM experiment, a clock deviation of 10 attoseconds corresponds to an error of about one degree in the measured phase. So in more general terms the problem is, how to distribute a high precision clock signal to distant sites.

To solve this problem Ma et. al. [164] found a simple workaround: sending part of the light back through the fiber and beating it with a light field at the local end will yield the round-trip phase. Assuming that the optical path length through the fiber has only changed insignificantly during the propagation time, the desired remote end phase can be approximated to be simply half the round trip phase.

This idea was first brought into the context of optical lattices for ultracold atoms at the Spinor experiment [101] in the Sengstock group. The topology of the original setup was refined, such that no components were required at the fiber remote end on the main apparatus side, where optical access to the atoms is scarce.

In this section I am going to present a modified setup for the general detection and steering of the phase of an optical field emerging from a glass fiber, which shows three improvements over the Spinor setup. Firstly, the restriction to non-polarization-maintaining fibers is removed. Secondly, it exposes a more favorable light power dependency of the error signal. And thirdly, less optical components are necessary, which makes it intrinsically less sensitive to vibrations.

While the conceptual idea behind the experiment by Ma et. al. holds true for any general kind of fiber stabilization, the stabilization of three beam (see Sec. 3.2.1) optical lattices constitutes a special case of fiber locking, where the absolute phase of a single beam is irrelevant. That means that the phases of the lattice beams only need to be stabilized relatively to each other as a simultaneous shift in phase of all beams does not yield any translation of the lattice potential. The previously mentioned essential problem of the distribution of the reference clock signal is not given here, and it would be sufficient to measure the relative phases purely at the remote ends of the fibers. Nevertheless, in the case of the BFM setup, we decided against the remote end measurement, because, as in most other atomic lattice experiments, the optical access to the main experimental apparatus is very scarce. A remote end measurement would require a stable interferometer that fills the full plane spanned by the telescopes and would therefore pose a big intervention in the existing setup.

9.1.1 Model

For the description of the OPLL it is necessary to approximate the optical light fields of the involved beams. The spatial dependence and the vectorial character of modes constituting a beam will be neglected, so that the electric field $E(x, t)$ of a beam can be described by a time (t) dependent scalar function of the optical path x along its main propagation axis

$$\begin{aligned} E(x, t) &= E_0 \exp(-i\varphi(x, t)) \\ \varphi(x, t) &= \omega_0 \left(t + \frac{x}{c} \right) + \varphi_0 \end{aligned} \quad (9.1)$$

For any type of OPLL it is necessary to change the phase and thereby frequency of the beam with time. Here it will be assumed that the associated changed spatial modes are sufficiently similar so that the optical path length can be considered constant. The instantaneous frequency is then defined as

$$\omega(x, t) = \frac{d\varphi(x, t)}{dt} \quad (9.2)$$

This relation can be, for example, used to determine the phase shift due to an AOM whose frequency is coherently swept to be

$$\varphi(t) = \int \omega_{\text{AOM}}(t) dt \quad (9.3)$$

Due to Eq. 9.2 it is fully sufficient to describe the signal by its phase. The action of a AOM will also be considered with regard to the phase of the beam. The driving RF signal can be expressed as

$$p_{\text{AOM}}(t) = \omega_c t + \varphi_{\text{AOM}}(t) \quad (9.4)$$

such that the imprinted phase of the light beam becomes

$$\varphi(x, t) = (\omega_0 + \omega_c) \left(t + \frac{x}{c} \right) + \varphi_0 + \varphi_{\text{AOM}} \quad (9.5)$$

9.1.2 Basic Phase Stabilization Scheme

In the basic setup as shown in Fig. 9.2-A the steering of the phase is achieved by coupling the first order of an AOM into the fiber. The phase at the remote end (i.e. experiment table side) of the fiber is discriminated indirectly by a Mach-Zehnder type interferometer at the local end (i.e. laser table side). One of the two beams that create a beat note on the photo diode is the unshifted incoming beam. The other beam is a small fraction of light that is retro-reflected at the flat uncoated fiber end at the remote end. On arrival at the photo diode, it has run twice through the fiber and has been diffracted twice into the same order at the AOM and thus forms a heterodyne beat signal together with the undiffracted beam at twice the driving frequency.

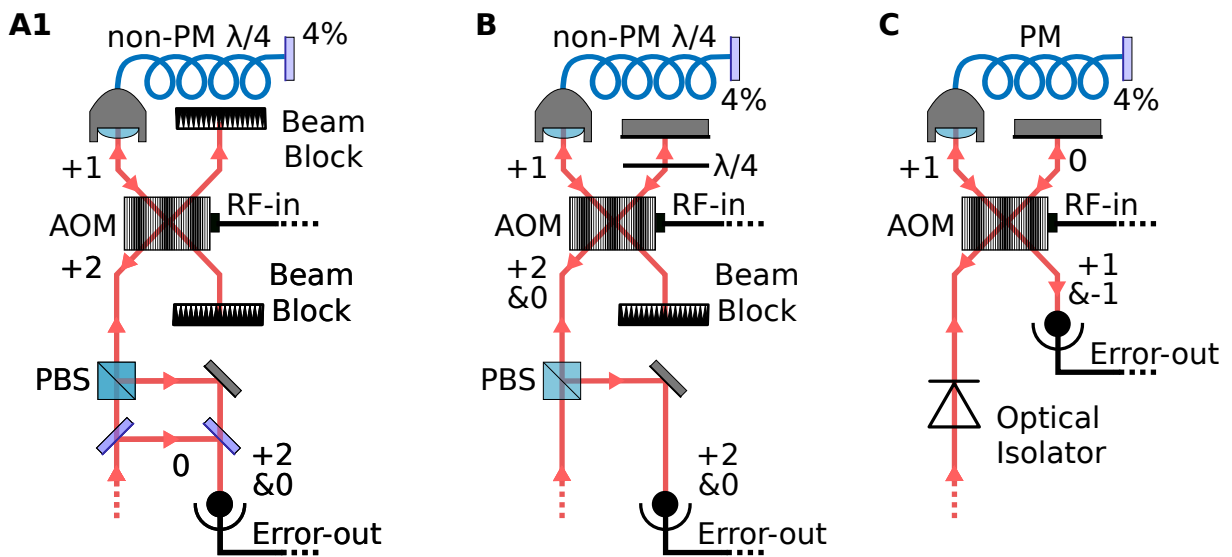


Figure 9.2: Schematics of the basic and improved optical setups. Subfigure A1 shows the basic setup, subfigure B shows a variation where the AOM acts as the central beamsplitter of the interferometer and subfigure C shows the improved setup, that lifts the restriction to PM-fibers.

Note that, the forward and backward propagating beams occupy almost identical spatial modes and therefore need to be separated in the interferometer. Here this is achieved by bringing the retro-reflected beam into an orthogonal polarization mode by means of manual fiber polarization controllers, which make the fiber act as a quarter wave plate. The two polarization modes are then simply separated using a PBS.

To understand the principle idea behind this setup I will for now make a simplifying assumptions for the description of the phase propagation and will postpone the more detailed discussion of their constraints to the next section. Here I assume that the optical path length of the setup can be considered as constant within the timescales of light propagation, i.e. the light picks up the same phase noise in both directions when passing through the fiber and it experiences the same frequency shift both times it is diffracted at the AOM. For a silica fiber and a beam of a wavelength of 1064 nm the index of refraction is about 01.45 [175], which leads to a round-trip time of 77 ns for an 8 m long fiber. The associated frequency is ca. 13 MHz and the delay can thus be neglected for relevant phase disturbances in the fiber in the range of up to some tens of kHz. Following the same argument the phase imprinted by the AOM is considered equal for the initial and the counter-propagating beam.

Having made this assumption, consider Fig. 9.3, where the phase propagation of the setup is sketched. The upper path shows the AOM and fiber twice, once for each passage. The added phase that the beam picks up when propagating through the fiber and AOM is denoted as $\Delta\varphi_1(t)$ and $\Delta\varphi_2(t)$ for the second passage, which are considered identical. The lower path symbolizes the reference beam that is needed for the beat.

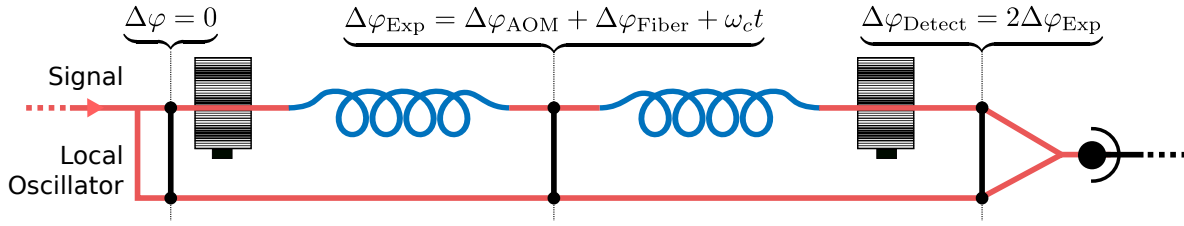


Figure 9.3

From here it is evident that the total phase difference $\Delta\varphi_{\text{Detect}}(t)$ at the chosen interferometer position, equals twice the phase difference $\Delta\varphi_{\text{Exp}}(t)$ at the fiber end up to a constant in time and a constant offset by the modulation frequency ω_c of the AOM

$$\Delta\varphi_{\text{Detect}}(t) = 2\Delta\varphi_{\text{Exp}}(t) + \text{const.} \stackrel{!}{=} 2\omega_c t \quad (9.6)$$

which means that if $\Delta\varphi(t)$ has been stabilized to twice the modulation frequency of the AOM plus a remaining stochastic noise distribution, so $\Delta\varphi_{\text{Exp}}(t)$ at the remote fiber end will be stabilized to ω_c plus half the noise amplitude.

If the signal were to be obtained without passing through the AOM a second time the linear relation between the measured beat phase and the phase at the fiber end would not be given anymore.

9.1.3 Improved Phase Stabilization Scheme

The basic concept as presented above relies on the use of different polarization modes to separate the initial beam from the retro-reflected that carries the desired phase information. As mentioned in the introduction the basic concept cannot be transferred without changes to the BFM setup, because here the use of high power PM-fibers is required. As the name suggests PM fibers are meant to maintain the polarization mode and therefore cannot act as QWP as the non-polarization-maintaining fibers did before. One could sacrifice the polarization maintaining property by placing a QWP just in front of the fiber coupler. But this would not lead to desired phase signal either, because the two polarization modes corresponding to the two polarization maintaining axes experience two different phase shifts and only the common mode phase changes will be measured as a phase signal.

Furthermore non-polarization-maintaining fibers possess a higher symmetry of the polarization modes and therefore couple weaker to mechanical deformations as compared to PM that are not coupled perfectly on axis. However one has to keep in mind that in the above presented basic concept, the incoming and reflected beams probe different polarization modes³, which possibly violates the previously made model assumptions and thereby cause an inaccuracy in the measured phase.

³Consider e.g. the first section of the fiber after the incoupling. If the beam possesses eg. vertical polarization here, the retroreflected will be of horizontal polarization as it passed twice the fiber that acts as a QWP. Only if mechanical and thermal disturbances induce the same phase shift for the vertical

An alternative solution to circumvent the problems entailed by using different polarization modes could be either using a non-polarizing beam splitter or a Faraday rotator in the place of the PBS of the interferometer. The BS comes with the huge drawback of a high power loss either in the lattice beam power or in the phase signal, depending on the splitting ratio. A Faraday rotator would solve the problem with only the minor drawback of a large footprint on the optical table and additional degrees of freedom to be adjusted but also at an immensely increased cost.

In the following I will present an improved setup that we developed to remove the polarization requirement of the basic concept without using any additional components.

The improved concept works very similarly to the basic concept, with the main difference that the interferometer section and the steering section have been fused into a single group of optical components. This is possible because of the optical properties of an AOM of not only shifting the phase of the diffracted mode, but also separating them spatially. It can therefore be employed as the central beam splitter of the phase detection interferometer.

Consider schematics B and C depicted in Fig. 9.2, where subfigure B is an intermediate step and subfigure C shows the actual schematic of the improved setup. The only difference between A and B is, that in B the undiffracted incoming Beam does not get dumped but is retro-reflected. Passing the QWP twice puts it into the orthogonal polarization mode, so that on its second undiffracted passage through the AOM it occupies the same spatial and polarization mode as the signal beam that has picked up the phase of the fiber and has been diffracted twice. At the PBS they get separated from the incoming beam and get finally steered onto the photo detector. Except for the different intensity dependencies (see Sec. 9.1.4 for a discussion) the two setups are clearly equivalent. Here the AOM has been used like a beam splitter to superimpose the two optical signals and thereby replacing the beam splitter in A. Thinking of the AOM as a beam splitter motivates to also use it to separate the incoming from the reflected modes in order to replace the PBS and thus lift the restriction to PM fibers. For that all four ports of the “beam splitter” have to be used.

As before in A and B, the incoming beam in C gets scattered at the AOM and picks up a phase $\Delta\varphi_{\text{AOM}}(t)$, travels through the fiber and back thus picking up another $2\Delta\varphi_{\text{Fiber}}(t)$ and now instead of guiding the mode that gets diffracted another time onto a photo diode as before, the undiffracted zeroth order is used. The missing phase difference that is needed for measuring the phase at the end of the fiber is now gathered by the reference beam, which picks up a phase of $-\Delta\varphi_{\text{AOM}}(t)$, with a minus sign as it is diffracted into the minus first order. Summing up all phases we get the same phase relation as before

$$\Delta\varphi_{\text{Detect}}(t) = [2\Delta\varphi_{\text{Fiber}}(t) + \Delta\varphi_{\text{AOM}}(t)] - (-\Delta\varphi_{\text{AOM}}(t))$$

The situation becomes very evident when considering the replacement schematic as shown in Fig. 9.4.

and horizontal polarization mode, the assumption is valid that the phaseshift of the vertical (incoming) polarization is given by half of the total (vertical+horizontal) phaseshift.

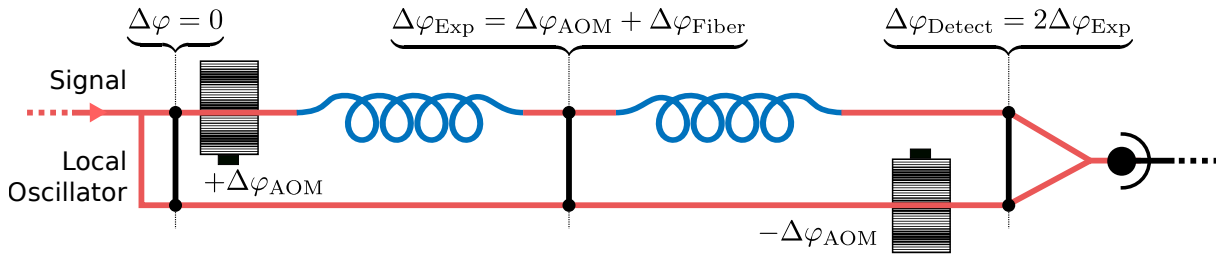


Figure 9.4: Replacement schematic for the Improved setup.

9.1.4 Comparison

In the following the two schemes will be compared regarding their susceptibility to mechanical noise and their capability to operate over a wide range of output powers, which is relevant here in the context of lattice depth ramps.

Stability

The mechanical and thermal stability of this local end setup are highly relevant for the aspired reduction of phase noise at the remote end of the fiber. Any thermal drift or vibrations of most of the optical components of the setup potentially induces phase noise at the remote end of the fiber. For the non-standard interferometers presented in this chapter (see e.g. Fig. 9.2) we distinguish three categories of vibration susceptibilities of components, depending on their position in the interferometer. Firstly there are the components the beam passes before it has been split up into the interferometer arms. Any additional phase shift introduced here is common mode and is therefore undetectable by the phase detector. It nevertheless leads to a phase noise at the remote end of the fiber. In the context of using the presented fiber lock for stabilizing an optical lattice, this means that the copies of the fiber lock setups for the individual arms are susceptible to vibrations and thermal drifts relative to each other. Secondly there are components that are either placed in the reference arm of the interferometer or are part of the feedback arm and are only passed once. These components lead to a change in OPL, causing a change of the phase signal measured at the photo diode, that does not reflect the actual change of phase at the remote end of the fiber and thereby constitutes an artifact. Thirdly there are components that are part of the feedback arm and get passed twice, like e.g. the fiber itself. Any phase perturbation is reflected in an accordingly changed signal at the phase detector and with a theoretical ideal lock, that is infinitely fast, these fluctuations could be fully compensated for.

Fig. 9.5 shows the vibration sensitive paths in a color code: red represents noise leading to artifacts, orange represents sources of noise that can be compensated for and gray represents elements that are insensitive to vibrations.

Our measurements presented later in this chapter (Sec. 9.3) are for those aforementioned reasons all prone to a broad spectrum of phase noise induced by the multitude of

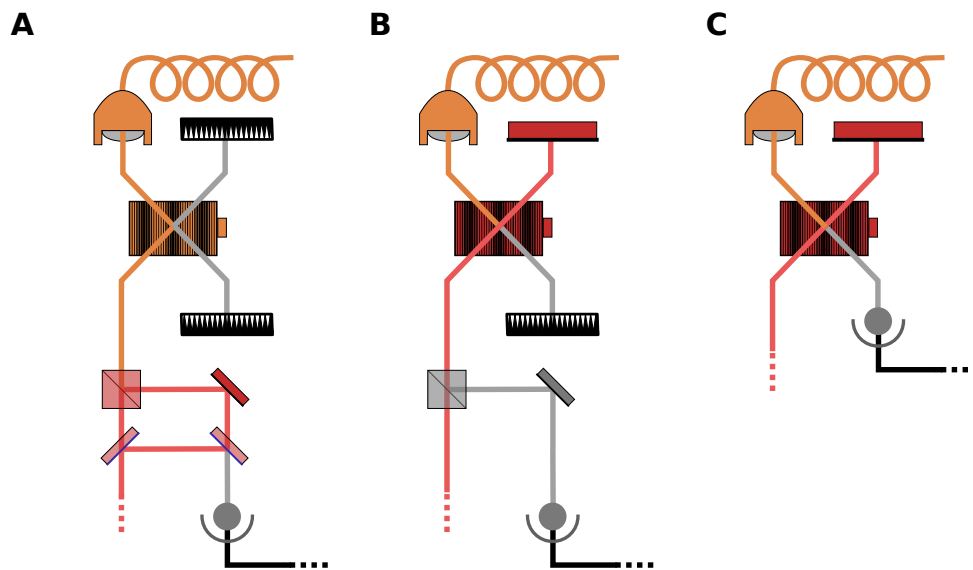


Figure 9.5: Schematic of the paths relevant for stability. Parts shown in red and orange are sensitive to vibrations. While vibrations of orange parts lead can be compensated for by the lock, while vibrations of the red parts cannot be compensated for.

contributing vibrational modes of the involved optical components. The data presented in this chapter is therefore supplemented with interferometer background spectra that show the phase noise without any fiber nor feedback.

Light intensities

For most experiments with ultracold atoms in optical lattices the capability of lattice ramps i.e. to gradually increase or decrease the depth of the lattice potential is very important. As for example when preparing a lattice state that entirely fills the lowest band, as it is done in the experiments presented in Chapt. 6 and 7, where the lattice beam intensity is linearly ramped from zero, up to the final lattice depths within an adiabatic timescale.

Therefore the fiber lock is required to work efficiently and seamlessly over a wide range of different intensities. As the lattice ramp is known a priori, the lock parameters could for example be electronically steered by a feed forward. Nevertheless, for obvious reasons is it desirable to obtain the best quality of the interference signal before electronically amplifying it. In both presented designs the beam intensities are regulated through the RF power of the same AOM as used for the phase lock. As it will be pointed out here, this leads to a nonlinear dependency of the error signal on the light intensity. Adding another AOM to decouple these two tasks is undesirable because it would not only further increase the complexity of the setup, but also reduce the maximally achievable lattice depth.

For analyzing the lattice depth dependent signal strength it is necessary to consider the intensities of the phase probing beam I_P and the reference beam I_R . For an AOM diffraction efficiency of η , an approximated zeroth order fraction of $1 - \eta$ and a beam

splitting ratio of γ of the first beam splitter of the basic setup that separates out the reference beam, the intensities for the different setups as depicted in Fig. 9.2 can be summarized by

$$\begin{aligned} I_{\text{P}}^{(\text{A})} &\propto (1 - \gamma)\eta^2 & I_{\text{R}}^{(\text{A})} &\propto \gamma \\ I_{\text{P}}^{(\text{B})} &\propto \eta^2 & I_{\text{R}}^{(\text{B})} &\propto (1 - \eta)^2 \\ I_{\text{P}}^{(\text{C})} &\propto \eta(1 - \eta) & I_{\text{R}}^{(\text{C})} &\propto \eta(1 - \eta) \end{aligned} \quad (9.7)$$

where the superscript index coincides with the subfigure index. The modulation intensity of the interference signal $I_{\text{mod}} = \sqrt{I_{\text{P}}I_{\text{R}}}$, i.e. the intensity corresponding to the modulation amplitude, are identical in cases B and C but differ from A:

$$\begin{aligned} I_{\text{mod}}^{(\text{A})} &\propto \eta\sqrt{\gamma(1 - \gamma)} \\ I_{\text{mod}}^{(\text{B/C})} &\propto \eta(1 - \eta) \end{aligned} \quad (9.8)$$

This relationship is also shown in Fig. 9.6. There, instead of plotting the modulation intensity as a function of the diffraction efficiency η , it is plotted as a function of the actual relative intensity at the fiber remote end. In the basic setup, the available remote end light power is diminished, because the reference beam intensity is split up from the main input beam and the relative remote end intensity is thus given by $(1 - \gamma)\eta$. The circles in Fig. 9.6 show the maximally available power assuming a diffraction efficiency of $\eta_{\text{max}} = 0.8$.

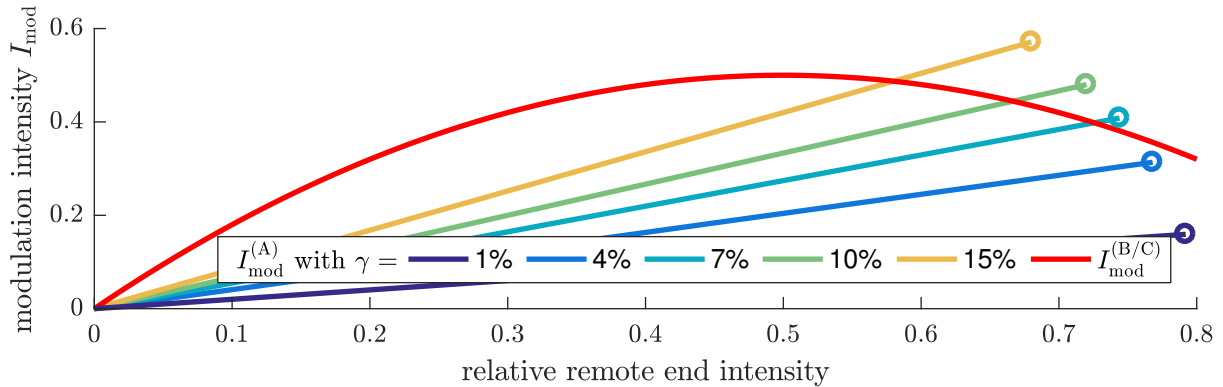


Figure 9.6: Comparison of the modulation intensities of the interference signal of setup A versus A/B for different relative reference beam strengths γ . The relative remote end intensity on the x axis is given by $(1 - \gamma)\eta$ and the circles indicate the maximally possible intensity for the according γ if a maximum diffraction efficiency of 80% is assumed.

Analyzing Fig. 9.6 reveals that the improved setup yields a stronger error signal over most of the range of η . Only at high diffraction efficiencies and high reference beam strengths γ does the basic setup provide a stronger signal, which however comes at the cost

of a reduced maximally achievable lattice depth. Especially in the range of low diffraction efficiencies which are important when the atoms are loaded into the lattice and the lattice intensity is ramped up from zero, the improved setups provide a significantly stronger error signal.

Under the previous considerations, the alternative improved setups B and C are seemingly equal with respect to their applicability to a wide range of intensities. However it is worth noting, that $I_P^{(B)}$ scales quadratically and $I_P^{(C)}$ linear in the first nonvanishing order. For shallow lattices in the case of the basic setup, a very small fraction of the input light intensity carries the phase information and is amplified by an extremely strong reference. This comes at the cost of a higher susceptibility to stray light and a higher DC offset that might saturate the photo detector. To make this point clearer consider, as an example, the concrete implementation that has been presented in Sec. 2.2. Here a total power of 5 W is used in every lattice arm and the actual power coupled into the fiber is ramped up starting from zero. At the beginning of this ramp, the AOM diffraction efficiency is close to zero. This means that almost the entire light power is retro-reflected and focused on the phase discrimination photo detector. For an attenuation of 96% of the reference beam, matching the reflectivity of the flat fiber end, this would still lead to 200 mW and thereby require a larger dynamic range of the photo detector. This effect increases drastically if the homodyning reference beam shall be stronger than the signal beam, i.e. at attenuation factors below 96%.

So additionally, one should consider the average light intensity for the two different setups. These are simply given by

$$\begin{aligned}\bar{I} &= I_P + I_R \\ \bar{I}^{(B)} &= L_P \eta^2 + L_R (1 - \eta)^2 \\ \bar{I}^{(C)} &= (L_P + L_R) \eta (1 - \eta)\end{aligned}$$

with the additional loss factors L_P and L_R for the round trip losses and attenuation of the beam carrying the fiber phase information and the reference beam respectively. The different average intensities cannot be compared straightforwardly as a function of the loss factors, because changing those loss factors also changes the modulation intensity. As a measure for comparison we therefore use the modulation depth

$$\mu = \frac{I_{\text{mod}}}{\bar{I}} \tag{9.9}$$

The modulation depth is plotted for a select set of ratios L_P/L_R in Fig. 9.7. The dashed and solid lines represent $\mu^{(B)}$ and $\mu^{(C)}$ respectively. The modulation depth $\mu^{(C)}$ is independent of the diffraction efficiency η while $\mu^{(B)}$ is strongly dependent on it. For the case $L_P > L_R$ (stronger attenuation of the reference) there is a window within the range $0 < \eta_1 < \eta_2 = 0.5$ in which setup C yields a smaller modulation depth. In the case of a stronger reference

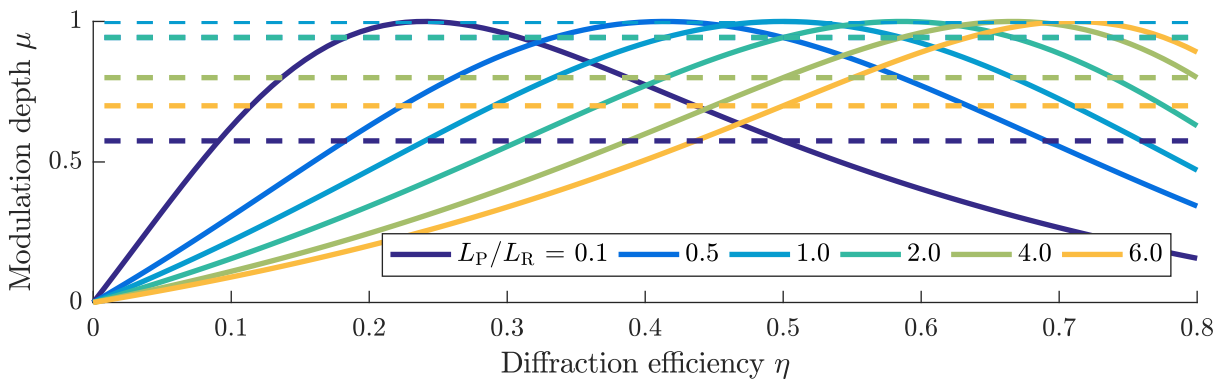


Figure 9.7: Comparison of the modulation depth dependency on the diffraction efficiency η of setup B (solid lines) versus C (dashed lines) for different attenuations of the reference beam (see legend).

the range is $0.5 = \eta_1 < \eta_2 < 1$. For a use case where a ramp from $\eta = 0$ is relevant, the behaviour of setup C is more favorable, since here the modulation depth does not drop to zero for small light powers. The ideal situation is reached for equal losses in both beams, where setup C exposes full modulation for all η .

9.2 All digital phase-locked loop

This section reports on the development of an all digital phase locked loop (PLL). In the context of the fiber stabilization a PLL is used to generate and control the phase of the driving signal for the phase control AOM such that the phase fluctuations of the interferometer beat signal are being minimized. The developed electronic setup is however by no means restricted to the purpose of fiber stabilization, but, as a general PLL, finds application in a wide range of different areas.

A PLL can be defined as a device that synchronizes the phase of its output signal to the phase of an input signal. Typically it is implemented as a feedback control loop that comprises three main components (see Fig. 9.8): a controllable oscillator, a phase or frequency detector and a controller.

For every one of the aforementioned three components there exists a variety of different classes of devices that can be chosen from, depending on the context in which the PLL is to



Figure 9.8: Components of a phase locked loop.

be employed. A typical implementation would e.g. be a *voltage controlled oscillator* (VCO) whose frequency is controlled by an PID-controller based on the error signal obtained from an analog phase detector.

The PLL developed in this work follows a rather unusual choice of components. Instead for the VCO, a so-called *direct digital synthesis* (DDS) *integrated circuit* (IC) generates the output signal. The RF signals generated by DDS ICs feature an extremely low background of phase noise [176]. The bandwidth of phase and frequency modulation, however, is lower than what can be achieved with VCOs⁴.

Because DDS ICs are digital devices, their integration into a feedback loop is fundamentally different as compared to analog frequency sources. The DDS IC generates a RF signal by sequential digital to analog conversion (DAC) of individual samples forming the desired waveform. The parameters of the generated signal, such as frequency or phase, can be changed dynamically by transferring their numerical values via a digital communication interface to the DDS IC.

Using DDS for a PLL therefore requires to replace the control signal, that is classically represented by a voltage proportional to the fed back phase or frequency, by a stream of digitally encoded and time discrete data points. This, however, entails the necessity of the other two PLL components also being digital: A digital controller to calculate and provide such a stream, and a phase detector with a digital interface or alternatively an analog to digital converter to digitize the analog error signal.

Here we implemented a discretized version of a proportional-integral-differential (PID) controller. The discretization leads to the following equation [177]

$$u_n = u_{n-1} + B_0 e_n + B_1 e_{n-1} + B_2 e_{n-2} \quad (9.10)$$

Here u_i is the discrete series of the actuation signal, where n refers to the latest time step, and e_i is the series of error signals. The parameters B can be linked to the P, I and D gains (K_x) via

$$\begin{aligned} B_0 &= K_p + K_i \frac{T_s}{2} + \frac{K_d}{T_s} \\ B_1 &= -K_p + K_i \frac{T_s}{2} - 2 \frac{K_d}{T_s} \\ B_2 &= \frac{K_d}{T_s} \end{aligned} \quad (9.11)$$

where T_s is the sampling rate.

⁴Comparing all relevant models from Analog Devices, one of the leading DDS manufacturers, leads to the conclusion that the minimal latency for setting a phase is under the best circumstances 60 ns. VCOs can, in contrast, easily modulated with several MHz

9.2.1 Hardware implementation

The hardware implementation is determined by a number of requirements imposed by the optical setup and the aspired loop pipeline delay, determining the bandwidth of the system. While a shorter pipeline delay is of advantage for any system, it will generally require more sophisticated and more specialized measures to be achieved. Therefore a trade-off decision had to be taken between speed on the one hand and extensibility, flexibility, ease of development and cost on the other hand.

Phase detector

As a digital phase detector a simple analog phase detector in combination with an analog digital converter is used. The analog phase detector generates an analog phase signal by down-conversion. For the down-conversion the interferometer photo diode signal is mixed with a DDS generated reference and subsequently the difference signal is extracted with a low pass filter. Employing a DDS reference guarantees that no significant phase noise artifacts are generated and furthermore adds a digital and non-phase-wrapped (see below) interface for the steering of the reference phase signal.

A disadvantage for analog phase detector is their non-linearity, i.e. their output voltage u is not proportional to the phase difference $\Delta\phi$ between the reference and interferometer signals, but behaves as $u \propto \sin \Delta\phi$, which exposes non-linear terms. The periodicity of the sin dependency also creates a phase wrapping, which describes the fact that all phase differences are effectively mapped onto an interval of $-\pi$ to π . In the context of the PLL phase wrapping can lead to phase slips: when $\Delta\phi$ changes more than π within one lock cycle period, the sign of the error signal will change, causing the controller to lock to the next multiple of 2π and thereby creating a phase slip between the reference and control signals.

To digitize the phase signal, which can be negative or positive a so-called bipolar analog to digital converter is required. We chose the LTC1419 by Linear Technologies, which samples at 800kHz with a precision of 14 bit. For the full contribution to the pipeline delay budget not only the acquisition time has to be taken into account but also the time required to transfer the data from the ADC to the controller. In this respect the chosen controller offers a minimal transfer pipeline delay by exposing the sampled data without additional delay at a parallel interface with the full width of 14 bit. High speed serial transfer would be a viable alternative that however comes at the expense of increasing complexity by adding additional serialization/deserialization units and requiring careful PCB design to handle the high frequency signals.

DDS IC

As a DDS IC we have chosen the AD9959 by Analog Devices. It offers good phase noise characteristics and with 500 MSps⁵ sampling rate it is suitable to drive common AOMs. Similarly to the speed considerations made for the ADC, two pipeline delays have to be taken into consideration: the internal delay for changing the phase of the output signal and the data transfer delay determined by the interface. To our knowledge there are no commercial alternatives that offer a significantly shorter data transfer delay than the 60 ns of the chosen model. The data transfer pipeline delay for the selected model is determined by the 4 channel SPI interface, that can be operated at 200MHz. There are models that offer a more parallel interfaces, these however would require a different choice of controller that exposes more high speed I/O lines.

Controller

For digital feedback loop controller so-called field programmable gate arrays (FPGA) have become a very popular choice. FPGAs are particularly suited for real-time data processing, because they can harness the full potential of speed and processing power offered by semiconductor technology by operating at the lowest possible abstraction layer. Opposed to microprocessors and digital signal processors (DSP), which are programmed by providing a list of commands, the functionality of FPGAs is determined by specifying the wiring of a grid of logic blocks like AND-gates and OR-gates. This way data can be processed extremely parallelized and highly optimized for a specific application.

The access to this low abstraction layer however also requires a fundamentally different development process, that may not only constitute an unnecessary or even insurmountable⁶ complication for developers without prior training, but is also associated with a generally increased design effort. To implement a certain functionality with an FPGA, instead of an ordinary program written in C or an assembly language as it is the case for microprocessors or DSPs, a hardware design must be created with a *Register Transfer Level design language*, like VHDL or Verilog. The development process, which typically involves many iterative versions, is further slowed down by long compilation times. Depending on the complexity compilation times range from minutes to hours, in contrast to usual sub-second to few seconds for μ Cs and DSPs. Another difficulty is, that the minimal pipeline delay for a controller implemented on a FPGA has a complex dependency on the hardware layout and can therefore only be determined after compilation.

The upper bound, i.e. the limit for an infinitely fast controller, for the closed loop cycle time is principally determined by the pipeline delay of the DDS and the propagation time of the acoustic wave in the crystal of the AOM and can be estimated to about

⁵Mega samples per second

⁶described as "insurmountable hurdle" for many without background by one of the main FPGA manufactures in an official application note. [https://www.xilinx.com/support/documentation/application_notes/xapp1163.pdf]

400 ns corresponding to a 2.5 MHz loop rate. The associated maximal bandwidth can be estimated [177] to be around 250 kHz.

The envisioned PID algorithm does not offer a lot of parallelization potential, so the speed gain by an FPGA be assumed to be moderate. A so-called finite impulse response filter (FIR) of higher order that can be implemented highly parallel would require manifold higher computation times on a processor. The algorithm (see also Eq. 9.10) for calculating a feedback similar to an analog PID-controller however can be expected to be fully sufficient in the present use case, where no sharp resonances in the feedback system itself, as it is for example the case for piezo controlled systems, can be expected.

For a quantitative estimation consider a micro processor driven controller running at 200 MHz, that is intended to have a pipeline delay equal to the minimal delay caused by the AOM and DDS, thereby reducing the bandwidth by a factor of one half. For this processor there will be time for 80 instructions cycles, which seems adequate for both computation and communication overhead.

Because the reported spectral range of phase noise induced by fibers of up to 1 kHz [164] and even an extended range of acoustic noise in the lab environment of up to 10 kHz can be covered by processor driven feedback loop and in prospect of a bandwidth increase below a factor of two for an FPGA based solution, we decided to implement a processor based controller.

Specifically we chose the AM3359 by Texas Instruments, which is a *system on a chip* (SoC) that unites, among other components, an Cortex-A8 core, which clocks with up to 1 GHz and two programmable real-time units (PRU), clocked at 200 MHz, on one die. The AM3359 offers a number of features that make it very suitable as a platform for a feedback loop controller.

Firstly, program execution on the PRU is deterministic. That means with every clock cycle a command is executed⁷, such that the execution time of every command of a program can be reliably predicted. For a feedback control program e.g. the associated pipeline delay is fixed and can be predicted from the source code. For ordinary non-real-time processors the command execution time can vary by a number of factors like task scheduling by the operating system, dynamic branch prediction and pipelined memory access, to name just a few [178].

Secondly, the PRUs are specifically designed [179, 180] to flexibly interface a broad range of external hardware components and offer therefore reading and writing access to a decent number of input and output pin within one clock cycle. For our use case as a loop controller, this means that the sampling output of the ADC connected via 14 parallel lines can be read into a register for further calculation with a single operation. It is common that access to I/O lines introduces further latency, by for example multiplexing.

And thirdly, monitoring, steering and programming of the PRU cores is comfortably available from the ARM core on which a full Gnu/Linux operating system can be run to

⁷with the exception of a few commands that take two clock cycles to execute.

implement all non-real-time functionality.

Mainboard

All of these presented main components need to be appropriately linked to each other and depend on further peripheral components for e.g. voltage supply, memory and filtering. For the DDS and ADC, development boards from the manufacturers, that provide periphery and expose communication interfaces at pin header rows have been used. For the controller a fully equipped single board computer⁸ has been used, that provides RAM, ethernet interface as well as power management and exposes most of the PRU I/O lines on two pin header sockets. Furthermore a custom PCB (see App. C.1 for details) has been designed to connect the components, translate logic levels and provide various voltage supplies from a single power supply.

9.2.2 Software implementation

For a fully functional and controllable phase lock not only a main locking algorithm for the PRU cores has been developed but also a complete software stack that allows to operate the lock remotely over the network. It is thus possible to, for example, set the central frequency, change the RF-power, adjust the PID constants and set point without delaying the lock loop and to read out the error signal. The software stack also opens many applications beyond locking, as for example the application as a dynamic frequency source with software-defined modulation up to a bandwidth of 2 MHz.

PRU Locking algorithm

The central locking algorithm had to be implemented in an assembly language specific for the PRUs-subsystem. The basic structure of the algorithm is very simple. Fig. 9.9 shows the three steps of the main loop: first data is captured from the ADC. Then a new phase value is computed according to Eq. 9.10 using the newly read phase value and the previous phase and error values. Finally the new phase value is transferred to the DDS.

The actual implementation of this scheme is however is rendered slightly more complicated by the fact, that only a subset of the possible 32 I/O-lines of each of the two PRU cores are routed to the ball point contacts of the package of the SoC. Therefore the ADC and DDS cannot be interfaced with a single PRU core and the connectivity has to be shared between the two cores. This implies that there are two separate programs, one running on each core, that need to synchronize and exchange data. Fig. 9.10 shows a sketch of the distributed implementation of the locking algorithm. It can be summarized by saying that PRU core number 0 (PRU0) is responsible for the communication with the DDS as well as for requesting a new ADC sample and PRU1 reads the ADC sample and calculates the corresponding control phase, which is subsequently passed together with a

⁸Beaglebone black

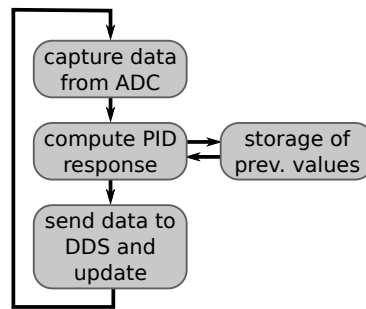


Figure 9.9: Basic structure of the locking algorithm.

status update into the so-called scratch pad, a type of delay free shared memory between the PRUs, from where it is received from the other PRU core to be serialized and sent to the DDS.

Using two PRU cores in parallel has the advantage of several idle time slots, i.e. time spans during which the one of the cores or both are not executing the lock algorithm but are waiting for an external event, as for example in IDLE0 (see Fig. 9.10), where PRU1 waits for PRU0 to finish transmitting the new phase to the DDS. Instead for waiting these idle times are used to implement an additional layer of communication with the host program running in the GNU/Linux environment on the main ARM core. Any transfer of larger chunks of data from the host program to the PRUs can only be done via the DDR memory of the system. Access to it is however pipelined and will cause stochastic waiting times, which would be undesirable outside of any idle time slot.

The both PRU cores feature 32 registers, which are 32 bits wide each. So operations within one core can be completed without using any RAM and there are enough registers to dedicate the values of the set point, B_i , e_i and u_i exclusively to a single register. For the actual calculation of Eq. 9.10 the *multiply and accumulate* (MAC) unit is used. It is an additional component of the SoC which supplies integer multiplication and addition in a single clock cycle, that is thereby ideally suited for the task at hand. One difficulty however is the restriction to integer numbers, that arises on second sight. As the actuated signal, i.e. the phase sent to the DDS, is itself an integer number and the error signal input from the ADC is encoded as a signed integer, using exclusively integers for a simple calculation does not seem to impose any problems. In practice however the granularity that created by requiring the feed back parameters B_i to be integers is unsatisfactory. We solved this problem by right shifting the actuation signal by seven bytes after the calculation. This corresponds to a (truncated integer)⁹ division of the actuating signal by 128 and thereby refines the resolution of the feed back parameters by the same factor. With a phase resolution of 14 bit of both the ADC and the DDS there is no risk in causing a overflow with the 32 bit wide registers.

Care has also to be taken with the representation of negative numbers. The ADC

⁹rounding could simply be included by branching according to first fractional bit.

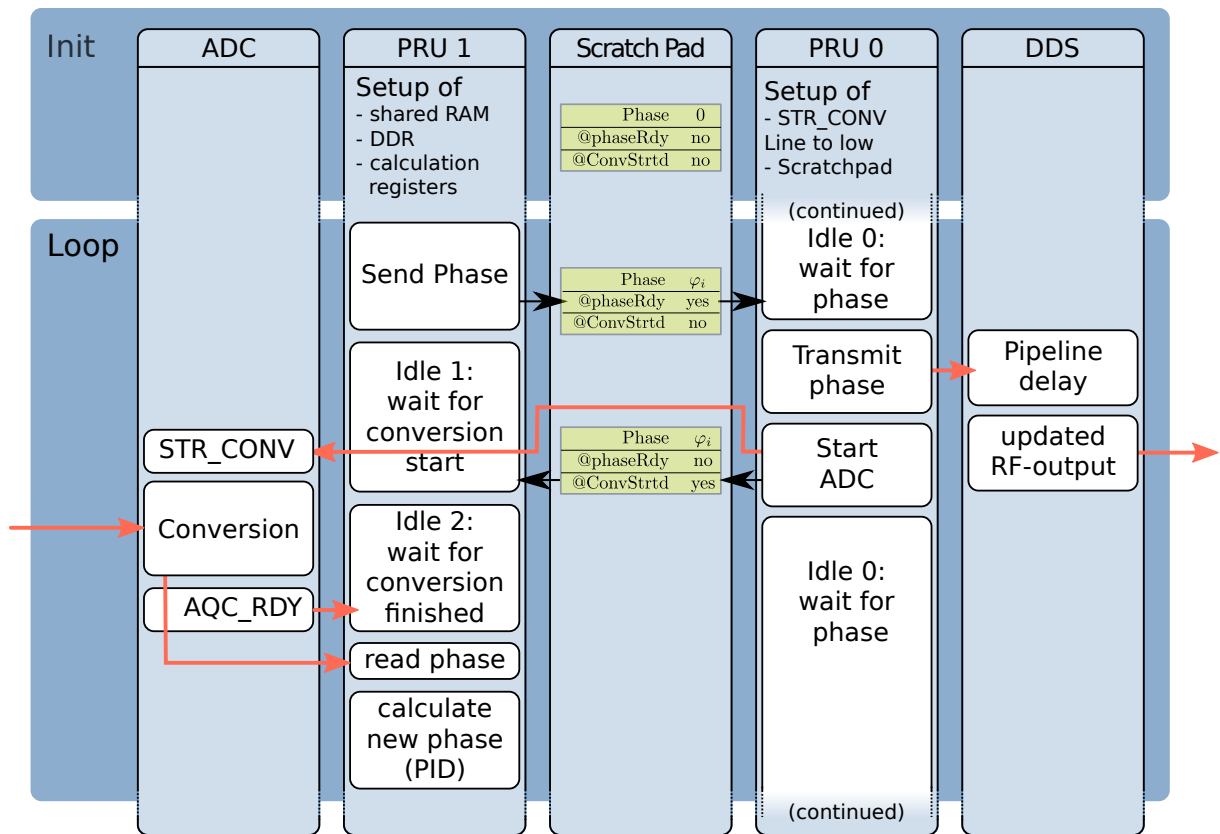


Figure 9.10: Locking algorithm. This graphic illustrates how the locking algorithm is executed on the two real time processors and how the data is exchanged between the involved components. The red arrows indicate communication via signal lines and the black arrows symbolize memory transfer. The @-sign is used to signal states: @phaseRdy indicates, that a new value has been acquired and @ConvStrtd, that an acquisition has been started. For simplicity not shown here is the communication to the DDR in the idle times, the communication with the multiply-accumulate-unit (MAC) in the PID calculation time slot and the communication with the shared memory in idle 2 phase to update the PID constants from network user input.

conveniently provides the input signal as a two's complement, with which multiplication and addition routines are identical for positive and negative numbers. Nevertheless the sign of the input value has to be determined so that the 14 bit two's complement value can be extended to the full width of the 32 bit register.

The pipeline delay of the main locking cycle is 70 instruction cycles, corresponding to 350 ns and thereby meets the expected requirements. The distribution over the individual tasks can be retrieved from Tab. 9.1. For the total pipeline delay the latency of the DDS of 60 ns and the acquisition time of 1250 ns have to be taken into account (see also Tab. 9.2). The total theoretical pipeline is therefore given by 1660 ns, which is expected to lead to a controlling bandwidth of 60 kHz if a factor of ten between frequency associated to the latency, and the bandwidth is assumed [177]. Note that the actual lock cycle frequency is

Function	instructions	time [ns]
PID calculation	17	85
DDS communication	43	215
ADC communication	6	30
PRU-PRU communication	4	20
total pipeline delay	70	350

Table 9.1: Timings of the controller operations.

component	time [ns]
controller	350
DDS	60
ADC	1250
total pipeline delay	1660

Table 9.2: Timings of the different components.

slightly higher because the cycle is not interrupted for the time the DDS takes for updating the phase. The expected cycle frequency is 625 kHz.

Host program and communication shells

The host program is opposed to the PRU programs an ordinary program that is executed by the ARM core and runs in the user space of the operating system. Its main purpose is to launch and control the PRU programs and to expose this control over a network interface for remote control. The PRUs are controlled over three communication channels. Firstly, the PRU shared memory, which is a small (12 kB) section of memory that can be access from all parties without delay and is therefore used to transfer the lock set point and PID constants from the host program to PRU1. Secondly the external DDR memory, of which 8 MB can be reserved for the PRU sub system by a Linux kernel module. The DDR memory is used to transfer the error and actuation signals to the ARM core, which in turn sends them over ethernet to the remote client, where it can be used to monitor the lock performance with low latency. And thirdly, an interrupt is used to notify the host over a successful halt of the PRU programs.

Because the lock controller does not have any physical buttons or displays a network interface is necessary for operation. A minimal script language interpreter has been implemented to exchange command sequences between a client and the host program. The lock controller can thus be operated as a VISA industry standard network device.

Alternatively it can simply be controlled from a telnet session or via a MATLAB library we developed for this purpose as a part of the software stack.

An overview of the software stack and the communication shell model is given in Fig. 9.11 and a minimal example on how a command issued from a matlab script cascades through all shells down to the hardware is presented in App. C.2.

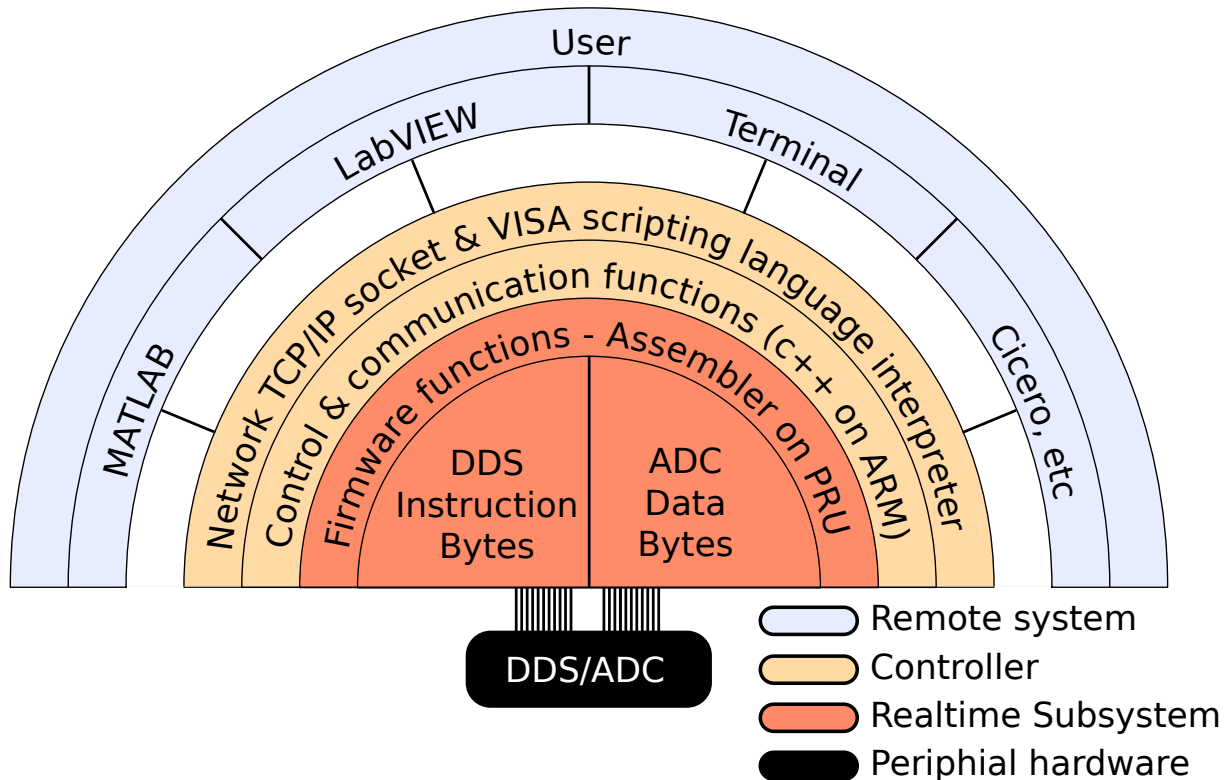


Figure 9.11: Shells of the fiber locking software stack. The separation into many shells enables a flexible use of the device. The user can use any VISA compatible interface to access the real time functionality of the fiber lock by writing custom scripts that are interpreted on the controller. Larger chunks of data are transferred in binary mode.

The implementation of the full software stack allowed us to essentially use the fiber lock similarly to a simple function call, so that measurements can be entirely written as a single MATLAB script. To control the lock we also created a user interface with MATLAB, where the PID parameters can be controlled with sliders and the current error signal and its Fourier transform are live-plotted.

9.3 Implementation and Performance

In order to test the performance of the fiber lock that has been presented in this chapter without risking any down time of the main apparatus, we constructed a separate setup

as shown in Fig. 9.12. The setup closely resembles the principal setup already described earlier (Fig. 2.1). For simplicity it is restricted to a single fiber. Furthermore an available fiber coupled DFB¹⁰ laser at a rubidium compatible wavelength of 780 nm and a fiber coupled output power of 3.4 mW together with typical AOMs (Crystal Tech 3080-124) with a center frequency at 80 MHz were used. Using a different wavelength is not expected to have any impact on the fiber lock performance. There are a few additions for benchmarking

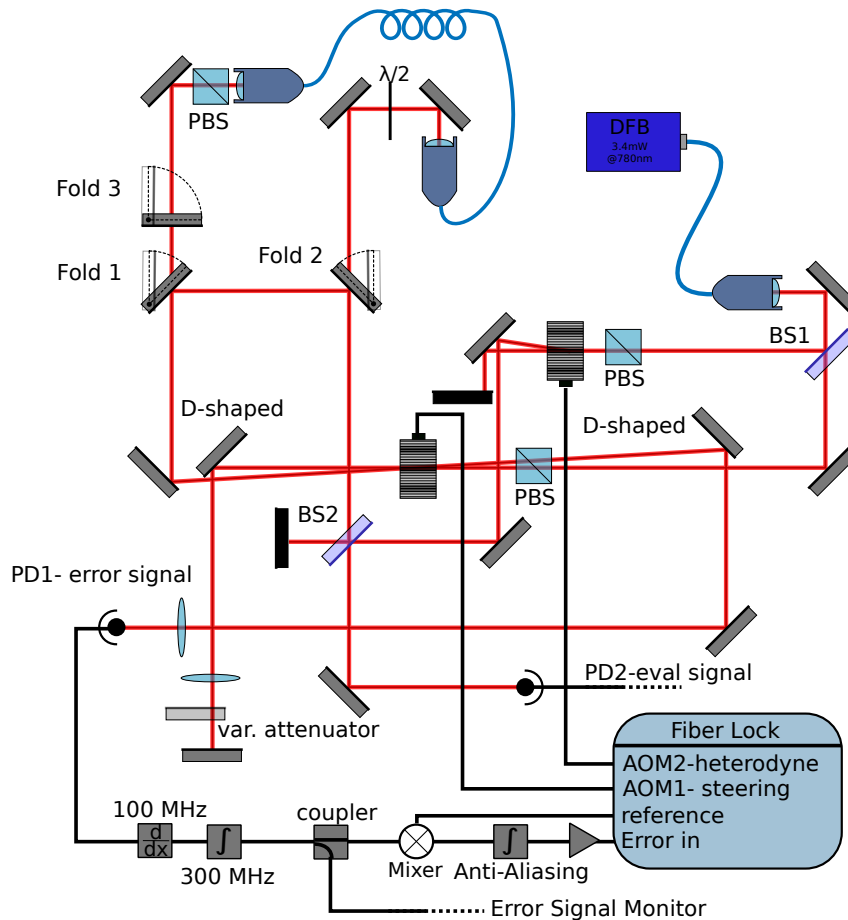


Figure 9.12: Schematic of the setup used for benchmarking the performance of the digital fiber lock.

purposes. Firstly, optics are added that enable heterodyne measurement of the phase of the beam emitted at the remote end of the fiber. For that a 10% fraction of the beam is picked up at BS1 and diffracted by another AOM and subsequently interfered via BS2 with the remote end beam. The interference signal is picked up by the photo detector PD2 (Thorlabs PDA10A EC). The HWP in the beam path serves the single purpose to align the polarization axes of the two interfering beams for the different PM-fibers that have not been key aligned. Secondly a pair of folding mirrors (1 and 2) is inserted bridge the

¹⁰Distributed Feedback Laser, homebuilt.

fiber, so that the phase stability of the interferometer without fiber induced shifts can be measured. Finally there is another folding mirror (3) for retro-reflection to mimic the back reflex signal from the flat end of the fiber, but without the noise induced by it. The retro-reflected signal has a very poor mode match with the incoming beam because there are no lenses to refocus the beam. This is however compensated to some degree by the high reflectivity as compared to the 4% in case of the fiber. It is necessary to have those two reference paths, because when the fiber is bridged with folding mirrors 1 and 2 no error signal is available and when using folding mirror 3 no evaluation signal is available. The modes are shaped through the fiber coupler to create a focus in the primary AOM, located half way between the couplers. To assure that the undiffracted beam is reflected into the same spatial mode a lens has been added to focus it onto the retro-reflection mirror. Additionally to this D-shaped mirrors are used to separate the diffraction orders early. Nevertheless, not the full potential for minimizing the spatial footprint of the setup has been exploited. As will be shown later, the stability of the interferometer itself is an important measure for the overall performance of the fiber lock. An essential detail that is not visible from Fig. 9.12 is the slight deviation from the horizontal plane of the beams passing AOM1. This was necessary to separate the reflexes of the AOM crystal from the actual signal beam as the signal beam here is of the order of 1% of the incoming light power and the anti reflection coating of the crystal is of a similar order of magnitude. The fiber that has been used for the presented benchmarks is a bare 20 m silica core PM fiber.

Both AOMs are steered by the fiber lock. AOM1 is connected to output of 80 MHz that is phase modulated according to the error signal input and AOM2 is driven with a fixed frequency of $80 \text{ MHz} + \Delta\nu_{\text{Heterodyne}}$ according to the desired heterodyne measurement frequency. The error signal is picked up from PD1 (Femto MK-S-S5972 with current amplifier HCA-200M-20K-C). After a simple high pass filter (100 MHz Minicircuits SHP-100H+) and a low pass filter (250 MHz Minicircuits BLP-250+), a 10 dB fraction of the signal is picked up by a directional coupler and is used as an input signal for the spectrum analyzer. The main signal is down converted at a mixer with a 160 MHz reference signal originating from the fiber lock. Finally the signal is pre-amplified (Minicircuits ZFL 500LN) and fed into the ADC of the fiber lock. At the entry port a socket for exchangeable capacitors between the input and ground has been added. The capacitors (if present) act together with the 50 Ohm input impedance of the ADC as a passive low pass filter of first order. Low passing at this point is essential for anti-aliasing purposes [177]. A capacitance leading to a low pass filter frequency lower than the actual lock cycle frequency will have a similar effect as applying a higher value to the integration constant of the PID algorithm. The reason for testing various different capacities is that capacitors have an exponential charging curve and thereby do not provide ideal anti-aliasing.

9.3.1 Cycle frequency

To reliably determine the cycle frequency of the lock, we operated the lock as usual but feed a 1 kHz signal to the error input and subsequently Fourier transform the acquired signal. The resulting frequency is given in units of inverse cycle durations $1/\Delta t_{\text{Step}}$ and thus enables the determination thereof. As a frequency source for the 1 kHz reference signal two unused ports of the DDS operated at 100 Mhz and 100.001 Mhz are mixed (standard Minicircuits ZAD-3+). As a reference clock for the DDS serves a calibrated commercial (Rohde&Schwarz SMB 100) RF source. The Fourier transform has been conducted at a basis of about $1 \cdot 10^6$ points corresponding to roughly 1300 periods, which should provide a sufficiently high accuracy. Surprisingly the Fourier analysis results in

$$T_{\text{Cycle}} = 1295 \text{ ns} \quad f_{\text{Cycle}} = 772 \text{ kHz} \quad (9.12)$$

which deviates significantly from the previously estimated value of 1600 ns (see Tab. 9.2¹¹). It is unlikely that such a big deviation stems from the execution time of the code on the controller. The data sheet of the LTC1419 reveals that the acquisition time is subject to deviations due to the manufacturing process and that only the maximal acquisition time is given by the previously assumed 1250 ns. The typical acquisition time is specified with 1040 ns. With the assumptions made about the code execution time we measure an acquisition time for our model of 945 ns.

9.3.2 Step Response

Without setting up any further electronics it is possible to measure the step response for the lock. For this we wrote a script that operates the lock at a certain set point for the phase and instantaneously changes the set point. The step response arises from the recorded error signal. In Fig. 9.13 data averaged over 1000 repetitions for 6 different settings of the PID-parameters is depicted. The feed back constants, shown in the legend, are given in integer units, which as explained earlier (Sec. 9.2.2) can be converted to the conventional units by dividing by 128. A small anti-aliasing capacity of 10 nF is used to maintain the highest possible resolution.

The observed behavior fully matches the expectations by resembling the behaviour of an analog PID controller. For low values of the feed back constants, e.g. the blue line in the top figure, an exponential approaching of the new set point value can be observed. For higher values (red in top figure) the value is approached quicker and slight overshooting occurs. For even higher values (yellow in top figure) a damped oscillatory behaviour manifests. The oscillatory frequencies lie between 150 kHz and 250 kHz.

¹¹The DDS pipeline delay is excluded here, because it does not influence the cycle time (see Fig. 9.10) as it happens in parallel to further computation. Nevertheless it is included in Tab. 9.2 as it determines the pipeline delay that is ultimately relevant for the performance of the lock.

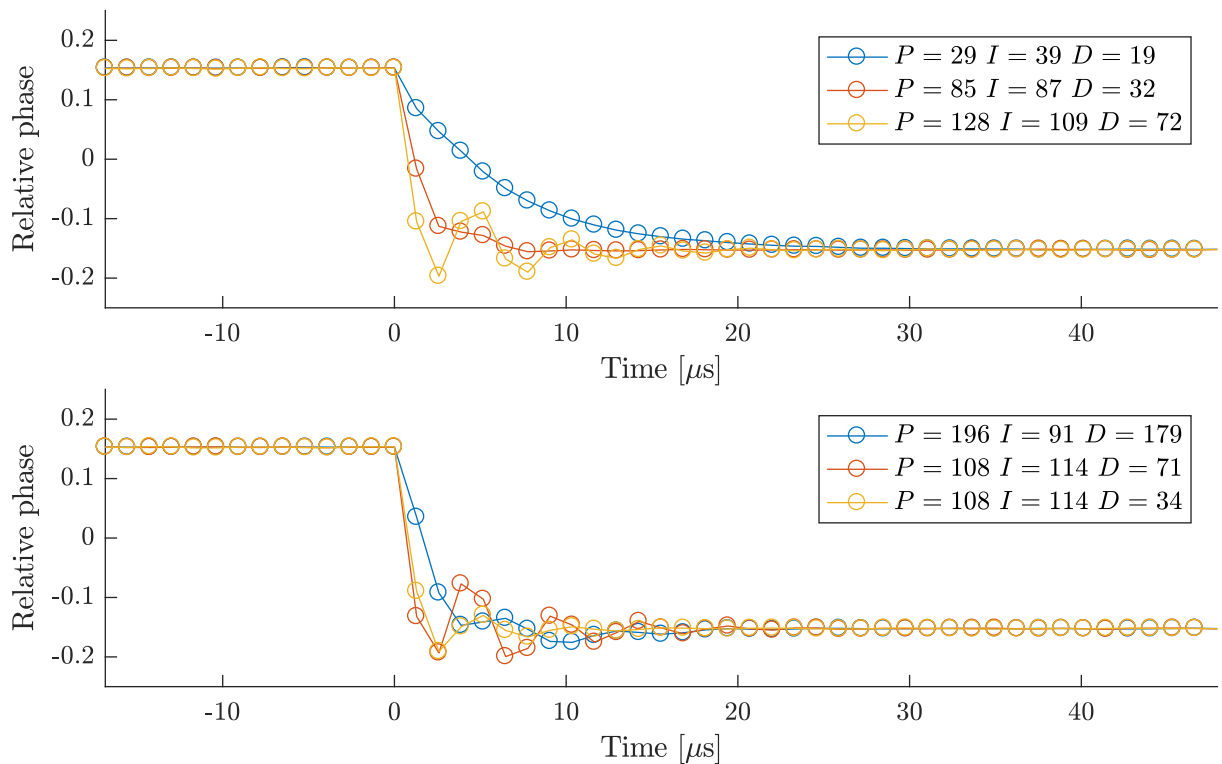


Figure 9.13: Step response of the fiber lock recorded with the fiber lock itself. With increasing strength of the feed back the typical transition from an exponential to an oscillatory behaviour can be seen.

9.3.3 Heterodyne Measurements

To benchmark the performance of the fiber lock we measured (Rohde&Schwarz FSV7) a power spectral density (PSD) estimator of the error signal (Error signal monitor in Fig. 9.12) around its carrier of 160 MHz and of the interference signal with a reference beam with a detuning of 1 MHz (eval signal in Fig. 9.12). To compare different settings we conducted seven measurement series with parameters summarized in Tab. 9.3. Additionally we measured the background spectrum of the interferometer. In the case of the error signal the background was produced by flipping folding mirror 3 and for the heterodyne signal by flipping mirrors 1 and 2. The series have been taken for 32000 points in two regions, one with a 500 kHz span, 100 Hz *resolution band width* (RBW) and 500 averages. The other one with a one with a 10 kHz span, 1 Hz RBW and 20 averages.

The PSDs for the heterodyne measurement are shown in Fig. 9.14. In Subfig. B, it can be seen that in the 5 kHz range all chosen series of different settings show a similar reduction of noise over the unlocked signal (blue) of about 20 dB. Additionally it is quite striking that for low frequencies in the range of 1 kHz a lot of sharp peaks appear. This regions is depicted enlarged in Subfig. C. The surprisingly these perturbations of the

series	K_P	K_I	K_D	Capacitance [nF]
1	0	0	0	0
2	29	39	19	10
3	85	87	32	10
4	128	109	72	10
5	196	91	179	47
6	108	114	71	5
7	31	35	20	470

Table 9.3: Filter parameters for the measurement series.

otherwise smooth spectrum show a strong correlation to perturbations of the background signal (black). The existence of a perturbed background signal means that even without any feedback, the interferometer is unstable and thereby impose a natural limit to the performance of the fiber lock. The initial measurements showed even more pronounced perturbations but the observation of the coincidence of the peaks with a 100 Hz grid (especially Subfig. B), let us discover a damaged connection of the power supply of the DFB laser source. Fixing the connection improved the spectra to those shown here. Inducing vibrations to the optical table caused only a slight deterioration of the spectra so that the mechanical origin for the perturbations could be ruled out. For those reasons it is highly probable that the noise is induced by the malfunctioning laser source.

The undemodulated error signal corresponding to the same measurement series are depicted in Fig. 9.15. Those spectra resemble the previously shown closely, which is a sign for the well functioning of the fiber lock. It is remarkable to see that similar noise floors are reached, when bearing in mind that it is result of the 4% reflection of a beam with an initial light power of merely 3.4 mW, that has passed twice through an AOM, has been fiber coupled, so that the final power at the photo detector are around 40 μ W.

Comparing the error signal at around 380 Hz shows how the fiber lock eliminates noise artifacts and thereby induces additional noise in the heterodyne signal.

For higher frequency it can be observed that the lock follows the typical behaviour of a PID controller by eliminating low frequency noise a creating so-called *servo bumps* between 120 kHz and 180 kHz of heightened noise levels. For most settings the point where the unlocked and locked spectra cross lies at around 50 kHz.

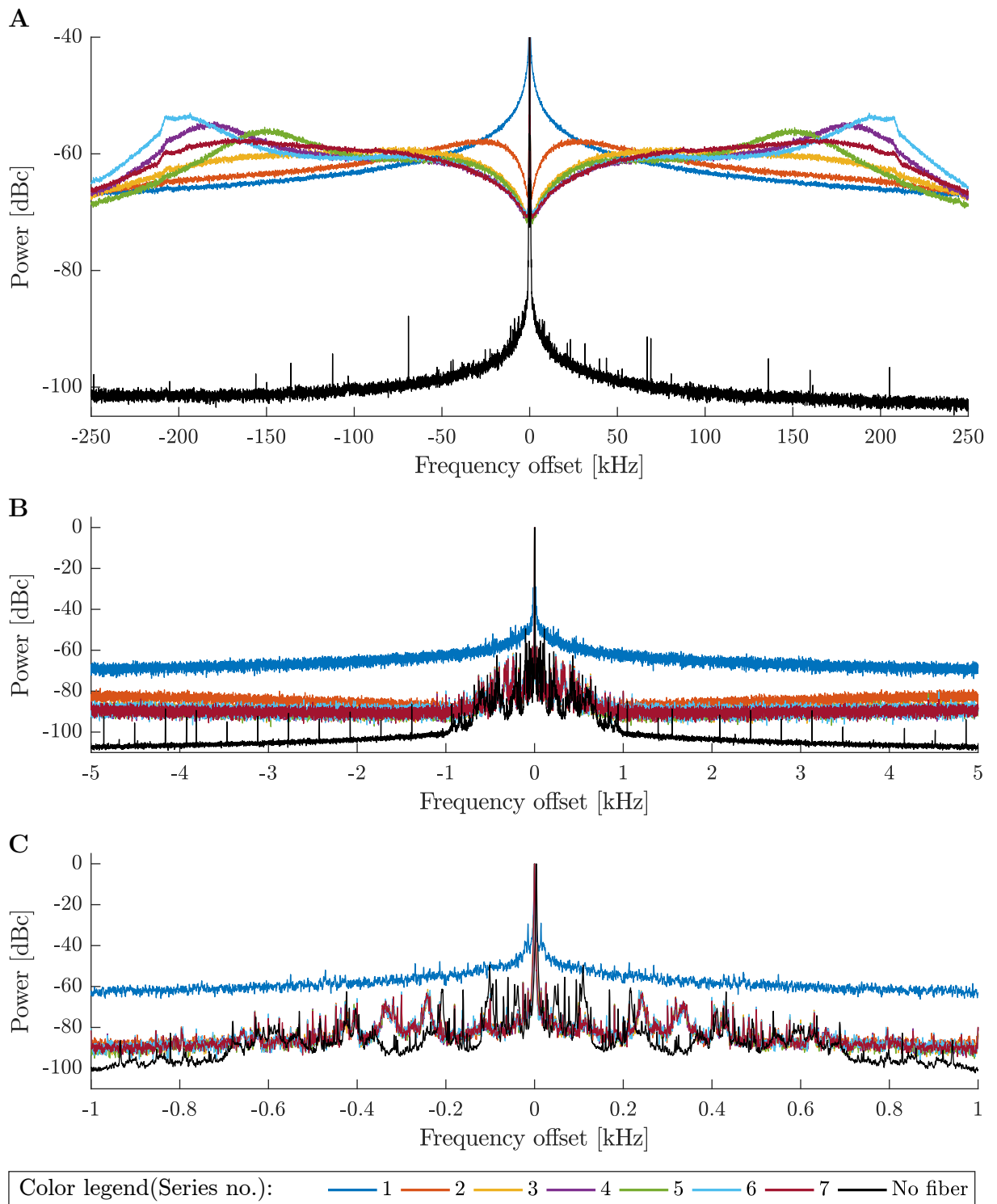


Figure 9.14: Power spectral density (PSD) of the fiber phase noise. Plotted are the PSDs of the interference signal of the beam emitted by the stabilized fiber with a reference beam that has not passed a fiber. The spectrum is shifted by the chosen homodyning frequency of 1 MHz. The color legend at the bottom applies to all plots, and associates the lock parameter series to the different spectra. The “background” trace has been acquired for the unregulated interference signal when the fiber is bypassed via a set of mirrors.

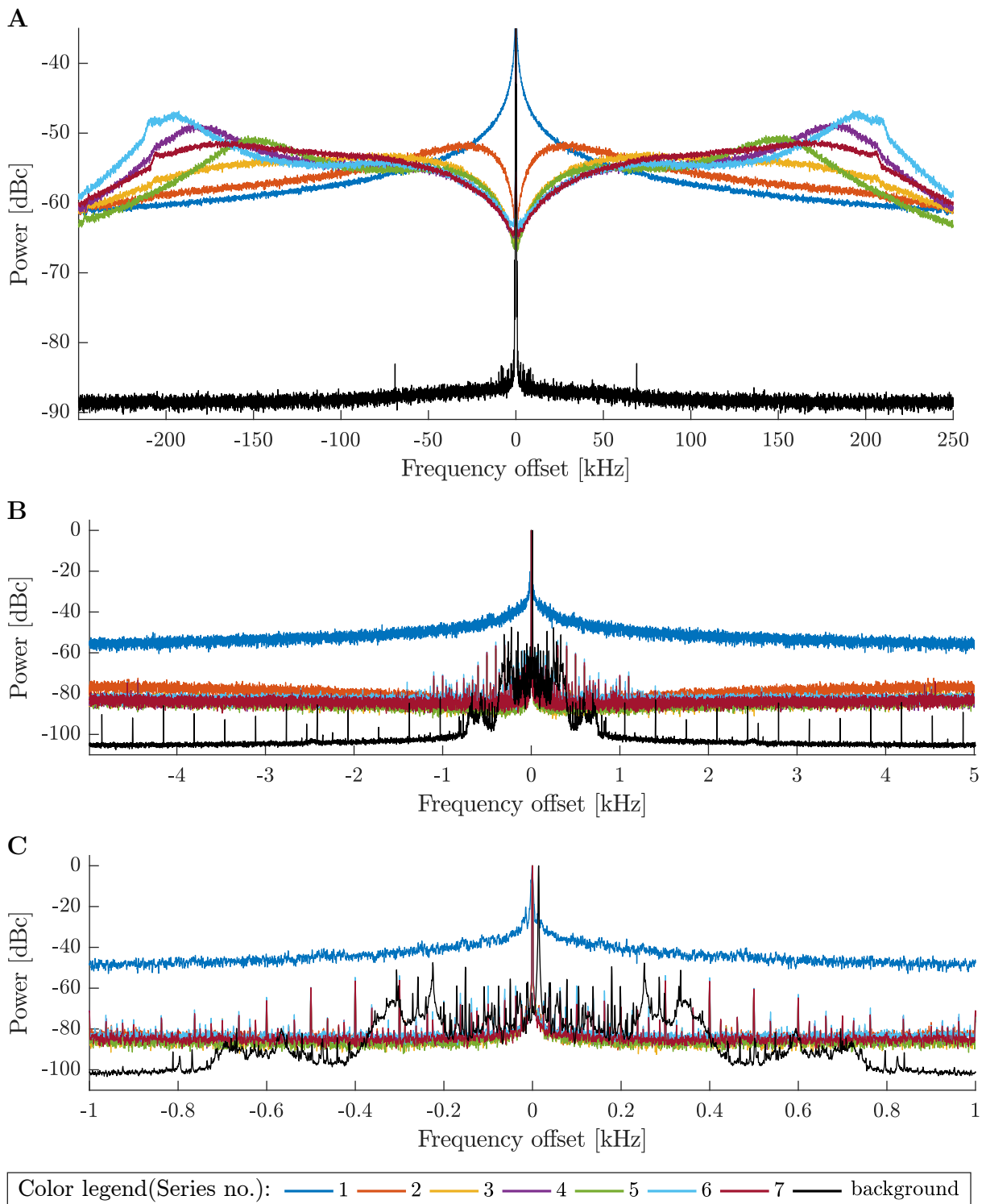


Figure 9.15: Power spectral density (PSD) of the homodyne error signal. Plotted are the PSDs of the interference signal between the fiber probing beam and the local oscillator beam. The homodyning frequency of 160 MHz (each beam 80 MHz upon AOM passage) has been subtracted. The color scale at the bottom applies to all spectra and indicates the measurement series for the chosen lock parameters. In the “no fiber” series the fiber has been replaced by a retro reflecting mirror.

9.4 Outlook

The bench mark of the fiber lock presented in this section, shows that it is capable of reducing the fiber induced phase noise for frequencies under 50 kHz significantly. It is expected to further improve the life time of atoms in optical lattices, where this frequency range is especially relevant for excitations that lead to heating. The current implementation of the fiber lock has proven to be extremely versatile especially through the additional controllable DDS output channels (4 in total) and the live transfer of the error signal. A permanent and automated observation of the fiber noise could be simply implemented and disturbances could even be associated with experiment run IDs¹² to post select perturbed runs. For future improvements, the possibility for implementing a digital phase detector should be investigated to improve the acquisition speed and quality.

¹²A network client that obtains the IDs has already been implemented for the lock.

A Lattice Definitions

The lattice geometry for the hexagonal lattice can be summarized by the following values. For the definition of the symbols refer to Chap. 3

$$\hat{\mathbf{k}}_1 = \begin{pmatrix} 0 \\ 1 \\ 0 \end{pmatrix} \quad \hat{\mathbf{k}}_2 = \begin{pmatrix} -\sqrt{3}/2 \\ -1/2 \\ 0 \end{pmatrix} \quad \hat{\mathbf{k}}_3 = \begin{pmatrix} \sqrt{3}/2 \\ -1/2 \\ 0 \end{pmatrix} \quad (\text{A.1})$$

$$\mathbf{b}_1 = k_L \begin{pmatrix} \sqrt{3}/2 \\ 3/2 \end{pmatrix} \quad \mathbf{b}_2 = k_L \begin{pmatrix} -\sqrt{3} \\ 0 \end{pmatrix} \quad \mathbf{a}_1 = \frac{2\pi}{k_L} \begin{pmatrix} 0 \\ 2/3 \end{pmatrix} \quad \mathbf{a}_2 = \frac{2\pi}{k_L} \begin{pmatrix} -\sqrt{3}/3 \\ 1/3 \end{pmatrix} \quad (\text{A.2})$$

$$\mathbf{B} = k_L \begin{pmatrix} \sqrt{3}/2 & 3/2 \\ -\sqrt{3} & 0 \end{pmatrix} \quad \mathbf{B}^{-1} = k_L^{-1} \begin{pmatrix} 0 & -\sqrt{3}/3 \\ 2/3 & 1/3 \end{pmatrix} \quad (\text{A.3})$$

$$\hat{\mathbf{p}}_1 = \begin{pmatrix} -1 \\ 0 \\ 0 \end{pmatrix} \quad \hat{\mathbf{p}}_2 = \begin{pmatrix} 1/2 \\ -\sqrt{3}/2 \\ 0 \end{pmatrix} \quad \hat{\mathbf{p}}_3 = \begin{pmatrix} 1/2 \\ \sqrt{3}/2 \\ 0 \end{pmatrix} \quad \hat{\mathbf{s}}_{(1,2,3)} = \begin{pmatrix} 0 \\ 0 \\ 1 \end{pmatrix} \quad (\text{A.4})$$

B Band structure Code

One central piece of code to calculate the band structure is the code defining the potential in the Fourier basis given the (relative) Fourier components. In order to show how the subindexing is managed a short MATLAB snippet defining the potential matrix V is given. Variables are named according to the nomenclature established in sec. 3.3.1. Note that the colon operator is used in matlab for index raveling and the apostrophe operator represents transposing.

```
Vmn = -V0 * [ dot(P1,P3)    dot(P1,P2)    0;
              dot(P2,P3)    P0            dot(P3,P2);
              0            dot(P2,P1)    dot(P3,P1) ];
S1 = meshgrid( c : -1 : -c );
s1 = S1(:)';
S2 = S1';
s2 = S2(:)';
[NN, MM] = meshgrid( 1:D, 1:D);
V = zeros(D);
Vmndim = size(Vmn,1);
min_k = -(Vmndim-1)/2;
max_k = -min_k;
for i=min_k:max_k
    for j=min_k:max_k
        V = V +Vmn(i-min_k+1,j-min_k+1)*(s1(NN)-s1(MM)== i)
            .*(s2(NN)-s2(MM)== j);
    end
end
```


C Fiber Lock

C.1 Electronics

The following figures show the schematics and pcb layout for the fiber lock electronics developed as part of this work.

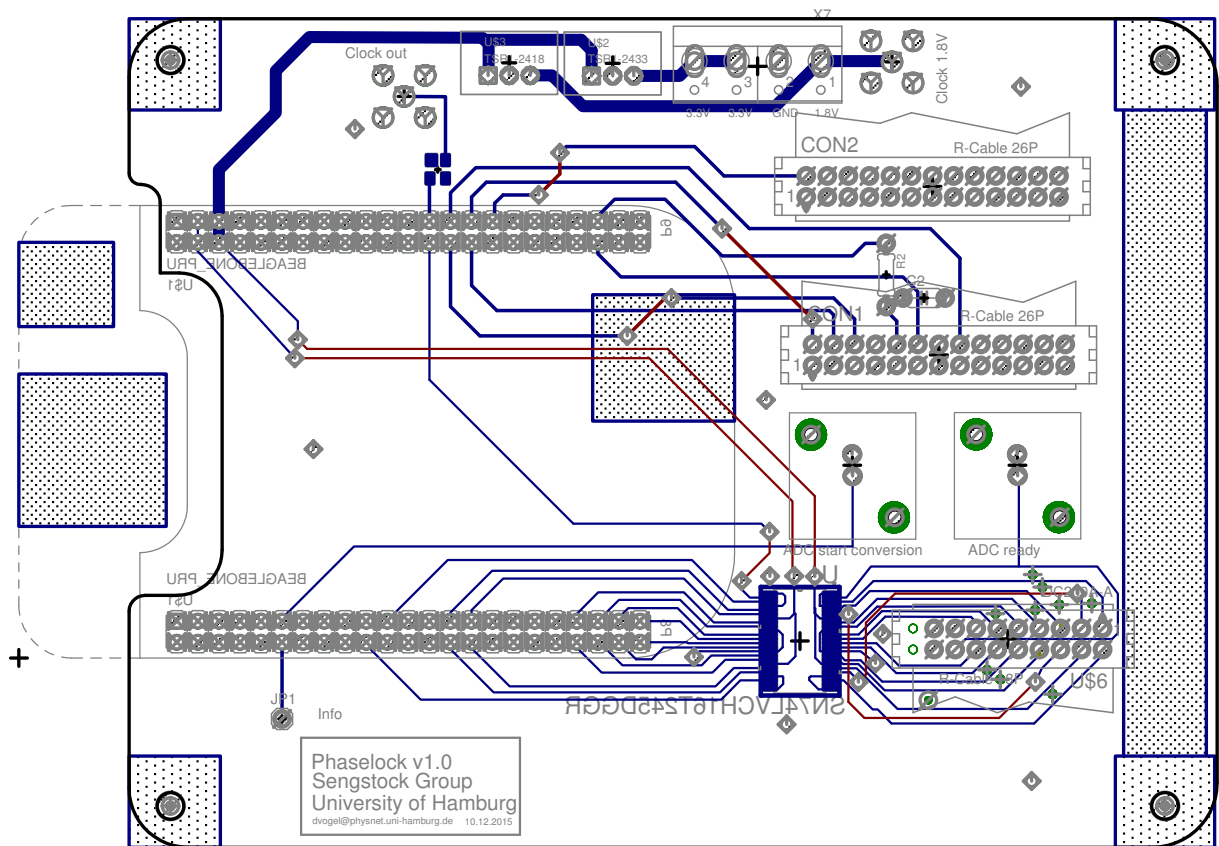


Figure C.1: PCB layout of the fiber lock mainboard.

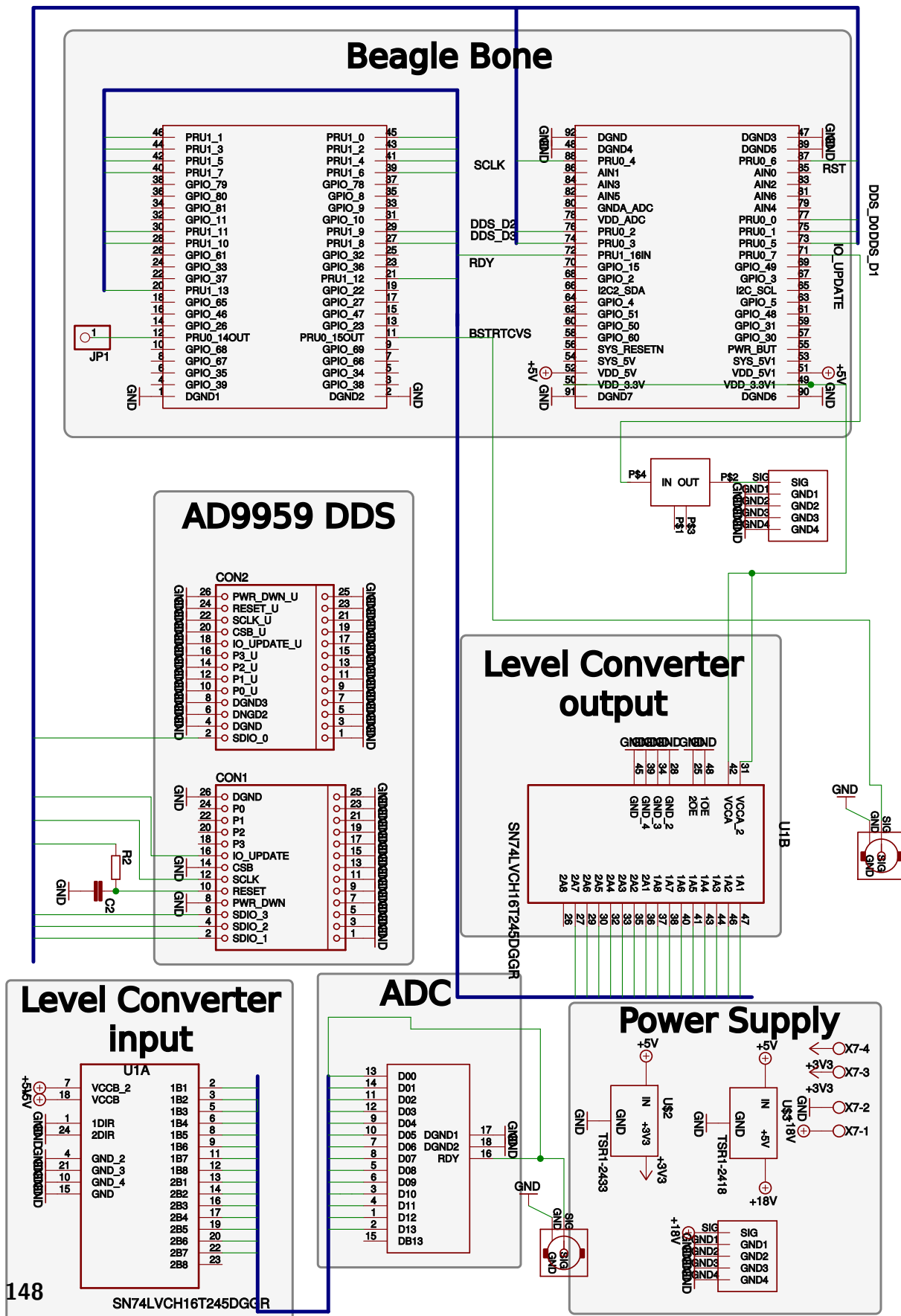


Figure C.2: Schematic of the fiber lock mainboard.

C.2 Fiber Lock Code

Here a simple example is given how a simple command for setting the frequency of the lock cascades through the software shells before it reached the actual device. For this example multiple wrapping of the same command might seem to create unnecessary overhead, but for more complicated scenarios it provides vital functionality on every layer, as in the case of another more complex example of a matlab scripts we implemented that allow to monitor and operate the controller by providing a GUI, that shows the error and steering signal, as well as their Fourier spectra, in realtime and allows to manipulate the PID constants via a slider bar without interrupting the lock.

The first code snippet in Fig. C.3 is a realistical use case where the error functions resulting from two different PID settings are compared.



Figure C.3: Code snippets for a simple command to set the frequency of the lock.

Bibliography

- [1] J. Oprea: “Geometry and the Foucault Pendulum”, Am. Math. Mon. **102** (6), 515–522 (1995). [↑1](#)
- [2] A. Einstein: “Zur Elektrodynamik bewegter Körper [AdP 17, 891 (1905)]”, Ann. Phys. **14** (S1), 194–224 (2005). [↑1](#)
- [3] A. Einstein: “Die Grundlage der allgemeinen Relativitätstheorie”, Ann. Phys. **354** (7), 769–822 (1916). [↑1](#)
- [4] Y. Aharonov and D. Bohm: “Significance of Electromagnetic Potentials in the Quantum Theory”, Phys. Rev. **115** (3), 485–491 (1959). [↑1](#), [↑55](#)
- [5] K. V. Klitzing, G. Dorda and M. Pepper: “New method for high-accuracy determination of the fine-structure constant based on quantized hall resistance”, Phys. Rev. Lett. **45** (6), 494–497 (1980). [↑1](#), [↑49](#)
- [6] K. Von Klitzing: “The quantized Hall effect”, Rev. Mod. Phys. **58** (3), 519 (1986). [↑1](#)
- [7] D. J. Thouless, M. Kohmoto, M. P. Nightingale and M. Den Nijs: “Quantized hall conductance in a two-Dimensional periodic potential”, Phys. Rev. Lett. **49** (6), 405–408 (1982). [↑1](#), [↑2](#), [↑49](#)
- [8] B. Simon: “Holonomy, the quantum adiabatic theorem, and Berry’s phase”, Phys. Rev. Lett. **51** (24), 2167–2170 (1983). [↑1](#), [↑2](#), [↑49](#), [↑52](#), [↑55](#)
- [9] M. Sato and Y. Ando: “Topological superconductors: a review”, Reports Prog. Phys. **80** (7), 76501 (2017). [↑1](#)
- [10] M. Z. Hasan and C. L. Kane: “Colloquium: Topological insulators”, Rev. Mod. Phys. **82** (4), 3045–3067 (2010). [↑2](#)
- [11] Y. Ando: “Topological insulator materials”, J. Phys. Soc. Japan **82** (10), 1–32 (2013). [↑1](#)
- [12] M. A. Nielsen and I. L. Chuang: *Quantum computation and quantum information*, Cambridge university press (2010). [↑1](#)

- [13] L. Fu and C. L. Kane: “Superconducting Proximity Effect and Majorana Fermions at the Surface of a Topological Insulator”, *Phys. Rev. Lett.* **100** (9), 096407 (2008). [↑1](#)
- [14] M. V. Berry: “Quantal Phase Factors Accompanying Adiabatic Changes”, *Proc. R. Soc. A Math. Phys. Eng. Sci.* **392** (1802), 45–57 (1984). [↑2](#), [↑49](#), [↑50](#), [↑54](#)
- [15] J. Dalibard, F. Gerbier, G. Juzeliunas and P. Öhberg: “Colloquium: Artificial gauge potentials for neutral atoms”, *Rev. Mod. Phys.* **83** (4), 1523–1543 (2011). [↑2](#), [↑3](#), [↑58](#)
- [16] S.-s. Chern: “On the Curvatura Integra in a Riemannian Manifold”, *Ann. Math.* **46** (4), 674–684 (1945). [↑2](#)
- [17] Y. Hatsugai: “Chern number and edge states in the integer quantum Hall effect”, *Phys. Rev. Lett.* **71** (22), 3697 (1993). [↑2](#)
- [18] A. K. Geim: “Graphene: Status and Prospects”, *Science* (80-.). **324** (5934), 1530–1534 (2009). [↑2](#)
- [19] A. K. Geim and K. S. Novoselov: “The rise of graphene”, *Nat. Mater.* **6**, 183 (2007).
- [20] A. H. Castro Neto, F. Guinea, N. M. R. Peres, K. S. Novoselov and A. K. Geim: “The electronic properties of graphene”, *Rev. Mod. Phys.* **81** (1), 109–162 (2009). [↑2](#)
- [21] D. Xiao, M. C. Chang and Q. Niu: “Berry phase effects on electronic properties”, *Rev. Mod. Phys.* **82** (3), 1959–2007 (2010). [↑3](#), [↑54](#), [↑56](#)
- [22] M. O. Goerbig: “Electronic properties of graphene in a strong magnetic field”, *Rev. Mod. Phys.* **83** (4) (2011). [↑3](#)
- [23] D. Jaksch and P. Zoller: “The cold atom Hubbard toolbox”, *Ann. Phys. (N. Y.)* **315** (1), 52–79 (2005). [↑3](#)
- [24] M. Lewenstein, A. Sanpera, V. Ahufinger, B. Damski, A. Sen(De) and U. Sen: “Ultracold atomic gases in optical lattices: mimicking condensed matter physics and beyond”, *Adv. Phys.* **56** (2), 243–379 (2007).
- [25] I. Bloch, J. Dalibard and W. Zwerger: “Many-body physics with ultracold gases”, *Rev. Mod. Phys.* **80** (3), 885–964 (2008). [↑66](#)
- [26] I. Bloch, J. Dalibard and S. Nascimbène: “Quantum simulations with ultracold quantum gases”, *Nat. Phys.* **8** (4), 267–276 (2012). [↑9](#)
- [27] P. Windpassinger and K. Sengstock: “Engineering novel optical lattices”, *Reports Prog. Phys.* **76** (8), 086401 (2013). [↑3](#), [↑4](#)

-
- [28] N. Cooper: “Rapidly rotating atomic gases”, *Adv. Phys.* **57** (6), 539–616 (2008). [↑3](#)
- [29] A. L. Fetter: “Rotating trapped Bose-Einstein condensates”, *Rev. Mod. Phys.* **81** (2), 647–691 (2009). [↑3](#)
- [30] N. Goldman and J. Dalibard: “Periodically driven quantum systems: Effective Hamiltonians and engineered gauge fields”, *Phys. Rev. X* **4** (3), 1–29 (2014). [↑3](#), [↑60](#), [↑63](#)
- [31] M. Aidelsburger, M. Atala, S. Nascimbène, S. Trotzky, Y.-A. Chen and I. Bloch: “Experimental Realization of Strong Effective Magnetic Fields in an Optical Lattice”, *Phys. Rev. Lett.* **107** (25), 255301 (2011). [↑3](#)
- [32] J. Struck, C. Ölschläger, R. Le Targat, P. Soltan-Panahi, A. Eckardt, M. Lewenstein, P. Windpassinger and K. Sengstock: “Quantum simulation of frustrated classical magnetism in triangular optical lattices”, *Science* (80-.). **333** (6045), 996–999 (2011). [↑3](#), [↑4](#)
- [33] J. Struck, C. Ölschläger, M. Weinberg, P. Hauke, J. Simonet, A. Eckardt, M. Lewenstein, K. Sengstock and P. Windpassinger: “Tunable gauge potential for neutral and spinless particles in driven optical lattices”, *Phys. Rev. Lett.* **108** (22), 1–5 (2012). [↑4](#), [↑25](#), [↑58](#)
- [34] C. J. Kennedy, W. C. Burton, W. C. Chung and W. Ketterle: “Observation of Bose-Einstein condensation in a strong synthetic magnetic field”, *Nat. Phys.* **11** (10), 859–864 (2015). [↑3](#)
- [35] J. Struck, M. Weinberg, C. Ölschläger, P. Windpassinger, J. Simonet, K. Sengstock, R. Höppner, P. Hauke, A. Eckardt, M. Lewenstein and Others: “Engineering Ising-XY spin-models in a triangular lattice using tunable artificial gauge fields”, *Nat. Phys.* **9** (11), 738 (2013). [↑3](#), [↑4](#)
- [36] M. Aidelsburger, M. Atala, M. Lohse, J. T. Barreiro, B. Paredes and I. Bloch: “Realization of the Hofstadter Hamiltonian with Ultracold Atoms in Optical Lattices”, *Phys. Rev. Lett.* **111** (18), 185301 (2013). [↑3](#)
- [37] H. Miyake, G. A. Siviloglou, C. J. Kennedy, W. C. Burton and W. Ketterle: “Realizing the Harper Hamiltonian with Laser-Assisted Tunneling in Optical Lattices”, *Phys. Rev. Lett.* **111** (18), 185302 (2013). [↑3](#)
- [38] P. G. Harper: “Single Band Motion of Conduction Electrons in a Uniform Magnetic Field”, *Proc. Phys. Soc. Sect. A* **68** (10), 874–878 (1955). [↑3](#)
- [39] D. R. Hofstadter: “Energy levels and wave functions of Bloch electrons in rational and irrational magnetic fields”, *Phys. Rev. B* **14** (6), 2239–2249 (1976). [↑3](#)

- [40] L. Tarruell, D. Greif, T. Uehlinger, G. Jotzu and T. Esslinger: “Creating, moving and merging Dirac points with a Fermi gas in a tunable honeycomb lattice”, *Nature* **483** (7389), 302–305 (2012). [↑3](#), [↑13](#), [↑25](#), [↑32](#)
- [41] P. Soltan-Panahi, J. Struck, P. Hauke, A. Bick, W. Plenkers, G. Meineke, C. Becker, P. Windpassinger, M. Lewenstein and K. Sengstock: “Multi-component quantum gases in spin-dependent hexagonal lattices”, *Nat. Phys.* **7** (5), 434–440 (2011). [↑4](#), [↑25](#)
- [42] I. B. Spielman: “Detection of topological matter with quantum gases”, *Ann. Phys.* **525** (10-11), 797–807 (2013). [↑3](#)
- [43] M. Atala, M. Aidelsburger, J. T. Barreiro, D. Abanin, T. Kitagawa, E. Demler and I. Bloch: “Direct measurement of the Zak phase in topological Bloch bands”, *Nat. Phys.* **9** (12), 795–800 (2013). [↑3](#)
- [44] M. Atala, M. Aidelsburger, M. Lohse, J. T. Barreiro, B. Paredes and I. Bloch: “Observation of chiral currents with ultracold atoms in bosonic ladders”, *Nat. Phys.* **10** (8), 588–593 (2014). [↑3](#)
- [45] G. Jotzu, M. Messer, R. Desbuquois, M. Lebrat, T. Uehlinger, D. Greif and T. Esslinger: “Experimental realization of the topological Haldane model with ultracold fermions”, *Nature* **515** (7526), 237–240 (2014). [↑3](#), [↑4](#), [↑25](#)
- [46] F. D. M. Haldane: “Model for a quantum hall effect without landau levels: Condensed-matter realization of the “parity anomaly””, *Phys. Rev. Lett.* **61** (18), 2015–2018 (1988). [↑3](#), [↑42](#), [↑46](#)
- [47] C. Becker, P. Soltan-Panahi, J. Kronjäger, S. Dörscher, K. Bongs and K. Sengstock: “Ultracold quantum gases in triangular optical lattices”, *New J. Phys.* **12** (2010). [↑4](#), [↑25](#), [↑32](#)
- [48] B. A. Bernevig and T. L. Hughes: *Topological Insulators and Topological Superconductors*, Princeton University Press (2013), ISBN 9780691151755. [↑4](#), [↑55](#)
- [49] M. Aidelsburger, M. Lohse, C. Schweizer, M. Atala, J. T. Barreiro, S. Nascimbène, N. R. Cooper, I. Bloch and N. Goldman: “Measuring the Chern number of Hofstadter bands with ultracold bosonic atoms”, *Nat. Phys.* **11** (2), 162–166 (2015). [↑4](#)
- [50] J. H. Shirley: “Solution of the schrödinger equation with a hamiltonian periodic in time”, *Phys. Rev.* **138** (4B) (1965). [↑4](#)
- [51] S. I. Chu and D. A. Telnov: “Beyond the Floquet theorem: Generalized Floquet formalisms and quasienergy methods for atomic and molecular multiphoton processes in intense laser fields”, *Phys. Rep.* **390** (1-2), 1–131 (2004).

-
- [52] F. Grossmann, T. Dittrich, P. Jung and P. Hänggi: “Coherent destruction of tunneling”, *Phys. Rev. Lett.* **67** (4), 516 (1991).
- [53] M. Grifoni and P. Hänggi: “Driven quantum tunneling”, *Phys. Rep.* **304** (5-6), 229–354 (1998).
- [54] P. Hänggi: “Driven quantum systems”, *Quantum Transp. Dissipation* (Wiley-VCH, Weinheim, 1998) pages 249–286 (1998).
- [55] T. Kitagawa, E. Berg, M. Rudner and E. Demler: “Topological characterization of periodically driven quantum systems”, *Phys. Rev. B - Condens. Matter Mater. Phys.* **82** (23), 1–12 (2010).
- [56] A. Gómez-León and G. Platero: “Floquet-Bloch theory and topology in periodically driven lattices”, *Phys. Rev. Lett.* **110** (20), 200403 (2013).
- [57] A. Eckardt: “Colloquium: Atomic quantum gases in periodically driven optical lattices”, *Rev. Mod. Phys.* **89** (1), 1–30 (2017). [↑4](#), [↑58](#), [↑59](#)
- [58] C. Sias, H. Lignier, Y. P. Singh, A. Zenesini, D. Ciampini, O. Morsch and E. Arimondo: “Observation of photon-assisted tunneling in optical lattices”, *Phys. Rev. Lett.* **100** (4), 40404 (2008). [↑4](#)
- [59] P. Hauke, O. Tieleman, A. Celi, C. Ölschläger, J. Simonet, J. Struck, M. Weinberg, P. Windpassinger, K. Sengstock, M. Lewenstein and A. Eckardt: “Non-Abelian Gauge Fields and Topological Insulators in Shaken Optical Lattices”, *Phys. Rev. Lett.* **109** (14), 145301 (2012). [↑4](#)
- [60] C. V. Parker, L.-C. Ha and C. Chin: “Direct observation of effective ferromagnetic domains of cold atoms in a shaken optical lattice”, *Nat. Phys.* **9** (12), 769–774 (2013).
- [61] W. Zheng and H. Zhai: “Floquet topological states in shaking optical lattices”, *Phys. Rev. A - At. Mol. Opt. Phys.* **89** (6), 1–5 (2014). [↑4](#)
- [62] N. Fläschner, B. S. Rem, M. Tarnowski, D. Vogel, D.-S. Luhmann, K. Sengstock and C. Weitenberg: “Experimental reconstruction of the Berry curvature in a Floquet Bloch band”, *Science* (80-.). **352** (6289), 1091–1094 (2016). [↑4](#), [↑7](#), [↑12](#), [↑71](#)
- [63] L. Duca, T. Li, M. Reitter, I. Bloch, M. Schleier-Smith and U. Schneider: “An Aharonov-Bohm interferometer for determining Bloch band topology”, *Science* (80-.). **347** (6219), 288–292 (2015). [↑4](#), [↑25](#), [↑55](#)
- [64] N. Fläschner, D. Vogel, M. Tarnowski, B. S. Rem, D.-S. Lühmann, M. Heyl, J. C. Budich, L. Mathey, K. Sengstock and C. Weitenberg: “Observation of dynamical

- vortices after quenches in a system with topology”, *Nat. Phys.* **14** (3), 265–268 (2018). [↑4](#), [↑7](#), [↑12](#), [↑72](#), [↑75](#), [↑76](#), [↑77](#), [↑99](#), [↑101](#), [↑102](#), [↑103](#), [↑105](#), [↑106](#), [↑108](#)
- [65] M. Tarnowski, F. N. Ünal, N. Fläschner, B. S. Rem, A. Eckardt, K. Sengstock and C. Weitenberg: “Characterizing topology by dynamics: Chern number from linking number”, *arXiv Prepr. arXiv1709.01046* **1**, 1–14 (2017). [↑4](#), [↑5](#), [↑109](#)
- [66] J. Yu: “Phase vortices of the quenched Haldane model”, *Phys. Rev. A* **96** (2), 1–7 (2017). [↑88](#), [↑109](#)
- [67] C. Wang, P. Zhang, X. Chen, J. Yu and H. Zhai: “Scheme to Measure the Topological Number of a Chern Insulator from Quench Dynamics”, *Phys. Rev. Lett.* **118** (18), 1–5 (2017). [↑4](#), [↑88](#), [↑109](#)
- [68] M. D. Caio, N. R. Cooper and M. J. Bhaseen: “Quantum Quenches in Chern Insulators”, *Phys. Rev. Lett.* **115** (23), 2–6 (2015). [↑4](#), [↑5](#)
- [69] L. D’Alessio and M. Rigol: “Dynamical preparation of Floquet Chern insulators”, *Nat. Commun.* **6** (1), 8336 (2015). [↑4](#), [↑88](#)
- [70] M. Heyl, A. Polkovnikov and S. Kehrein: “Dynamical quantum phase transitions in the transverse-field ising model”, *Phys. Rev. Lett.* **110** (13), 1–5 (2013). [↑4](#), [↑5](#), [↑79](#), [↑90](#), [↑91](#), [↑95](#), [↑99](#)
- [71] M. Heyl: “Dynamical quantum phase transitions: a review”, *arXiv* (2017). [↑94](#)
- [72] A. A. Zvyagin: “Dynamical quantum phase transitions (Review Article)”, *Low Temp. Phys.* **42** (11), 971–994 (2016). [↑4](#)
- [73] R. A. Blythe and M. R. Evans: “Lee-Yang zeros and phase transitions in nonequilibrium steady states”, *Phys. Rev. Lett.* **89** (8), 080601/1–080601/4 (2002). [↑5](#)
- [74] P. Arndt: “Yang-Lee theory for a nonequilibrium phase transition”, *Phys. Rev. Lett.* **84** (5), 814–7 (2000).
- [75] B. B. Wei and R. B. Liu: “Lee-Yang zeros and critical times in decoherence of a probe spin coupled to a bath”, *Phys. Rev. Lett.* **109** (18), 3–7 (2012).
- [76] B.-B. Wei, S.-W. Chen, H.-C. Po and R.-B. Liu: “Phase transitions in the complex plane of physical parameters”, *Sci. Rep.* **4** (1), 5202 (2015). [↑5](#)
- [77] A. LeClair, G. Mussardo, H. Saleur and S. Skorik: “Boundary energy and boundary states in integrable quantum field theories”, *Nucl. Physics, Sect. B* **453** (3), 581–618 (1995). [↑5](#), [↑91](#)

-
- [78] M. Schmitt and S. Kehrein: “Dynamical quantum phase transitions in the Kitaev honeycomb model”, *Phys. Rev. B - Condens. Matter Mater. Phys.* **92** (7), 1–13 (2015). [↑5](#)
- [79] S. Vajna and B. Dóra: “Topological classification of dynamical phase transitions”, *Phys. Rev. B - Condens. Matter Mater. Phys.* **91** (15), 1–5 (2015). [↑5](#), [↑85](#), [↑92](#), [↑93](#), [↑94](#), [↑95](#), [↑109](#)
- [80] Y. Hu, P. Zoller and J. C. Budich: “Dynamical Buildup of a Quantized Hall Response from Nontopological States”, *Phys. Rev. Lett.* **117** (12), 1–5 (2016).
- [81] F. N. Ünal, E. J. Mueller and M. O. Oktel: “Nonequilibrium fractional Hall response after a topological quench”, *Phys. Rev. A* **94** (5), 1–7 (2016). [↑5](#)
- [82] M. Heyl: “Scaling and Universality at Dynamical Quantum Phase Transitions”, *Phys. Rev. Lett.* **115** (14), 1–5 (2015). [↑5](#), [↑92](#)
- [83] S. Pancharatnam: “Generalized theory of interference, and its applications”, *Proc. Indian Acad. Sci. - Sect. A* **44** (5), 247–262 (1956). [↑5](#), [↑50](#)
- [84] J. C. Budich and M. Heyl: “Dynamical topological order parameters far from equilibrium”, *Phys. Rev. B* **93** (8), 1–7 (2016). [↑5](#), [↑82](#), [↑85](#), [↑94](#), [↑96](#)
- [85] S. Sharma, U. Divakaran, A. Polkovnikov and A. Dutta: “Slow quenches in a quantum Ising chain: Dynamical phase transitions and topology”, *Phys. Rev. B* **93** (14), 1–9 (2016). [↑5](#)
- [86] T. D. Lee and C. N. Yang: “Statistical theory of equations of state and phase transitions. II. Lattice gas and ising model”, *Phys. Rev.* **87** (3), 410–419 (1952). [↑5](#), [↑91](#)
- [87] C. N. Yang and T. D. Lee: “Statistical theory of equations of state and phase transitions. I. Theory of condensation”, *Phys. Rev.* **87** (3), 404–409 (1952). [↑5](#), [↑91](#)
- [88] X. Peng, H. Zhou, B. B. Wei, J. Cui, J. Du and R. B. Liu: “Experimental observation of Lee-Yang zeros”, *Phys. Rev. Lett.* **114** (1), 1–5 (2015). [↑5](#)
- [89] N. Fläschner, D. Vogel, M. Tarnowski, B. S. Rem, D.-S. Lühmann, M. Heyl, J. C. Budich, L. Mathey, K. Sengstock and C. Weitenberg: “Observation of a dynamical topological phase transition”, *arXiv Prepr. arXiv1608.05616* (2016). [↑5](#), [↑73](#), [↑88](#), [↑96](#), [↑99](#), [↑102](#), [↑103](#), [↑109](#)
- [90] P. Jurcevic, H. Shen, P. Hauke, C. Maier, T. Brydges, C. Hempel, B. P. Lanyon, M. Heyl, R. Blatt and C. F. Roos: “Direct Observation of Dynamical Quantum Phase Transitions in an Interacting Many-Body System”, *Phys. Rev. Lett.* **119** (8), 080501 (2017). [↑5](#), [↑99](#), [↑109](#)

- [91] J. Zhang, G. Pagano, P. W. Hess, A. Kyprianidis, P. Becker, H. Kaplan, A. V. Gorshkov, Z. X. Gong and C. Monroe: “Observation of a many-body dynamical phase transition with a 53-qubit quantum simulator”, *Nature* **551** (7682), 601–604 (2017). [↑5](#)
- [92] K. Brandner, V. F. Maisi, J. P. Pekola, J. P. Garrahan and C. Flindt: “Experimental Determination of Dynamical Lee-Yang Zeros”, *Phys. Rev. Lett.* **118** (18) (2017). [↑5](#), [↑99](#), [↑109](#)
- [93] E. J. Sie, J. W. McIver, Y. H. Lee, L. Fu, J. Kong and N. Gedik: “Valley-selective optical Stark effect in monolayer WS₂”, *Nat. Mater.* **14** (3), 290–294 (2015). [↑9](#), [↑58](#)
- [94] A. Damascelli: “Probing the Electronic Structure of Complex Systems by ARPES”, *Phys. Scr.* **T109**, 61–74 (2004). [↑9](#)
- [95] A. Bostwick, T. Ohta, T. Seyller, K. Horn and E. Rotenberg: “Quasiparticle dynamics in graphene”, *Nat. Phys.* **3** (1), 36–40 (2007). [↑9](#)
- [96] N. Fläschner: “Ultracold Fermions in Tunable Hexagonal Lattices: From High-Precision Spectroscopy to the Measurement of Berry Curvature”, Univ. Hambg. - PhD Thesis (2016). [↑9](#), [↑11](#), [↑12](#), [↑14](#), [↑15](#)
- [97] M. Tarnowski: “Implementation and Characterization of a Gray Molasses and of Tunable Hexagonal Optical Lattices for 40K”, Univ. Hambg. - Master Thesis (April) (2015). [↑9](#), [↑11](#), [↑15](#), [↑113](#)
- [98] M. Langbecker: “Tunable Interactions and Lattice Geometries in Fermionic Quantum Gases”, Univ. Hambg. - Master Thesis (October) (2013). [↑9](#), [↑13](#), [↑15](#), [↑113](#)
- [99] C. Ospelkaus: “Fermi-Bose mixtures — From mean-field interactions to ultracold chemistry”, PhD Thesis - Univ. Hambg. (2006). [↑10](#), [↑11](#)
- [100] S. Ospelkaus-Schwarzer: “Quantum Degenerate Fermi-Bose Mixtures of 40K and 87Rb in 3D Optical Lattices”, PhD Thesis - Univ. Hambg. (2006). [↑10](#), [↑11](#)
- [101] C. Becker: “Multi component Bose-Einstein condensates”, PhD Thesis - Univ. Hambg. (2008). [↑10](#), [↑14](#), [↑15](#), [↑37](#), [↑112](#), [↑115](#)
- [102] S. E. Dörscher: “Creation of ytterbium quantum gases with a compact D- / D-MOT setup”, PhD Thesis - Univ. Hambg. (2013).
- [103] A. Bick: “Interfacing Ultracold Atoms and a Cryogenic Micromechanical Oscillator”, Univ. Hambg. - PhD Thesis (2015). [↑10](#)
- [104] T. G. Tiecke: “Properties of Potassium”, *Physics* (College. Park. Md). **02** (20), 1–14 (2010). [↑10](#)

-
- [105] C. J. Foot: *Atomic physics*, Oxford master series in physics, Oxford University Press (2005), ISBN 9780198506966. [↑10](#), [↑11](#)
- [106] W. Ketterle, K. B. Davis, M. A. Joffe, A. Martin and D. E. Pritchard: “High densities of cold atoms in a dark spontaneous-force optical trap”, *Phys. Rev. Lett.* **70** (15), 2253–2256 (1993). [↑10](#)
- [107] R. Grimm, M. Weidemüller and Y. Ovchinnikov: “Optical dipole trap for neutral atoms”, *Adv. At. Mol. Opt. Phys.* **42**, 95 (2000). [↑11](#), [↑26](#)
- [108] H. Kogelnik and T. Li: “Laser Beams and Resonators”, *Appl. Opt.* **5** (10), 1550–1567 (1966). [↑12](#), [↑27](#)
- [109] A. Kobayakov, M. Sauer and D. Chowdhury: “Stimulated Brillouin scattering in optical fibers”, *Adv. Opt. Photonics* **2** (1), 1 (2010). [↑14](#)
- [110] C. F. Ockeloen, A. F. Tauschinsky, R. J. Spreeuw and S. Whitlock: “Detection of small atom numbers through image processing”, *Phys. Rev. A - At. Mol. Opt. Phys.* **82** (6) (2010). [↑18](#), [↑21](#)
- [111] J. Kronjäger: “Coherent dynamics of spinor Bose-Einstein condensates”, *Laser Phys.* **48** (6), 1041–1046 (2007). [↑18](#), [↑19](#)
- [112] M. Erhard: “Experimente mit mehrkomponentigen Bose-Einstein-Kondensaten”, Doktorarbeit, Univ. Hambg. page 161 (2004). [↑18](#), [↑21](#)
- [113] W. Ketterle, D. S. Durfee and D. M. Stamper-Kurn: “Making, probing and understanding Bose-Einstein condensates”, *arXiv Prepr. cond-mat/9904034* (1999). [↑19](#), [↑21](#)
- [114] A. Hemmerich and T. W. Hänsch: “Two-dimensional atomic crystal bound by light”, *Phys. Rev. Lett.* **70** (4), 410–413 (1993). [↑25](#)
- [115] P. S. Jessen, C. Gerz, P. D. Lett, W. D. Phillips, S. L. Rolston, R. J. Spreeuw and C. I. Westbrook: “Observation of quantized motion of Rb atoms in an optical field”, *Phys. Rev. Lett.* **69** (1), 49–52 (1992).
- [116] P. Verkerk, B. Lounis, C. Salomon, C. Cohen-Tannoudji, J. Y. Courtois and G. Grynberg: “Dynamics and spatial order of cold cesium atoms in a periodic optical potential”, *Phys. Rev. Lett.* **68** (26), 3861–3864 (1992). [↑25](#)
- [117] M. H. Anderson, J. R. Ensher, M. R. Matthews, C. E. Wieman and E. A. Cornell: “Observation of Bose-Einstein Condensation in a Dilute Atomic Vapor”, *Science* (80-). **269** (5221), 198–201 (1995). [↑25](#)

- [118] G. Grynberg, B. Lounis, P. Verkerk, J. Y. Courtois and C. Salomon: “Quantized motion of cold cesium atoms in two- and three-dimensional optical potentials”, *Phys. Rev. Lett.* **70** (15), 2249–2252 (1993). [↑25](#)
- [119] P. Soltan-Panahi, D. S. Löhmann, J. Struck, P. Windpassinger and K. Sengstock: “Quantum phase transition to unconventional multi-orbital superfluidity in optical lattices”, *Nat. Phys.* **8** (1), 71–75 (2012). [↑25](#)
- [120] T. Li, L. Duca, M. Reitter, F. Grusdt, E. Demler, M. Endres, M. Schleier-Smith, I. Bloch and U. Schneider: “Bloch state tomography using Wilson lines”, *Science* (80-.). **352** (6289), 1094–1097 (2016). [↑51](#)
- [121] F. Görg, M. Messer, K. Sandholzer, G. Jotzu, R. Desbuquois and T. Esslinger: “Enhancement and sign reversal of magnetic correlations in a driven quantum many-body system”, *Nat. Publ. Gr.* **553** (7689), 481–485 (2017). [↑25](#)
- [122] K. I. Petsas, A. B. Coates and G. Grynberg: “Crystallography of optical lattices”, *Phys. Rev. A* **50** (6), 5173–5189 (1994). [↑28](#)
- [123] J. D. Cloizeaux: “Analytical properties of n-dimensional energy bands and wannier functions”, *Phys. Rev.* **135** (3A) (1964). [↑41](#), [↑43](#)
- [124] W. Kohn: “Analytic properties of Bloch waves and Wannier functions”, *Phys. Rev.* **115** (4), 809–821 (1959). [↑41](#), [↑42](#)
- [125] N. Marzari, A. A. Mostofi, J. R. Yates, I. Souza and D. Vanderbilt: “Maximally localized Wannier functions: Theory and applications”, *Rev. Mod. Phys.* **84** (4), 1419–1475 (2012). [↑42](#)
- [126] R. Walters, G. Cotugno, T. H. Johnson, S. R. Clark and D. Jaksch: “Ab initio derivation of Hubbard models for cold atoms in optical lattices”, *Phys. Rev. A* **043613**, 1–13 (2013).
- [127] D. Monaco and G. Panati: “Topological Invariants of Eigenvalue Intersections and Decrease of Wannier Functions in Graphene”, *J. Stat. Phys.* **155** (6), 1027–1071 (2014).
- [128] D. S. Lühmann, O. Jürgensen, M. Weinberg, J. Simonet, P. Soltan-Panahi and K. Sengstock: “Quantum phases in tunable state-dependent hexagonal optical lattices”, *Phys. Rev. A - At. Mol. Opt. Phys.* **90** (1) (2014).
- [129] J. Ibañez-Azpiroz, A. Eiguren, A. Bergara, G. Pettini and M. Modugno: “Tight-binding models for ultracold atoms in honeycomb optical lattices”, *Phys. Rev. A* **87** (1), 11602 (2013).

-
- [130] J. Ibañez-Azpiroz, A. Eiguren, A. Bergara, G. Pettini and M. Modugno: “Self-consistent tight-binding description of Dirac points moving and merging in two-dimensional optical lattices”, *Phys. Rev. A - At. Mol. Opt. Phys.* **88** (3), 1–11 (2013).
- [131] D. Fiorenza, D. Monaco and G. Panati: “Construction of Real-Valued Localized Composite Wannier Functions for Insulators”, *Ann. Henri Poincare* **17** (1), 63–97 (2016). [↑42](#)
- [132] M. Lebrat: “Engineering artificial gauge fields in time-modulated optical lattices”, Master thesis (2013). [↑42](#), [↑60](#)
- [133] G. W. Semenoff: “Condensed-Matter simulation of a three-Dimensional anomaly”, *Phys. Rev. Lett.* **53** (26), 2449–2452 (1984). [↑42](#), [↑45](#)
- [134] D. Sticlet, F. Piéchon, J. N. Fuchs, P. Kalugin and P. Simon: “Geometrical engineering of a two-band Chern insulator in two dimensions with arbitrary topological index”, *Phys. Rev. B - Condens. Matter Mater. Phys.* **85** (16), 1–10 (2012). [↑47](#), [↑86](#)
- [135] T. Ando: “Theory of Quantum Transport in a Two-Dimensional Electron System under Magnetic Fields. IV. Oscillatory Conductivity”, *J. Phys. Soc. Japan* **37** (5), 1233–1237 (1974). [↑49](#)
- [136] J. Anandan and L. Stodolsky: “Some geometrical considerations of Berry’s phase”, *Phys. Rev. D* **35** (8), 2597–2600 (1987). [↑50](#)
- [137] J. Samuel and R. Bhandari: “General Setting for Berry Phase”, *Phys. Rev. Lett.* **60** (June), 2339–2342 (1988). [↑50](#), [↑52](#), [↑54](#)
- [138] A. Messiah: *Quantum mechanics*, number v. 2 in Quantum Mechanics, North-Holland Pub. Co. (1962). [↑50](#)
- [139] F. Wilczek and A. Zee: “Appearance of gauge structure in simple dynamical systems”, *Phys. Rev. Lett.* **52** (24), 2111–2114 (1984). [↑51](#)
- [140] J. H. Hannay: “Angle variable holonomy in adiabatic excursion of an integrable Hamiltonian”, *J. Phys. A* **18** (2), 221–230 (1985). [↑53](#)
- [141] J. Kübler and C. Felser: “Berry curvature and the anomalous Hall effect in Heusler compounds”, *Phys. Rev. B - Condens. Matter Mater. Phys.* **85** (1), 2–5 (2012). [↑54](#)
- [142] J. N. Fuchs, F. Piéchon, M. O. Goerbig and G. Montambaux: “Topological Berry phase and semiclassical quantization of cyclotron orbits for two dimensional electrons in coupled band models”, *Eur. Phys. J. B* **77** (3), 351–362 (2010). [↑56](#)

- [143] E. Alba, X. Fernandez-Gonzalvo, J. Mur-Petit, J. K. Pachos and J. J. Garcia-Ripoll: “Seeing topological order in time-of-flight measurements”, *Phys. Rev. Lett.* **107** (23), 1–5 (2011). [↑57](#), [↑65](#), [↑66](#)
- [144] J. Dalibard: “Introduction to the physics of artificial gauge fields”, Collège Fr. Lab. Kastler Bross. (2014). [↑58](#)
- [145] E. Arimondo, D. Ciampini, A. Eckardt, M. Holthaus and O. Morsch: *Kilohertz-Driven Bose-Einstein Condensates in Optical Lattices*, volume 61, Elsevier Inc. (2012), ISBN 9780123964823. [↑58](#)
- [146] T. Oka and H. Aoki: “Photovoltaic Hall effect in graphene”, *Phys. Rev. B - Condens. Matter Mater. Phys.* **79** (8), 1–4 (2009). [↑58](#)
- [147] N. Goldman, G. Juzeliūnas, P. Öhberg and I. B. Spielman: “Light-induced gauge fields for ultracold atoms”, *Reports Prog. Phys.* **77** (12), 126401 (2014). [↑58](#), [↑63](#)
- [148] H. Sambe: “Steady states and quasienergies of a quantum-mechanical system in an oscillating field”, *Phys. Rev. A* **7** (6), 2203–2213 (1973). [↑59](#), [↑60](#)
- [149] M. Bukov, L. D’Alessio and A. Polkovnikov: “Universal high-frequency behavior of periodically driven systems: From dynamical stabilization to Floquet engineering”, *Adv. Phys.* **64** (2), 139–226 (2015). [↑59](#), [↑60](#)
- [150] P. Hauke, M. Lewenstein and A. Eckardt: “Tomography of band insulators from quench dynamics”, *Phys. Rev. Lett.* **113** (4), 1–5 (2014). [↑65](#), [↑66](#), [↑78](#)
- [151] E. Alba, X. Fernandez-Gonzalvo, J. Mur-Petit, J. J. Garcia-Ripoll and J. K. Pachos: “Simulating Dirac fermions with Abelian and non-Abelian gauge fields in optical lattices”, *Ann. Phys. (N. Y.)* **328**, 64–82 (2013). [↑65](#)
- [152] H. Schmidt: “Dynamische Kontrolle der Geometrie optischer Gitter”, Ph.D. thesis, University of Hamburg (2015). [↑66](#)
- [153] F. Gerbier, S. Trotzky, S. Fölling, U. Schnorrberger, J. D. Thompson, A. Widera, I. Bloch, L. Pollet, M. Troyer, B. Capogrosso-Sansone, N. V. Prokof’ev and B. V. Svistunov: “Expansion of a quantum gas released from an optical lattice”, *Phys. Rev. Lett.* **101** (15), 1–5 (2008). [↑66](#)
- [154] M. Köhl, H. Moritz, T. Stöferle, K. Günter and T. Esslinger: “Fermionic atoms in a three dimensional optical lattice: Observing Fermi surfaces, dynamics, and interactions”, *Phys. Rev. Lett.* **94** (8), 1–4 (2005). [↑68](#)
- [155] W. Burger and M. J. Burge: *Principles of Digital Image Processing: Fundamental Techniques*, Undergraduate Topics in Computer Science, Springer London (2010), ISBN 9781848001916. [↑80](#)

-
- [156] J. Billy, V. Josse, Z. Zuo, A. Bernard, B. Hambrecht, P. Lugan, D. Clément, L. Sanchez-Palencia, P. Bouyer and A. Aspect: “Direct observation of Anderson localization of matter waves in a controlled disorder”, *Nature* **453** (7197), 891–894 (2008). [↑90](#)
- [157] G. Roati, C. D’Errico, L. Fallani, M. Fattori, C. Fort, M. Zaccanti, G. Modugno, M. Modugno and M. Inguscio: “Anderson localization of a non-interacting Bose–Einstein condensate”, *Nature* **453** (7197), 895–898 (2008).
- [158] M. Schreiber, S. S. Hodgman, P. Bordia, H. P. Luschen, M. H. Fischer, R. Vosk, E. Altman, U. Schneider and I. Bloch: “Observation of many-body localization of interacting fermions in a quasirandom optical lattice”, *Science* (80-.). **349** (6250), 842–845 (2015). [↑90](#)
- [159] M. Vojta: “Quantum phase transitions”, *Reports Prog. Phys.* **66** (12), 2069–2110 (2003). [↑90](#)
- [160] S. Sachdev: *Quantum phase transitions*, Wiley Online Library (2007). [↑90](#)
- [161] J. Eisert, M. Friesdorf and C. Gogolin: “Quantum many-body systems out of equilibrium”, *Nat. Phys.* **11**, 124 (2015). [↑90](#)
- [162] M. E. Fisher: “The theory of equilibrium critical phenomena”, *Reports Prog. Phys.* **30** (2), 615 (1967). [↑91](#)
- [163] N. Fläschner, M. Tarnowski, B. S. Rem, D. Vogel, K. Sengstock and C. Weitenberg: “High precision spectroscopy of ultracold atoms in optical lattices”, *arXiv Prepr. arXiv1801.05614* (2018). [↑107](#)
- [164] L. S. Ma, P. Jungner, J. Ye and J. L. Hall: “Delivering the same optical frequency at two places: accurate cancellation of phase noise introduced by an optical fiber or other time-varying path.”, *Opt. Lett.* **19** (21), 1777–1779 (1994). [↑112](#), [↑115](#), [↑128](#)
- [165] Y. Pang, J. J. Hamilton and J.-P. Richard: “Frequency noise induced by fiber perturbations in a fiber-linked stabilized laser”, *Appl. Opt.* **31** (36), 7532–7534 (1992). [↑112](#)
- [166] S. M. Foreman, K. W. Holman, D. D. Hudson, D. J. Jones and J. Ye: “Remote transfer of ultrastable frequency references via fiber networks”, *Rev. Sci. Instrum.* **78** (2), 0–25 (2007). [↑112](#)
- [167] D. Greif, T. Uehlinger, G. Jotzu, L. Tarruell and T. Esslinger: “Short-Range Quantum Magnetism of Ultracold Fermions in an Optical Lattice”, *Science* (80-.). **340** (6138), 1307–1310 (2013). [↑112](#), [↑113](#)

- [168] W. S. Bakr, J. I. Gillen, A. Peng, S. Fölling and M. Greiner: “A quantum gas microscope for detecting single atoms in a Hubbard-regime optical lattice”, *Nature* **462**, 74 (2009). [↑112](#)
- [169] J. F. Sherson, C. Weitenberg, M. Endres, M. Cheneau, I. Bloch and S. Kuhr: “Single-atom-resolved fluorescence imaging of an atomic Mott insulator”, *Nature* **467** (7311), 68–72 (2010). [↑112](#)
- [170] J. Bernardoff: “A setup for imprinting artificial magnetic fields on ultracold atoms”, Master Thesis - Ludwig-Maximilians-Universität München (2013). [↑112](#), [↑113](#)
- [171] C. Wei, S. Yan, A. Jia, Y. Luo, Q. Hu and Z. Li: “Compact phase-lock loop for external cavity diode lasers”, *Chin. Opt. Lett.* **14** (5), 51403 (2016).
- [172] F. Seidler: “Digital high bandwidth feedback controller”, Master Thesis - Friedrich-Wilhelms-Universität Bonn (2015).
- [173] J. B. Naber, J. Vos, R. J. Rengelink, R. J. Nusselder and D. Davtyan: “Optical techniques for Rydberg physics in lattice geometries: A technical guide”, *Eur. Phys. J. Spec. Top.* **225** (15-16), 2785–2816 (2016). [↑112](#)
- [174] C. Robens, S. Brakhane, W. Alt, D. Meschede, J. Zopes and A. Alberti: “Fast, high-precision optical polarization synthesizer for ultracold-atom experiments”, *arXiv Prepr. arXiv1611.07952* pages 1–9 (2016). [↑113](#)
- [175] I. H. Malitson: “Interspecimen Comparison of the Refractive Index of Fused Silica*,†”, *J. Opt. Soc. Am.* **55** (10), 1205 (1965). [↑117](#)
- [176] “4-Channel 500 MSPS DDS with 10-Bit DACs”, Technical report, Analog Devices (2005). [↑125](#)
- [177] J. Bechhoefer: “Feedback for physicists: A tutorial essay on control”, *Rev. Mod. Phys.* **77** (3), 783–836 (2005). [↑125](#), [↑128](#), [↑131](#), [↑135](#)
- [178] I. Lee, J. Y. T. Leung and S. H. Son: *Handbook of Real-Time and Embedded Systems*, Chapman Hall/CRC Computer and Information Science Series, CRC Press (2007), ISBN 9781420011746. [↑128](#)
- [179] T. Instruments: “AM335x Sitara™ Processors 1”, Data sheet (2016). [↑128](#)
- [180] T. Instruments: “AM335x PRU-ICSS Reference Guide”, Technical Report May 2012 (2013). [↑128](#)